Universitat Autònoma de Barcelona

Departament de Geologia
Unitat de Petrologia i Geoquímica

Evolució del mantell subcontinental litosfèric del NE d'Ibèria a partir de l'orientació cristal·logràfica preferent i la geoquímica de xenòlits mantèl·lics

Tesis doctoral

Mercè Fernàndez-Roig

Dirigida per Gumer Galán

2017

CAPÍTOL 12

GEOQUÍMICA DE ROCA TOTAL (MAJORS I TRAÇA) I ELEMENTS TRAÇA EN CLINOPIROXÈ

12. 1. Elements majors en roca total

L'anàlisi d'elements majors en xenòlits mantèl·lics peridotítics dóna informació del grau de fertilitat del mantell, ja sigui conseqüència de processos d'empobriment per fusió parcial (Frey & Green, 1974), d'interaccions roca-fos que causin la refertilització del mateix (Bodinier & Godard, 2003; Beyer et al., 2006; O'Reilly & Griffin, 2013) o d'altres processos metasomàtics (Menzies, 1987; Coltorti & Grégoire, 2008).

En la primera part d'aquest capítol ens centrarem en:

- L'avaluació de la composició en elements majors dels xenòlits estudiats.
- La seva trajectòria evolutiva.
- Les similituds i diferències que presenten respecte a les estudiades anteriorment.
- La relació entre la composició geoquímica i el context geodinàmic d'aquest MSCL.
- La seva comparació respecte a la composició en elements majors d'altres xenòlits mantèl·lics pròxims de la Península Ibérica, el Massís Central Francès i els massissos peridotítics del Pirineu oriental.

En la taula 12.1 es representen les composicions d'elements majors de dotze lherzolites estudiades, classificades segons la seva microestructura, a més de set harzburgites. Totes van ser considerades per les anàlisis dels minerals. Les lherzolites BB.08.97 i BB.08.54 són les úniques d'entre elles que tenen amfíbol. La majoria de les anàlisis mostren una pèrdua al foc ("loss on ignition", abreviat en anglès LOI) menor de 0,55 %. Les excepcions més notables són tres lherzolites de Sant Corneli amb valors entorn al 1%, que podrien explicar-se per una patina groguenca d'alteració freqüent que presenten les mostres d'aquest volcà. Lherzolites i harzburgites tenen un contingut en SiO_2 comparable (lherzolites: 41,6< SiO_2> 46,5; harzburgites: 40,7< SiO_2< 44,7), però es diferencien per el contingut en els altres òxids, com Al_2O_3 (lherzolites: 2,02< Al_2O_3< 5,07; harzburgites: 0,65< Al_2O_3< 1,27), MgO (lherzolites:

36,3< MgO< 43,7; harzburgites: 45,0< MgO< 47,9), CaO (lherzolites: 1,82< CaO< 3,80; harzburgites: 0,47< CaO< 1,03), que inclús mostren una petita llacuna entre els dos tipus de peridotites. El paràmetre #Mg [#Mg=100*MgO/(MgO+FeO_T) en mols] decreix gradualment de lherzolites a harzburgites, mentre que el paràmetre #Cr [#Cr =100*Cr_2O_3/(Cr_2O_3+Al_2O_3) en mols] augmenta, encara que aquest últim mostra un "gap" entre les dos peridotites: lherzolites: 88,3< #Mg< 90,8; 6,3< Cr_2O_3< 11,7; harzburgites: 90,0< #Mg< 91; 16,1< #Cr≤ 21,8).

Aquestes composicions químiques es van utilitzar en primer lloc per estimar una composició modal de les peridotites per balanç de masses, a partir de la composició mitjana del minerals de cadascuna de les roques (capítol 8), utilitzant la fulla d'Excel MINSQ (Herrmann & Berry, 2002). Aquestes estimacions modals en % en massa tenen una suma dels residus al quadrat ("SSQ" dels autors) inferior a 1,0. Després es van transformar a % en volum, utilitzant les densitats dels minerals corresponents (Deer et al., 1992) (Taula 12.1). La comparació d'aquesta moda estimada amb la determinada amb el comptador de punts (Taula 7.1) ens indica que hi ha una bona correlació per a l'olivina i el clinopiroxè (Fig.12.1a,c) amb desviacions inferiors al 26 i 30% respectivament. Les majors desviacions corresponen al clinopiroxè, l'ortopiroxè i l'espinel·la de lherzolites porfiroclàstiques i a l'olivina i l'ortopiroxè de les harzburgites, normalment amb sobreestimacions per al comptatge de punts (Fig.12.1) Aquestes diferències s'expliquen per que els dos mètodes mostren avantatges i inconvenients: el comptatge precís es veu dificultat per la disminució de la mida dels neocristalls en les lherzolites porfiroclàstiques i equigranulars. D'altra banda, la mida de gra més gran d'algunes harzburgites (Ø> 2 mm) requeriria una quantitat de mostra per a analitzar més abundant que la que es pot extreure d'alguns xenòlits disponibles. Finalment, l'espinel·la, que mostra la major desviació, en algunes mostres té una distribució irregular que fa que l'efecte "nugget" llavor pugui ser notable. Tot i aquestes diferències, la projecció de les estimacions modals en el diagrama de la figura 12.2 mostra un solapament molt important entre la moda estimada i la moda comptada per a les lherzolites. En el cas de les harzburgites, més de la mitat de les mostres (BB.12.02, BB.12.03, BB.12.09, BB.12.04) es desvien cap al vèrtex de l'olivina (Fig.12.1a) i el xenòlit BB.12.02 es projecta fins i tot en el domini de les dunites.

En la figura 12.3 es compara la composició modal estimada amb la de xenòlits circumcratònics i cratònics d'arreu del món en front a dos índex d'empobriment diferents, el #Mg (Walter, 2003) i el % Al_2O_3 (Pearson et al., 2003) de la roca total. En el primer cas

(Fig.12.3a-c), s'observa que tant l'olivina com el clinopiroxè es situen dins del camp dels xenòlits circumcratònics amb rares excepcions, però l'ortopiroxè és projecta molt dispers i en molts casos per sobre d'aquest camp. Majoritàriament, són les lherzolites porfiroclàstiques i equigranulars (BB.08.18, BB.08.97, CA.12.03, SC.11.16, SC.11.49, SC.11.52, BB.08.54) les que tenen una abundància major del 30% en aquesta fase mineral. En el segon cas (Fig.12.3d-e), les mostres estudiades també es situen dins del camp dels xenòlits circumcratònics, exceptuant dues lherzolites (CA.12.03, SC.11.49) amb continguts d'ortopiroxè per sobre del 37%, i quatre harzburgites (BB.12.02, BB.12.03, BB.12.09, BB.12.04) amb continguts baixos en ortopiroxè (<12%) que es situarien en el camp dels xenòlits cratònics. En aquestes figures també es projecten les estimacions modals de xenòlits de la ZVC estudiats anteriorment (Galán & Oliveras, 2014) que es solapen amb les d'aquest estudi. A més, també es representa com evolucionarien les composicions modals com a resultat d'un empobriment d'un MP per fusió fraccionada a diferents valors de pressió. Les nostres estimacions modals es desvien molt de les trajectòries teòriques, principalment en el cas de l'olivina i de l'ortopiroxè. L'olivina esta per sota de les trajectòries evolutives en la majoria dels casos, amb valors inferiors als del MP en moltes lherzolites. Per contra, la moda de l'ortopiroxè és molt superior a la dels models. Assumint que les estimacions modals són representatives, les diferencies observades respecte dels models teòrics de fusió fraccionada podrien explicar-se per:

1. La composició d'aquestes peridotites no seria només el resultat d'una fusió parcial, sinó de processos d'interacció roca-fos, aquest últim ric en SiO_2 per a dissoldre l'olivina d'acord amb la reacció: forsterita+ SiO_2= enstatita (Kelemen et al., 1998; Simon et al., 2003) o bé processos d'interacció roca-fluids de subducció enriquits en SiO_2 (McInnes et al., 2001; Ionov, 2010; Soustelle et al., 2010), o d'una mescla de residu+ cúmulus d'ortopiroxè (Herzberg, 1993; 1999; Lee et al., 2003).
2. La sobreestimació de l'ortopiroxè, que predomina entre els porfiroclasts de les lherzolites, en detriment de l'olivina.

Si el primer cas fos cert, s'ha de ressaltar que l'enriquiment en ortopiroxè del mantell és característic d'alguns xenòlits cratònics i de peridotites de zones de subducció actuals (Herzberg, 2004).

En els diagrames de variació dels components basàltics vers % MgO (Fig.12.4a-f) observem una variació gradual de les lherzolites a les harzburgites, especialment si es tenen en compte

les mostres estudiades anteriorment, amb una bona correlació negativa per a l'Al_2O_3 i el CaO i pitjor per la SiO_2, TiO_2, Na_2O i FeO_T. També es constata que:

1. Tres de les lherzolites noves i una de les ja estudiades tenen un contingut en MgO menor que el MP (McDonough & Sun, 1995) (BB.08.18, SC.11.49 i SC.11.52).
2. Hi ha un petit solapament entre la composició de les dos peridotites pel que fa al contingut en MgO.
3. El contingut en FeO_T de les harzburgites és variable.
4. No hi ha una variació composicional significativa entre els tres tipus principals de lherzolites: protogranulars (-porfiroclàstiques), porfiroclàstiques i equigranulars; les composicions dels tres tipus es solapen i les composicions més fèrtils corresponen a lherzolites porfiroclàstiques.

Les tres lherzolites més "fèrtils" que el MP tenen el major contingut modal de clinopiroxè (14-17% Taula 12.1), d'ortopiroxè i dels més baixos d'olivina (Fig.12.3). Cal tenir en compte que dues d'aquestes lherzolites mostren corones amb plagiòclasi al voltant de l'espinel·la (BB.08.18, SC.11.49) que podrien ser el resultat de la reacció de l'espinel·la primària amb fosos/fluids infiltrants, com es va mencionar als capítols 7 i 8. Això explicaria que la lherzolita protogranular- porfiroclàstica (BB.08.18) fos també més rica en Al_2O_3, CaO i TiO_2 que el MP i que la lherzolita porfiroclàstica SC.11.49, amb feldspat K en les corones d'espinela (capítol 8) tingui continguts en Na_2O (Fig.12.4e) i en K_2O (Taula 12.1) més elevats que el MP.

L'evolució de les peridotites en alguns diagrames de variació como els de la figura 12.4 va ser utilitzada per a diferenciar peridotites cratòniques enriquides en ortopiroxè respecte de les que es troben en zones de subducció actuals (Herzberg, 2004; Fig.12.4c, f). Tant unes com les altres mostren un enriquiment fort en SiO_2, mentre que l'evolució en el diagrama %FeO_T vs. %MgO seria contraria en els dos casos: en les peridotites cratòniques, el FeO_T tendeix a disminuir, mentre que en les de subducció la tendència és a l'enriquiment en Fe. En el nostre cas, només dos de les lherzolites estudiades (CA.12.03, SC.11.49) i algunes considerades anteriorment mostren un contingut en SiO_2 anòmalament elevat, característic de xenòlits mantèl·lics en context de subducció, i dues lherzolites (SC.11.52, BB.12.01) i dues harzburgites (BB.12.09, BB.12.04) que es projecten en les zones més enriquides en FeO_T. La resta tampoc mostra una tendència contrària clara, és a dir cratònica. Per tant, no es pot concloure res al respecte amb aquestes dades ja que les composicions trobades no permeten discriminar entre aquests dos contexts.

La relació CaO/Al_2O_3 en vers MgO, mostraria una lleugera tendència negativa de les peridotites fèrtils a les més refractàries, encara que la majoria de les mostres tenen valors al voltant del MP (0,8), excepte la lherzolita equigranular tabular BB.08.57 que tindria una relació major d'1 (Fig.12.5). De les mostres estudiades prèviament, una harzburgita (Galán et al., 2008) i les lherzolites i harzburgites de Bianchini et al. (2007) tenen una relació CaO/Al_2O_3 més elevada. Un increment d'aquesta relació podria indicar la formació de clinopiroxè per un procés de refertilització (interacció roca-fos basàltic). Cal mencionar que les tres lherzolites més "fèrtils" que el MP tenen una relació CaO/Al_2O_3 igual o lleugerament superior a la del MP.

12.1.1. Química dels minerals en relació a la de roca total

La composició dels minerals és funció de la composició global de la roca (és a dir, dels processos petrogenètics que la van afectar), però també de les condicions de P, T i fO_2 que van experimentar durant la seva evolució subsolidus. En la figura 12.6, es mostren alguns diagrames de correlació entre paràmetres químics equivalents de roca total i dels minerals. Tant el valor de la fosterita de l'olivina com el #Mg dels piroxens mostren una correlació positiva general amb #Mg de roca total (Fig.12.6a-c), però la dispersió és sempre major per a les lherzolites, especialment si es tenen en compte els xenòlits prèviament estudiats. Aquesta dispersió és més notable en el cas del clinopiroxè. El contingut en Al_2O_3 del clinopiroxè mostra una bona correlació positiva amb l'Al_2O_3 de la roca entre les harzburgites, però una gran dispersió entre les lherzolites (Fig.12.6d); es constata que el clinopiroxè de les tres lherzolites més "fèrtils" no tenen un contingut en Al_2O_3 més elevat que el de la resta, però tant el contingut en Fo de l'olivina com #Mg dels piroxens són dels més baixos. El #Cr de l'espinel·la també mostra una bona correlació negativa amb l'Al_2O_3 de la roca total entre les harzburgites, però aquest paràmetre, no solament té valors clarament més baixos en les lherzolites sinó que es manté gairebé constant en l'espinel·la d'aquestes. Tampoc, l'espinel·la de les lherzolites més "fèrtils" registra el major contingut en Al_2O_3 (Fig.12.6e). Un valor quasi constant de #Cr i baix (10-20) podria ser consistent amb percentatges de fusió< 10% per aquestes roques, mentre que per les harzburgites el percentatge de fusió seria > 15% (Hellebrand et al., 2001). Aquestes conclusions són semblants a les que es van deduir a partir del diagrama d'Arai (1994) a la figura 8.24. Com que el clinopiroxè és un dels minerals que concentra la majoria del titani, també s'ha comparat amb el TiO_2 de la roca total (Fig.12.6f). Tot i mostrar una correlació positiva de les harzburgites a les lherzolites, s'observa força dispersió, sobretot pel que fa a aquestes últimes, i fins i tot dues tendències

diferents. Tots aquests diagrames confirmen que la variació composicional observada no només s'explicaria per processos de fusió parcial a partir d'un MP per als dos tipus de peridotites, i que fins i tot l'historia d'aquesta fusió de lherzolites i harzburgites no hauria perquè haver estat simultània (Fig.12.6d), possibilitat que ja va ser considerat per Bianchinini et al. (2007), encara que el buit composicional entre les dues peridotites que van trobar aquests autors es demostri que va ser un problema de mostreig.

12.1.2. Comparació amb zones pròximes a la ZVC

El MSCL està representat en zones pròximes per xenòlits de: el Camp Volcànic de Calatrava (CVC) (Villaseca et al., 2010), la zona de Tallante en la Serralada Bètica (Beccaluva et al., 2004) i el Massís Central Francès (MCF) (Lenoir et al., 2000), i a més de pels massissos peridotítics orogènics del Pirineu oriental (Bodinier et al., 1988, 1989; Burnham et al., 1998). Tots aquests exemples tenen lherzolites i harzburgites amb espinel·la± amfíbol, excepte els xenòlits de CVC en el que únicament es van descriure lherzolites i rares wehrlites. En la comparació només s'han tingut en compte les lherzolites i harzburgites de tots aquests exemples. Com referència es va partir dels xenòlits del MCF, a partir dels quals Lenoir et al. (2000) van establir dos dominis del MSCL diferents: la part nord (MCF N) més refractaria i la part sud més fèrtil (MCF S). En totes dues hi ha lherzolites i harzburgites, però les lherzolites de MCF N no superen el 3% d'Al_2O_3, mentre que aquestes són freqüents en el MCF S.

En la figura 12.7, es pot observar que els xenòlits mantèl·lics de la ZVC tenen composicions i tendències similars als xenòlits i massissos de zones pròximes, però les lherzolites són més fèrtils que les del MCF N ja que el contingut en Al_2O_3 de diferents mostres és > 3%. Aquest és el cas de la majoria de xenòlits lherzolítics de la Península Ibèrica i dels massissos peridotítics pirinencs. Pel que fa als altres components, les lherzolites del MCF N són també més empobrides en Na_2O (Fig.12.6d) i sobretot en TiO_2 (Fig.12.6e) que la resta. En el cas de les harzburgites, les composicions de les estudiades són més refractaries que les del MCF S i en general que la resta, excepte les de Tallante que són les més semblants. Tot i això, les harzburgites de la ZVC són més pobres en SiO_2 (Fig.12.7a) i riques en Na_2O (Fig.12.7d) que les altres.

12.1.3. Relació entre la geoquímica de elements majors del MSCL i el context geodinàmic

Griffin et al. (1999) van fer una classificació del MSCL basada en l'edat de l'últim esdeveniment tectonotèrmic que va afectar a l'escorça que esta per sobre. En concret, la majoria dels xenòlits dels **Arcons** estarien englobats per kimberlites que intrueixen les àrees

més antigues, les quals no haurien estat afectades per cap esdeveniment tectonotèrmic des de fa més de 2,5Ga; els xenòlits dels **Protons** representarien un mantell que hauria experimentat un esdeveniment tectonotèrmic entre els 2,5 i 1Ga; i per últim els xenòlits dels **Tectons** es troben en roques volcàniques recents, representarien un mantell afectat per esdeveniments tectonotèrmics fa menys d'1Ga. El MSCL típic d'Arcons es caracteritza per una concentració baixa en CaO i Al_2O_3, tot al contrari del MSCL típic de Tectons que seria només una mica més empobrit que el MP. Els xenòlits tipus Tecton es divideixen en: **YETI** (en anglès: Young Extensional Terrains, Intraplate), corresponents a rifts actius i a la formació de conques; **TILE** (en anglès: Tectons Incipient or Little Extension), situats en àrees continentals on l'extensió no és evident; **OCEAN**, en illes oceàniques; i **SUBD** (subducció), en context de marges convergents.

En el diagrama Al_2O_3 vs. CaO (Fig.12.8a) es pot observar com el valor de la mediana que integra totes les peridotites del MSCL de la ZVC es situa pròxima de la composició de la mitjana d'un mantell **Proton**. Separadament, la mediana de les lherzolites es situa a cavall entre **Proton** i **Tecton**, mentre que la mediana de les harzburgites es situa pròxima al **Arcon**. Per un altre banda, la mediana global es projecta en el domini TILE (domini extensional incipient) que és coherent amb el context regional, però també en el de OCEAN i SUBD. Griffin et al. (1999) van interpretar un MSCL en context TILE com una barreja entre un MSCL antic i una mantell ascendent més jove. Més recentment, Griffin et al. (2009) es ratifiquen en aquesta interpretació i van proposar un procés dicotòmic per a l'evolució del MSCL en lloc d'un procés secular; en un procés dicotòmic, el MSCL de tipus **Arcon** estaria representat per les composicions més refractaries d'una zona. Després, durant episodis de subducció, col·lisió i magmatisme donarien lloc a una major variació composicional dels Arcons per refertilització, i fins i tot a un mantell més fèrtil de tipus **Proton** (Fig.12.9). Aquest últim provindria d'una fusió moderada d'un MP donant lloc a un MSCL juvenil amb 2,5- 4% Al_2O_3 com s'observa en els Protons i en la majoria dels Tectons. S'ha de tenir en compte que les tendències que mostrarien el procés de fusió parcial d'un MP amb diferents edats (evolució secular) i el procés de refertilització d'un mantell molt empobrit per reacció amb fosos basàltics (evolució dicotòmica) serien similars (però en direccions oposades), i difícils de diferenciar en diagrames de roca total d'elements majors (Griffin et al., 2009). Així doncs, si s'assumeix la hipòtesis d'evolució dicotòmica per l'exemple estudiat, i tenim en compte que les úniques edats disponibles sobre les peridotites són edats model Lu-Hf de 1,0- 0,6 Ga (Proterozoic Superior) per a dues lherzolites (Bianchini et al., 2007), les harzburgites podrien representar un mantell més antic arqueà (?), posteriorment refertilitzat durant episodis

tectonotèrmics del Proterozoic, al que al mateix temps es podria haver acrecionat un mantell més juvenil que estaria representat per algunes lherzolites. De ser certa aquesta interpretació, els esdeveniments tectonotèrmics més notables i posteriors en l'escorça, com l'orogènia Herciniana, no quedarien reflectits en la geoquímica del mantell o bé, que les edats disponibles de les lherzolites no són complertes o representatives. Per exemple, algunes lherzolites d'edat proterozoica podrien haver estat refertilitzades per episodis magmàtics més recents, durant el Fanerozoic, a les que es podrien acrecionar altres lherzolites fèrtils i juvenils d'aquesta edat, no registrades en les edats disponibles. En contra de l'origen arqueà de les harzburgites estaria el fet de que tenen un contingut en FeO_T (8± 1%) superior i més típic de Protons i Tectons (Griffin et al., 2009) que d'un MSCL dels Arcons (6- 4%). Per contra, si s'assumeix la hipòtesis de l'evolució secular, lherzolites i harzburgites podrien ser totes dues de tipus Proton, resultat d'un procés de fusió parcial d'un MP, o bé de diferents episodis de fusió durant el Proterozoic. Una altra hipòtesis possible seria que les dos peridotites representarien un MSCL de tipus **Proton**, però que posteriorment algunes haurien estat refertilitzades per percolació de fosos basàltics després dels 0,6 Ga, i als que també es podrien haver acrecionat lherzolites juvenils procedents de la fusió d'un MP (no hi hauria registre d'edats). És a dir, hi hauria lherzolites resultat d'un procés de fusió parcial, com les que donen una edat Proterozoic Superior (molt empobrides en elements traça incompatibles, Bianchini et al., 2007) i altres que podrien ser el resultat de la refertilització del mantell (Galán & Oliveras, 2014; Galán & Fernández-Roig, 2016; Galán et al., 2016) durant el Proterozoic i/o Fanerozoic.

Si comparem les medianes de xenòlits pròxims (Fig.12.8), observem que el MSCL de Calatrava seria el més fèrtil, mentre que el més empobrit seria el corresponent a la zona de Tallante. Tot i les diferències observades anteriorment (Fig.12.4), la mediana de la sèrie nord del MCF seria la més semblant a la mediana global de la ZVC, excepte per el contingut en TiO_2 (Fig.12.9b), mentre que la mediana de la sèrie MCF S seria força més fèrtil. Finalment, la mediana del massissos peridotítics pirinencs és menys fèrtil que la mediana de la ZVC. Hem de tenir en compte que aquests resultats de la mediana estarien molt condicionats per la quantitat de peridotites de cada tipus seleccionades per els autors.

12.2. Elements traça en roca total

Els elements traça, com els majors, també són útils per a avaluar els processos de fusió parcial i refertilització, però especialment ho són per a avaluar els possibles agents i processos metasomàtics degut al fraccionament important que presenten alguns elements incompatibles entre si durant aquests processos.

En aquest apartat seguirem la mateixa marxa que en l'anterior: primer es presentaran els resultats per a les mostres estudiades i després es farà una comparació amb les estudiades anteriorment i les d'altres àrees pròximes.

Les anàlisis dels elements traça en roca total s'han fet en les mateixes mostres de peridotites que les d'elements majors, tenint en compte els tipus litològic i les varietats microestructurals de les lherzolites. Els resultats s'inclouen en la taula 12.2 així com algunes relacions entre els: $(La/Yb)_N$, $(La/Sm)_N$, $(Gd/Yb)_N$, Y/Yb, $(Th/U)_N$, $(Nb/Ta)_N$, $(Zr/Hf)_N$.

Les dades de la taula 12.2 indiquen que la concentració d'alguns elements traça està per sota del límit de detecció en varies mostres (e.g., Hf, Lu, Pb, Tl, U, V). La principal diferència entre lherzolites i harzburgites és el contingut en elements compatibles (e.g., Ni, Co) i en alguns elements moderadament incompatibles (e.g., Ga, Sc, Y, Yb) (Canil et al., 2004). El Ni i el Co són generalment més abundants en les harzburgites (2400≤ Ni≤ 2070; 452≤ Co≤ 765) que en les lherzolites (1560≤ Ni≤ 2140; 184≤ Co≤ 801), amb rares excepcions, mentre que és a l'invers per als elements moderadament incompatibles (e.g., 7≤ Sc en harzburgites ≤ 8; 10≤ Sc en lherzolites ≤ 16; 0,6≤ Ga en harzburgites ≤ 1,9; 2,5≤ Ga en lherzolites ≤ 6,2). La concentració dels elements més incompatibles es solapa àmpliament en les dues peridotites.

12.2.1 Covariació dels elements traça vs. %MgO total

En els diagrames de variació de la figura 12.10 es pot observar com el Ni mostra una bona correlació positiva amb el MgO, però més de la meitat de les lherzolites tenen valors més baixos en Ni que el MP (Fig.12.10a), de les quals 5 mostren un contingut modal en piroxens major del 45% i un contingut en olivina menor del 50%, és a dir, són de les més fèrtils. Per altra banda, entre els elements moderadament incompatibles, el Cr mostra una correlació negativa en les harzburgites (Fig.12.10b), i una tendència diferent a la de les lherzolites que és totalment dispersa. El contingut en Cr de les dues peridotites es solapa àmpliament. Al contrari, altres elements moderadament incompatibles presenten una bona correlació

negativa vs. MgO (e.g., Ga, Sc, Y, Yb; Fig.12.10c-f). El Cu mostra tendències oposades en lherzolites respecte de les harzburgites (Fig.12.10g); són notables algunes lherzolites porfiroclàstiques amb valors de Cu molt superiors als del MP, on dues d'elles (SC.11.49, SC.11.16) tenen sulfurs de Cu (Fig.7.13h). Els elements LIL (litòfils de gran radi iònic en anglès) o amb esforç de camp o potencial iònic baix (LFS en anglès) com el Rb, Sr i Ba mostren una forta dispersió (Fig.12.11a-c). És el mateix cas que les LREE (Fig.12.11d-e), i els elements HFS (amb esforç de camp o potencial iònic elevat en anglès), com el Nb, Th i Zr (Fig.12.11f-h). El contingut en elements traça incompatibles és en molt de casos superior al del MP, excepte en el cas del Zr (Fig.12.11g). La bona correlació entre elements compatibles i moderadament incompatibles amb l'índex de diferenciació, com el % MgO, es pot interpretar com el resultat d'un empobriment per fusió parcial o bé com resultat de la refertilització ígnia del mantell. L'adició de clinopiroxè per refertilització es traduiria per un valor variable de Sc per a un mateix grau de fusió (Canil et al., 2004), la qual cosa no s'observa clarament a la figura 12.10d, excepte amb el cas d'una lherzolita de Bianchini et al. (2007). Tot i això, les trajectòries teòriques de fusió són corbades perquè el coeficient de partició d'aquests elements varia per a graus de fusió elevats. Això no s'observa en les figures 12.10c-f, fet que va ser utilitzat per alguns autors per suggerir l'origen d'aquesta tendència recta com deguda a processos de mescla (O'Reilly & Griffin, 2013), per exemple entre una peridotita refractària i un fos basàltic percolant. Per altra banda la dispersió observada en els elements més incompatibles seria fruit de processos metasomàtics subseqüents, no lligats a la possible refertilització, on la interacció roca-fos(fluids) seria a baixa relació fos/roca, sense donar lloc a la modificació de la moda mineral de la peridotita (Takazawa et al., 2000).

12.2.2. Covariació entre elements traça

Entre els elements traça més incompatibles i dispersos vs. %MgO hi ha una correlació general positiva, e.g., Sr, Ba, Rb, Th vs. LREE representades pel Ce (Fig.12.12a-e), la qual cosa significaria que tots aquest elements van ser afectats per processos metasomàtics. Aquestes correlacions són més bones amb el Sr, Ba i el Th. Per contra, hi ha dispersió dels elements moderadament incompatibles respecte de les LREE (e.g., Y vs. Ce), es a dir, els elements moderadament incompatibles no semblen afectats per metasomatismes posteriors a la fusió(ns) parcial(s), i als possibles processos de refertilització, experimentats pel MSCL. Entre aquests elements moderadament incompatibles la correlació és bona (e.g., Y vs. Yb, Fig.12.13, amb una relació Y/Yb=7,1-16,7 comparable o superior a la del MP= 9,8). Els valor

més elevats d'aquesta relació són de les harzburgites. Entre les LREE i altres elements HFS, com Nb i Zr també hi ha dispersió (Fig.12.2d-f), però hi ha una correlació positiva amb el Th (Fig.12.12e).

Com ja passava amb els elements majors no hi ha diferències clares entre el contingut en elements traça de les lherzolites amb diferents microestructures.

12.2.3 Diagrames REE i multielementals

Els valors de les REE de lherzolites i harzburgites, s'han normalitzat a la Condrita (C1) de McDonough & Sun (1995) per projectar-los en els diagrames de la figura 12.14. Les lherzolites mostren una gran variabilitat d'espectres. Totes les lherzolites estudiades en aquesta tesis tenen ∑REE≥ condrita i la majoria HREE> condrita i poc fraccionades entre elles: $(Gd/Yb)_N$= 0,7-1,6. En els espectres de les lherzolites es poden diferenciar tres grups segons el seu enriquiment en LREE (Fig.12.13a-c):

1) Molt enriquides (e.g., BB.08.18, CA.12.03) amb $(La/Yb)_N$= 10,2-26,1 i $(La/Nd)_N$= 2,8-21,4.

2) Lleugerament enriquides (e.g., BB.08.80) fins a lleugerament empobrides (e.g., SC.11.52) amb $(La/Yb)_N$= 0,8-5,2 i $(La/Nd)_N$= 0,9-2,0 .

3) Molt empobrides (e.g., SC.11.16) amb $(La/Yb)_N$= 0 i $(La/Nd)_N$= 0.

Les lherzolites protogranulars i protogranulars- porfiroclàstiques tenen espectres REE de tipus 1 i 2 (Fig.12.14a), les lherzolites porfiroclàstiques tenen els tres tipus (Fig.12.14b) i les equigranulars el tipus 2 (Fig.12.14c). Les lherzolites d'estudis anteriors són principalment de tipus 2, si bé algunes de les de Bianchini et al. (2007) es diferencien per un espectre en forma d'"u" (Fig.12.14a), es a dir enriquides en LREE i empobrides en MREE

La relació Eu/Eu* [$Eu^*= Eu_N/\sqrt{(Sm_N*Gd_N)}$] és molt pròxima a 1 en tots els casos excepte per la lherzolita porfiroclàstica SC.11.16 que és 0,76, és a dir, aquest espectre presenta una petita anomalia negativa en Eu. Com a cas particular, la lherzolita equigranular BB.08.54 mostra una anomalia negativa en Ce (Fig.12.14c).

Els espectres de REE de les harzburgites es diferencien dels de les lherzolites pels valors menors en HREE (Fig.12.14d), en la majoria de casos per sota dels de la condrita, i a més perquè en la majoria de casos estan fraccionades entre elles: $(Gd/Yb)_N$=1,0 (BB.12.04) -3,7 (BB.08.52). El fraccionament de les LREE respecte a les HREE és sempre elevat: $(La/Yb)_N$ varia

entre 7,76 (BB.12.04) i 27,2 (BB.08.52), i més moderada entre les LREE: $(La/Nd)_N$= 0,9- 5,8. A més les MREE també estan fraccionades respecte a les HREE excepte en un cas (BB.12.02): $(Sm/Yb)_N$=1,6- 6,3. En els espectres de REE de les harzburgites es poden diferenciar dos grups, un més empobrit en LREE i MREE (BB.12.02, BB.12.04, CA.12.02, BB.12.03) que l'altre (BB.08.20, BB.08.52, BB.12.09). Tres d'aquestes harzburgites més empobrides són a més de les més refractaries (veure Fig.12.2). Les harzburgites estudiades per Bianchini et al. (2007) s'aproximen a les més empobrides, mentre que les de Galán & Oliveras (2014) es solapen amb els dos tipus.

En els diagrames multielementals (Fig.12.15), els valors dels diferents elements traça s'han normalitzat al mantell primitiu de McDonough & Sun (1995). En moltes lherzolites, es poden observar anomalies positives molt significatives en Ta i Pb, menys notable en Nb i negatives en Zr. El Ta no va ser analitzat en referències prèvies (Bianchini et al. 2007; Galán & Oliveras, 2014), i en el nostre cas el contingut elevat podria ser degut a un artefacte analític. Per exemple, la precisió de mesura del Ta és millor d'11% (1s) per al patró OREAS 146, però la desviació és del 21%. L'anomalia en Pb també és qüestionable perquè encara que la precisió per al Pb també és millor de l'11%, la desviació respecte a l'estàndard MRGeo 08 és del 97%. Altres anomalies que s'observen són:

1) Anomalia negativa petita en Ti (BB.08.18, BB.12.01, BB.08.80, BB.08.54).

2) Increment en el contingut de Th-U amb el contingut en LREE (BB.08.101, BB.12.01, BB.08.18, CA.12.03, BB.08.80, BB.08.38, BB.08.57, BB.08.20, BB.08.52). Quan un o els dos elements no estan per sota del límit de detecció, la relació $(Th/U)_N$< 1, es a dir, estan fraccionats.

3) Anomalia positiva petita en Sr respecte a MREE en lherzolites enriquides en LREE (BB.08.38, CA.12.03) i negativa en la lherzolita molt empobrida (SC.11.16).

4) Anomalia positiva en Hf respecte a Zr (SC.11.52, BB.08.101, BB.12.01, BB.08.54), amb una relació $(Zr/Hf)_N$< 1 quan alguns dels elements no està per sota del límit de detecció.

5) Anomalia positiva petita en Rb respecte a Ba (SC.11.49, SC.11.52, BB.12.01).

En general, les lherzolites amb patrons REE de tipus 1 tenen major contingut en Ba, Th i U que les que tenen patrons REE de tipus 2 i 3.

Algunes mostres particulars són: la lherzolita porfiroclàstica SC.11.16 molt empobrida en LREE i MREE; només mostra una anomalia positiva en Nb-Ta i registra Th, U, Hf i Zr per sota

del límit de detecció. Les lherzolites BB.08.97 i BB.08.54, que contenen escassos cristalls d'amfíbol, mostren espectres REE no fraccionats entre LREE i HREE. Les lherzolites amb corones entorn a espinel·la que contenen plagiòclasi com la BB.08.18 i la SC.11.49, i que són de les més fèrtils, en la figura 12.14 tenen espectres REE diferents entre elles, la primera està molt enriquida en LREE (tipus 1), mentre que la segona mostraria un espectre REE pla (tipus 2). En els diagrames multielementals, la BB.08.18 mostra enriquiment en Th-U, Ta i Pb, mentre que la SC.11.49 mostra l'anomalia positiva més elevada en Rb. És a dir, les lherzolites més fèrtils que el MP (BB.08.18, SC.11.49, SC.11.52) no mostren cap patró característic REE o multielemental, excepte l'anomalia positiva notable en Ta, que podria ser un artefacte analític. La comparació amb lherzolites prèvies ens indica que els diagrames són comparables, però l'anomalia negativa en Zr és més general en les nostres mostres respecte a les de Bianchini et al. (2007) i també que algunes es presenten més enriquides en Th-U respecte de mostres estudiades anteriorment.

Entre les harzburgites es diferencien els dos grups mencionats anteriorment en el diagrama de REE (Fig.12.15d). Les harzburgites més enriquides en REE tenen diagrames multielementals comparables als d'algunes lherzolites, amb anomalies positives significatives en Ta i Pb (?) i negatives en Zr i Ti. Les harzburgites més empobrides en REE ho són també en elements LIL i HFS (Th-U, Hf, Zr i Ti). Respecte de les estudiades anteriorment, algunes harzburgites són lleugerament més enriquides en LILE, Th i U.

El diagrama de la figura 12.16a és una altra manera de descriure els espectres de REE; representa el fraccionament entre les LREE vs. MREE/HREE: la majoria de harzburgites i algunes lherzolites estan enriquides en LREE i MREE, altres lherzolites no mostren enriquiment o només estan enriquides en LREE respecte a MREE i finalment, únicament dues lherzolites estan lleugerament empobrides en LREE i una molt empobrida que no figura en el diagrama (SC.11.16).

Les relacions $(Zr/Hf)_N$ i $(Nb/Ta)_N$ són molt baixes, en les lherzolites varien de 0,01 a 0,18 i de 0,18 a 0,37, i en les harzburgites de 0,14 a 0,28 i 0,17 a 0,29, respectivament. La seva projecció en el diagrama de la figura 12.16b és molt diferent de la d'altres xenòlits comparables de zones pròximes. Finalment, en la figura 12.16c es pot observar que l'enriquiment en LREE es correlaciona negativament amb el grau de fertilitat representat per el contingut en CaO, si bé hi ha dues mostres fèrtils que estan molt enriquides en LREE (CA.12.03 i BB.08.18). La mostra BB.08.18 es remarca perquè té freqüents corones amb plagiòclasi al voltant de l'espinel·la.

Pel que fa a la interpretació d'aquestes dades, d'una banda, la correlació negativa entre MgO i els elements moderadament incompatibles planteja una vegada més el dilema entre processos de fusió parcial del mantell i refertilització. D'altra banda, la correlació negativa, però dispersa en les lherzolites, entre la relació $(Ce/Sm)_N$ en vers al CaO de la roca (Fig.12.16c) ens indica que no hi ha relació entre fertilitat i grau d'enriquiment en els elements més incompatibles, com és habitual en aquestes roques. És a dir, els processos metasomàtics responsables de l'enriquiment en els elements més incompatibles serien posteriors a la fusió i als possibles processos de refertilització que hagessin afectat aquest mantell. A l'hora de traçar aquests processos metasomàtics són útils el fraccionament d'alguns elements incompatibles respecte d'altres, d'aquesta manera per exemple, les anomalies negatives en elements HFS (Nb-Ta, Zr-Hf, Ti) respecte a LREE i MREE es van considerar característiques d'agents metasomàtics carbonatítics o d'agents fluids, així com relacions Zr/Hf i Nb/Ta elevades (Rudnick et al., 1993; Green, 1995) i Th/U< 1 (Foley et al., 2001), però aquests fets van ser qüestionats posteriorment, perquè a més de la natura dels agents metasomàtics, aquests fraccionaments entre elements poden ser causats pel flux porós reactiu mitjançant la formació de minerals que capten uns elements traça respecte d'altres, cas de la formació d'amfíbol, òxids de Ti, o bé per la percolació prèvia d'un fos/fluid metasomàtic a través de roques mantèl·liques amb granat, mineral que captura una gran quantitat de HREE i de Hf i Zr respecte a MREE (Rivalenti et al., 2004 i referències incloses). En el nostre cas, les relacions baixes de $(Nb/Ta)_N$ i $(Zr/Hf)_N$ (Fig.12.16b) de la majoria de mostres, així com la manca d'una anomalia negativa molt significativa en Ti, suggereixen un component metasomàtic tipus fos alcalí silicatat, però les harzburgites més empobrides, amb relacions $(Zr/Hf)_N$ molt baixes, podrien haver estat afectades per un metasomatisme carbonatític. Es tornarà sobre aquesta qüestió amb els elements traça determinats en clinopiroxè que també serviran per a contrastar algunes anomalies dubtoses en roca total. D'altra banda, les variacions de les relacions $(Nb/Ta)_N$ vers $(Zr/Hf)_N$ (Fig.12.16b) van ser utilitzades per Lenoir et al. (2000) per mostrar les diferències del metasomatisme que va afectar els dos dominis del MCF. Una relació $(Zr/Hf)_N$ <1 en el sector N del MCF implicaria un metasomatisme extensiu, mentre que una relació $(Nb/Ta)_N$< 1 implicaria un metasomatisme subtil. Tot i això, en el nostre cas, aquestes relacions en roca total no són discriminatòries perquè de ser certes, les dos són baixes. A més, si tenim en compte que el nivell d'enriquiment dels elements afectats per metasomatisme (LREE, MREE, Th, U, Nb, Ta (?), Pb (?) y Sr) és comparable en les dues peridotites, es dedueix que totes dues van ser afectades

pel mateix(os) tipus de metasomatisme amb efectes molt variables en les lherzolites i més generals en les harzburgites.

12.2.4 Comparació amb altres zones pròximes

S'ha utilitzat el diagrama de la figura 12.16a on es projecten les relacions La/Nd en front Sm/Yb per la comparació dels patrons de REE dels xenòlits peridotítics que apareixen en diferents zones pròximes a la ZVC, com el CVC (Villaseca et al., 2010), Tallante (Beccaluva et al., 2004) i les dues sèries del MCF (Lenoir et al., 2000). Com ja passava amb els elements majors, les peridotites estudiades són comparables a les dades del MSCL de la sèrie Sud del MCF, Tallante i CVC, i clarament diferents de la tendència que defineixen tant les lherzolites com les harzburgites de la sèrie Nord del MCF. Per altra banda, la correlació general negativa entre $(Ce/Sm)_N$ en vers al CaO de la roca total, (Fig.12.16c), també s'observa a altres àrees (Fig.12.16b). Aquest diagrama també mostra que les harzburgites de la sèrie nord del MCF són més enriquides que la resta.

Els diagrames multielementals de la figura 12.17 permeten una comparació més detallada: (1) respecte al xenòlits del MCF, les lherzolites de la ZVC són mes semblants a les de la sèrie Sud de Lenoir et al. (2000) que a les de la sèrie N (Fig.12.17a), però les de la ZVC són de les més enriquides en HREE i MREE i mostren una anomalia negativa en Zr més pronunciada; les harzburgites son també més enriquides en MREE i LREE que les del Sud del MCF i també presenten una anomalia negativa més marcada en Zr (Fig.12.17b); (2) amb respecte als xenòlits de Tallante (Beccaluva et al., 2004), les lherzolites de la ZVC són lleugerament més enriquides en HREE i MREE i les harzburgites en MREE, totes dues amb una anomalia negativa més marcada en Zr (Fig.12.17c-d); i (3), les lherzolites de la ZVC són molt semblants a les de Calatrava (Villaseca et al., 2010).

En resum, les peridotites de la ZVC mostren una variació gradual des de lherzolites molt fèrtils a harzburgites molt refractàries pel que fa als components basàltics (Al_2O_3, CaO, TiO_2, Na_2O), elements traça moderadament incompatibles i MgO. Aquesta variació composicional no mostra relació amb les varietats microestructurals de les lherzolites, tot i que les lherzolites més fèrtils són porfiroclàstiques. La trajectòria evolutiva de lherzolites a harzburgites en diagrames de variació, com Al_2O_3, CaO (Fig.12.4a-b), elements compatibles (Ni; Fig.12.10a) i moderadament incompatibles (Sc, Ga, Y, Yb) vs. MgO (Fig.12.10c-f), CaO vs. Al_2O_3 (Fig.12.9), es podria correspondre a una evolució secular del MSCL, és a dir per fusió parcial d'un MP en un o varis episodis d'edats diferents, o bé a una evolució dicotòmica on

un mantell refractari i antic s'hauria refertilitzat durant episodis magmàtics més recents que podrien també haver donat lloc a la formació d'un MSCL més fèrtil i juvenil. La desviació de la moda de l'olivina i de l'ortopiroxè respecte a trajectòries evolutives teòriques d'un procés de fusió parcial fraccionada d'un MP (Fig.12.3a-b), així que la major dispersió de les lherzolites en diagrames de covariació d'elements majors, estaria més d'acord amb processos d'interacció roca-fos percolant. Ara bé, tot i que algunes mostres presenten un enriquiment en ortopiroxè modal, el contingut en SiO_2 i en FeO_T d'aquestes peridotites no arriba als valors més típics dels xenòlits de zones de subducció o de xenòlits cratònics rics en ortopiroxè, la formació del qual podria ser deguda a la interacció amb un fos saturat en SiO_2. D'acord amb la composició mediana global en elements majors del mantell estudiat correspondria a un tipus Proton, en consonància amb les edats model disponibles (Bianchini et al., 2007). A més, els diagrames de covariació entre els elements traça més incompatibles (Fig.12.12a-d) i la correlació negativa entre fertilitat i enriquiment indicarien que posteriorment a la fusió parcial i possible refertilització d'aquest mantell, tant les harzburgites com algunes lherzolites haurien estat afectades per processos metasomàtics. El fet de que els continguts dels elements traça mostrin patrons similars en els dos tipus de peridotites, suggereix que es tractaria dels mateixos esdeveniments metasomàtics, però la variabilitat dels espectres en les lherzolites, que van de molt empobrits a molt enriquits (Fig.12.14a-c), indicaria que els efectes del metasomatisme van ser molt desiguals en aquestes. Les relacions molt baixes Zr/Hf en la majoria dels xenòlits, així com la absència d'una anomalia negativa en Ti respecte a les MREE, serien característics d'un metasomatisme de tipus fos silicatat alcalí més que de tipus carbonatític. Aquest metasomatisme rarament es va manifestar per la formació d'amfíbol en algunes lherzolites (Fig.8.16). Tot i això, algunes harzburgites més empobrides en Zr-Hf i Ti, podrien haver estat afectades per un metasomatisme carbonatític, que podria ser independent o lligat a l'anterior per un procés de percolació reactiva que donaria derivats carbonatítics (Bodinier et al., 2004; Galán et al., 2008). Finalment, les dues lherzolites on es van trobar corones de reacció amb plagiòclasi entorn a espinel·la, i que a més són de les més fèrtils, no presenten cap característica especial excepte que, en aquella mostra on es va localitzar feldspat K en la corona (SC.11.49) presenta una petita anomalia en Rb.

Una visió més amplia dels processos metasomàtics que van afectar aquest mantell s'avaluarà amb un anàlisis conjunt entre els elements traça de roca total i de clinopiroxè en l'apartat següent.

12.3. Elements traça en clinopiroxè i amfíbol: comparació amb les dades de roca total

Com el clinopiroxè és el mineral que capta una major quantitat d'elements traça incompatibles de tots els minerals presents en les peridotites (excepte l'amfíbol que només esta present de manera ocasional en algunes de les nostres mostres) (Garrido et al., 2000; Downes et al., 2003), creiem oportú comparar l'evolució de les dades dels elements traça d'aquest mineral i les de roca total, i així poder precisar algunes de les possibles hipòtesis plantejades en els apartats anteriors d'aquest capítol. Les dades mitjanes obtingudes de les mostres analitzades (les mateixes que en roca total) es troben en la taula 12.3, junt amb un anàlisi d'amfíbol de la lherzolita BB.08.97 i de clinopiroxè de la websterita olivínica BB.12.17. D'aquesta última no hi ha anàlisis químics de roca total.

En aquest apartat només es faran referències puntuals a altres xenòlits semblants, però sense una comparació detallada.

La majoria dels elements traça analitzats es troba per sobre del límit de detecció, exceptuant el Rb, Ba, Ta, Th i U en algunes mostres. L'últim element no va ser mesurat en totes les mostres. Les composicions mitjanes de la taula 12.3 estan basades en anàlisis puntuals d'un o més cristalls d'un mateix xenòlit que no mostren diferències significatives. És a dir, la distribució dels elements traça en el clinopiroxè sembla haver arribat també l'equilibri.

La principal diferència entre el clinopiroxè de lherzolites i harzburgites és el contingut en Ti més elevat en les primeres (1950≤ Ti≤ 4014) que en les segones (269≤ Ti≤ 1023). Aquest element també va ser analitzat per EPMA i s'han comparat les dades amb les obtingudes per LA-ICP-MS. Les desviacions obtingudes són millors del 3%. També es diferencien perquè el clinopiroxè de les lherzolites té menor contingut en Ni i major en V, Ga, Y i Yb (Taula 12.3).

12.3.1 Covariació dels elements traça vs. %MgO total

En la figura 12.18 s'observa que hi ha una correlació positiva del Ni i negativa amb la majoria dels elements moderadament incompatibles (Ga, V, Y, Yb) respecte al MgO, però hi ha diferències respecte a les tendències en roca total: (1) la dispersió dels elements moderadament incompatibles és més notable que en el cas dels anàlisis de roca total (Fig.12.10); (2), el Sc té valors comparables en lherzolites i harzburgites (Fig.12.18b), mentre que en els anàlisis de roca total aquestes estan clarament diferenciades (Fig.12.10); (3), la composició en Y i Yb del clinopiroxè mostra una clara separació entre lherzolites i harzburgites Fig.12.18c, e-f) però la del Ni, Sc, V es solapa (Fig.12.18a-b, d). La mala

correlació d'alguns d'aquests elements moderadament incompatibles amb el MgO podria ser deguda a que són captats per altres minerals (e.g., Ni per l'olivina; Sc per l'olivina i ortopiroxè; Stosch, 1981; V per l'espinel·la; Horn et al., 1994). Tampoc les dades d'elements traça en clinopiroxè separen els tres tipus microestructurals de les lherzolites, però els clinopiroxens de les porfiroclàstiques i equigranulars són els que tenen un major contingut en Ga, V, Y i Yb. Cal fer notar que les mostres més "fèrtils" esmentades en els apartats de roca total (BB.08.18, SC.11.49 i SC.11.52) no són les que mostren els continguts més elevats en aquests elements. El clinopiroxè de la websterita olivínica es projecta entre el de les harzburgites. Les dades dels estudis previs es solapen amb els d'aquesta tesis però el clinopiroxè de les piroxenites estudiades anteriorment té un contingut en Ni més baix (Fig.12.18a) Per altra banda, també els elements traça més incompatibles mostren una forta dispersió respecte el MgO, com ja passava en els diagrames de roca total (Fig.12.19, 12.11). Tot i això, El Zr es diferència per presentar dues trajectòries negatives diferents amb el MgO, una per les lherzolites i una altre per les harzburgites (Fig.12.19h).

12.3.2. Covariació entre elements traça

La correlació entre el elements traça més incompatibles és positiva i bona per l'Sr, Nb i Th respecte el Ce (Fig.12.20b, d, e-f), com s'observa en les dades de roca total (Fig.12.12b, d, e-f). El Ba i el Rb es mostren més dispersos que en la roca total (Fig.12.20a,c; Fig.12.12a,c). Per altra banda, el Zr del clinopiroxè torna a mostrar dues tendències positives: una per les lherzolites i una altre per les harzburgites, que acaben convergint cap als valors més elevats d'aquests dos elements (Fig.12.20f). També en front del Ti, el Zr mostra dues tendències diferents per les lherzolites i les harzburgites (Fig.12.21a). En aquesta figura el clinopiroxè de les piroxenites es diferència del de les harzburgites per un valor més elevat en Ti. Finalment, els elements moderadament incompatibles, com el Y (Fig.12.21b) o el Yb es projecten dispersos respecte les LREE, però com en el cas dels de roca total, Yb en front Y mostra una bona correlació positiva de les lherzolites a les harzburgites (Fig.12.21c), amb relacions Y/Yb= 5,33-14,95 comparables a les de roca total i al voltant de Y/Yb en el MP=9,8. El clinopiroxè de la websterita es projecta entre els d'aquestes últimes.

12.3.3. Diagrames REE i multielementals

Els diagrames de REE normalitzats als valors de la condrita C1 es troben en la figura 12.22. En el cas de les lherzolites també s'han separat tenint en compte els diferents tipus microestructurals.

Tots els clinopiroxens tenen una concentració de HREE≥ condrita i estan poc fraccionades entre si $(Gd/Yb)_N$= 0,76-1,26. També en aquest cas, es diferencien 3 grups d'espectres en les lherzolites, segons el seu contingut en LREE, i que en la majoria del casos coincideixen amb els de roca total.

1. Espectres molt enriquits (BB.08.18; CA.12.03) amb $(La/Yb)_N$= 10-30 i $(La/Nd)_N$= 3,5-25
2. Espectres de lleugerament enriquits (BB.12.01) a empobrits (la majoria, e.g., BB.08.80) amb $(La/Yb)_N$=2,0-0,1 i $(La/Nd)_N$=1,30-0,2
3. Espectres molt empobrits (SC.11.16; BB.08.57) amb valors de $(La/Yb)_N$ i $(La/Nd)_N$=0,0

Les anomalies en Eu, en el cas d'existir, són poc significatives: Eu/Eu*=0,9-1,2

La majoria de les lherzolites mostren espectres REE del grup 2; només una protogranular-porfiroclàstica i una porfiroclàstica tenen espectres del grup 1 i les dues mostres amb espectres de grup 3 són porfiroclàstica i equigranular. Les lherzolites porfiroclàstiques mostres els tres tipus d'espectres, les protogranulars i la protogranular- porfiroclàstica del grup 1 i 2 i les equigranulars del grup 2 i 3, és a dir, com ja passava en les dades de roca total, no hi ha relació entre les microestructures i l'enriquiment en LREE. En general, els espectres REE de les lherzolites i del seu clinopiroxè són força paral·lels. Només en dos casos, els diagrames REE de roca total tenen una relació $(La/Nd)_N$ clarament superior a les del seu clinopiroxè (Fig.12.23): una d'elles és la BB.08.80 amb microestructura porfiroclàstica i la BB.08.57 amb microestructura equigranular, la qual no mostra en roca total l'empobriment extrem en LREE que s'observa en el seu clinopiroxè (Fig.12.13c, Fig.12.22c). Aquestes diferències es podrien explicar per la localització dels elements traça més incompatibles, com les LREE, en inclusions de fosos i/o fluids en el clinopiroxè (Garrido et al., 2000).

En el cas de l'amfíbol de la lherzolita BB.08.97, el seu espectre és pràcticament indistingible de l'espectre del clinopiroxè coexistent (Fig.12.24), que és del grup 2. És a dir, aquests dos minerals estarien en equilibri, en coherència amb el valors semblants en #Mg i #Cr que presenten (Taules 8.3 i 8.5).

Els espectres REE del clinopiroxè de les harzburgites també es diferencien dels de les lherzolites per un menor contingut en HREE (Fig.12.22d) i pel seu fraccionament més elevat entre REE, com ja passava en els de roca total (Fig.12.14d), com per exemple $(La/Yb)_N$= 1,25-23,2 i $(Sm/Yb)_N$= 0,23-8,08, és a dir, estan considerablement més enriquides en LREE i MREE

que en HREE, tot al contrari que la majoria de les lherzolites. Només hi ha una excepció, la mostra BB.12.04, que és de les més pobres en REE i té un espectre en forma de U (Fig.12.22d). En general, les LREE estan poc fraccionades entre si: $(La/Nd)_N$=0,6-2,0 i dues d'elles amb aquesta relació per sota d'1, fet que dóna a aquests espectres una forma convexa (cullera invertida o amb forma de n) (BB.12.03, BB.12.09). Tant en el clinopiroxè com en roca total es poden diferenciar 2 grups de harzburgites a partir del seu continguts en REE (Fig.12.22d):

1. Més enriquides en MREE i HREE (BB.08.20, BB.12.09, CA.12.02)
2. Més empobrides (BB.08.52, BB.12.02, BB.12.03, BB.12.04)

Aquesta diferència és coherent amb la que s'observa en els espectres de roca total, excepte en dues mostres que apareixen en grups diferents: CA.12.02 i BB.08.52. Tots els espectres de roca total i clinopiroxè són força paral·lels excepte en dues mostres: BB.12.04, amb una forma de U que no s'observa en roca total; i la BB.12.02 amb una certa tendència en U que no s'observa en el clinopiroxè.

Finalment, l'espectre REE del clinopiroxè de la websterita té un contingut en HREE comparable al de les harzburgites, però es diferencia de la majoria d'aquestes per tenir una forma convexa o en forma de "n", amb una relació $(La/Nd)_N$=0,68, és a dir, semblant a la de les harzburgites BB.12.03 i BB.12.09 (Fig.12.22d). Aquest tipus d'espectre de REE és comú en el clinopiroxè de piroxenites que apareixen en diferents contexts i per a les que s'han suggerit diversos orígens: **(1)** segregació de cristalls a partir d'un fos magmàtic que percola pel mantell (Irving, 1980; Python & Ceuleneer, 2003; Puzievick et al., 2011; Ackerman et al., 2012); **(2)** fosos cristal·litzats que resultarien de la fusió de les peridotites adjacents (Van Calsteren, 1978); **(3)** restes d'una escorça oceànica subduïda i reciclada per la convecció mantèl·lica (Allègre & Turcotte, 1986; Komprobst et al., 1990); i **(4)**, productes de la interacció roca-fos (Porreca et al., 2006; Le Roux et al., 2016; Tilhac et al., 2016 i referències incloses).

La varietat d'espectres del clinopiroxè de les lherzolites estudiades coincideix amb la dels estudis previs (Bianchini et al., 2007; Galán et al., 2008; Galán & Oliveras, 2014), i la majoria dels de les harzburgites també, encara que en aquestes últimes no s'havien observat fins ara espectres del clinopiroxè molt empobrits amb forma d'"u" (Fig.12.22d). Finalment, l'espectre del clinopiroxè de la websterita seria comparable al dels xenòlits estudiats anteriorment, encara que estaria una mica més empobrit en HREE.

Els diagrames multielementals de les lherzolites amb espectres REE del grup 1 es caracteritzen a més per ser pobre en Rb i Ba i amb valors elevats de Th-U, però sense anomalia positiva respecte les LREE (Fig.12.25a-b). Aquests dos elements estan fraccionats respecte el MP amb valors menors d'1 [$(Th/U)_N$=0,48-0,51], igual que en el cas de la roca total. A més, presenten una marcada anomalia negativa en Nb-Ta i en un cas, el Ta es troba per sota del límit de detecció. També mostren anomalies negatives en els elements HFS més compatibles (Zr, Hf i Ti). Els diagrames són força comparables als de roca total, dels quals es diferencien per: **(1)** l'absència de l'anomalia positiva en Nb-Ta que en roca total és molt marcada; a més la relació $(Nb/Ta)_N$> 12,86 en el clinopiroxè, mentre que en roca total és < 1, molt possiblement degut a problemes analítics amb el Ta, com ja es va explicar; **(2)** l'absència de l'anomalia positiva en Pb; **(3)** anomalies negatives menys significatives en Hf-Zr en el clinopiroxè, encara que la relació $(Zr/Hf)_N$ també té valors <1 (0,86-0,70), però aquests dos elements estan menys fraccionats respecte al MP que en la roca total; i **(4)**, anomalies negatives en Ti una mica més marcades que en la roca total (Fig.12.25a-b; Taula 12.3). L'absència de l'anomalia positiva en Nb-Ta s'explicaria pel fet de que el clinopiroxè no capta aquests elements, els quals poden ser incorporats per l'ortopiroxè, l'olivina i l'espinel·la (Garrido et al., 2000) o perquè el clinopiroxè estigui equilibrat amb microfases riques en Nb-Ta (Bodinier et al., 1996); però en qualsevol cas, no amb l'amfíbol ja que no es troba present en aquestes mostres.

Els diagrames multielementals de les lherzolites amb espectres REE del grup 2 (Fig.12.25a-c) són força coherents amb els de roca total: només una mostra (BB.08.80) té el clinopiroxè lleugerament més empobrit en LREE que el de la roca, com ja s'ha mencionat anteriorment. En general, les lherzolites de Sant Corneli tenen una mica més de Rb (±Ba) en roca total que en el clinopiroxè, fet que podria ser degut a que algunes d'elles mostren una major impregnació de la lava encaixant (e.g., SC.11.49) o a la alteració superficial més intensa observada en aquestes mostres (veure apartat 7.1). El contingut en Th (U) és més baix que en el grup anterior, concordant amb el contingut menor en LREE del clinopiroxè, en aquelles mostres on s'ha mesurat l'U, la relació $(Th/U)_N$<1 (0,19-0,80), com en roca total. Tots el diagrames multielementals del clinopiroxè del grup 2 també mostren una anomalia negativa en Nb-Ta, amb una relació $(Nb/Ta)_N$ entre 1,4 i 8,1 en els casos on s'ha pogut mesurar el Ta. El clinopiroxè no mostra anomalies positives en Pb, i en el cas de ser-hi presents, són negatives (e.g., BB.08.97, SC.11.52). Tampoc s'observen anomalies negatives en Sr respecte MREE o són petites (e.g., SC.11.49). Finalment, encara que el clinopiroxè mostri anomalies negatives en Hf-Zr, el fraccionament entre aquests dos elements tampoc és tant marcat

[$(Zr/Hf)_N$ Cpx= 0,67-0,88] com en roca total (0,01-0,13): l'anomalia en Zr no és tant pronunciada com en el cas de la roca (Fig.12.25a-b). Cal destacar el contrast entre els diagrames del clinopiroxè i l'amfíbol de la lherzolita BB.08.97 (Fig.12.26). L'espectre de l'amfíbol es diferencia del clinopiroxè per una concentració més elevada en Rb-Ba, una anomalia positiva en Nb-Ta, major concentració en Pb i petites anomalies positives en Sr i Ti. També destaca que el seu contingut en Zr i Hf i el fraccionament entre ells és similar al del clinopiroxè, tot al contrari de l'observat per altres autors, els quals mencionen el desdoblament en el comportament d'aquests dos elements, tant pel que fa als amfíbols en venes com en els disseminats (Moine et al., 2001). Les característiques de l'amfíbol de la lherzolita BB.08.97 són comparables a les que descriu Zanetti et al. (1996) pels amfíbols en venes d'hornblendites en el massís de Lherz (amb anomalies positives en Ba, Nb, Sr i Ti i negatives en Zr respecte REE), però en l'amfíbol aquí estudiat $(La/Yb)_N$ és més baix (0,69) i similar a la dels amfíbols disseminats en aquest massís (0,69), fet que es coherent amb la classificació dels amfíbols en el xenòlits estudiats a tipus disseminat, a partir dels components majors (Fig.8.15; 8.16).

El clinopiroxè de les lherzolites amb espectres REE del grup 3 (BB.08.57, SC.11.16) només concorda amb els diagrames multielementals de roca total per a la lherzolita SC.11.16 (Fig.12.25b; 12.14b). En el cas del clinopiroxè de la BB.08.57, es diferencia per tenir un menor contingut en LREE, MREE i Sr que la roca total (Fig.12.25c). Aquest fet podria ser degut, com s'ha explicat abans, a la presència d'aquests elements més incompatibles en inclusions de fosos i/o fluids en el clinopiroxè. La concordança amb el diagrames multielementals és millor per als elements més compatibles entre els que s'observa una petita anomalia negativa en Ti i més notable en Zr, en el cas del clinopiroxè, amb $(Zr/Hf)_N$=0,20-0,35. És a dir, aquests dos elements estan més fraccionats respecte al MP que en el clinopiroxè de les lherzolites anteriors. En el clinopiroxè d'aquest tipus 3 tampoc es detecta una anomalia positiva en Pb ni en Nb-Ta o bé el Ta es troba per sota del límit de detecció, fet que reitera en l'observació de que aquests elements no van ser ben mesurats en la roca total. Finalment, el clinopiroxè de la SC.11.16 tampoc mostra la anomalia positiva en Rb que s'observa en roca total i en altres mostres de Sant Corneli.

Pel que fa a les harzburgites, els diagrames multielementals del clinopiroxè (Fig.12.25d) de les més enriquides es caracteritzen per una anomalia negativa en Pb, al contrari del que s'observava en roca total. Tots tenen una anomalia negativa en Ti més marcada que en la roca total i no s'observen anomalies negatives o són poc marcades en Hf-Zr en comparació

amb l'anomalia negativa marcada en Zr que s'observa en roca total. A més, Zr i Hf amb prou feina estan fraccionats respecte al MP $(Zr/Hf)_N$= 0,85-1,15 i arriben a valors >1, fet que no passa en el clinopiroxè les lherzolites. El contingut en Th-U es troba en concordança amb el de les LREE, és a dir, és més elevat que en les lherzolites amb espectres REE del grup 2 i 3. S'observen petites anomalies negatives en Nb-Ta, amb $(Nb/Ta)_N$>1 (4,04-5,42), també al contrari de la de roca total [$(Nb/Ta)_N$=0,19-0,25]. La relació $(Th/U)_N$ oscil·la entre 0,63- 0,89, més elevada que en les lherzolites. El contingut en Ba és baix (menor que en roca total) i no hi ha anomalies en Sr. Les harzburgites més empobrides en HREE i MREE es diferencien en els diagrames multielementals del clinopiroxè només perquè tenen un contingut menor en Hf-Zr i en Ti (Fig.12.25d), amb una anomalia més marcada en Zr-Hf que en les altres harzburgites. Si tenim en compte que dues d'aquestes harzburgites es troben entre les més refractàries, l'empobriment en aquests elements podria ser degut a una fusió més intensa. La relació $(Zr/Hf)_N$ (0,72-1,05) es comparable a la de les altres harzburgites, però la relació $(Nb/Ta)_N$=5,46-9,10 és més elevada. Tots els diagrames tenen anomalies negatives en Ti més marcades que en roca total, exceptuant la BB.12.04.

Finalment, el diagrama multielemental de la websterita és molt semblant al de les harzburgites, amb un contingut en els elements més incompatibles semblant a les harzburgites més empobrides, mentre que els elements menys incompatibles es situen entre els dos tipus (Fig. 12.25d).

Un resum del fraccionament interelemental mencionat anteriorment pels diferents grups de lherzolites i harzburgites i del seu clinopiroxè agrupats segons els tres tipus d'espectres REE es troba en la taula 12.4.

El diagrama de la figura 12.27a és una altra manera de presentar la forma dels espectres REE del clinopiroxè i així comparar-los amb els de roca total. Els espectres en forma de U (quadrant superior esquerra) i els que estan clarament molt empobrits en LREE i MREE (quadrant inferior esquerra) són poc comuns. Ressalten les lherzolites BB.08.57 i SC.11.16 per tenir valors Sm/Nd (0,78-1,09) més elevats que la resta (0,13-0,45). Aquests valors més elevats són típics del clinopiroxè de les peridotites de la sèrie nord del Massís Central Francès (Downes et al., 2003), amb valors que poden ser >1 i que es van atribuir a la presència de granat durant els primers episodis de fusió, i que més tard seria substituït per espinel·la. Això encaixaria també amb el fet que els clinopiroxens d'aquestes lherzolites tinguin $(Gd/Yb)_N$ <1 (Taula 12.3) (Galán et al., 2008). Els espectres en aquestes dues mostres són comparables als de les lherzolites Olt 4e i Olt 7f de Bianchini et al. (2007), i que aquests

autors també atribueixen a la presència de granat durant les primeres etapes de fusió. A més, es diferencien per presentar una anomalia negativa i profunda en Zr (FIg.12.25b-c) i gairebé sense anomalia negativa en Ti. L'empobriment extrem en LREE-MREE també suggeriria que aquestes lherzolites estarien poc metasomatitzades. La resta dels espectres encaixarien amb els del clinopiroxè de la sèrie sud del MCF, com ja s'havia relacionat en treballs anteriors (Galán & Oliveras, 2014). La superposició amb el domini dels espectres de roca total en la figura 12.24a és força bona.

La relació Zr/Hf oscil·la al voltant del MP (Fig.12.27b) i és força constant, mentre que la relació Nb/Ta és variable, però sempre superior al MP. L'evolució en aquest diagrama és contrària a la que s'observa en roca total. Els valors de la relació Nb/Ta en el clinopiroxè podrien ser deguts a la presència de microfases que capten el Ta, fet que faria disminuir la relació Nb/Ta en la roca total, o bé a un error analític en la mesura del Ta en roca, com ja es va mencionar anteriorment. En el cas de la relació Zr/Hf, la diferència podria ser ocasionada pel fet de qui hi hagi una altra fase present (e.g., ortopiroxè) que capturi aquests dos elements en diferents proporcions al clinopiroxè. Tampoc es pot descartar que el Zr mesurat en roca total mostri un error sistemàtic, però els valors trobats no són diferents dels que proporcionen altres autors (Fig.12.11h, Fig.12.12f). Cal mencionar que un desdoblament similar en el fraccionament d'aquests elements HFS del clinopiroxè respecte de la roca va ser observat als xenòlits peridotítics de Kilbourne Hole, en el rift de Rio Grande (SO dels Estats Units) (Harvey et al., 2012). En aquests xenòlits, el desdoblament es va relacionar amb l'existència de dos episodis metasomàtics diferents: un primer episodi, amb un volum de fluid/fos baix, causaria el fraccionament de la relació Nb/Ta en el clinopiroxè i la roca, mentre que el segon episodi tindria lloc amb una relació fluid/roca més elevada i modificaria la relació $(Nb/Ta)_N$ de la roca però no la del clinopiroxè.

Si, com hem fet per les anàlisis de roca total, assumim que la relació $(La/Yb)_N$ en el clinopiroxè representa un índex del grau de metasomatisme experimentat pel mantell i l'abundància de CaO en roca total un índex de fertilitat (condicionat per la moda del clinopiroxè), es pot observar en la figura 12.27c que existeix una bona correlació inversa per la majoria de les harzburgites, però en el cas de les lherzolites, la dispersió és més notable, per exemple, les lherzolites amb un contingut en CaO entre el 2 i el 3% tenen una relació $(La/Yb)_N$ que varia en més de quatre ordres. Aquestes conclusions són semblants a les deduïdes per a roca total (veure Fig.12.16b). En la figura 12.27c destaquen especialment quatre lherzolites: dues (SC.11.16, BB.08.57) per ser moderadament fèrtils (9-12% de

clinopiroxè respectivament) i tenir un clinopiroxè extremadament empobrit en LREE, i unes altres dues (BB.08.18, CA.12.03) per mostrar una fertilitat elevada (11-17% de clinopiroxè) i tenir un clinopiroxè molt enriquit en LREE. El clinopiroxè de tres d'aquestes mostres (SC.11.16, BB.08.18, CA.12.03) té un contingut en Al_2O_3 (4,71-6,29%) i un #Mg similar (89,1-89,6), però la BB.08.57 es diferència per tenir menys Al_2O_3 (3,95%) i un #Mg més elevat (91,8). A més, aquesta, és una mostra que presenta la relació CaO/Al_2O_3 més elevada de totes les lherzolites (Fig.12.6), fet que podria ser degut a un increment del clinopiroxè per refertilització. La figura 12.27c també indicaria que normalment les harzburgites més refractàries van ser més metasomatitzades, el que explicaria el seu enriquiment en elements més incompatibles. Donat que el nivell d'enriquiment d'aquests elements és comparable en les dues peridotites, el component metasomàtic que les va afectar seria comparable en els dos casos. En el diagrama $(La/Yb)_N$ en front Ti/Eu de Coltorti et al. (1999) (Fig.12.28) pot servir per discriminar la natura d'aquest component. En aquest s'observa que només dues harzburgites es situen en el domini del metasomatisme carbonatític (BB.08.20, BB.12.02), una d'elles corresponent a les del grup enriquit en LREE i l'altre al grup de les més empobrides. Tot i això, aquestes harzburgites no presenten altres característiques típiques d'aquest metasomatisme, com són les anomalies pronunciades en Ti i Zr (només en el cas de BB.12.02), el fraccionament significatiu entre Th/U i la relació Zr/Hf elevada (cap de les dues es diferencia de les altres harzburgites) (Taules 12.3 i 12.4) (Rivalenti et al., 2004 i referències incloses). Les altres harzburgites i algunes lherzolites haurien estat metasomatitzades per un component silicatat i alcalí, donat el contingut elevat en LREE del seu clinopiroxè (Fig.12.22a-b). L'avaluació dels processos i agents metasomàtics es farà en profunditat en el següent capítol (Discussió).

En resum, l'abundància, fraccionament i evolució dels elements traça en el clinopiroxè ens aporten sobre el ja observat en roca total la següent informació: l'evolució del elements traça mitjanament incompatibles és coherent amb processos de fusió parcial, però les diferents evolucions en alguns d'ells en lherzolites i harzburgites, suggereix que les dues peridotites han pogut estar afectades per diferents episodis (Fig.12.19h, Fig.12.20f). Aquesta fusió podria haver començat en presencia de granat en alguns casos i seguir en presència d'espinel·la, fet que quedaria registrat en molt poques mostres [dues lherzolites i una harzburgita amb espectres REE molt empobrits (BB.08.57, SC.11.16) i en forma d'"u" (BB.12.04)]. Si més no, una d'aquestes mostres té un contingut modal en clinopiroxè que no es correspon ni amb el seu contingut en Al_2O_3 ni en LREE, la qual cosa no es pot explicar per fusió parcial i confirmaria així l'existència de processos de refertilització (BB.08.57). Les

mostres de lherzolites anòmalament "fèrtils", dues d'elles amb corones entorn a espinel·la (BB.08.18, SC.11.49), no presenten espectres del clinopiroxè uniformes: BB.08.18 esta molt enriquit en LREE i l'altre lleugerament empobrit, per la qual cosa es dedueix la formació d'aquestes corones no estaria lligat al metasomatisme general que va afectar aquestes roques. Aquest metasomatisme va afectar a totes les harzburgites, algunes d'elles molt refractàries, i a algunes lherzolites. Les primeres es van enriquir en LREE-MREE i només en LREE les segones. Altres elements aportats pel metasomatisme són el Th-U, Nb, Sr i Zr, encara que hi hagi una anomalia negativa en Nb i Zr. Alguns espectres molt enriquits en LREE suggereixen que van actuar processos de fraccionament cromatogràfic (Navon & Sloper, 1987). Finalment, la naturalesa del(s) agent(s) metasomàtic(s) sembla haver estat la d'un fos silicatat alcalí, fet que explicaria el nivell d'enriquiment en LREE, l'absència d'una anomalia molt significativa en Ti, així com la introducció de Zr i els valors baixos en la relació Zr/Hf (Rudnick et al., 1993; Ionov et al., 1993; Coltorti et al., 1999; Blundy & Dalton, 2000). Només dues harzburgites tenen relacions $(La/Yb)_N$ vs. Ti/Eu característiques d'un metasomatisme carbonatític, però la seva baixa relació en Ti/Eu també podria ser deguda a un elevat grau de fusió parcial anterior. Per últim, les dades de la websterita analitzada ens indiquen que també hi ha diferents tipus de piroxenites pel que es refereix al contingut en REE: unes menys diferenciades i més empobrides, com la mostra BB.12.17 estudiada en aquesta tesis, i altres més enriquides, com la mostra BB.83.04 estudiada anteriorment (Galán et al., 2008; Oliveras, 2009). El clinopiroxè de la primera té forma de cullera invertida semblant al d'algunes harzburgites, però amb un contingut més elevat en Ti (Fig.12.19, 12.21a).

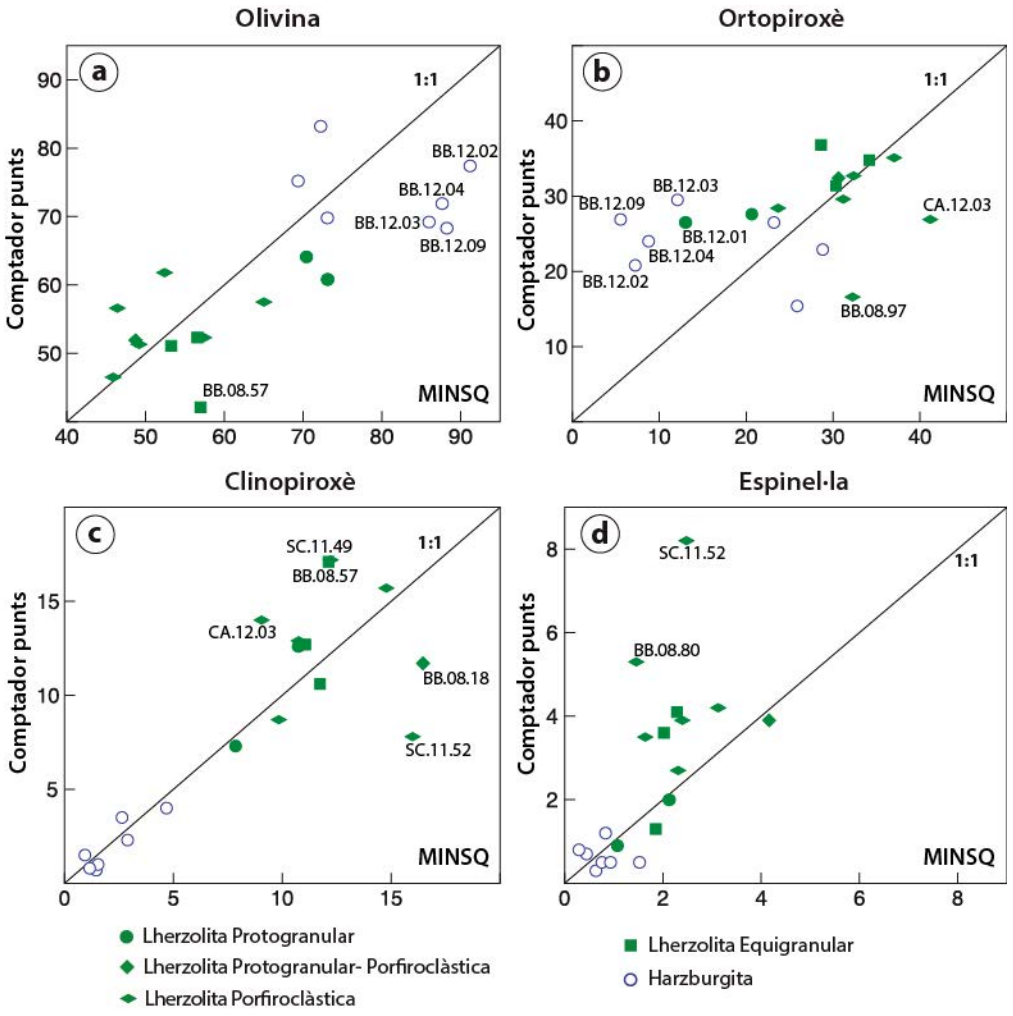

Fig.12.1. Diagrames de comparació entre les composicions modals a partir del comptador de punts vs. les estimacions per balanç de masses amb les anàlisis de roca total dels minerals.

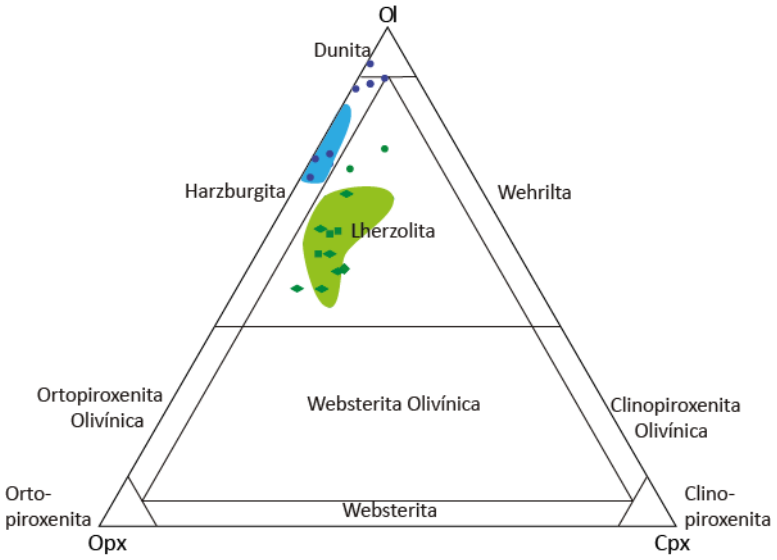

Fig. 12.2. Diagrama de classificació per a roques ultramàfiques de Le Maître (2002) amb la projecció de les estimacions modals per balanç de masses i els dominis establerts per comptatge de punts (capítol 7). Símbols equivalents a la figura 12.1

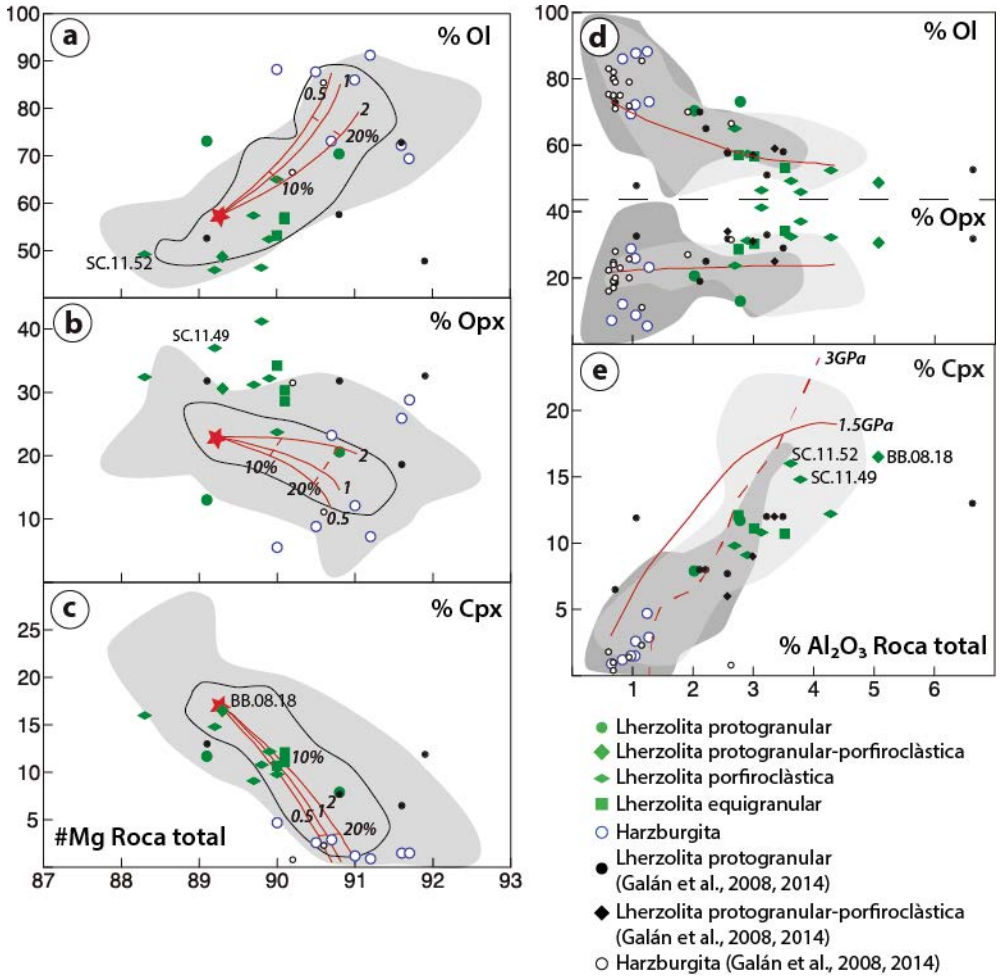

Fig.12.3 a-c) Composicions modals estimades vs. #Mg de roca total. Camps en gris corresponents a lherzolites amb espinel·la circumcratòniques de diferents localitats i el camp delimitat per la línia negre corresponent a peridotites abissals (figura 9 de Walter, 2003). L'estrella= mantell primitiu (McDonough & Sun, 1995). S'indica també el grau de fusió. d-e Moda estimada vs. %Al_2O_3 en roca total. Els camps gris clar es corresponen a xenòlits circumcratònics i els gris fosc als xenòlits cratònics de diferents localitats (taula 6 en Pearson et al., 2003). Les línies vermelles en totes les figures es corresponen a variacions modals calculades en el residu sòlid d'un procés de fusió fraccionada. En (a), (b) y (c) la modelització s'ha fet a 0,5, 1 i 2 Gpa. En d) i e) estan calculades a 1,5GPa i 3GPa segons Canil (2002).

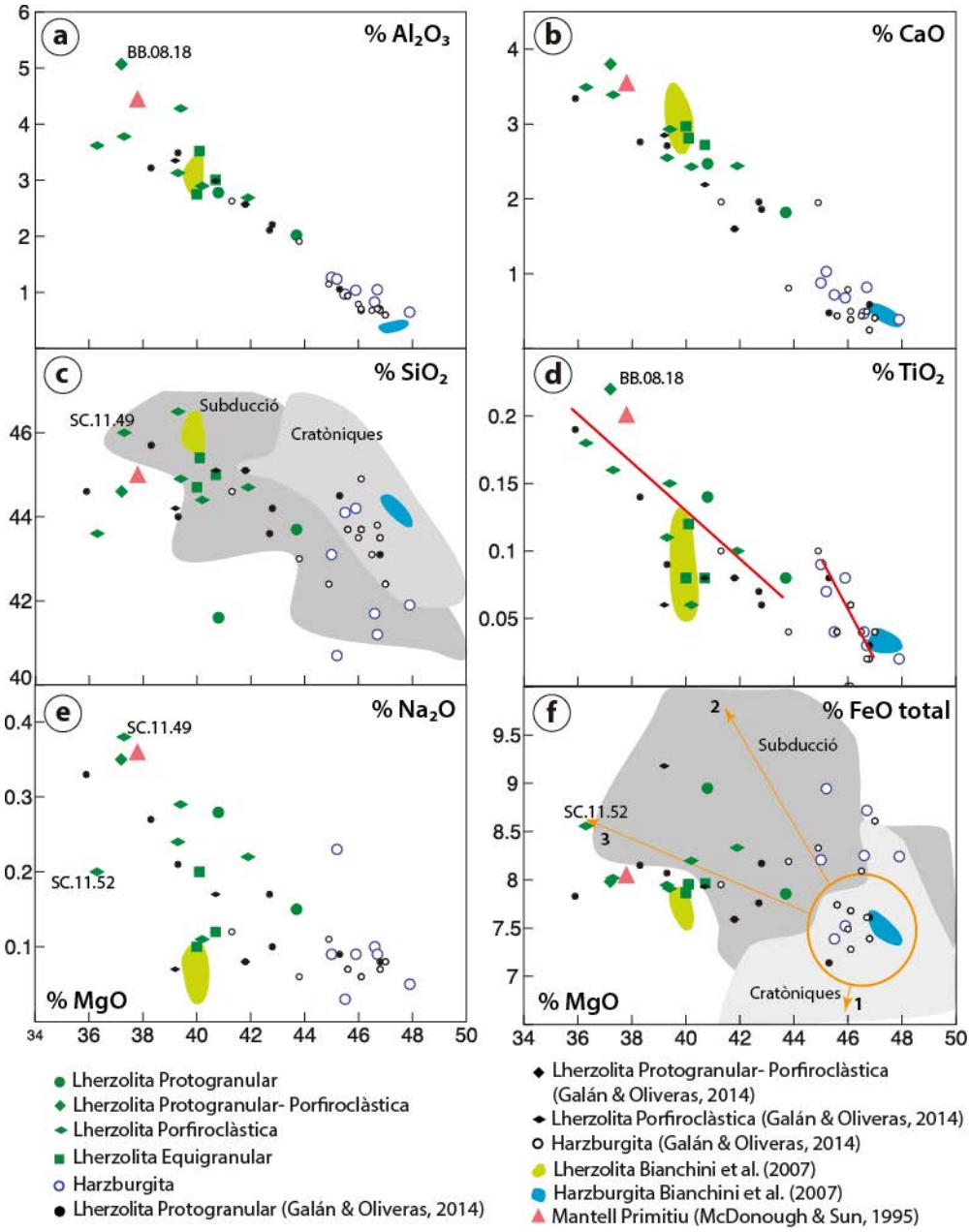

Fig.12.4. Diagrames de variació dels diferents òxids vers MgO. En aquests diagrames s'han considerat les anàlisis de Galán et al. (2008; 2014) i Bianchini et al. (2007). En la figura (c), la pendent negativa de lherzolites i harzburgites és diferent. En les figures (c) i (f) hi figuren els camps que representen la composició de peridotites em xenòlits cratònic enriquits en ortopiroxè i de les peridotites en zones de subducció actuals. En (f) s'indiquen dos tendències evolutives contraries: (1) a FeO_T decreixent per a peridotites cratòniques i creixent (2, 3) per a peridotites de zones de subducció (Herzberg, 2004). El

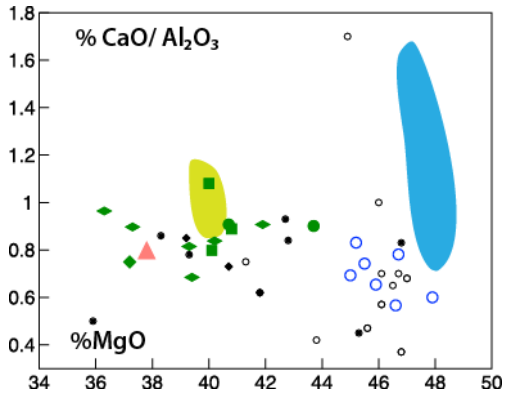

Fig.12.5. Relació CaO/Al_2O_3 en % vs. MgO. En general, la majoria de les harzburgites de Bianchini et al. (2007) mostren una relació CaO/Al_2O_3 més elevada que les d'aquest estudi. Símbols equivalents als de la figura 12.4.

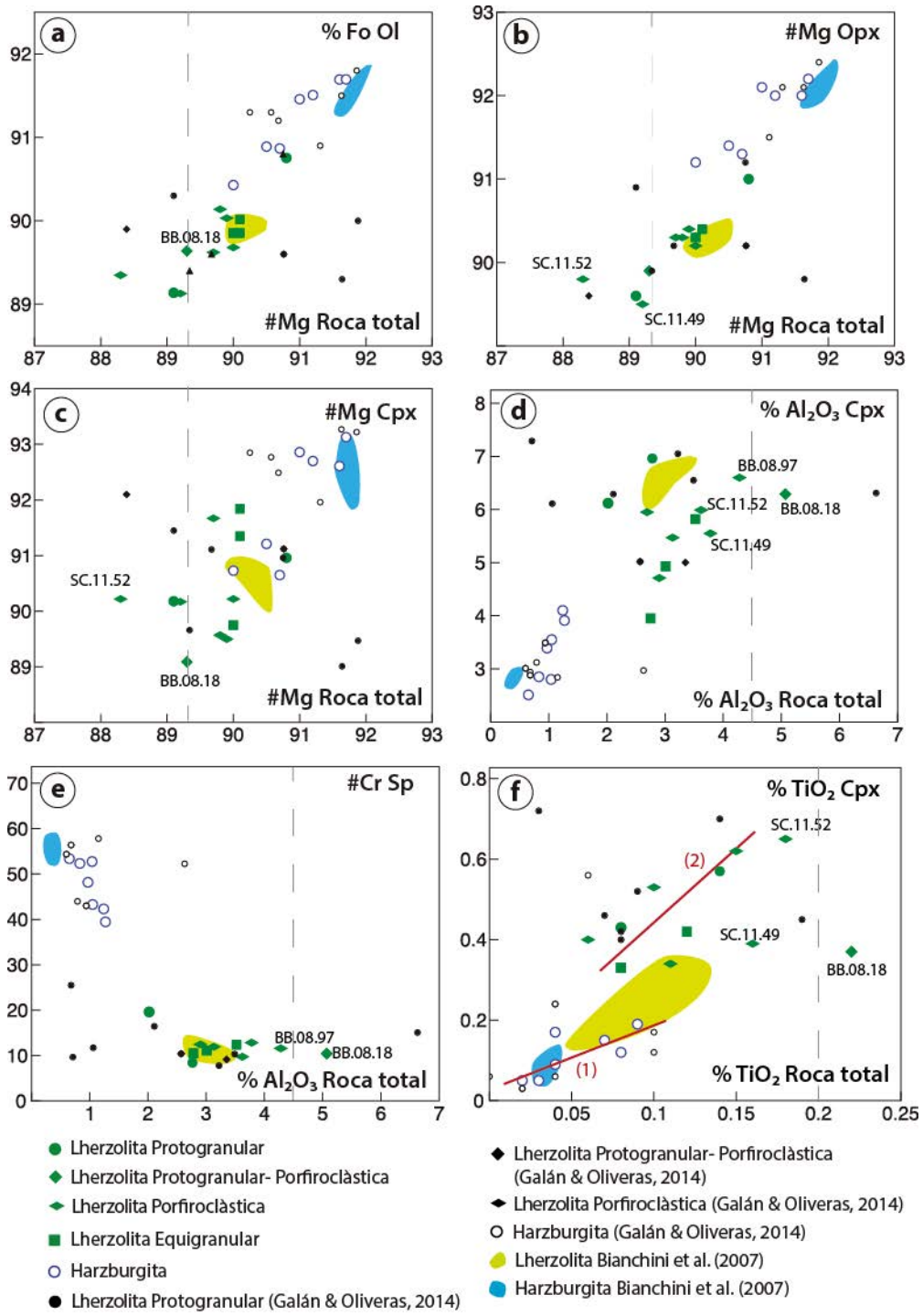

Fig.12.6. Diagrames de variació del % en fosterita de l'olivina (a), del #Mg de l'ortopiroxè i (c) del clinopiroxè vs. #Mg de roca total:, Al_2O_3 del clinopiroxè (d), #Cr de l'espinel·la (e) vers el % Al_2O_3 de roca total; TiO_2 del clinopiroxè en front del TiO_2 de la roca total els dos en % en pes, les línies vermelles marquen dues tendències diferents per harzburgites i lherzolites. La línia discontínua marca la composició del mantell primitiu (McDonough & Sun, 1995)

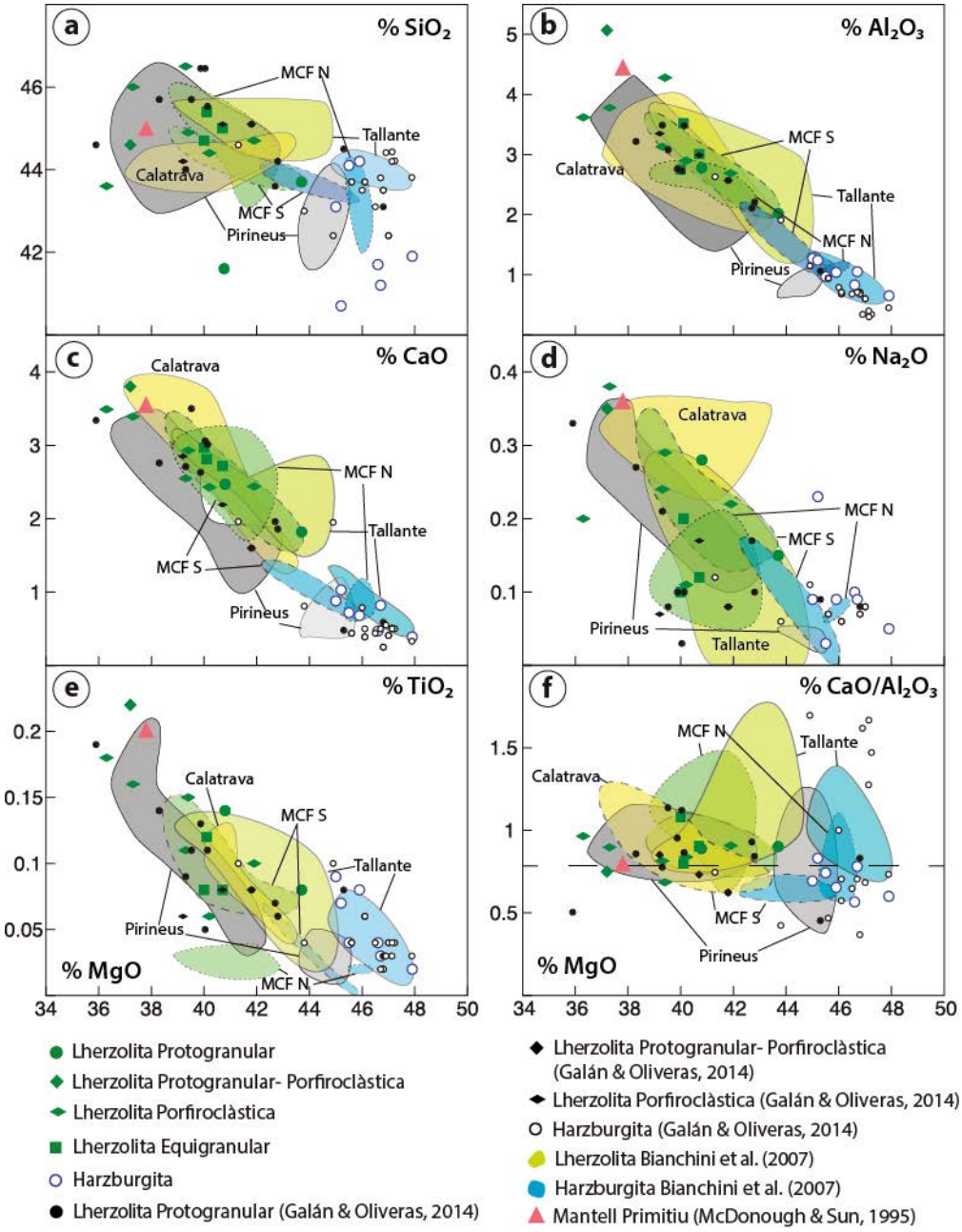

Fig.12.7. Diagrames de variació de diversos òxids I de la relació CaO/Al_2O_3 vs. MgO amb els camps de xenòlits peridotítics de diferents zones pròximes a la ZVC (Calatrava: Villaseca et al., 2010; MCF: Lenoir et al, 2000; Tallante: Beccaluva et al., 2004) i massissos peridotítics de l'est dels Pirineus (Bodinier et al., 1988, 1989; Burnham et al., 1998)

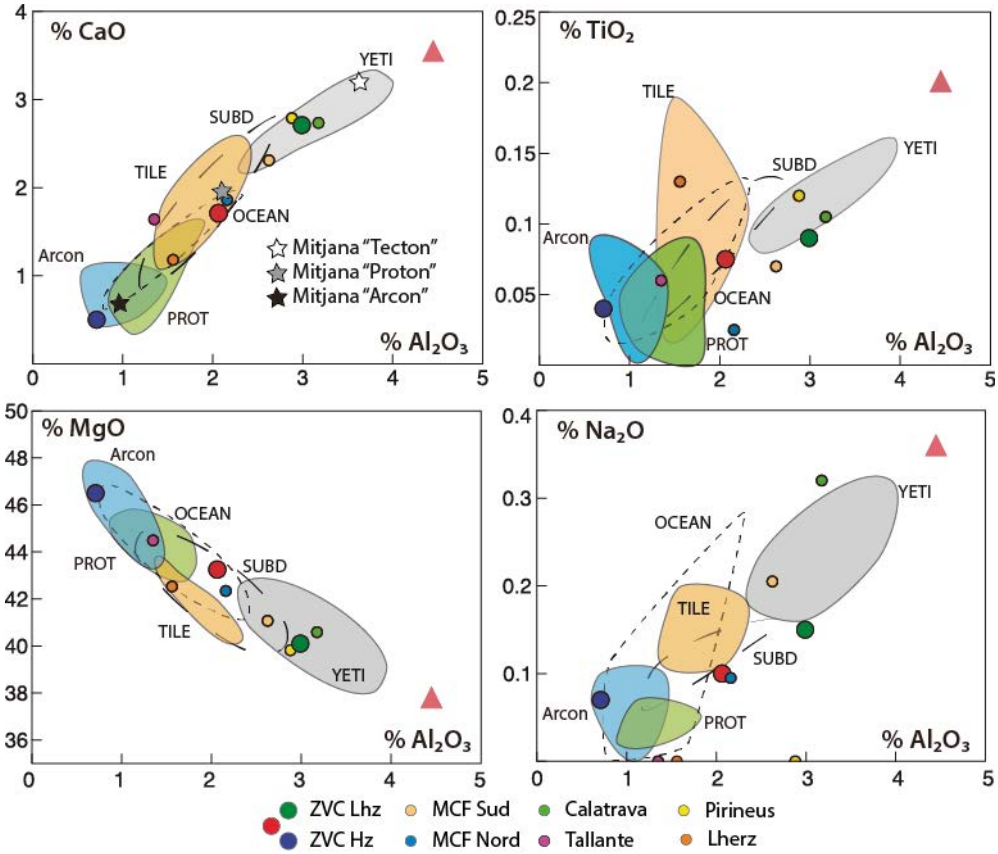

Fig.12.8. Diagrames de variació del CaO, TiO_2, MgO i Na_2O vers Al_2O_3 en roca total amb els camps YETI, TILE, OCEAN, SUBD Tecton), Proton i Arcon proposats per Griffin et al. (1999). Medianes global i parcials de lherzolites i harzburgites de la ZVC junt amb les medianes de les diferents zones del MSCL amb les que s'han comparat (Calatrava: Villaseca et al. 2010; MCF Sud i Nord: Lenoir et al. 2000; Tallante: Beccaluva et al. 2004; Lherz i resta de massissos dels Pirineus: Griffin et al. 1999). Les estrelles representen mitjanes del MSCL tipus Tecton, Proton i Arcon de Griffin et al. (1999).

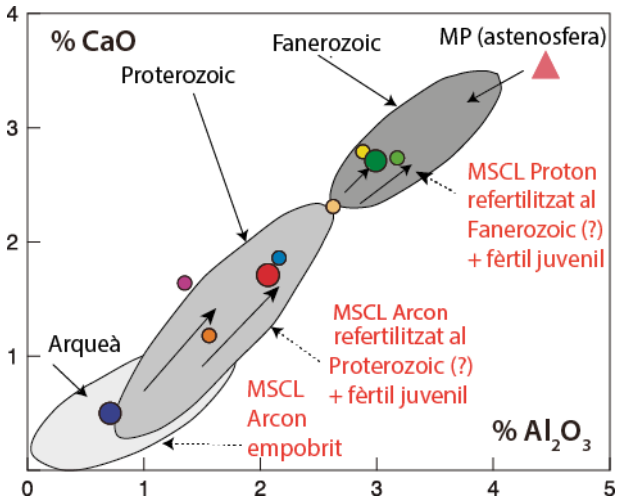

Fig.12.9. Diagrama $\%Al_2O_3$ vs. %CaO en roca total, on es representen les medianes globals i parcials de la ZVC i de diferents zones pròximes, veure llegenda figura 12.8. Esdeveniments tectonotèrmics (en negre) i la possible evolució dicotòmica del MSCL (en vermell) de Griffin et al. (2009).

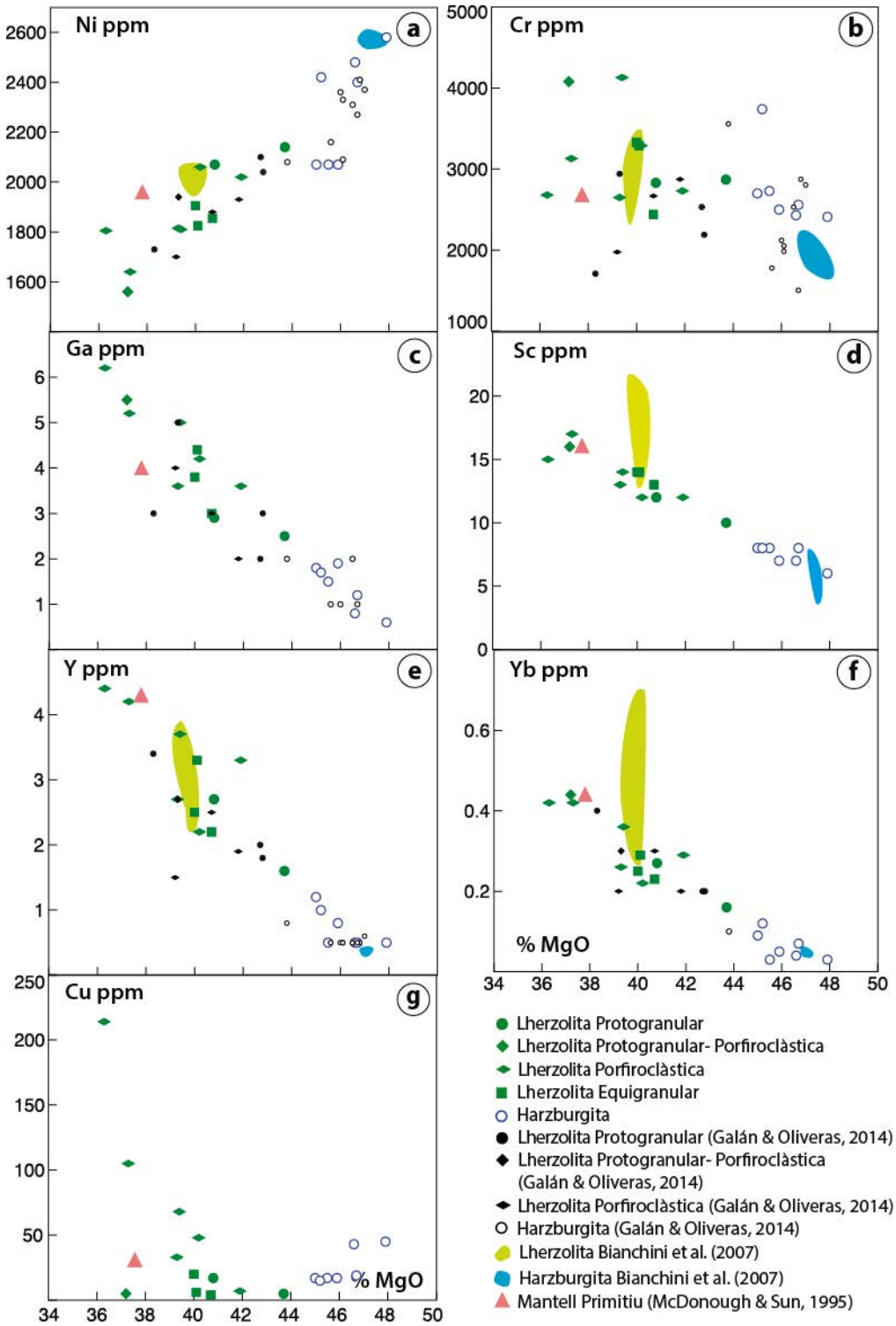

Fig.12.10 Diagrames de covariació entre alguns elements de trancisió i elements moderadament incompatibles en front del %MgO de roca total.

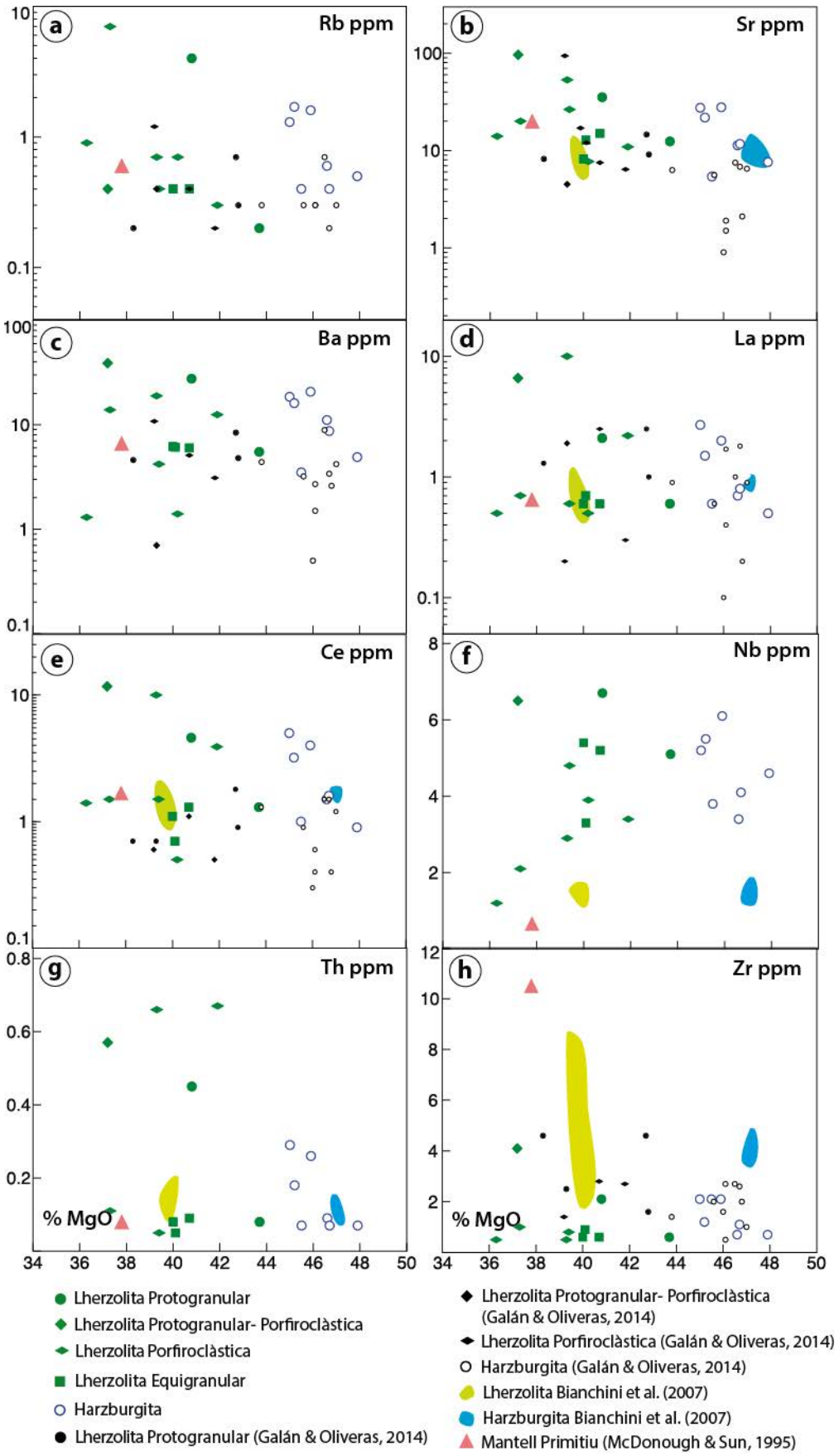

Fig.12.11 Diagrames de covariació d'alguns elements LIL, LRE i HFS en front a % MgO de roca total. Els camps es corresponen a les dades de Bianchini et al. (2007)

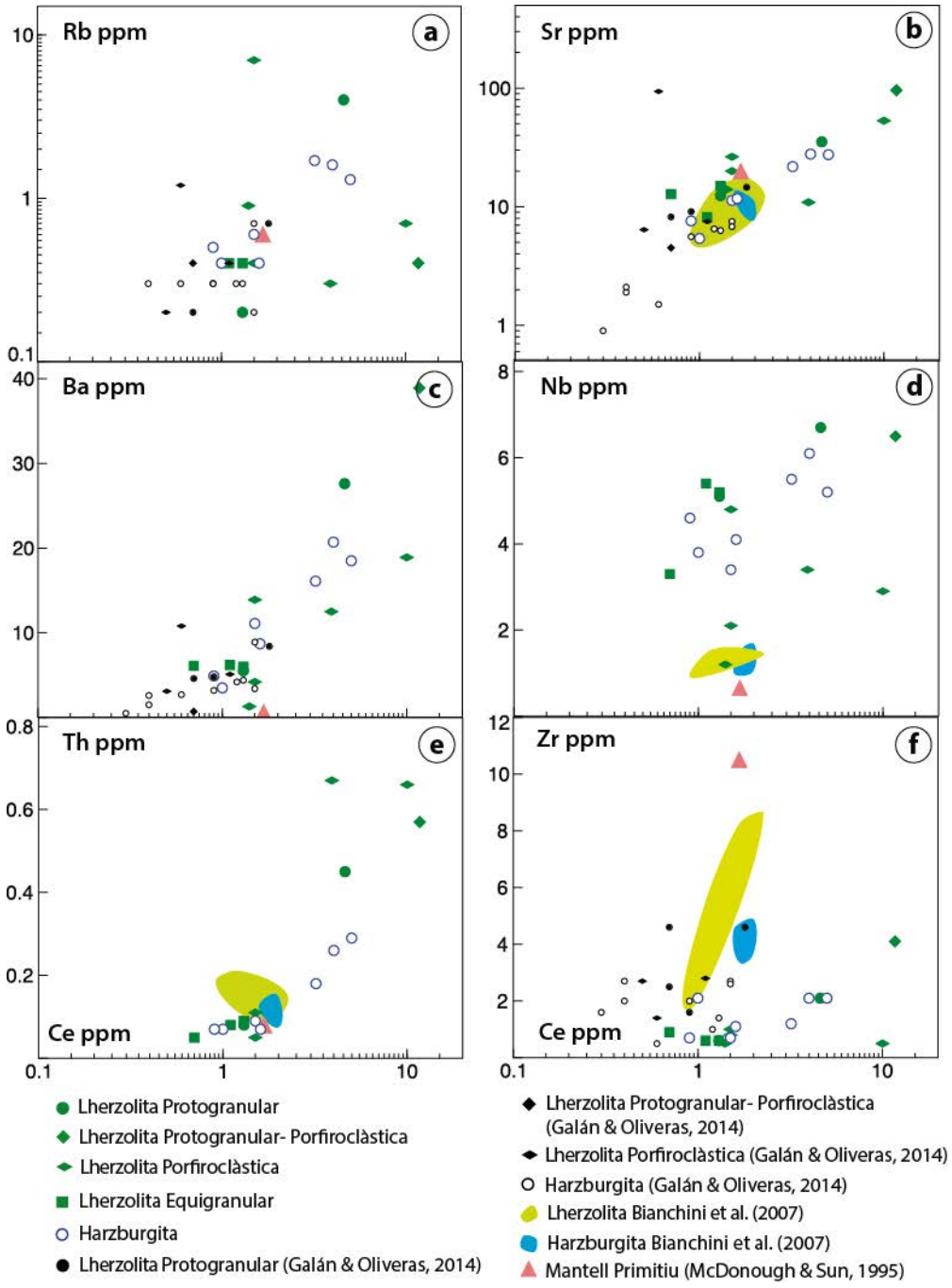

Fig.12.12. Diagrames de covariació d'alguns elements traça en front Ce (en escala logarítmica). Els camps es corresponen amb les dades de Bianchini et al. (2007)

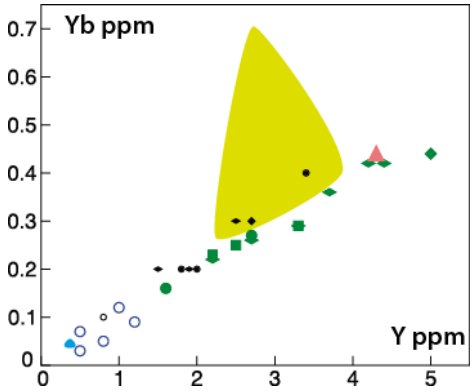

Fig.12.13 Diagrama de variació Yb en front Y. Els símbols són equivalents als de la figura 12.12.

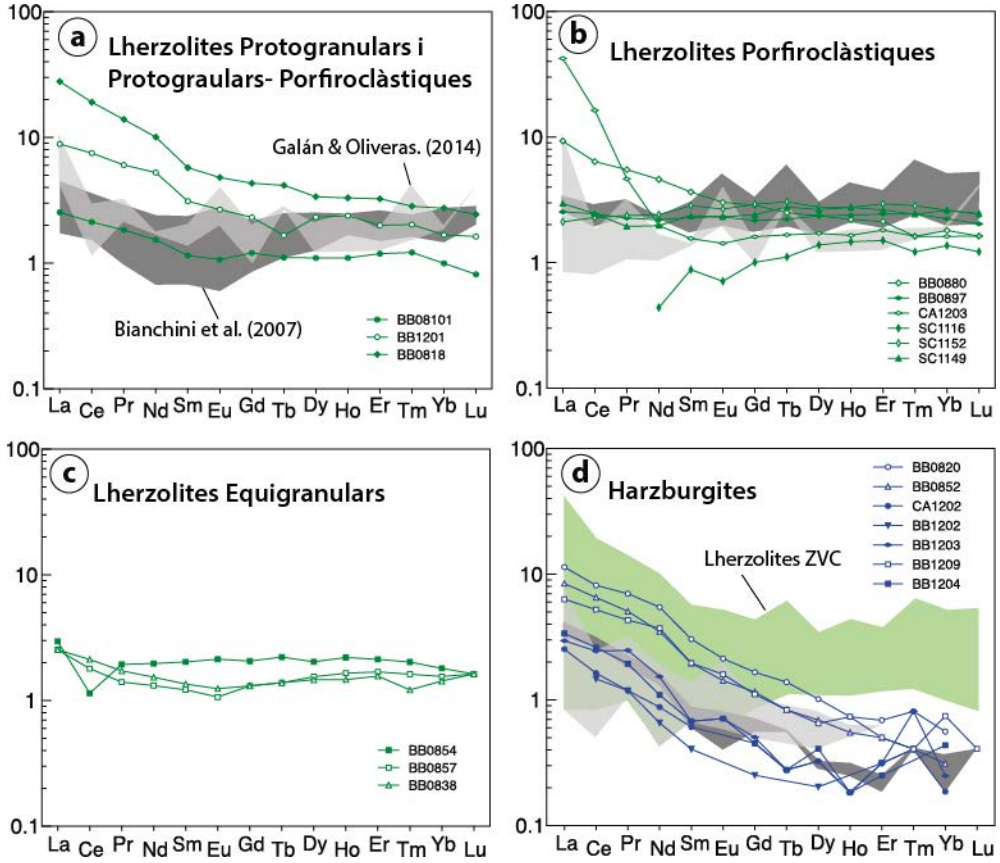

Fig.12.14. Espectres de REE amb valors normalitzats al C1 de McDonough & Sun (1995). Els camps en gris es corresponen a les dades anteriors de Galán & Oliveras (2014) (gris clar) i Binachini et al. (2007) (gris fosc).

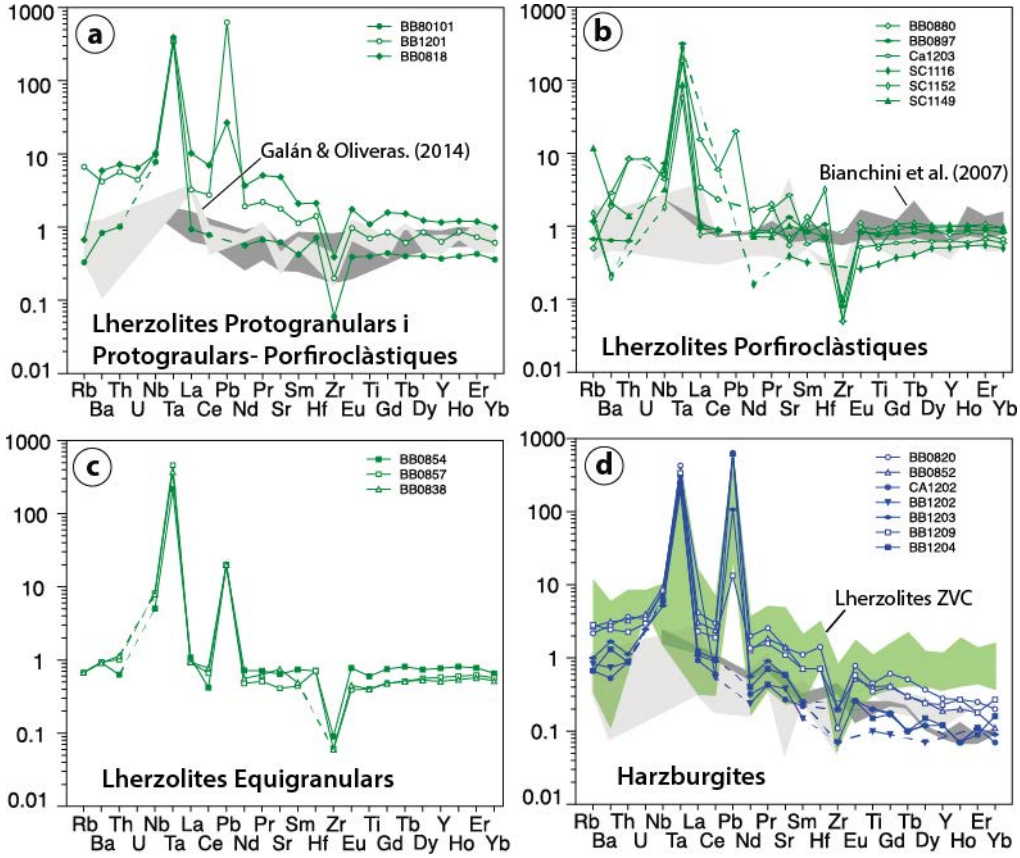

Fig.12.15. Diagrames multielementals amb valors normalitzats a la Pirolita de McDonough & Sun (1995). Els camps en gris es corresponen a les dades anteriors de Galán & Oliveras (2014) (gris clar) i Binachini et al. (2007) (gris fosc).

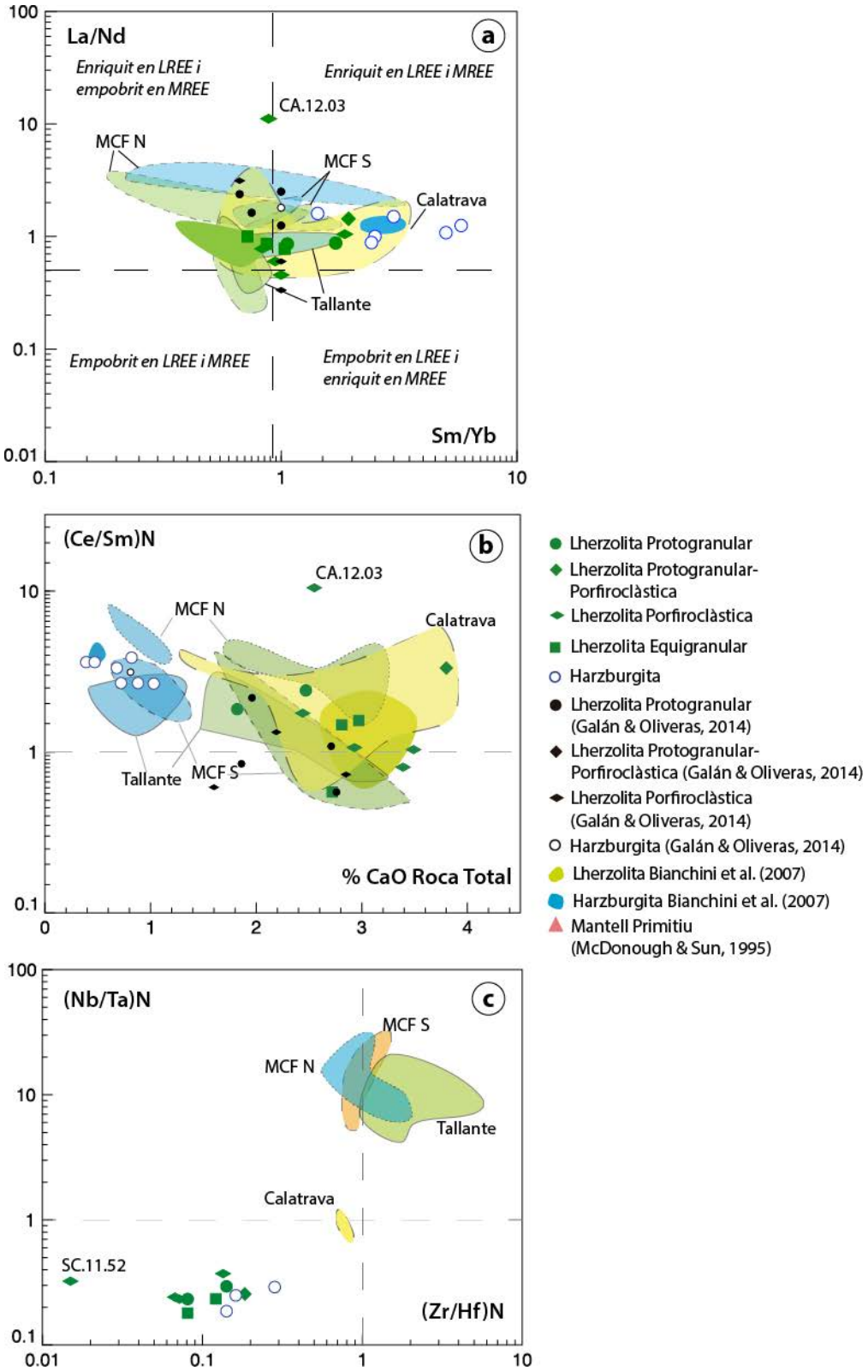

Fig.12.16. a) Covariació de les relacions La/Nd en front a Sm/Yb. b) $(Ce/Sm)_N$ vs. %CaO en roca total, els valors estan normalitzats a C1 de McDonough & Sun (1995). ***c) Relacions $(Nb/Ta)_N$ en front $(Zr/Hf)_N$.*** *També es projecten els camps de lherzolites (verd) i harzburgites (blau) de diferents zones pròximes (Calatrava: Villaseca et al., 2010; MCF: Lenoir et al., 2000; Tallante: Beccaluva et al., 2004), a més de dades dels xenòlits anteriorment estudiats anteriorment a la ZVC (Galan & Oliveras., 2014 i Bianchini et al., 2007)*

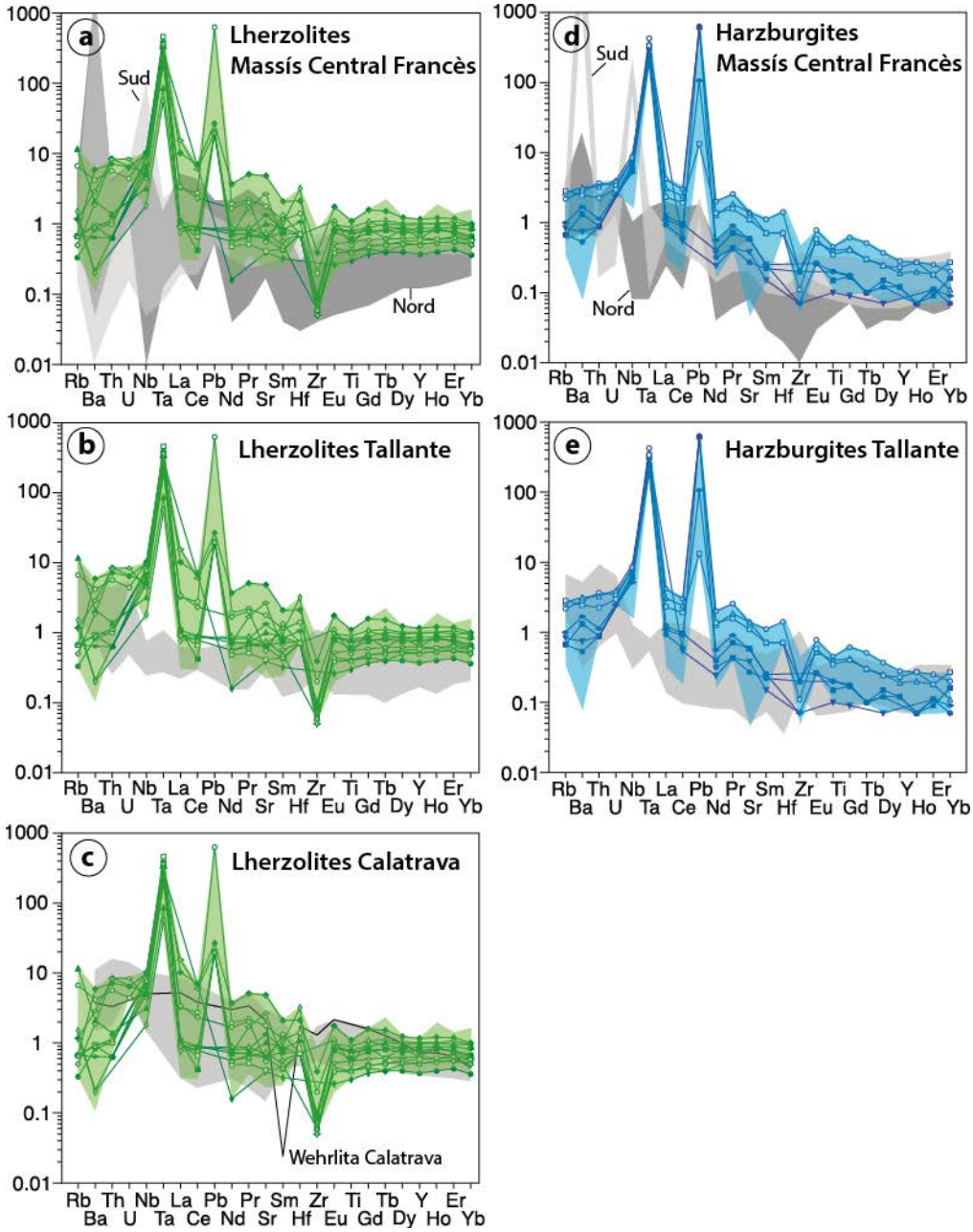

Fig.12.17 Diagrames multielementals per roca total amb valors normalitzats a la Pirolita de McDonough & Sun (1995). Els camps en gris es corresponen a les dades de les diferents zones amb que s'han comparat (Calatrava: Villaseca et al., 2010; MCF: Lenoir et al., 2000; Tallante: Beccaluva et al., 2004). Els camps en color verd (lherzolites) i blau (harzburgites) inclouen les d'aquest estudi i les estudiades per Galan & Oliveras (2014) i Bianchini et al. (2007).

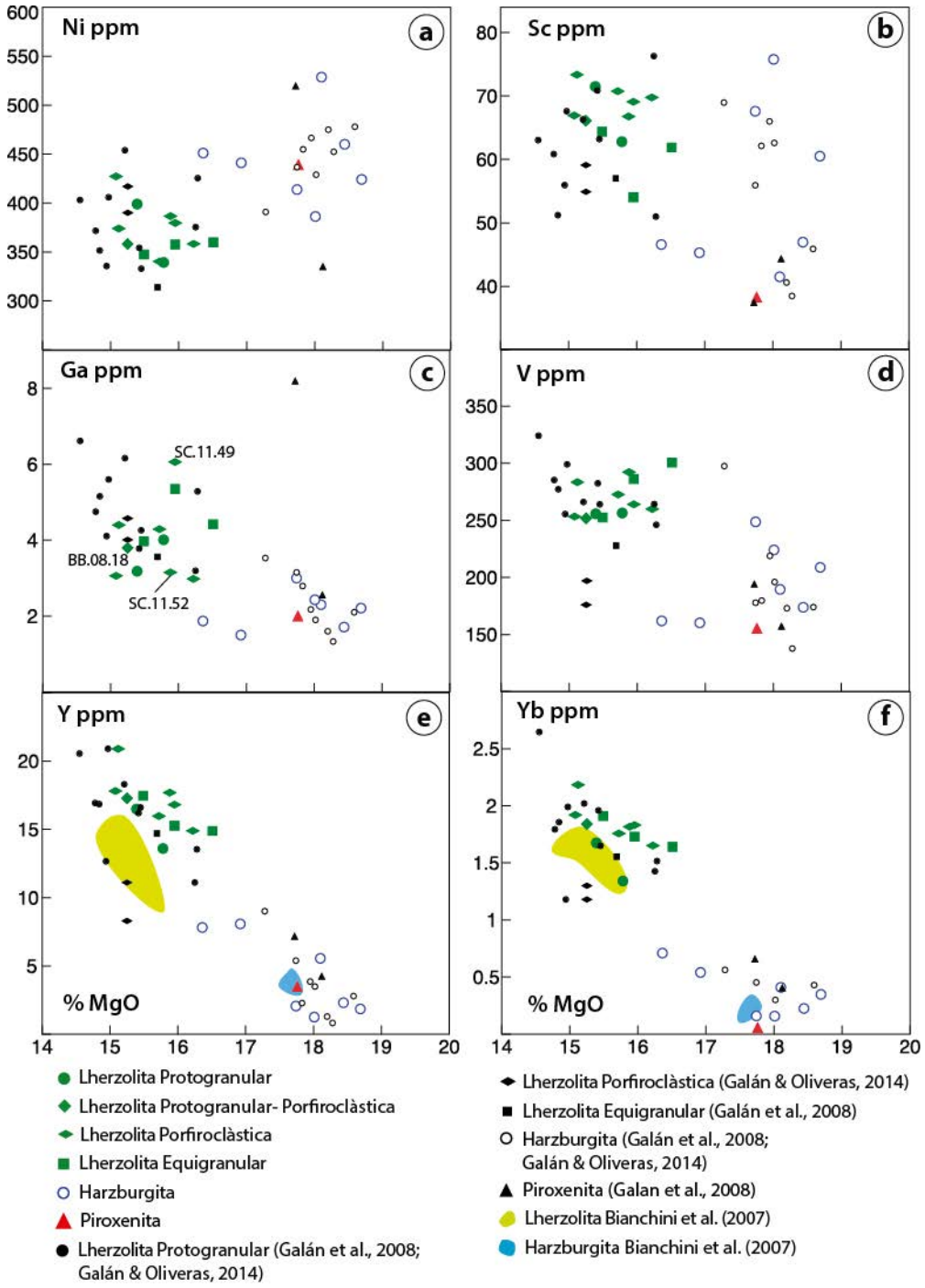

Fig.12.18. Diagrames de covariació entre alguns elements de trancisió i elements moderadament incompatibles en front del %MgO del clinopiroxè

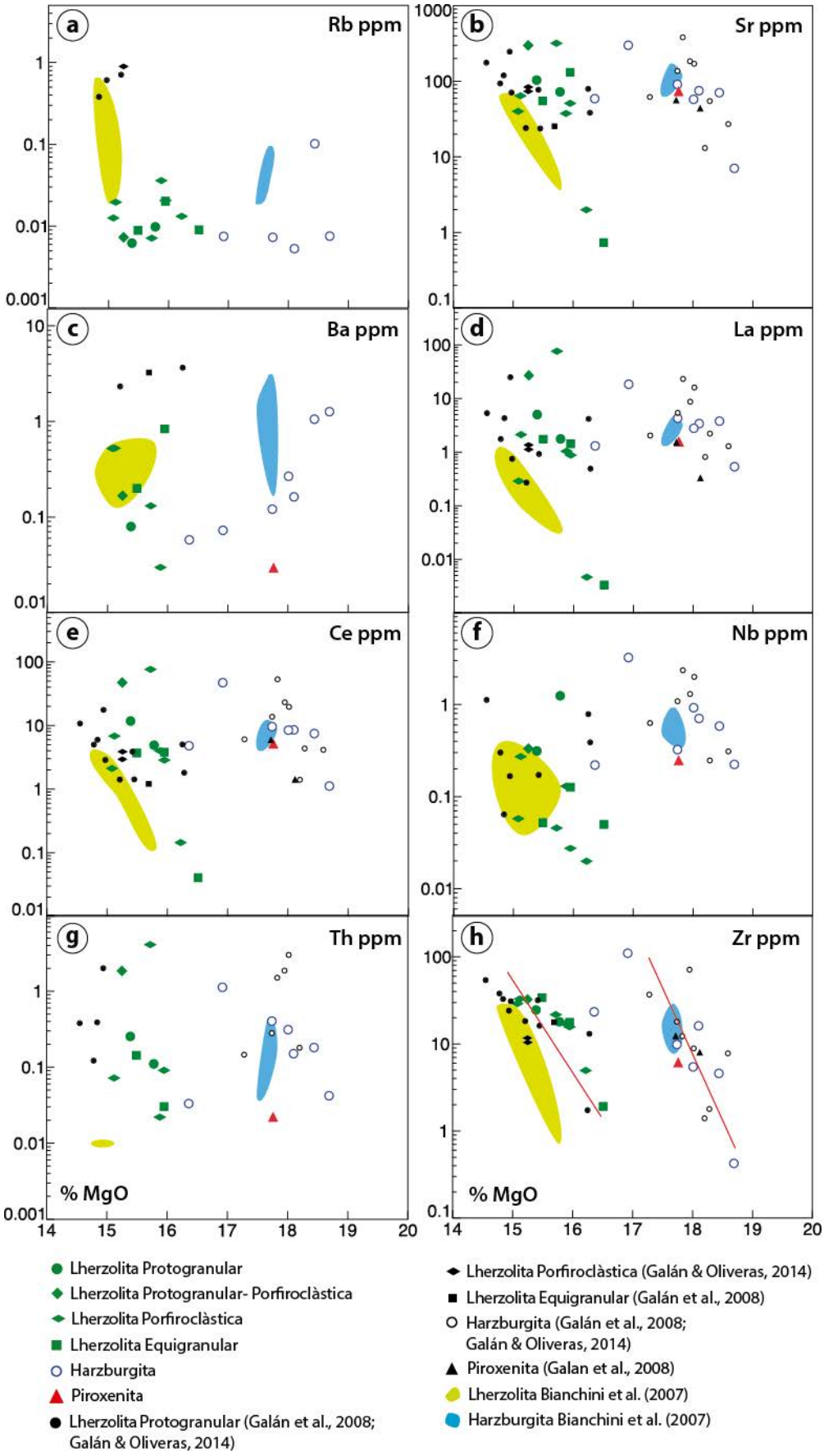

Fig.12.19. Diagrames de covariació d'alguns elements LIL, LRE i HFS en front a % MgO del clinopiroxè

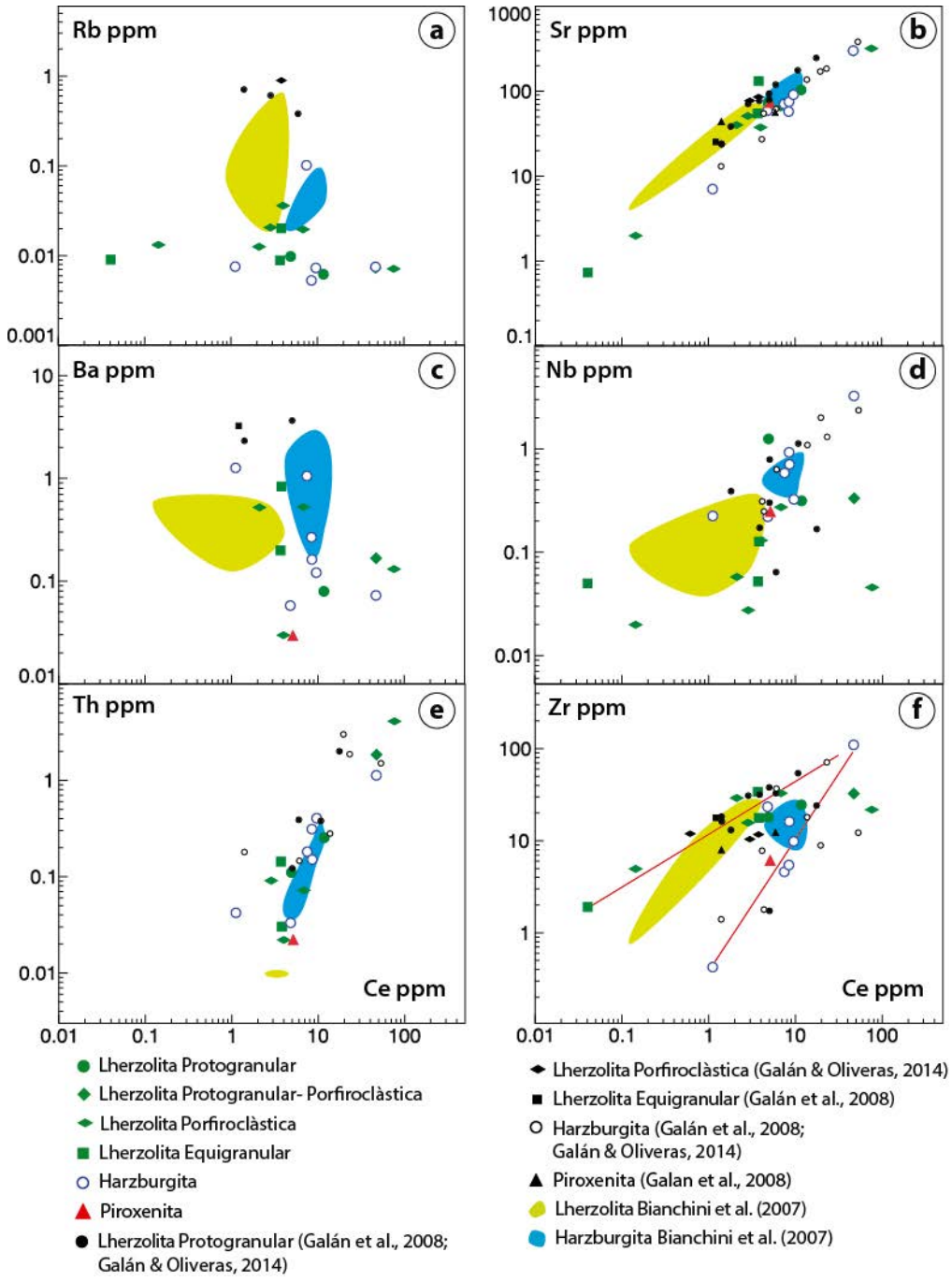

Fig.12.20. Diagrames de covariació d'alguns elements traça en front Ce (en escala logarítmica).

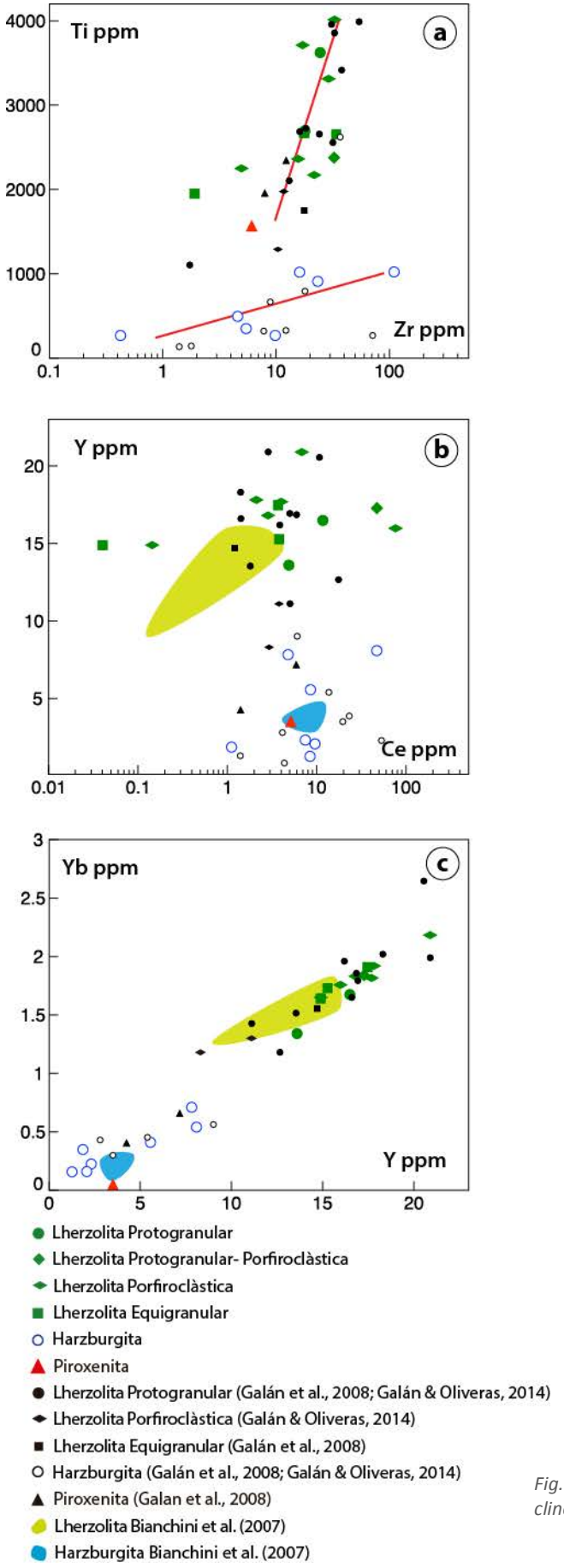

Fig.12.21. Diagrames de variació del clinopiroxè: a) Ti vs Zr; b) Y vs. Ce; i c) Yb i Y.

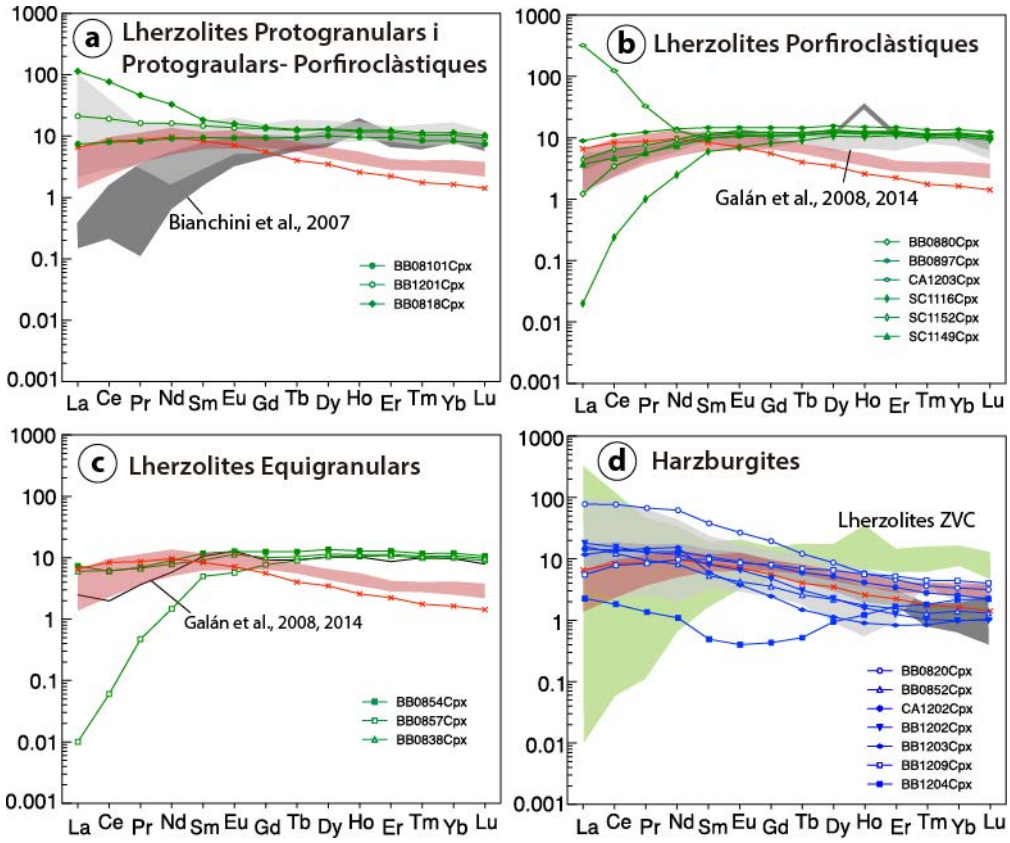

Fig.12.22. Espectres de REE del clinopiroxè amb valors normalitzats al C1 de McDonough & Sun (1995). Els camps en gris es corresponen a les dades anteriors de Galán et al. (2008) i Galán & Oliveras (2014) (gris clar), els camps en vermell als clinopiroxens de les piroxenites de Galán et al. (2008) i Binachini et al. (2007) (gris fosc).

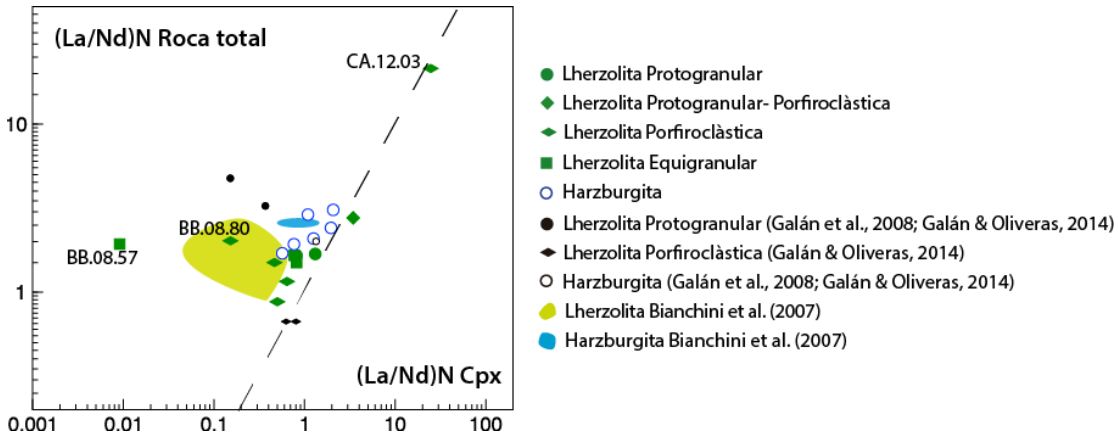

Fig. 12.23 Diagrama de variació $(La/Nd)_N$ en roca total en front $(La/Nd)_N$ en el clinopiroxè

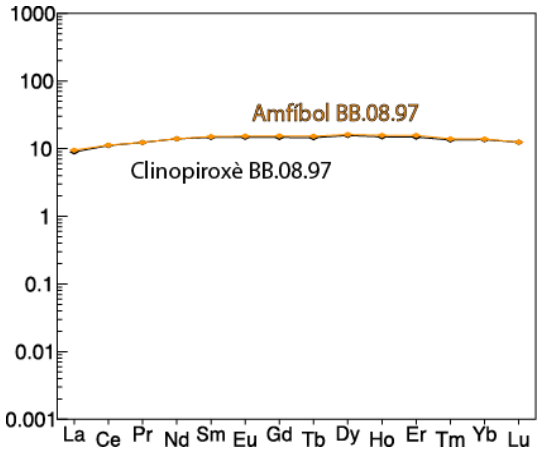

Fig. 12.24 Espectres de REE del clinopiroxè (negre) i l'amfíbol (taronja) de la lherzolita BB.08.97, amb valors normalitzats al C1 de McDonough & Sun (1995)

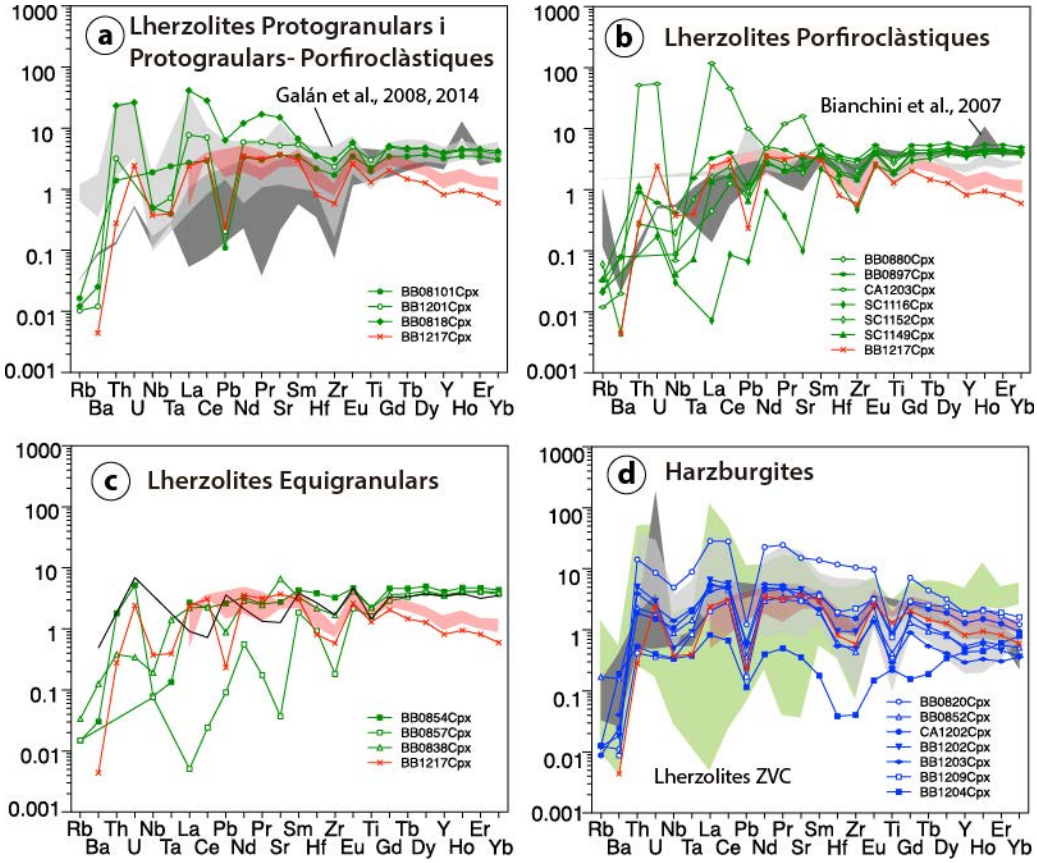

Fig.12.25. Diagrames multielementals del clinopiroxè. amb valors normalitzats a la Pirolita de McDonough & Sun (1995). Els camps en gris es corresponen a les dades anteriors de Galán et al. (2008) i Galán & Oliveras (2014) (gris clar), els camps en vermell als clinopiroxens de les piroxenites de Galán et al. (2008) i Binachini et al. (2007) (gris fosc).

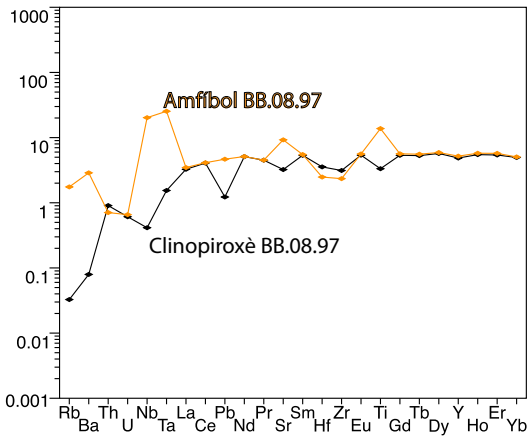

Fig.12.26 Diagrama multielemental del clinopiroxè (negre) i l'amfíbol (taronja) de la lherzolita BB.08.97, amb valors normalitzats al C1 de McDonough & Sun (1995)

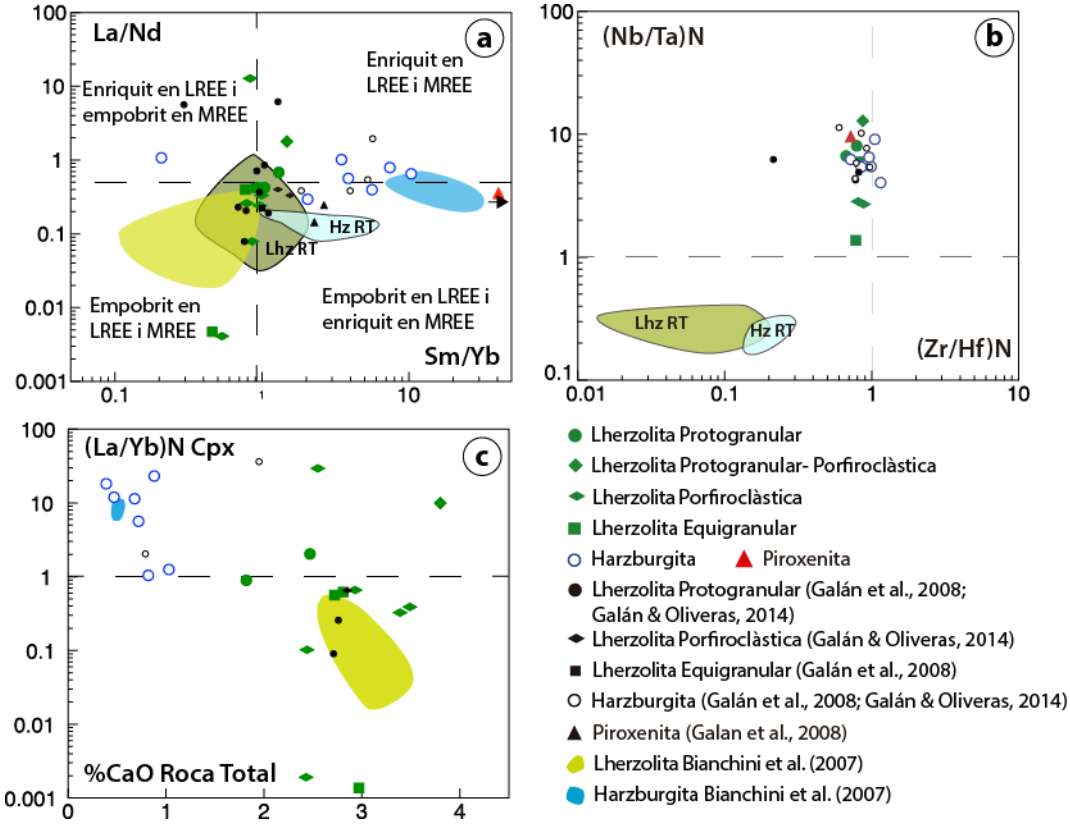

Fig.12.27. Covariació de les relacions La/Nd en front a Sm/Yb en el clinopiroxè), $(Nb/Ta)_N$ en front $(Zr/Hf)_N$ en el clinopiroxè b), i $(La/Yb)_N$ en el clinopiroxè en front CaO de roca total, els valors estan normalitzats a C1 de McDonough & Sun (1995).

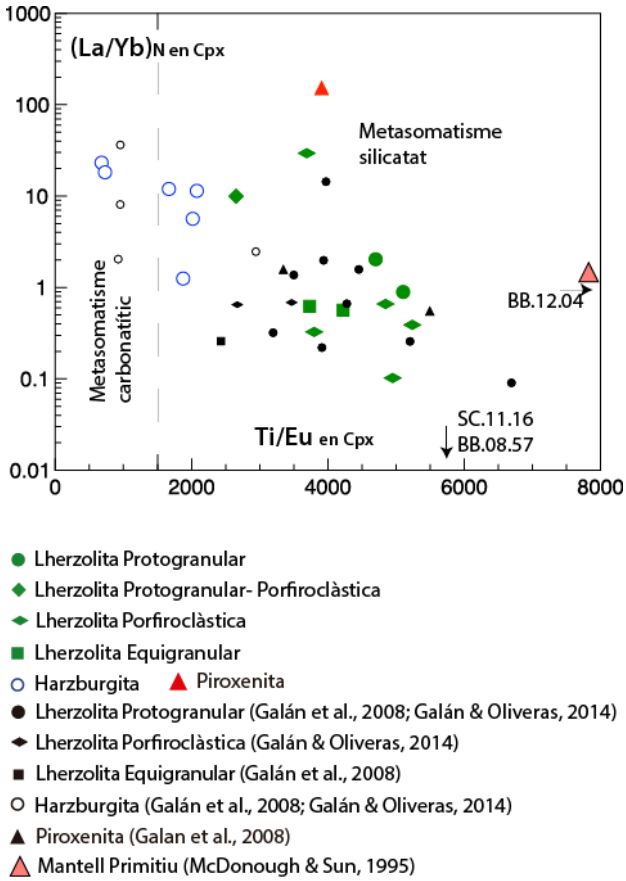

Fig.12.28. Diagrama de variació de $(La/Yb)_N$ en front Ti/Eu de Coltorti et al. (1999) amb els camps diferenciats de metasomatisme carbonatític i silicatat

Mostra	Precisió % 1σ	BB.08. 101	BB.12. 01	BB.08. 18	BB.08. 80	BB.08. 97	CA.12. 03	SC.11. 16	SC.11. 49	SC.11. 52
Micro-estructura		Lhz Pg	Lhz Pg	Lhz PgPc	Lhz Pc	Lhz Pc	Lhz Pc	Lhz Pc	Lhz Pc	Lhz Pc
% Òxids										
SiO_2	5	43,7	41,6	44,6	44,7	44,9	46,5	44,4	46,0	43,6
Al_2O_3	5	2,02	2,78	5,07	2,69	4,28	3,13	2,90	3,78	3,62
FeO_t	5	7,86	8,94	7,98	8,33	7,91	7,95	8,20	8,02	8,56
CaO	5	1,82	2,47	3,80	2,44	2,93	2,55	2,43	3,39	3,49
MgO	8	43,7	40,8	37,2	41,9	39,4	39,3	40,2	37,3	36,3
Na_2O	5	0,15	0,28	0,35	0,22	0,29	0,24	0,11	0,38	0,20
K_2O	5	0,01	0,14	0,02	0,01	0,01	0,04	0,02	0,31	0,01
TiO_2	8	0,08	0,14	0,22	0,10	0,15	0,11	0,06	0,16	0,18
MnO	18	0,13	0,13	0,14	0,14	0,13	0,14	0,13	0,14	0,13
LOI	6	0,36	0,39	0,55	0,14	0,28	0,21	1,11	0,99	1,30
Total		100,7	98,7	100,8	101,6	101,2	101,1	100,5	101,4	98,3
#Mg		90,8	89,1	89,3	90,0	89,9	89,8	89,7	89,2	88,3
#Cr		11,7	7,4	7,0	8,4	8,3	7,2	9,4	7,1	6,3
CaO/Al_2O_3		0,9	0,9	0,7	0,9	0,7	0,8	0,8	0,9	1,0
% Ol		70,4	73,1	48,7	65,0	52,4	46,4	57,4	45,9	49,2
% Opx		20,6	13,0	30,6	23,7	32,2	41,2	31,2	37,0	32,4
% Cpx		7,9	11,7	16,5	9,8	12,2	10,8	9,1	14,8	16,0
% Sp		1,1	2,1	4,2	1,5	3,1	1,6	2,4	2,3	2,5
SSQ residual		0,0	0,0	0,1	0,4	0,2	0,0	0,0	0,2	0,8

Mostra	BB.08. 38	BB.08. 54	BB.08. 57	BB.08. 20	BB.08. 52	CA.12. 02	BB.12. 02	BB.12. 03	BB.12. 09	BB.12. 04
Micro-estructura	Lhz Eg	Lhz Eg	Lhz Eg Tab	Hz Pg	Hz Pg	Hz Pg	Hz Pg	Hz Pg	Hz Pg	Hz Tab
% Òxids										
SiO_2	45,0	45,4	44,7	43,1	44,2	44,1	41,9	41,7	40,7	41,2
Al_2O_3	3,01	3,52	2,75	1,27	1,04	0,97	0,65	0,83	1,24	1,05
FeO_t	7,96	7,96	7,87	8,21	7,52	7,39	8,24	8,25	8,95	8,72
CaO	2,72	2,81	2,97	0,88	0,68	0,72	0,39	0,47	1,03	0,82
MgO	40,7	40,1	40,0	45,0	45,9	45,5	47,9	46,6	45,2	46,7
Na_2O	0,12	0,20	0,10	0,09	0,09	0,03	0,05	0,10	0,23	0,09
K_2O	0,01	<0,01	0,01	0,04	0,07	0,01	0,06	0,08	0,14	0,08
TiO_2	0,08	0,12	0,08	0,09	0,08	0,04	0,02	0,04	0,07	0,03
MnO	0,14	0,13	0,13	0,13	0,12	0,12	0,12	0,11	0,12	0,12
LOI	0,42	0,41	0,37	0,86	0,31	0,50	0,11	0,04	0,06	0,23
Total	101,0	101,5	99,9	100,6	100,9	100,2	100,4	99,1	98,7	100,0
#Mg	90,1	90,0	90,1	90,7	91,6	91,7	91,2	91,0	90,0	90,5
#Cr	7,0	7,9	10,3	16,7	18,0	20,8	21,8	18,5	18,2	16,1
CaO/Al_2O_3	0,9	0,8	1,1	0,7	0,6	0,7	0,6	0,6	0,8	0,8
% Ol	56,6	53,2	57,0	73,1	72,2	69,4	91,2	86,0	88,2	87,7
% Opx	30,3	34,2	28,6	23,2	25,9	28,8	7,2	12,1	5,5	8,8
% Cpx	11,1	10,7	12,1	2,9	1,5	1,5	0,9	1,2	4,7	2,6
% Sp	2,0	1,9	2,3	0,8	0,4	0,3	0,6	0,8	1,5	0,9
SSQ residual	0,1	0,6	0,0	0,1	0,2	0,0	0,2	0,4	0,3	0,3

Taula.12.1. Anàlisis químics d'elements majors (% en pes) en roca total i composició modal calculada a partir d'aquests. Lhz: Lherzolita; Hz: Harzburgita Pg: protogranular; PgPc: Protogranular- Porfiroclàstica; Pc: Porfiroclàstica; Eg: Equigranular, Tab: tabular, LOI: Pèrdua al foc.

Mostra	Precisió % 1σ	BB.08. 101	BB.12. 01	BB.08. 18	BB.08. 80	BB.08. 97	CA.12. 03	SC.11. 16	SC.11. 52	SC.11. 49	BB.08. 54
Micro-estructura		Lhz Pg	Lhz Pg	Lhz PgPc	Lhz Pc	Lhz Pc	Lhz Pc	Lhz Pc	Lhz Pc	Lhz Pc	Lhz Eg
ppm											
Ni	10	2140	2070	1560	2020	1810	1815	2060	1805	1640	1825
Co	16	592	765	627	371	373	686	509	184	195	419
Cu	10	5	17	5	7	68	33	48	214	105	6
Zn	10	54	248	69	50	63	49	61	57	50	55
Sc	27	10	12	16	12	14	13	12	15	17	14
Ga	10	2,5	2,9	5,5	3,6	5	3,6	4,2	6,2	5,2	4,4
Cr	14	2870	2830	4080	2730	4130	2650	3290	2680	3130	3290
Rb	11	0,2	4	0,4	0,3	0,4	0,7	0,7	0,9	7	<0,2
Ba	11	5,5	27,6	38,9	12,5	4,2	18,9	1,4	1,3	13,9	6,1
Th	10	0,08	0,45	0,57	0,67	0,05	0,66	<0,05	<0,05	0,11	0,05
U	12	<0,05	0,09	0,13	<0,05	<0,05	0,17	<0,05	<0,05	<0,05	<0,05
Nb	10	5,1	6,7	6,5	3,4	4,8	2,9	3,9	1,2	2,1	3,3
Ta	11	12,4	12,9	14,4	7,2	11,7	6,8	10,3	2,1	3,2	8
La	10	0,6	2,1	6,6	2,2	0,6	10	<0,5	0,5	0,7	0,7
Ce	10	1,3	4,6	11,7	3,9	1,5	10	<0,5	1,4	1,5	0,7
Pb	10	<2	94	4	<2	<2	3	<2	<2	<2	3
Nd	10	0,7	2,4	4,6	2,1	1	0,9	0,2	1,1	0,9	0,9
Pr	10	0,17	0,56	1,29	0,51	0,21	0,43	<0,03	0,22	0,18	0,18
Sr	10	12,4	35,3	96,2	10,9	26,4	53,2	7,7	14	20	12,8
Sm	9	0,17	0,46	0,85	0,54	0,34	0,23	0,13	0,42	0,35	0,3
Hf	13	0,2	0,4	0,6	0,2	0,3	0,2	<0,2	0,9	0,2	0,2
Zr	18	0,6	2,1	4,1	<0,5	0,8	0,5	<0,5	0,5	1	0,9
Eu	8	0,06	0,15	0,27	0,17	0,13	0,08	0,04	0,15	0,13	0,12
Ti		479	839	1319	599	899	659	360	1079	959	719
Gd	10	0,24	0,46	0,86	0,57	0,43	0,32	0,2	0,58	0,48	0,41
Tb	10	0,04	0,06	0,15	0,09	0,08	0,06	0,04	0,11	0,1	0,08
Dy	10	0,27	0,57	0,83	0,58	0,58	0,42	0,34	0,68	0,65	0,5
Y	10	1,6	2,7	5	3,3	3,7	2,7	2,2	4,4	4,2	3,3
Ho	10	0,06	0,13	0,18	0,12	0,13	0,09	0,08	0,15	0,15	0,12
Er	10	0,19	0,32	0,52	0,34	0,39	0,29	0,24	0,47	0,42	0,34
Yb	11	0,16	0,27	0,44	0,29	0,36	0,26	0,22	0,42	0,42	0,29
$(La/Yb)_N$		2,55	5,28	10,2	5,15	1,13	26,1	-	0,81	1,13	1,64
$(La/Sm)_N$		2,20	2,85	4,85	2,54	1,10	27,1	-	0,74	1,25	1,46
$(Gd/Yb)_N$		1,21	1.38	1,58	1,59	0,97	1,00	0,74	1,12	0,92	1,14
Y/Yb		10,0	10,0	11,4	11,4	10,3	10,4	10,0	10,5	10,0	10,4
$(Th/U)_N$		-	0,69	0,60	-	-	0,54	-	-	-	-
$(Nb/Ta)_N$		0,23	0,29	0,26	0,27	0,23	0,24	0,21	0,32	0,37	0,23
$(Zr/Hf)_N$		0,08	0,14	0,18	-	0,07	0,07	-	0,01	0,13	0,12

Taula.12.2. Anàlisis químics d'elements traça (en ppm) en roca total i relacions entre diferents elements normalitzats al C1 de McDonough & Sun (1995).Lhz: Lherzolita; Hz: Harzburgita Pg: protogranular; PgPc: Protogranular- Porfiroclàstica; Pc: Porfiroclàstica; Eg: Equigranular; Tab: tabular

Mostra	BB.08. 54	BB.08. 57	BB.08. 38	BB.08. 20	BB.08. 52	CA.12. 02	BB.12. 02	BB.12. 03	BB.12. 09	BB.12. 04
Micro-estructura	Lhz Eg	Lhz EgTab	Lhz Eg	Hz Pg	Hz Pg	Hz Pg	Hz Pg	Hz Pg	Hz Pg	Hz Tab
ppm										
Ni	1825	1905	1855	2070	2070	2070	2580	2480	2420	2400
Co	419	801	576	765	765	765	502	371	597	452
Cu	6	20	4	17	17	17	45	43	15	19
Zn	55	56	50	248	248	248	54	52	61	52
Sc	14	14	13	8	7	8	6	7	8	8
Ga	4,4	3,8	3	1,8	1,9	1,5	0,6	0,8	1,7	1,2
Cr	3290	3330	2440	2700	2500	2730	2410	2430	3740	2560
Rb	<0,2	0,4	0,4	1,3	1,6	0,4	0,5	0,6	1,7	0,4
Ba	6,1	6,2	6	18,5	20,7	3,5	4,9	11,1	16,1	8,7
Th	0,05	0,08	0,09	0,29	0,26	0,07	0,07	0,09	0,18	0,07
U	<0,05	<0,05	<0,05	0,07	0,08	<0,05	<0,05	0,05	0,06	<0,05
Nb	3,3	5,4	5,2	5,2	6,1	3,8	4,6	3,4	5,5	4,1
Ta	8	17	13,8	15,8	11,9	9	11,2	7,2	12,5	8,9
La	0,7	0,6	0,6	2,7	2	0,6	<0,5	0,7	1,5	0,8
Ce	0,7	1,1	1,3	5	4	1	0,9	1,5	3,2	1,6
Pb	3	3	3	94	94	94	<2	16	2	<2
Nd	0,9	0,6	0,7	2,5	1,6	0,4	0,3	0,7	1,7	0,5
Pr	0,18	0,13	0,16	0,65	0,47	0,11	0,11	0,23	0,4	0,18
Sr	12,8	8,2	15	27,5	27,8	5,4	7,6	11,3	21,8	11,7
Sm	0,3	0,18	0,2	0,45	0,29	0,09	0,06	0,1	0,29	0,1
Hf	0,2	0,2	<0,2	0,4	0,2	<0,2	<0,2	<0,2	0,2	<0,2
Zr	0,9	0,6	0,6	2,1	2,1	2,1	0,7	0,7	1,2	1,1
Eu	0,12	0,06	0,07	0,12	0,08	<0,03	<0,03	0,04	0,09	0,04
Ti	719	479	479	539	479	240	120	240	420	180
Gd	0,41	0,26	0,26	0,33	0,23	0,09	0,05	0,1	0,22	0,09
Tb	0,08	0,05	0,05	0,05	0,03	0,01	<0,01	0,01	0,03	0,01
Dy	0,5	0,38	0,36	0,25	0,17	0,08	0,05	0,08	0,16	0,1
Y	3,3	2,5	2,2	1,2	0,8	0,5	<0,5	<0,5	1	0,5
Ho	0,12	0,09	0,08	0,04	0,03	0,01	<0,01	0,01	0,04	0,01
Er	0,34	0,27	0,25	0,11	0,08	0,05	0,05	0,05	0,08	0,04
Yb	0,29	0,25	0,23	0,09	0,05	0,03	<0,03	0,04	0,12	0,07
$(La/Yb)_N$	1,64	1,63	1,77	20,4	27,2	13,6	-	11,8	8,49	7,76
$(La/Sm)_N$	1,46	2,08	1,87	3,75	4,31	4,16	-	4,37	3,23	5,00
$(Gd/Yb)_N$	1,14	0,84	0,91	2,97	3,72	2,43	-	2,02	1,48	1,04
Y/Yb	10,4	10,0	9,6	13,3	16,0	16,7	-	-	8,33	7,14
$(Th/U)_N$	-	-	-	0,57	0,45	-	-	0,25	0,41	-
$(Nb/Ta)_N$	0,23	0,18	0,21	0,19	0,29	0,24	0,23	0,27	0,25	0,26
$(Zr/Hf)_N$	0,12	0,08	-	0,14	0,28	-	-	-	0,16	-

Taula.12.2. Continuació

Mostra Litologia Micro-estructura	Precisió % 1σ	BB.08. 101 Lhz Pg (3)	BB.12. 01 Lhz Pg (3)	BB.08. 18 Lhz Pg-Pc (3)	BB.08. 80 Lhz Pc (5)	BB.08. 97 Lhz Pc (4)	*BB.08. 97** *Lhz Pc* (3)	CA.12. 03 Lhz Pc (3)	SC.11. 16 Lhz Pc (4)	SC.11. 49 Lhz Pc (4)	SC.11. 52 Lhz Pc (4)
Sc	1,2	69,76	54,04	62,79	73,35	70,75	*42,56*	69,08	66,77	64,38	61,89
Ti	0,5	2696	3624	2378	3312	4014	*16578*	2172	2250	2363	3712
V	0,9	259,9	286,2	256,4	283,4	272,6	*368,5*	264,0	292,2	252,6	300,6
Ni	0,5	358,3	357,7	339,3	374,0	340,4	*739,5*	379,7	386,6	347,5	359,9
Ga	1,6	2,98	5,35	4,01	4,40	4,29	*8,27*	6,06	3,15	3,97	4,42
Rb	2,2	0,01	0,01	0,01	0,01	0,02	*1,05*	0,01	0,01	0,02	0,04
Sr	1,8	72,52	103,70	299,00	40,09	64,32	*183,90*	318,65	1,99	51,14	37,57
Y	0,3	13,60	16,49	17,27	17,81	20,89	*22,34*	15,97	14,89	16,81	17,69
Zr	0,2	17,97	24,52	32,52	29,10	32,84	*24,62*	21,73	4,95	15,69	17,17
Nb	0,8	1,25	0,31	0,33	0,06	0,27	*13,31*	0,05	0,02	0,03	0,13
Ba	3,0	bd	0,08	0,17	0,52	0,53	*18,99*	0,13	bd	bd	0,03
La	2,2	1,76	5,01	26,93	0,29	2,12	*2,25*	76,06	0,00	0,88	1,04
Ce	2,7	4,89	11,74	47,21	2,11	6,81	*6,90*	76,18	0,14	2,86	4,00
Pr	2,7	0,77	1,51	4,30	0,51	1,14	*1,15*	3,04	0,09	0,52	0,70
Nd	2,5	4,17	7,38	15,07	3,66	6,38	*6,41*	5,95	1,14	3,38	4,31
Sm	2,5	1,40	2,18	2,72	1,64	2,17	*2,23*	1,46	0,88	1,44	1,75
Eu	3,0	0,53	0,77	0,90	0,67	0,83	*0,86*	0,59	0,39	0,62	0,71
Gd	2,5	1,87	2,65	2,77	2,41	2,91	*3,07*	2,15	1,63	2,16	2,44
Tb	2,3	0,34	0,44	0,46	0,44	0,52	*0,55*	0,39	0,32	0,40	0,43
Dy	2,8	2,48	3,15	3,22	3,25	3,85	*3,98*	2,96	2,61	3,06	3,27
Ho	2,3	0,52	0,64	0,68	0,69	0,82	*0,86*	0,63	0,57	0,65	0,68
Er	2,4	1,51	1,87	1,99	2,04	2,37	*2,51*	1,86	1,75	1,95	1,98
Tm	2,2	0,21	0,26	0,28	0,29	0,33	*0,34*	0,26	0,24	0,27	0,28
Yb	2,5	1,34	1,68	1,84	1,92	2,18	*2,23*	1,76	1,65	1,83	1,82
Lu	2,1	0,18	0,23	0,25	0,27	0,31	*0,31*	0,24	0,23	0,25	0,25
Hf	2,0	0,62	0,99	1,00	0,92	1,01	*0,70*	0,83	0,39	0,51	0,57
Ta	1,8	0,09	0,03	0,01	bd	0,06	*0,94*	bd	bd	0,00	0,03
Pb	12,2	0,02	0,03	0,95	0,13	0,18	*0,70*	1,50	0,01	0,10	0,14
Th	2,8	0,11	0,25	1,85	bd	0,07	*0,06*	4,10	bd	0,09	0,02
U	1,7	nd	nd	0,54	nd	0,01	*0,01*	1,10	0,004	nd	nd
Eu/Eu*		1,00	0,98	1,00	1,03	1,00	*1,01*	1,01	0,99	1,07	1,04
$(La/Yb)_N$		0,89	2,03	9,94	0,10	0,66	*0,69*	29,45	0,002	0,33	0,39
$(La/Er)_N$		0,79	1,81	9,14	0,10	0,60	*0,60*	27,67	0,00	0,30	0,35
$(La/Nd)_N$		0,81	1,31	3,45	0,15	0,64	*0,68*	24,64	0,01	0,50	0,47
$(Sm/Yb)_N$		1,13	1,42	1,61	0,93	1,08	*1,09*	0,90	0,58	0,86	1,05
Sm/Er		0,92	1,16	1,37	0,81	0,92	*0,89*	0,79	0,50	0,74	0,88
Sm/Nd		0,33	0,30	0,18	0,45	0,34	*0,35*	0,25	0,78	0,43	0,41
Ti/Eu		5103	4700	2653	4950	4845	*19187*	3689	5784	3798	5238
$(La/Sm)_N$		0,79	1,44	6,18	0,11	0,61	*0,63*	32,53	0,00	0,38	0,37
$(Gd/Yb)_N$		1,13	1,28	1,22	1,02	1,08	*1,11*	0,99	0,80	0,96	1,09
Y/Yb		10,14	9,84	9,39	9,27	9,57	*10,03*	9,09	9,02	9,18	9,74
$(Th/U)_N$		-	-	0,48	-	0,80	*0,58*	0,51	-	-	-
$(Nb/Ta)_N$		8,05	6,65	12,86	-	2,70	*8,03*	-	-	5,73	2,84
$(Zr/Hf)_N$		0,79	0,67	0,87	0,86	0,88	*0,95*	0,70	0,35	0,83	0,81

*Taula.12.3. Anàlisis químics d'elements traça (en ppm) en clinopiroxè i relacions entre diferents elements normalitzats al C1 de McDonough & Sun (1995). Lhz: Lherzolita; Hz: Harzburgita Pg: protogranular; PgPc: Protogranular- Porfiroclàstica; Pc: Porfiroclàstica; Eg: Equigranular; Tab: tabular. *Anàlisis corresponent a l'amfíbol. bd: anàlisis per sota del límit de detecció, nd: anàlisis no determinat. La precisió anàlitica és la mateixa que per la roca total.*

Mostra	BB.08.38	BB.08.54	BB.08.57	BB.12.02	BB.12.03	BB.12.04	BB.12.09	BB.08.20	BB.08.52	CA.12.02	BB.12.17
Litologia Micro-estructura	Lhz Eg *(5)*	Lhz Eg *(3)*	Lhz Eg Tab *(5)*	Hz Pg *(3)*	Hz Pg *(3)*	Hz Pg Tab *(3)*	Hz Pg *(3)*	Hz Pg *(4)*	Hz Pg *(4)*	Hz Pg *(4)*	Wb Pg *(3)*
Sc	71,48	66,10	66,92	45,30	46,96	41,50	67,59	75,77	46,59	60,51	38,29
Ti	2667	2657	1950	270	351	269	911	1023	496	1020	1566
V	255,7	251,7	253,3	160,2	173,8	189,5	248,7	224,1	161,9	208,8	155,3
Ni	399,0	358,2	427,3	441,1	460,1	528,7	413,8	386,3	451,1	424,1	439,1
Ga	3,18	3,80	3,06	1,50	1,71	2,30	3,00	2,43	1,87	2,21	2,00
Rb	0,02	0,01	0,01	0,01	bd	0,01	bd	0,01	0,10	0,01	bd
Sr	131,61	54,96	0,74	91,05	57,71	7,06	58,98	300,03	70,65	75,11	73,74
Y	15,27	17,46	14,89	2,07	1,26	1,86	7,82	8,08	2,31	5,56	3,50
Zr	17,69	34,00	1,91	9,84	5,45	0,42	23,38	110,05	4,59	16,14	6,10
Nb	0,13	0,05	0,05	0,32	0,92	0,22	0,22	3,25	0,58	0,71	0,25
Ba	0,83	0,20	bd	0,12	0,27	1,26	0,06	0,07	1,05	0,16	0,03
La	1,43	1,74	0,00	4,28	2,78	0,53	1,31	18,41	3,78	3,40	1,56
Ce	3,79	3,70	0,04	9,58	8,44	1,12	4,79	47,02	7,46	8,53	5,13
Pr	0,62	0,65	0,04	1,18	1,36	0,13	0,78	6,24	0,87	1,20	0,80
Nd	3,61	4,12	0,67	5,41	7,02	0,50	4,44	28,28	3,73	6,02	4,42
Sm	1,35	1,74	0,74	1,19	0,89	0,07	1,45	5,61	0,78	1,59	1,24
Eu	0,64	0,71	0,32	0,37	0,21	0,02	0,49	1,51	0,24	0,51	0,40
Gd	2,00	2,49	1,53	0,95	0,49	0,08	1,59	3,87	0,71	1,51	1,11
Tb	0,37	0,45	0,32	0,11	0,05	0,02	0,25	0,44	0,09	0,22	0,14
Dy	2,82	3,35	2,56	0,56	0,28	0,23	1,61	2,13	0,54	1,28	0,86
Ho	0,61	0,71	0,57	0,09	0,05	0,07	0,31	0,32	0,10	0,22	0,14
Er	1,82	2,05	1,73	0,20	0,13	0,27	0,84	0,73	0,25	0,55	0,36
Tm	0,26	0,29	0,24	0,03	0,02	0,04	0,11	0,09	0,03	0,07	0,04
Yb	1,72	1,91	1,60	0,16	0,16	0,35	0,71	0,54	0,23	0,41	0,26
Lu	0,24	0,26	0,22	0,02	0,03	0,05	0,10	0,08	0,03	0,05	0,03
Hf	0,61	1,09	0,26	0,27	0,15	0,01	0,55	3,32	0,17	0,51	0,23
Ta	0,05	0,00	bd	0,03	0,08	0,01	0,03	0,33	0,05	0,07	0,01
Pb	0,13	0,39	0,01	0,08	0,10	0,02	0,03	0,18	0,05	0,04	0,04
Th	0,03	0,14	bd	0,40	0,31	0,04	0,03	1,13	0,18	0,15	0,02
U	0,01	0,11	bd	0,06	nd	0,01	0,01	0,17	0,04	0,03	0,06
Eu/Eu*	1,19	1,04	0,92	1,06	0,98	0,88	0,97	0,98	0,98	0,99	1,04
$(La/Yb)_N$	0,56	0,62	0,001	18,21	11,97	1,04	1,25	23,18	11,42	5,64	4,06
$(La/Er)_N$	0,53	0,57	0,00	14,40	14,05	1,35	1,05	16,96	10,36	4,15	2,96
$(La/Nd)_N$	0,76	0,82	0,01	1,53	0,76	2,07	0,57	1,26	1,96	1,09	0,68
$(Sm/Yb)_N$	0,85	0,99	0,50	8,08	6,10	0,23	2,23	11,29	3,78	4,21	5,13
Sm/Er	0,74	0,85	0,43	5,92	6,64	0,27	1,73	7,65	3,18	2,87	3,47
Sm/Nd	0,37	0,42	1,09	0,22	0,13	0,14	0,33	0,20	0,21	0,26	0,28
Ti/Eu	4174	3731	6070	730	1667	11848	1876	680	2077	2017	3907
$(La/Sm)_N$	0,66	0,63	0,00	2,25	1,96	4,63	0,56	2,05	3,01	1,34	0,79
$(Gd/Yb)_N$	0,94	1,05	0,77	4,80	2,50	0,20	1,81	5,80	2,54	2,98	3,43
Y/Yb	8,87	9,14	9,30	12,92	7,98	5,33	11,03	14,95	10,27	13,56	13,37
$(Th/U)_N$	0,60	0,19	-	0,93	-	0,71	0,63	0,89	0,69	0,69	0,05
$(Nb/Ta)_N$	1,37	5,96	-	5,46	6,50	9,10	4,04	5,59	6,23	5,42	9,57
$(Zr/Hf)_N$	0,78	0,84	0,20	0,99	0,96	1,05	1,15	0,89	0,72	0,85	0,72

Taula.12.3. Continuació

	Lhz RT Tipus1	Lhz Cpx Tipus1	Lhz RT Tipus2	Lhz Cpx Tipus2	Lhz Cpx Tipus3	Hz RT Tipus1	Hz Cpx Tipus1	Hz RT Tipus2	Hz Cpx Tipus2
$(La/Yb)_N$	26,1- 10,2	29,45- 9,94	5,28- 0,80	2,03- 0,10	0,99- 0,92	27,2- 8,49	23,18- 1,25	13,6- 7,76	18,21- 1,04
$(La/Er)_N$	23,27- 8,56	27,67- 9,14	4,43- 0,71	1,81- 0,10	0	16,87- 12,65	16,96- 1,05	13,5- 8,1	14,40- 1,35
$(La/Nd)_N$	21,42- 2,76	24,64- 3,45	1,92- 0,87	1,31- 0,15	0,01	2,41- 1,70	1,26- 0,57	3,08- 0	2,07- 0,76
$(Sm/Yb)_N$	2,10- 0,96	1,61- 0,90	2,02- 0,78	1,42- 0,85	0,58- 0,50	6,30- 2,62	11,29- 2,23	3,26- 1,55	8,08- 0,23
Ti/Eu	8241- 4883	3689- 2653	7991- 3525	5238- 3731	6070- 5784	5993- 4495	2017- 680	5993- 4495	11848- 730
$(La/Sm)_N$	27,1- 4,85	32,53- 6,18	2,85- 0,74	1,44- 0,11	0	4,31- 3,23	2,05- 0,56	5,0- 4,16	4,63- 1,96
$(Gd/Yb)_N$	1,58- 1,00	1,22- 0,99	1,38- 0,84	1,28- 0,94	0,80- 0,77	3,72- 1,48	5,80- 1,81	2,43- 1,04	4,8- 0,2
Y/Yb	11,4- 10,4	9,39- 9,09	11,4- 9,60	10,14- 8,87	9,30- 9,02	16,0- 8,33	14,95- 11,03	16,7- 7,14	12,92- 5,33
$(Th/U)_N$	0,60- 0,54	0,51- 0,48	0,69	0,80- 0,19	-	0,57- 0,41	0,89- 0,63	0,25	0,93- 0,69
$(Nb/Ta)_N$	0,26- 0,24	12,86	0,32- 0,18	8,05- 1,37	-	0,29- 0,19	5,59- 4,04	0,27- 0,23	9,10- 5,46
$(Zr/Hf)_N$	0,18- 0,07	0,87- 0,70	0,14- 0,01	0,88- 0,67	0,35- 0,20	0,28- 0,14	1,15- 0,85	-	1,05- 0,72

Taula.12.4. Taula resum dels rangs del fraccionament interelemental pels diferents grups de lherzolites i harzburgites segons els tipus d'espectres de REE, en roca total (RT) i en clinopiroxè (Cpx).

CHAPTER 13

DISCUSSION

To approach the discussion of previous data, we will consider separately the main results of each chapter and integrate all them in a section entitled "the evolution of the subcontinental lithospheric mantle in NE Iberian Peninsula" to finish with an intent of comparison between our results and others from the subcontinental lithospheric mantle (SCLM) in neighbouring zones (Massif Central and Pyrenees in France and Calatrava and Tallante in Spain).

13.1. What does the new sampling tell us about the SCLM beneath the Catalan Volcanic Zone?

Although we looked for mantle xenoliths in basaltic rocks from the three sub-zones that form the Catalan Volcanic Zone (CVZ), we only found them in La Selva (Sant Corneli neck) and La Garrotxa, but not in in the oldest volcanic rocks of l'Empordà. The most productive volcanoes from La Garrotxa (Banya del Boc, Canet d'Adri) had been previously sampled by Oliveras (2009) and the main results published by Oliveras & Galán (2006, 2007), Galán et al. (2008, 2011) and Galán & Oliveras (2014).

The new sampling confirms that the SCLM under the CVZ is mainly formed by spinel lherzolites (ca. 56% of the total mantle xenoliths studied so far) and harzburgites (ca. 40%), with subordinate presence of pyroxenites (4%), which are olivine websterites in the new sampling. The distribution of these lithologies is not homogeneous: lherzolites dominate in La Selva outcrops, whereas both peridotites and websterites were found in La Garrotxa subzone. The new sampling also reveals that although protogranular microstructure is characteristic of lherzolites, harzburgites and websterites, porphyroclastic and equigranular lherzolites are frequent (15 and 10% of the total amount of lherzolite samples, respectively), especially in xenoliths from La Selva where porphyroclastic lherzolites dominate. In the volcanoes from La Garrotxa, all types of microstructural lherzolites were found along with protogranular

harzburgites and olivine websterites. Taken into account that in La Garrotxa the three types of lherzolites crop out in a single volcanic vent (Banya del Boc and Canet d'Adri), it is inferred that the formation of porphyroclastic and equigranular lherzolites must be related to heterogeneously distributed narrow shear zones in this SCLM rather than to shear zones located in the borders of ascending asthenospheric diapirs (Downes, 1990).

13.2. Petrography and mineralogy

The mineral mode of peridotites corresponds mainly to spinel (<5%) bearing lherzolites and harzburgites, with rare spinel (>5%) lherzolites and harzburgites without spinel. Plagioclase only coexists with spinel in coronae surrounded the spinel in a few lherzolites and in a microband of gabbronorite, also found in a lherzolite (Fig.7.5e). No spinel was found in the websterites. A few lherzolites (protogranular-porphydoclastic, porphydoclastic and equigranular) also include brown amphibole as accessory mineral forming anhedral disseminated crystals, often at the core of patches, which also include glass and new small crystals of olivine, clinopyroxene and spinel (Fig.7.6e-f). The presence of accessory amphibole within patches provides evidence of: (1) the existence of modal metasomatism due to melt-rock reaction at low melt/rock ratio, and (2) later destabilization of amphibole to give the reaction products in the patches. Phlogopite as accessory mineral was previously mentioned in harzburgites and websterites (Oliveras, 2009), but it was only found in olivine websterites of the new sampling, as rare anhedral disseminated crystals (Fig.7.6b). Base metal (Cu-Fe-Ni) sulphides are other frequent accessory minerals, especially in porphyroclastic lherzolites from the Sant Corneli neck (up to 1,9%). Four textural types of sulphides were differentiated according to their relationships with silicates (Fig.7.13), which are the classical types in mantle xenoliths (Lorand & Conqueré, 1983; Szabó & Bodnar, 1995; Shaw, 1997; Guo et al., 1999): (1) inclusions in silicates and spinel, (2) trails of small inclusions, (3) interstitial sulphides and (4) sulphides in overgrowth microstructures and microveins. Sulphide mineral associations are dominated by the breakdown products of high temperature Ni-Fe monosulphide solid solution (MSS) but also of Cu intermediate solid solution (iss) (Table 7.2). The breakdown products of iss are more frequent in these xenoliths than in previously studied samples (Cruz et al., 2014; Galán et al., 2016).

In the olivine-orthopyroxene-clinopyroxene triangular diagram of Le Maître (2003) (Fig.7.2), the new xenoliths overlap the field of the previously studied samples, but olivine mode expands to higher and lower values. Other interesting points to highlight on the mineral mode are:

(1) There is a negative correlation between all clinopyroxene, orthopyroxene and spinel mode with respect to the olivine mode (Fig.7.3) suggesting a melt depletion trend. However, overlapping between lherzolite and harzburgite mineral modes and the wide scattering of lherzolites in these diagrams suggest that melt-rock reaction processes [e.g., igneous refertilization of this mantle via percolation of basaltic melts; (Bodinier & Godard, 2003)] could have also occurred. Evidence of melt-rock reaction, apart from the presence of amphibole already mentioned, are: lower modal amount of olivine in some lherzolites than in the Primitive Mantle (PM; Ol mode: 55% according to Walter, 2003), high modal amount of clinopyroxene (up to 21% in sample BB.12.07; Table 7.1), rare presence of grabbronorite microveins (Fig.7.5e) and composite xenoliths with clinopyroxene enriched microbands (lherzolite BB.08.83b);

(2) Superposed trends for lherzolites and harzburgites (Fig.7.3c) also suggest that melting episodes could have been different for both peridotites.

Microstructures of mantle rocks are clue in the interpretation of deformation episodes and petrogenetic processes. General microstructures already mentioned (viz., protogranular, porphyroclastic, equigranular) along with intergranular and occasional overgrowth microstructures (spongy rims, coronae and patches including amphibole) were considered in this study. Descriptive terminology used for general microstructures is after Mercier & Nicolas (1975) with grain-size precision by Harte (1977). The protogranular (Fig.7.4a-c) or tabular protogranular microstructure characterizes many lherzolites (ca. 31% of the total xenoliths), harzburgites and websterites. Olivine and orthopyroxene grain size is >2 mm in these rocks, whereas clinopyroxene and spinel grain size is < 1mm. Other characteristics are: (1) straight or slightly curved grain boundaries with frequent triple junctions, although orthopyroxene crystals can show more interlobate grain boundaries against olivine crystals, with mutual inclusions between both minerals (Fig.7.5h); (2) spinel crystals are usually amoeboid (Fig.7.4a), but there are also interstitial crystals, vermicular crystals related to pyroxenes, and lamellae of spinel within pyroxenes; and (3), deformation features, such as subgrains and undulose extinction are sporadic and mostly present in olivine crystals. Protogranular harzburgites differ by larger size of

olivine and orthopyroxene crystals (2-6 mm) with respect to protogranular lherzolites, and because spinel forms mostly isolated and interstitial crystals (Fig.7.5f-h). Finally, in the websterites, olivine crystals are smaller (size<1 mm) than pyroxene crystals (ca. 2 mm) and triple junctions between grains are less frequent than in the peridotites (Fig.7.6a-b). It is worth noting that microstructural features such as orthopyroxene embayment (replacement) by olivine (Fig.7.5h) and olivine inclusions in orthopyroxene have been interpreted as evidence of melt-rock reaction. In the former case, olivine crystallization would result from reaction of the peridotite with an orthopyroxene-undersaturated percolating melt (Kelemen et al., 1998; Dijkstra et al., 2003), whereas in the latter case orthopyroxene would be increased at the expense of olivine, if the percolating melt were SiO_2 (or orthopyroxene) saturated (Kelemen et al., 1992; 1998; Dijkstra et al., 2003). Since we have observed mutual replacement between olivine and orthopyroxene (Fig.7.5h) in the same sample and only in two lherzolites (BB.08.98, BB.12.01) and one harzburgite (CA.12.02), it is inferred that the percolating melt would have been at or just below orthopyroxene saturation (i.e., the reaction olivine+ high-Si melt <=> orthopyroxene+ low-Si melt would be close to equilibrium). Protogranular lherzolites pass gradually to porphyroclastic lherzolites which show orthopyroxene (grain size up to 1 cm), olivine and more rarely clinopyroxene and spinel porphyroclasts in a strain-free matrix of the same minerals (crystal size< 1mm), with frequent boundaries at 120° (Fig.7.4d). In these samples, orthopyroxene and olivine porphyroclasts show close-spaced deformation features, such as clinopyroxene and spinel deformed lamellae in orthopyroxene, kink bands, subgrains (Fig.7.4g), undulose extinction. Moreover, the porphyroclasts can be orientated and along with a tabular matrix define a foliation. Spinel forms holly-leaf shaped porphyroclasts, small anhedral neocrystals in the matrix and frequent lamellae in clinopyroxene porphyroclasts and neocrystals. By decreasing the amount of porphyroclasts, lherzolites become equigranular or tabular equigranular (porphyroclasts< 5% and grain size< 1mm), with dominant strain-free neocrystals showing triple junction boundaries (Fig.7.5c). Spinel is mostly as tiny anhedral interstitial crystals. From previous data, it is deduced that either protogranular lherzolites were affected locally by deformation episode(s) that led to their finer-grained recrystallization (Falus et al., 2008; Palasse et al., 2012; Kaczmarek & Tommasi, 2011) or the opposite, finer-grained lherzolites followed later static recrystallization (annealing) and grain growth and developed protogranular microstructure (Vauchez & Garrido, 2001). Both hypotheses will be evaluated below using

mineral compositions, temperature (T) and pressure (P) estimates, and crystal-preferred orientations.

Overgrowth microstructures appear in a few lherzolites. They are:

(1) Fine spongy rims (also called sieve-textured rims; Wang et al., 2012) in both earlier and neocrystals of clinopyroxene (Fig.7.6c) with glass or empty dendrites;

(2) Spinel coronae mostly developed in contact with orthopyroxene and formed of new olivine-clinopyroxene-Cr enriched spinel (with respect to the reactant spinel)-plagioclase and a Ti mineral (ilmenite?) (Fig.7.6c-d; 7.9; 7.10). Plagioclase appears either as microlites or interstitial glass (?) and in one sample (SC.11.49). K feldspar composition was identified among the interstitial glass. The spinel coronae are deduced to post-date the clinopyroxene spongy rims that appear reabsorbed in contact with the coronae.

(3) Amphibole coronae and patches (Fig.7.6e-f), where the amphibole and possible earlier spinel and orthopyroxene were reactants and new olivine-clinopyroxene-Cr-rich spinel and glass were reaction products.

Since these overgrowth microstructures are located within the xenoliths and they do not show preferential development towards the host lava, they are not considered of pyrometamorphic origin (Pike & Schwarzman, 1976; Shaw & Klüguel, 2002; Shaw et al. 2006; Galán et al., 2016) following the criteria of Su et al. (2011) and Wang et al. (2012). They are most likely due to melt (fluid)-rock reaction, at low melt(fluid) fraction, before the mantle fragmentation and transport by the host lava (Bonadiman et al., 2008; Ionov et al., 1995; 2005; Wang et al., 2012). This issue would be discussed below.

The sole gabbronorite microvein found in the equigranular lherzolite (BB.08.38) (Fig.7.5e) neither seems to be related to pyrometamorphism, since orthopyroxene is not stable in alkali basalts and basanites. This microband also reflects melt percolation in this SCLM as it has been observed elsewhere (e.g., in ophiolitic peridotites by Rampone et al., 2008 and reference there in). However, reaction of the gabbronoritic melts with the lherzolite must have been limited because the formation of an orthopyroxene boundary between them. Interesting enough, this microband does not show equigranular microstructure as the host lherzolite. On the contrary,

plagioclase in the microband forms poikilitic crystals including smaller skeletal crystals of olivine, clinopyroxene and orthopyroxene along with spinel crystals showing fine spongy rims (or sieve rims). Therefore, it is inferred that this melt percolation also post-dated the formation of the equigranular microstructure in the lherzolite.

Pyrometamorphic microstructures could be the orthopyroxene coronae developed preferentially at the contact with the host lava or with basaltic microveins (Fig.7.7a), and the basaltic microveins themselves, which penetrate the xenoliths from the contact with the host lava. However, the orthopyroxene corona described in sample BB.08.18 (chapter 7; Fig.7.8b), formed of olivine-clinopyroxene-plagioclase-Cr-rich spinel, is in contact with a spinel corona and could be related to it rather than to the host lava.

13.3. Mineral chemistry

Mineral chemistry is particularly useful to get insight into the petrogenetic processes envisaged in the previous section and to estimate re-equilibration P-T conditions of these mantle rocks during subsolidus evolution (section 13.5). In the paragraphs which follow, the chemistry of minerals will be divided into four sections: (1) essential silicates and spinel; (2) accessory silicates; (3) phases in the overgrowth microestructures, the gabbronorite microband and in pyrometamorphic microstructures; and (4), sulphides.

13.3.1. Essential silicates and spinel

The ranges of Mg# and Cr# for these phases appear in Table 13.1. Both Mg# (Fo% in olivine) and Cr# generally increase from lherzolites towards harzburgites, except in spinel where Mg# decreases (i.e., both parameters show reverse correlation) (Fig.8.12a; 8.13). Trends in these figures also include previous studied xenoliths (Oliveras, 2009; Galán et al., 2008, 2011; Galán & Oliveras, 2014). Slight overlapping for Mg# and a small compositional gap for Cr# is observed between both peridotites, except in the spinel, where the Cr# gap is more significant. The websterite silicates show compositions comparable to those in harzburgites. These compositions are less evolved than in previous studied pyroxenites (Galán et al., 2008, 2011). Another conclusion from table 13.1 is that no clear differences exist between minerals from the three microstructural types of lherzolites, although compositions of porphyroclastic and equigranular lherzolites are among the most differentiated or fertile.

The overall evolution of Mg# and Cr# (Fig.8.2; 8.4; 8.7; 8.22; 8.23; 8.24) is consistent with mantle depletion by removal of basaltic melts (Downes, 2001 and references there in; Ackerman et al., 2007; Galán et al., 2008), as they are: (1) the general positive correlation of Fo% in olivine vs. the olivine mode (Fig.8.2); (2) the general negative correlations of Al, Ti and Na vs. Mg# and opposite, the positive correlations of Ca and Cr# vs. Mg# in pyroxenes (Fig.8.4; 8.7); and (3), the negative correlation of the ratio clinopyroxene/clinopyroxene+orthopyroxene vs. Cr# in spinel (Fig.8.21). Assuming a melt depletion trend, the compositions of spinel and olivine (Fig.8.24) in lherzolites could result from <10% fractional melting, whereas harzburgites would require more severe melting, between 18 and 30% (Arai, 1994).

However, trends in all these diagrams can be also interpreted in the opposite way, i.e., resulting from igneous refertilization of a refractory mantle by percolation of basaltic melts (Fig.2.5) (Bodinier & Godard, 2003; Griffin et al., 2009; O'Reilly & Griffin, 2013). In fact, scattering of lherzolites in most diagrams would be better explained if melt-rock reaction had also taken place during the evolution of this piece of mantle. For example, in figure 8.21, the ratio clinopyroxene/clinopyroxene+orthopyroxene is very variable for the same value of Cr# (ca. 10) in spinel, with one lherzolite (BB.08.97) standing out for being very rich in clinopyroxene. Since this sample also has amphibole, it is likely that refertilization caused not only the formation of this mineral, but also of new clinopyroxene crystals, difficult to distinguish from the refractory ones. Another case in point in figure 8.21, is the composite xenolith BB.08.83b, the spinel of which shows refractory composition for the high clinopyroxene mode of this rock.

In addition, the wide gap between the degree of fractional melting inferred for lherzolites and harzburgites (Fig.8.24), along with the significant compositional gap observed for Cr# in Spl between both peridotites (Fig.8.12a), suggests a different history of melt depletion and/or may be in different geological settings. On the one hand, the high degree of melting registered by the compositions of harzburgite minerals could be the result of discontinuous partial melting (e.g., different melting episodes) (Féménias et al., 2004), or favoured by melting at high P_{H2O} in a suprasubduction zone (SSZ) (Parkinson & Pearce, 1998; Ionov et al., 2010; Riches & Rogers, 2011). SSZ harzburgites would be consistent with their plotting within the field of peridotites from suprasubduction settings in figure 8.24 and with available Sr and Nd isotopic compositions for these rocks, with values between EMI and EMII mantle reservoirs (Bianchini et al., 2007; Galán & Oliveras, 2014) (see below). However, TiO_2 and Al_2O_3 contents in most harzburgite

clinopyroxene from the CVZ are higher (Table 8.3) than in harzburgites from SSZ (TiO_2<0.05%; Al_2O_3< 2.4%) (Parkinson & Pearce, 1998; Ionov, 2010), although TiO_2 concentration could have increased during later metasomatism. Moreover, Cr# in harzburgite spinel does not reach the highest values of the SSZ harzburgites (Cr# up to 66; McInnes et al., 2001; Ionov, 2010). Finally, there is rare evidence of this melting event at high P_{H2O}, except for the presence of low-Ti phlogopite (Fig.8.17) in a couple of harzburgite xenoliths previously studied (Galán et al., 2008; Oliveras 2009). Alternatively, both lherzolites and harzburgites could have experimented the same melting event in the same geological setting (MORB mantle, abyssal peridotites, passive margin? Fig.8.24). In such a case, the Cr# gap in the spinel would be due to increasing compatibility of Cr with this phase during partial melting (Hellebrand et al., 2001).

Finally, subsolidus re-equilibration is registered by mineral compositions and their evolving trends. For instance, orthopyroxene and clinopyroxene porphyroclasts show mutual and spinel lamellae and exsolved compositions show lower Al, Ti, Cr, Na and Ca abundances (in the orthopyroxene) than integrated compositions [unfocused (Des) analyses in Tables 8.2; 8.3] (Fig.8.4; 8.5; 8.7). It is worth noting that although there is no relationship between mineral chemistry and microstructures of lherzolites, subsolidus re-equilibration of both pyroxenes and spinel is more significant in porphyroclastic and equigranular than in protogranular lherzolites: (1) orthopyroxene and clinopyroxene of porphyroclastic and equigranular lherzolites show lower Al, Na, Ti and higher Ca than in protogranular lherzolites (Fig.8.4; 8.5; 8.10a); (2) jadeitic substitution in clinopyroxene decreases from protogranular lherzolites towards porphyroclastic and equigranular types (Fig.8.9a); and (3), spinel in porphyroclastic and equigranular lherzolites defines a different trend from spinel in protogranular harzburgites and lherzolites; Mg# and Cr# of spinel are negatively correlated in both peridotites. However, the slope is higher in porphyroclastic and equigranular than in protogranular lherzolites because spinel in the first two types becomes more aluminous (trend 2 in Fig.8.12b) than in the third type. This could be explained because in porphyroclastic and equigranular lherzolites, spinel re-equilibrates with less aluminous orthopyroxene and clinopyroxene (Voigt & Handt, 2011) after expelling spinel lamellae. The spinel trend from protogranular harzburgites towards protogranular lherzolites (trend 1 in Fig.8.12b) could be interpreted as a depletion and/or refertilization trend.

13.3.2. Accessory silicates

Disseminated amphibole is Mg-hastingsite and Mg-hornblende with Mg# and Cr# comparable to those in co-existing clinopyroxene. This amphibole has lower Ti than that from veins, higher Ti with respect to amphibole of suprasubduction zones, and more similar to that of within-plate settings (Coltorti et al., 2004, 2007; Fig.8.15; 8.16). Phlogopite is Ti-rich but not as rich as in previous analysed websterites (Galán et al., 2008). Mg# of phlogopite is slightly lower than in coexisting pyroxenes and they plot between the fields of disseminated and vein phlogopites (Fig.8.17; Ionov et al., 1997). They clearly differ from phlogopite compositions in harzburgites (Galán et al., 2008; Oliveras, 2009) which show much lower Ti.

These Ti-rich compositions of phlogopite along with the higher amount of Ti in pyroxenes from websterites than for harzburgites at similar Mg# (Fig.8.4b; 8.7e) suggest an origin of webserites related to alkaline melts, either as cumulates (Irving, 1980; Python & Ceuleneer, 2003; Galán et al., 2008; Puzievick et al., 2011; Ackerman et al., 2012) or as alkaline melt-rock interaction products (Porreca et al., 2006; Le Roux et al., 2016; Tilhac et al., 2016 and references there in).

13.3.3. Phases in overgrowth microstructures, gabbronorite microband and in pyrometamorphic microstructures

Spongy or sieve-textured rims of *clinopyroxene* show more refractory compositions than earlier lherzolite clinopyroxene, with decreasing Al, Na and increasing Ca in the spongy rims (Fig.8.8). Ti does not define any tendency, Mg# stays either constant or increases and Cr# increases. These spongy rims are also characterized by lower jadeite component respect to non-spongy core composition (Fig.8.9a). Complementary *glass* in the dendrites of the clinopyroxene spongy rims is sodic alkaline, low in Ti and with trachyandesite and basaltic trachyandesite compositions (Fig.8.19). Lower jadeite component in these clinopyroxene spongy rims and the presence of glass in the dendrites relate their development to decompression-induced melting (Su et al., 2011), which was most likely enhanced by percolating fluids (Carpenter et al., 2004; Llovet & Galán 2003; Gudmics et al., 2008) or melts (Coltorti et al., 1999; Ionov et al., 2005). Heating is an alternative explanation, for example caused by abundant percolating melts (Wang et al., 2012), but it does not seem likely since previous T estimates using compositions of clinopyroxene spongy rims do not differ from T estimates using compositions from non spongy-textured clinopyroxene (Llovet & Galán, 2003; Galán et al., 2011). The fact that most spongy-textured

crystals display well preserved shapes and clear boundaries with surrounding grains (Fig.7.6c), for example with orthopyroxene, is also against destruction mechanism typical of melt percolation at high melt fraction causing heating (Su et al., 2011). Nevertheless, partial melting by decompression alone is also unlikely: available T estimates with the two- pyroxene thermometer (Brey & Kölher, 1990) for lherzolite BB.08.18, using non-spongy clinopyroxene compositions, are typically subsolidus (942± 3 °C; Table 9.1). Therefore, if local clinopyroxene melting took place at such low T, this would be favoured not only by decompression, but also by a limited percolation of fluids that decreased the melting point since non hydrous phases are formed.

Compositions of minerals in the *spinel coronae* show the main following characteristics with respect to earlier minerals: Fo and Ca content in new olivine crystals are higher (Fig.8.25a); clinopyroxene is also diopside-augite, but with higher Mg# and lower Al (Fig.8.25b) and Na compositions than in the main lherzolite clinopyroxene, spongy rims included; spinel compositions in the spongy rims and in the tiny isolated crystals of the coronae are Cr enriched and Mg depleted with respect to the reactant spinel; also, there is compositional gradation between reactant spinel and the new spinel, except for lherzolite SC.11.49, where there is a compositional gap between the two generations (Fig.8.25d); plagioclase either as microlites or as interstitial phase (glass?) is andesine-labradorite (Fig.8.18); K-feldspar compositions were detected as interstitial phase in spinel coronae of lherzolite SC.11.49. The formation of plagioclase and less aluminous spinel as reaction products implies that these coronae are related to mantle decompression. In such a case, plagioclase could have a subsolidus origin (e.g., Borghini et al., 2011; Galán et al., 2011; Su et al., 2011). However, plagioclase can be also formed by melt-rock reaction in impregnated peridotites (Delpech et al., 2004, Rampone et al., 2008, Fialin & Wagner, 2015; Lu et al., 2015). The latter hypothesis would be more in agreement with the presence of K feldspar in one of these coronae (in SC.11.49), since there are no K minerals among the primary phases. Assuming both decompression and impregnation, the latter must have taken place before the xenolith transport by the host lava (Bonadiman et al., 2008; Ionov et al., 1995; 2005), since these coronae are developed inside the xenolith and not preferentially at the contact with the lava. Dissolution or melting of earlier spinel could be caused by: (1) heating (Maaloe & Prinzlau, 1979); (2) decompression-induced melting (Su et al., 2011); (3) fluid percolation (Coltorti et al., 2000); and (4), invading melt (Perinelli et al., 2008).

Hypothesis (1) is excluded for the same reasons as for the clinopyroxene spongy rims: subsolidus T estimates for the two lherzolites with spinel coronae are too low (BB.08.18, SC.11.49 in Table 9.1); hypothesis (2) is discarded since the formation of the K-rich phase could not be explained, whereas decompression associated with limited fluid or melt percolation (hypotheses 3 and 4) would help in decreasing the spinel melting point, without much disturbing the interface of the coronae with neighbouring grains. The limited amount of percolating fluid (or melt) could result from the amphibole breakdown (Shaw & Klügel, 2002; Ban et al., 2005; Ismail et al., 2008) and the formation of the amphibole patches observed in sporadic xenoliths. Percolation of these fluids (melts) could have triggered the local partial melting of clinopyroxene and of orthopyroxene. The resulting SiO_2-rich melts could have enhanced the reaction of earlier spinel to form the new minerals in the corona. This would explain that clinopyroxene spongy rims are found in the same samples as spinel coronae, which reabsorbed them, and that the spinel coronae are preferentially developed against orthopyroxene crystals.

Compositions of phases in the *amphibole coronae* or patches show similarities and differences with respect to those in spinel coronae. Among the similarities it is to mention: Fo content in the new olivine crystals is higher than in the main olivine of the lherzolite (Fig.8.25a) and the spinel of the patch is Cr-enriched with respect to the main lherzolite spinel. Among the differences, clinopyroxene in the amphibole patch shows more variable composition, from Al-rich wollastonite at the contact with the reactant amphibole to diopside towards the contact with the other lherzolite minerals (Fig.8.25d; 8.26). Mg# and SiO_2 in this new clinopyroxene increase from the amphibole towards the coronae interface with orthopyroxene, while Ti decreases. Finally, interstitial glass shows compositions of trachibasalt to dacite through basaltic andesite (Fig.8.19), with SiO_2 increasing towards the contact of the patch with orthopyroxene. There are also several hypotheses on the origin of amphibole coronae and patches:

(1) the new minerals would be the thermal-breakdown products of incongruent melting of amphibole (Ban et al., 2005; Shaw, 2009); operative reaction would be:

$$amphibole \leftrightarrow clinopyroxene + spinel + olivine + melt\ (I)$$

$$melt1\ + orthopyroxene \leftrightarrow olivine + clinopyroxene + melt2\ (II)$$

Reaction (II) would occur if orthopyroxene was involved (Ban et al., 2005).

(2) Amphibole breakdown would be favoured by percolating melts distinct from the host lava (Bali et al., 2008 and references there in).

(3) Amphibole breakdown and reaction with xenolith minerals would be favoured by infiltration of melt/fluids related to the host lava, shortly before the xenolith transport (Shaw & Klüguel, 2002; Shaw, 2009).

(4) The patches would be related to the amphibole formation caused by basalt infiltration and melt-rock reaction, shortly before or during the xenolith transport (Coltorti et al., 2004), rather than to the amphibole breakdown. In this hypothesis, the nature of the infiltrated melt would be carbonatitic according to the glass compositions in our amphibole patches (Fig. 8.20).

Hypothesis (1) followed by reaction with xenolith minerals could be feasible in the case study: the process could have been favoured by the presence of CO_2 fluids on grain boundaries (Ban et al., 2005) and by a thermal event shortly before the transport of the xenolith by the host lava. A short event would agree with disequilibrium between the patch phases, i.e., with the heterogeneous compositions of clinopyroxene and glass. According to experiments by Shaw (2009), significant amphibole breakdown would take place at >1000 °C, between 0 and 1.2 GPa, whereas our T_{Bkn} estimate for lherzolite BB.08.24, including the amphibole patch, is only 925 °C. Therefore, it is deduced that the amphibole breakdown must have been enhanced by the percolation of melts/fluids not related (hypothesis 2) or related (hypothesis 3) to the host lava. In case (3), the amphibole breakdown would have taken place prior to the xenolith transport since these patches are not developed preferentially against the contact with the host lava. In addition, it is likely that the amphibole breakdown took place along with reactions with xenolith minerals. The percolating melt according to glass compositions in the patch could be carbonatitic (Coltorti et al., 2000; Fig.8.20), but if reactions with xenolith minerals took place, composition of glass would be seriously modified and hence, not related to the nature of the percolating melts (González-Jiménez et al., 2014). Finally, hypothesis (4) above is not consistent with amphibole crystals showing embayed and smooth forms suggesting its dissolution (Fig.7.6f; 7.12) rather than its formation.

In the only *gabbronorite microband* found, Fo in olivine is also slightly higher (91.4%) with respect to the host lherzolite olivine (90.1%) and orthopyroxene also shows similar composition, but for higher Cr#. Gabbronorite spinel has similar composition to lherzolite spinel, but for

higher Mg# and lower Cr# in the former (Fig.8.11). Anorthite of plagioclase is 66% (Fig.8.18). Since mineral compositions in this gabbronorite are not much evolved with respect to the wall lherzolite, it is likely that the orthopyroxene saturation of the percolating melt could have been achieved by its interaction with the host peridotite via orthopyroxene dissolution (Rampone et al., 2008). Another possibility is that this orthopyroxene-saturated melt was related to the rare magmatism with tholeiitic affinity linked to the earlier episodes of the European Cenozoic Rift System (ECRIS) in the CVZ (Neumann et al.; 1999). This hypothesis would fit with the post-kinematic character of this gabbronorite microband with respect to the wall-rock equigranular lherzolite (Fig.7.5e) (see sections 13.6 and 13.7 below).

In *basaltic microveins* crosscutting the mantle xenoliths (i.e., of pyrometamorphic origin), olivine compositions are more differentiated (Fo_{73}) than in the xenoliths, plagioclase microlites have 51-52% An and glass shows variable compositions, from trachibasaltic andesite, andesite-dacite to trachidacite (Fig.8.19). This glass is sodic and shows higher Ti than glass related to the other overgrowth microstructures (Fig.8.20). Therefore, it could be related to sodic-alkaline percolating melts, comparable to the host volcanic rocks, according to analyses of López Ruiz & Rodriguez Badiola (1985), plotted in the diagram K_2O vs. Na_2O of Middlemost (1975) (not represented). Finally, the only overgrowth microstructure that appears preferentially developed at the contact of xenoliths with the host lava is surrounding orthopyroxene. However, we only have analyses of phases (olivine, clinopyroxene, plagioclase, spinel) in an orthopyroxene corona close to a spinel corona (lherzolite BB.08.18), with similar compositions to each other (Fig.8.18; 8.25a-d). Therefore, we are not sure of the pyrometamorphic origin for the orthopyroxene corona.

13.3.4. Sulphides

Compositions of the three textural types of base metal sulphides (BMS) analysed (viz., 1: inclusions in silicates and spinel, 3: interstitial grains, 4: in overgrowth textures and microveins) are similar (Fig.8.27; 8.28), which is at contrast with previous results (Cruz et al., 2014; Galán et al., 2016). Type 4 sulphides in previous references were Ni enriched respect to types 1 and 3. This difference could be explained by the fact that most overgrowth microstructures of this study, where most type-4 sulphides are located, are not of pyrometamorphic origin. Sulphide compositions correspond mainly to low T Ni-Fe monosulphide solid solutions (mss1 and mss2),

but with mss2 compositions very close to pentlandtite. Moreover, there are rare pyrrhotite, Cu intermediate solid solution (iss) and/or the low T breakdown products of it (chalcopyrite, cubanite ± haycockite± bornite) (Sugaki et al., 1975). Bulk compositions for these sulphides are equivalent to high T MSS equilibrated at 1000-900 °C with a relatively Ni-Cu rich sulphide melt (Fig.8.29) (Craig & Kullerud, 1969). Later re-equilibrium at lower T (from 600 to <100 °C) would cause the formation of the breakdown products of MSS and iss. Assuming these are equilibrium temperatures, sulphide blebs could have stayed partially melted at the subsolidus equilibrium conditions of this SCLM (see next section) and then registered lower re-equilibrium T than silicates. The latest re-equilibrium conditions would have occurred during cooling of the host lava.

Two main hypotheses for the origin of BMS in off-craton xenoliths are envisaged (Lorand et al., 2013 and references there in). They could be either restitic, i.e., formed from immiscible sulphide melts trapped as blebs in the silicates during mantle partial melting, or metasomatic, i.e., formed during residence in the SCLM. In the latter case, there are two further options: BMS could be crystallization products of immiscible sulphide-rich melts (Szabo & Bodnar, 1995; Guo et al.; 1999) or could derive from sulphurization reactions between S-rich fluids and olivine, or metals dissolved in highly alkaline, volatile-rich melts and/or carbonatite melts (Lee, 2002; Lorand et al., 2003; Alard et al., 2011). It is also worth noting that several generations of sulphides can co-exist in the same rock (Alard et al., 2000, Powell & O'Reilly 2007, Harvey et al., 2010). For the sulphides in previously studied mantle xenoliths from the CVZ, Galán et al. (2016) suggested a restitic origin based on: (1) their major presence in lherzolites that had experimented less mantle melting than that estimated for S-consumption; (2) the predominance of mss1 and/or mss2 in the sulphide parageneses; and (3), that cryptic metasomatism did not affect severely the lherzolites. The three arguments are also valid in our case. However, Galán et al. (2016) did not exclude the likely of a metasomatic origin for these BMS because they found lower values for the Ni-exchange coefficient between the high-temperature MSS and olivine than for those reflecting equilibrium between these two phases. Interesting enough, our results include a more frequent presence of Ni-Cu rich sulphides than in xenoliths studied by Galán et al. (2016). These sulphides have been considered the result of sulphurization reactions during metasomatic processes (Lorand et al., 2013 and references there in), which leaves open the polygenetic origin of the BMS in this SCLM.

13.4. T, P, fO_2 equilibrium conditions

Features of the general microstructures, such as slightly curved or interlobate grain boundaries between phases, along with homogeneous composition of the main minerals suggest that these rocks attained microstructural and chemical equilibrium before their entrainment by the host lava. Therefore, only heterogeneous compositions in the overgrowth microstructures would reflect chemical disequilibrium.

The most consistent T estimates at 1.5 GPa are based on the enstatite (or diopside) exchange between the two pyroxenes, calibrated as two thermometers: the two-pyroxene thermometer (Brey & Köhler, 1990; Taylor, 1998, named T_{Bkn} and T_{t98} in Table 9.1, respectively) and the Ca-in-orthopyroxene thermometer (T_{Ca} in Table 9.1). The correlation between the estimates with these three calibrations is good overall (Fig.9.1a-b), therefore, we will use the T_{Bkn} values to make a synthesis of the results. T_{Bkn} values for protogranular harzburgites (1072±49 °C) and protogranular lherzolites (1063±28 °C) are comparable and higher than those provided by protogranular-porphyroclastic (956±24 °C), porphyroclastic (918±27 °C) and equigranular (913±73 °C) lherzolites, which overlap between them. T_{Bkn} values of the olivine websterites are similar (1048±28 °C) to those of protogranular peridotites. Either no significant differences were found between T_{Bkn} estimates using porphyroclast and neocrystal compositions for each sample or T_{Bkn} from neocrystals were lower (e.g., CA.12.03 in Table 9.1). However, T_{Bkn} estimates from unfocused analyses of orthopyroxene and/or clinopyroxene porphyroclasts showing mutual and/or spinel lamellae (i.e., from pre-exsolved compositions) are higher than those from exsolved compositions. Moreover, T_{Bkn} estimates from unfocused compositions of porphyroclastic lherzolites are either higher or similar to T_{Bkn} values for protogranular peridotites (Table 9.1; Fig.9.1a). This fact is more in favour of porphyroclastic and equigranular lherzolites were the result of deformation and finer-grained recrystallization of protogranular lherzolites at decreasing T than the other way round (see section 13.2 above). Finally, figures 9.2a-c illustrate that although equilibrium temperatures for harzburgites are slightly higher than for lherzolites, they are not related to differentiation indexes of the three types of microstructural lherzolites.

Most P estimates with the clinopyroxene-olivine thermobarometer of Köhler & Brey (1990) (P_{Kb90} in Table 9.1) are inconsistent with the spinel-lherzolite stability or they show great

uncertainty. Therefore, being aware of the limitations of this barometer (O'Reilly et al., 1997), only the few consistent values with the lowest uncertainty are assessed and included in Table 9.1 and in figure 9.3. P_{Kb90} consistent estimates are higher for protogranular lherzolites (15.1-6.1 kb), than for protogranular-porphyroclastic (9.8 kb), porphyroclastic (6.7 kb) and equigranular lherzolites (6 kb), (Fig.9.3). Harzburgites give values from 12.8 to 7.8 kb.

Finally, the fO_2 estimates (Balhaus et al., 1991) using T_{Bkn} at 1.5 GPa (fO_2 from +0.6 to -1.8) overlapfor lherzolites and harzburgites (Fig.9.5). No relationship has been observed between fO_2 values and equilibrium T (Fig.9.4a-b) or differentiation indexes (Fig.9.4c-d). Most averaged fO_2 values for the different types of peridotites are similar to those found in continental xenoliths elsewhere and in peridotites of the nearby Pyrenees, but harzburgites values are close again to those of the subduction settings such as xenoliths from British Columbia (Fig.9.5; Frost & McCammon, 2008). It is worth noting that the lowest values are provided by rims of zoned porphyroclasts and neocrystals of spinel, the former surrounded by coronae (Fig.9.4).

The following conclusions stem from comparing T-P-fO_2 estimates of the present study with previous ones (Galán et al., 2011) : (1) it is confirmed that equilibrium T of porphyroclastic and equigranular lherzolites is lower than that of protogranular harzburgites, lherzolites and websterites; (2) bulk compositions of pyroxenes with mutual and/or spinel lamellae provide higher T than re-equilibrated porphyroclasts and neocrystals, therefore, it is inferred that the deformation episode that caused finer-grained recrystallization of lherzolites took place not only at decreasing T but also P, according to the lower jadeite component of the clinopyroxene in these rocks (Fig.8.9a); and (3), assuming the paleo-fO_2, between -1 and -2, estimated by Galán et al. (2011) during the mantle partial melting, fO_2 would have been subsequently increased by melt-rock interaction or metasomatic processes and later on, decreased during the percolation of fluids (melts) which led to the formation of spinel coronae, shortly before the xenolith transport by the host lava.

13.5. Crystal-preferred orientations (CPO) of minerals: deformation episodes, tectonic settings and correlation with P-T-fO_2 conditions.

The results of this part of the thesis are published (Fernández-Roig et al., 2017, in press, see appendix) and the reader is referred to these articles for a larger discussion on this issue. Here we will present a brief summary of these results and conclusions.

The dominant olivine deformation fabric is [010]-fiber (or AG-type of Ben Ismaïl & Mainprice, 1998). This fabric is present in 72% of the total studied samples (Fig.10.7, Table 10.1), including protogranular harzburgites, most protogranular lherzolites and the wesbsterite, also with protogranular microstructure. This CPO type also shows the highest fabric strength or J index (Bunge, 1982) (Fig.10.11a; Table 10.1). The remaining lherzolites show A-type (Jung & Karato, 2001) or orthorhombic fabric (Tommasi et al., 1999), except in one xenolith which shows D-type fabric (Karato et al., 2008) (also named [100]-fiber fabric). These other olivine fabrics and transitional types between them and with the [010]-fiber type are mainly characteristic of porphyroclastic and equigranular lherzolites (Fig.10.11b), all showing lower J index with respect to peridotites with protogranular microstructure (Fig.10.11c).

The deformation fabric of orthopyroxene is well defined and coherent with olivine fabric in eight xenoliths (44% of the total): all are characterized by the alignment of orthopyroxene [001] and olivine [100] axes. Among the orthopyroxene CPO, three different types were identified according to Jung et al. (2010): AC-type, BC-type and ABC-type. In this nomenclature, the first and last capital letters represent the slip plane and slip direction, respectively (Table 10.1). In one more lherzolite and in the websterite, the orthopyroxene fabric is less well defined, but these samples do show coherent fabrics with olivine. In seven other lherzolites and one harzburgite (44% of the total) (Table 10.1), the olivine and orthopyroxene fabrics are incoherent (Table 10.1). Among these samples, lherzolite CA.44.05 stands out because orthopyroxene [010] and olivine [100] axes align, therefore, the slip direction for orthopyroxene would be [010]. Lherzolite SC.11.16 and harzburgite BB.12.04 also stand out because [100] axes of both minerals are subparallels; [001] axes of both minerals are also aligned and normal to the olivine [100] axis in SC.11.16 (Fig.10.7). For those samples where the analysis of orthopyroxene CPO was statistically reliable (Fig.10.7; Table 10.1), values of J indices are similar to, or higher than, those found in lherzolite olivine, whereas the reverse holds true in harzburgites.

As regards the clinopyroxene fabrics, 44% of the studied samples have clinopyroxene [010] and [001] axes normal and parallel, respectively, to olivine [100] axis, i.e., both minerals were deformed coherently (Table 10.1). The dominant slip system would be {110}[001] (Bascou et al., 2002; Zhang et al., 2006). Moreover, in these samples both pyroxenes are coaxial (Table 10.1; Fig.10.7). In addition, there are 50% incoherent samples, which are most of them porphyroclastic and equigranular lherzolites. It is worth noting that in five of these incoherent

samples, the [100] axes of both olivine and clinopyroxene align (Fig.10.7). The slip direction of clinopyroxene in these samples would be [100]. However, very few dislocations have Burgers vector b=[100] (Zhang et al., 2006). For instance, the (010)[100] and (001)[100] slip systems have been rarely observed (Philippot & Van Roermund, 1992; Godard & Van Roermund, 1995; Palasse et al., 2012). Clinopyroxene fabric types (Table 10.1) have been classified numerically according to LS index values as follows: S-type or flattening fabric, L-type or constriction fabric; and the intermediate SL-type for most lherzolites and the websterite (Helmstadt et al., 1972; Zhang et al., 2006) (Table 10.1; Fig.10.13). In samples where the number of both pyroxene crystals per thin section is > 100, J values for clinopyroxene are higher than those of orthopyroxene in each sample (Table 10.1). The highest values of J index of both pyroxenes are always associated with protogranular and protogranular-porphyroclastic rocks and the lowest with porphyroclastic lherzolites. Finally, LS index is broadly negatively correlated to olivine J index (Fig.10.13b).

There are overall positive correlations of olivine mode and equilibrium T with respect to the fabric strength: the J index decreases from protogranular harzburgites, clinopyroxene-poor lherzolites and websterite towards porphyroclastic and equigranular lherzolites equilibrated at lower T (Fig.10.12b-c) and P (considering the roughly falling of jadeite component from protogranular to porphydoclastic and equigranular lherzolites) (Fig.10.12a). There is no clear relationship with fO_2 (Fig.10.12d).

Several hypotheses are envisaged for the origin of the olivine fabrics found in these rocks. These hypotheses along with the relationships of the olivine CPO with pyroxene fabrics and T-P equilibrium conditions are largely discussed by Fernández-Roig et al. (2017) taking into account the regional context. The main conclusions of this paper are: (1) olivine [010]-fiber or AG-type fabric is due to deformation by dislocation creep at high T, dry conditions and low stress, related to late- Hercynian simple shear or transpression, and to subsequent annealing during late Hercynian decompression, Permian and Cretaceous rifting episodes; and (2), olivine AG-type fabric was transformed later on into orthorhombic (A-type) and [100]-fiber (D-type) fabrics through subgrain rotation and grain boundary migration recrystallization, taking place at higher stress and decreasing T and P with repect to the AG-type. This would have been due to changes in the deformation regime, from simple shear or transpression to mainly transtension, during

late Alpine extensional movements that led to the formation of Neogene basins (i.e., during the ECRIS development).

13.6. Mantle anisotropy and structure

These data were also included in Fernández-Roig et al. (2017) and were used to discuss the lithospheric mantle structure. Here we only present a brief summary of these results and of the discussion.

Seismic properties of the mantle [viz., velocity and anisotropy of the P (Vp, A) and S-waves (Vs1, Vs2, AVs)] estimated from mineral CPO are included in Table 11.1.

Vp patterns are similar in most samples (Fig.11.4): Vp distribution displays a well-defined maximum aligned with the maximum of olivine [100] axis and a minimum subparallel to the maximum of olivine [010] axis. AVp> 6% are found in protogranular harzburgites, protogranular lherzolites and the websterite, whereas lower values correspond to porphyroclastic and equigranular lherzolites, although there are a few exceptions (e.g., CA.12.03).

S-wave birrefringence patterns are more heterogeneous (Fig.11.4). In most samples, the highest AVs values tend to form one maximum (AVs max), two maxima, or a girdle within the structural XY plane ("foliation" defined from the CPO). In the first and the third case, the maximum is normal to the olivine [100] axis ("lineation" defined from the CPO), whereas in the second case, the two maxima are at 45° of the "lineation". Three other lherzolites (BB.08.59, SC.11.16, SC.11.52) are noteworthy because AVs maximum values tend to form a girdle normal to the "foliation" plane and with AVs max only normal to the "lineation". AVs maximum values> 4% are registered by most protogranular harzburgites and lherzolites and lower values by porphyroclastic, equigranular lherzolites and the websterite (Table 11.1). Finally, S1 tends to be polarized in a plane that contains the propagation direction and the olivine [100] maxima except for SC.11.16 where S1 is polarized in a direction subnormal to the olivine [100] axis (Fig.11.4). Figure 11.4 and table 11.1 also include the estimates for the average seismic properties of the local SCLM using samples weighted according to their abundance [viz., 40% harzburgites, 34% protogranular (-porphyroclastic) lherzolites, and 26% porphyroclastic and equigranular lherzolites, according to section 3], their respective simplified mode, spinel excluded, and the CPO data in a common standard orientation (the one used for displaying the CPO in Fig.10.7).

This method would provide a maximum estimate for the local SCLM anisotropy since coherent deformation (similar orientation of foliation and lineation) for the whole mantle column is assumed. The Vp and S-wave birrefringence patterns are similar to those of most protogranular xenoliths.

Relationships between seismic anisotropy patterns and olivine deformation fabrics of the studied xenoliths are as follows: AG-and A-type fabrics share similar seismic anisotropy patterns. However, maximum values of Vp and AVs within the "foliation" plane tend to be more dispersed for AG-type than for A-type fabric (Fig.11.4). SC.11.16, with olivine D-type symmetry, shows highly distinctive seismic properties, where the highest AVs values and the S1 polarization plane are orthogonal to the "foliation" (XY) plane, whereas in the other samples they are parallel to it. Moreover, there are positive correlations of AVp and AVs with respect to J indices (Fig.11.5a-b), which means that the dynamic recrystallization observed in porphyroclastic and equigranular lherzolites probably decreased seismic anisotropy. Finally, there are general positive and negative correlations of AVp vs. olivine mode and orthopyroxene mode (Fig.11.6a-b), respectively. No relationship has been observed with clinopyroxene mode. Variation of AVs with respect to mineral mode is similar, but there is a broadly negative correlation with the clinopyroxene mode (not shown).

Contrasting the average seismic anisotropy of the SCLM estimated from the studied mantle xenoliths with seismic data may help to assess the thickness of the lithosphere and the deformation regime in the area. Shear-wave splitting using SKS phases serves to explore the uppermost mantle anisotropy. However, this method does not provide information about the depth distribution of the anisotropy. The fast polarization directions (FDPs) deduced from SKS-wave splitting are expected to be parallel to the mantle flow direction (Silver & Chan, 1988) and related to the CPO of olivine (Nicolas & Christensen, 1987). Barruol et al. (1998) and more recently Díaz et al. (2015) deduced the FPDs around N 120 °E and delay time (δt) range of 0.6-1.1 s for stations nearby La Garrotxa sub-zone. Below the CVZ, AVs estimates range from 2.19 to 7.95%, therefore, the SCLM cannot be discarded in the interpretation of the SKS-wave splitting. However, assessing the SCLM contribution is hindered by the fact that mantle xenoliths provide no information on their original position and orientation. Therefore, we have assumed that Vp max, the highest AVs values and the S1 polarization plane of most samples match the fast polarization directions (FPD) deduced from SKS-wave splitting in the area. That is to say, the

olivine [100] axis is generally oriented ≈ N120 °E as the FPD, defining a "lineation" within the "foliation" plane, the orientation of which is unknown.

In order to constrain the orientation of this "foliation" plane and to estimate the thickness of the anisotropic layer that cause the observed delay times, we have used the following equation by Mainprice & Silver (1993):

$$\delta t = L \times \frac{AVs}{<Vs>} \qquad (1)$$

where δt is the local S-wave splitting delay time, L is the SKS-wave effective path length, AVs=[Vs max-Vs min]/<Vs> in a particular direction and <Vs>=[Vs max+Vs min]/2 for the average SCLM. Assuming that δt is mainly due to the SCLM anisotropy (Mainprice & Silver, 1993), with a smaller contribution made by the crust (0.1 s per 10 km; Barruol & Mainprice, 1993), the thickness of which is 30-26 km in this area (Gallart et al., 1984, 1991; Dañobeitia et al., 1992; Galán et al., 2011), then L is the SKS effective path length within the SCLM, i.e., its thickness. For the estimates, two end-member orientations were considered: (i) vertical "foliation" and horizontal olivine [100] maxima or "lineation" and (ii) horizontal "lineation" and "foliation" (Fig.11.10). SKS-wave splitting δt range (0,6-1,1 s) was taken from Díaz et al. (2015). L estimates so determined (Fig.11.10) were compared to existing data on the lithosphere-asthenosphere limit (LAL) in this area. Setting aside the crustal thickness, the thickness average is 51 km for the SCLM in case (i) (Fig.11.10a). This is consistent with the depth estimate for the lithosphere asthenosphere limit (LAL) (70-75 km), using gravity and geoid modelling in the shoreline of the Valencia Trough (Ayala et al., 2003) and thermobarometric data in mantle xenoliths from the CVZ (Galán et al., 2011). By contrast, the SCLM thickness average in case (ii) (Fig.11.10b) is much thicker (251 km). Therefore, it is inferred that most of the measured seismic anisotropy would be explained by the lithospheric contribution, if the SCLM fabrics record mainly transpression and transtensional deformation. This inference means that the fabrics have the olivine [100] maxima ("lineation") horizontal and orientated ca. N120 °E, like that of the FPD, and the olivine [001] maxima (structural Y direction) vertical. If this were not the case, the seismological data may also be explained by other orientations of the SCLM fabric and a larger contribution of an asthenospheric deformation fabric (Díaz et al., 2015), as has been suggested for other European zones (Klébetz et al., 2015).

13.7 Whole-rock major and trace element geochemistry, clinopyroxene trace element geochemistry: inferences on the type of mantle and on petrogenetic processes

13.7.1. The nature of the studied SCLM

Compositions of this SCLM vary from fertile lherzolites, even more fertile than the PM, to very refractory harzburgites (Fig.12.3). Whole-rock major element compositions, as major element mineral compositions, are not related to microstructural types of lherzolites. Mineral mode estimates based on mass balance from whole-rock and mineral analyses are similar to off-craton type xenoliths in most cases (Fig.12.3b, d). Exceptions are several porphyroclastic lherzolites, whose orthopyroxene mode overestimates that of off-craton xenoliths, and the most refractory harzburgites, which plot within the field of cratonic type xenoliths. In other classifications based on median major-element compositions of the whole-lot of xenoliths, this SCLM is Proton-type, that is to say structured 2.5-1Ga ago (Griffin et al., 1999). However, considering separately lherzolite and harzburgite medians, the former are between Proton and Tecton-type (age of deformation <1Ga) mantle and the latter are Arcon type (age of deformation >2.5 Ga) (Fig.12.8a). However, FeO_T compositions of harzburgites (8±1% FeO_T) are too high to be classified as such (FeO_T in Arcon-type mantle= 4-6%) (Griffin et al., 2009). Diagrams in figures 12.8 (Griffin et al., 1999) based on median mantle composition do not discriminate between the three possible tectonic settings of the Proton-type mantle: TILE (tectonic, incipient, litte extension), OCEAN (oceanic islands) and SUBD (convergent margin) settings. Orthopyroxene enriched mantle xenoliths as the ones studied here (Fig.12.3a) were found in subduction and cratonic settings. Those of subduction zones tend to show increasing FeO_T, while cratonic xenoliths show the opposite trend (Herzberg, 2004). None of these trends are well defined in figure 12.4f.

It is worth noting that a Proton-type mantle underneath the CVZ, based on the classification of Griffin et al. (1999), suggests that it was mainly deformed during Proterozoic tectonothermal events, which is at odd with our interpretation of CPO data (section 13.5). Nevertheless, it is to bear in mind that this mantle classification relies on a median estimate that can be very much constrained by the selection of xenoliths considered.

13.7.2. Petrogenetic processes

Lithospheric mantle compositions are the result of the petrogenetic processes experimented. These processes can be summarized as follow: (1) depletion due to melt extraction (Frey et al., 1985); (2) melt-rock interaction at high melt/rock ratio due to the percolation of mantle melts formed at deeper levels; this interaction can lead to dissolution of pre-existing minerals and crystallization of new ones depending on the nature of the percolating melt; if the new minerals are the same as the primary ones, the effects of this process are difficult to distinguished from the effects of (1) and the process is known as refertilization (Bodinier & Godard, 2004; Tang et al., 2011) or stealth metasomatism (O'Reilly & Griffin, 2013); and finally (3), ion-exchange reaction between rock and percolating melt(fluids) but at low melt(fluid)/rock ratio; this process can modified the composition of minerals and whole-rock without changing significantly the mineral mode and is classically known as metasomatism; if new minerals are different form the common ones, the metasomatism is called modal (Harte, 1983); if metasomatism only affects the composition of previous minerals, it is called cryptic (Dawson, 1984). It is understood that the limits between processes (2) and (3) could be difficult to fix and the effects of (1) and (2) processes difficult to discern because they can result in similar compositional trends (Fig.2.5).

In previous sections, there is evidence of the three processes in the studied SCLM.

(1) Points in favour of ***Melt depletion*** were already mentioned in sections 13.2 and 13.3. Melt depletion is also supported by whole-rock major and trace element compositions and by trace-element concentrations in clinopyroxene. For instance: (i) whole-rock gradual compositional variation, with good geochemical coherence and negative correlation between oxides, such as Al_2O_3 and CaO respect to MgO (Fig.12.4a-b); (ii) CaO/Al_2O_3 ratios for most lherzolites and harzburgites similar to the PM ratio (Fig.12.5); (iii) positive correlation between Ni and Mg# and negative correlation between most mildly incompatible elements and Mg#, in both whole-rock and clinopyroxene (Fig.12.10a; 12.10c-f; 12.18a,c,d,f); (iv) decreasing HREE from lherzolites to harzburgites and in the clinopyroxene of both rocks (Fig.12.14; 12.22); and (v), good positive correlation between mildly incompatible elements themselves, such as Y and Yb, in whole-rock and clinopyroxene (Fig.12.13; 12.21), with Y/Yb ratios straddling the PM values (Y/Yb in whole-rock=7,1-16,7; Y/Yb in clinopyroxene= 5,3-15; Y/Yb in PM=9,8).

As it was discussed before (sections 13.2 and 13.3; see also Fig. 8.24), lherzolites and harzburgites could represent residues after partial melting but they could have followed different melting episodes and/or in different settings. Other geochemical arguments for are: (i) different trends shown by lherzolites and harzburgites in several diagrams (e.g., orthopyroxene mode vs. olivine mode in figure 7.3c; TiO_2 in clinopyroxene vs. TiO_2 in whole-rock in figure 12.6f; Zr vs. MgO, Zr vs. Ce and Ti vs. Zr concentrations in clinopyroxene in figures 12.19h, 12.20f and 12.21a); (ii) change in the trending slope (e.g., TiO_2 vs. MgO diagram for whole-rocks; Fig.12.4d); and (iii), gaps in element abundances or ratio values between the two peridotites (e.g., the Cr# gap in spinel in figure 8.12a, Y and Yb gaps in clinopyroxene in figures 12.18e-f). Different tectonic settings for lherzolites (MORB mantle) and harzburgites (suprasubduction zones-SSZ) (see Fig. 8.24) would be consistent with these compositional gaps, although there is also an alternative explanation for them: they could be also caused by changes of the mineral-melt partition coefficients for these elements during partial melting (Hellebrand et al., 2001, Canil et al., 2004). Other geochemical strengths for the hypothesis of SSZ harzburgites are their MgO abundance > 44% and very low Al_2O_3 (<1,27%) and CaO contents (<1,03%) (Table 12.1). On the other hand, weaknesses for SSZ harburgites are: (i) TiO_2 and Na_2O concentrations are higher than in other typical SSZ harzburgites (TiO_2> 0,01; Na_2O> 0,03; Ionov, 2010); (ii) SiO_2 abundance does not show the highest discriminatory concentrations of the recent SSZ harzburgites (Herzberg, 2004; Fig.13.1c); and (iii), few of the new studied harzburgites show the discriminatory FeO_T enriched trend of SSZ mantle (Herzberg, 2004; Fig.12.4f). Only harzburgites BB.12.09 and BB.12.04 are slightly Fe enriched. In addition, FeO_T vs. MgO diagram in figure 12.4f for whole-rock compositions does not suggest a different tectonic setting for the two peridotites. Other drawbacks for relating the studied harzburgites to SSZ are based on trace element data. Neither whole-rock nor clinopyroxene multielement patterns show systematic significant spikes at Rb, Ba, U, Pb (the last element only considered in clinopyroxene) and Sr (Downes, 2001; Grégoire et al., 2001; Ionov, 2010) (Fig.12.15d; 12.25d). In summary, in spite of the fact that harzburgites show some typical geochemical characteristics of a SSZ, we cannot conclude for certain that they are residues of mantle partial melting in this setting. However, these typical characteristics could be mitigated by later petrogenetic processes.

Since most peridotites include spinel as Al-phase, it is thought that melting took place in P-T conditions of spinel lherzolites. Nevertheless, the presence of extremely LREE-MREE depleted

patterns (Fig.12.22b-c; 12.27a,c) in clinopyroxene from lhezolites SC.11.16 and BB.08.57, with $(Gd/Yb)_N$<0.80-0.77, points to melting starting in the conditions of garnet lherzolite. This could be also the case of harzburgite clinopyroxene BB.12.04, with u-shaped REE pattern, before being affected by LREE enrichment due to later metasomatism (Fig.12.22d; 12.27a). These LREE-MREE depleted clinopyroxene patterns were explained by Johnson et al. (1990) with a multistage melting model as follow: (i) relatively high degree of melting in the garnet stability field leaving residual garnet; (ii) decompression reaction of garnet to form the two pyroxenes+ spinel; and (iii), continued melting in the spinel stability field. If most primary clinopyroxene was consumed during melting in the garnet stability field, decompression-induced breakdown of garnet would have produced new clinopyroxene by the reaction:

$$olivine + garnet \leftrightarrow enstatite + spinel + clinopyroxene\ (III)$$

This new clinopyroxene would inherit the general shape of the garnet REE pattern (i.e., it would be HREE enriched), mitigated by interphase partitioning of REE. Later on, further melting and recrystallization in spinel lherzolite P-T conditions would produce clinopyroxene with REE patterns that are more fractionated than the rest. Similar clinopyroxene patterns in lherzolites from the CVZ were previously found by Bianchini et al. (2007) and by Galán et al. (2008), although they are not as frequent as in mantle xenoliths from west and central Europe (e.g., North Massif Central, France; Reno-Hercynian Massif, Germany; Bohemian Massif, Poland) (see section 2.3; Fig.2.4a-b). These clinopyroxene REE patterns with garnet signature are also characterized by a significant negative anomaly at Zr not accompanied by a similar Ti anomaly (Bianchini et al., 2007) (Fig.12.25.b-d).

To calculate partial melting degrees (F), several inverse methods can be used based on whole-rock major and trace element compositions (e.g., Johnson et al., 1990; Niu, 1997, 2004; Walter, 2003; Herzberg, 2004), whole-rock and olivine compositions (Takazawa et al., 2000), clinopyroxene compositions (Norman, 1998), and spinel compositions (Helebrand et al. 2001). Melting degrees based on spinel compositions were mentioned in previous section 13.4 (Fig. 8.24). The model of Niu (1997) was previously contrasted with major element compositions of xenoliths from the CVZ by Oliveras (2009). Both isobaric (at 20 kb) batch melting and polybaric fractional melting (30-8, 25-8, 15-8 kb) from the PM (McDonough & Sun, 1995) were considered (Fig.13.2a). Batch melting requires unrealistic F to explain the compositions of harzburgites,

whereas the three types of decompression incremental fractional melting could explain the compositions of lherzolites with 5%<F<20%. However, harzburgites show lower Al_2O_3 than the model estimates. The best fit was provided by a discontinuous fractional melting from 30 to 8kb that estimates 5%< F< 20% for lherzolites and F ≈30% for harzburgites, using Al_2O_3 and MgO abundances. In figure 13.1, we contrast the compositions of all xenoliths from the CVZ with the fractional melt-depletion trends by Herzberg (2004). It can be observed that the best fit is also provided by Al_2O_3 vs. MgO trends (Fig.13.1a) indicating that fractional melting starting at 3-1GPa could explain most lherzolite compositions, with 5%<F<20%, and most harzburgite composition, with 20%<F≤35%. These results are in agreement with previous ones by Oliveras (2009). In addition, in figure 13.1a, it is observed that the more fertile the lherzolites are, the more they are off the melt-depletion trends. Also to note is that F in lherzolites SC.11.16 and BB.08.57, showing the garnet signature in clinopyroxene REE patterns, would be residues left after < 10% melt extraction, whereas harzburgite BB.12.04 would result from F≈30%. The models of Herzberg (2004) were also thought to relate the mantle trends with the geodynamic setting where the melt depletion took place. In figures 13.1, the green field represents abyssal peridotites, the yellow field corresponds to the Ronda peridotites as example of a hotter mantle than the abyssal peridotites, the orange field includes cratonic mantle peridotites and the violet field the peridotites from active subduction zones. It is shown that there is a large intersection of the four mantle geodynamic settings and that most of the studied peridotite xenoliths plot within this intersection, but some conclusions can be extracted from this model: (i) rare harzburgites are as much depleted as the cratonic mantle and supra subduction zone (SSZ) peridotites; (ii) only three lherzolites show as much FeO_T as those from SSZ (Fig.13.1b); (iii) only four lherzolites are SiO_2-enriched as SSZ peridotites are; and (iv), several lherzolites are more fertile than the abyssal peridotites and four even more fertile than the PM (Fig.13.1a). In summary, the peridotite xenoliths as a whole from the CVZ are similar to a "hotter" mantle residue, that is to say related to a fossil plume or mantle diapir, as the Ronda massif in figure 13.1 (Herzberg, 2004).

Modelling of melt depletion based on whole-rock trace elements was also tested by Oliveras (2009). He used Y and Yb that are mildly incompatible elements apparently not affected by metasomatism since they plot scatterd respect to LREE (Fig.12.21b). Moreover, they show similar mineral-melt partition coefficients during mantle melting and display a good positive

correlation between them, with Y/Yb ratio similar to the PM ratio (Fig.12.21b-c). Following the same procedure, we estimated F for both batch and fractional non modal eutectic melting considering the mineral mode of the PM and the mineral mode entering the melt as in Johnson et al. (1990). Partition coefficients of both elements for the main minerals and spinel were also by Johnson et al. (1990), except for clinopyroxene (Gaetani et al., 2003). Results are illustrated in figures 13.2b-c. Anhydrous batch melting results indicate F< 25% for lherzolites and F >30% for harzburgites, which are unrealistic high values. According to this modelling clinopyroxene would disappear of the residue at F=26%. This implies that the clinopyroxene of our harzburgites and of those studied by Bianchini et al. (2007) would not have a restititic origin (Fig.13.2b). Anhydrous fractional melting estimates provide lower F for lherzolites (<18%) and for harzburgites 20%< F< 30%. Therefore, if anhydrous fractional melting occurred, harzburgite clinopyroxene could be restitic. However, if the mantle melting was hydrous, for instance in a SSZ mantle wedge, partition coefficients for Yb are lower and F would decrease (Gaetani et al., 2003): 18%< harzburgites F<25% for hydrous non modal fractional melting (Fig.13.2c). Similar F estimates to previous modelling were calculated for Y and Yb of residual clinopyroxene following the approach of Norman (1998) with the mineral-melt partition coefficients of Gaetani et al. (2003) for anhydrous melting. Again batch melting results with this model give unrealistic high F values for harzburgites (Fig.13.2d), whereas fractional melting fits better the Yb vs. Y trend of clinopyroxene for lower degree of melting (F≤10% for lherzolites; 10%< F< 36% for harzburgite) (Fig.13.2e). It is worth noting that these estimates are strongly dependent on the partition coefficients used. For instance, Galán et al. (2008) provided lower F values (<16% for lherzolites and between 16-30% for harzburgites) using partition coefficiets after Wood & Blundy (1997).

Finally, we have tried the Takazawa et al. (2000) inverse method to estimate F because it offers the advantage of considering each xenolith individually. The calculation was based on masse balance for FeO_T and MgO contents between the PM and residual peridotites:

$$C^o = C^L F + C^R (1 - F) \quad (2)$$

Where:

C^0= concentration of the oxide in the PM (McDonough & Sun, 1995)

C^L= unknown concentration of the oxide in the melt

C^R= concentration of the oxide in the residual peridotite

F= unknown degree of melting

By writing equation (2) for FeO_T and MgO independently and solving for F, equation (3) is obtained:

$$F = 1 - \frac{(FeO)^0 - \alpha(MgO)^0}{(FeO)^R - \alpha(MgO)^R} \quad (3)$$

Where parenthesis indicate molar composition and $\alpha=(FeO)^L/(MgO)^L$. This ratio is unknown but it can be calculated from olivine composition using the olivine-melt partition coefficient Fe-Mg K_D =0.30-0.35 of Roeder & Emslie (1970):

$$\alpha = (FeO / MgO)^{ol} / K_D \quad (4)$$

For batch melting, $(FeO/MgO)_{Ol}$ in equation (4) is the olivine composition at the end of melting. However, for fractional melting the olivine composition in equilibrium with the melt changes throughout the melting interval, from the value in the initial source to the value in the final residue and the integrated composition must be used for the calculation. However, the range of Fo contents in olivine of our xenoliths is small (89.1-91.7%), so that average Fo% was used for fractional melting estimates. Results for an intermediate value of K_D are included in Table 13.2. It can be seen that there is no significant difference between F values for batch and fractional melting and that F ranges for lherzolites (5.3-20.1%) and for harzburgites (19.2-28.4%) match estimates with previous inverse methods. The three lhezolites with negative F are those more fertile than the PM (BB.08.18, SC.11.49, SC.11.52). BB.08.18 and SC.11.49 are porphyroclastic lherzolites and have spinel surrounded by coronae that could result from later melt (fluid) impregnation of the SCLM (see section 13.4 above). The former sample also shows high spinel mode (4,2%, Table 12.1) that could produce a "nugget" effect on the whole-rock analyses. As regards lherzolite SC.11.52, it shows high LOI because of superficial alteration that could also influence the whole-rock analysis.

A summary of F estimates for anhydrous fractional melting from previous inverse methods is included in Table 13.3. The conclusions to extract are: estimates from different methods are similar and lherzolites and harzburgites could result from a continuous decompression fractional melting of a PM, although other possibilities rest open.

(2) ***Melt-rock interaction at high melt/rock ratio*** have been invoked in previous sections 13.2 and 13.3 to explain: (i) scattering among lherzolites in co-variation diagrams based on mineral mode (Fig.7.3); (ii) low olivine mode with respect to the PM (Walter, 2003) in several lherzolites; (iii) composite xenoliths with clinopyroxene enriched microbands (only one sample is of this type and unluckily with small size); (iv) orthopyroxene embayment by olivine and olivine inclusions in orthopyroxene in sporadic lherzolites and one harzburgite; (v) variable clinopyroxene/clinopyroxene+orthopyroxene ratio for similar Cr# in lherzolite spinel (Fig.8.21); and (vi), high Mg# typical of refractory peridotites in the composite xenolith with high clinopyroxene mode (i.e., decoupling between differentiation index and fertility). Whole-rock major and trace element geochemistry also provides some clues on melt-rock interaction at high melt fraction: (i) the presence of the three lherzolites more fertile than the PM, although two of them might show later melt-impregnation; (ii) the mineral mode estimates from mass balance using whole-rock and mineral compositions that also reveal that most lherzolites are depleted and enriched in olivine and orthopyroxene, respectively, with respect to melt depletion trends from the PM (Fig.12.3a-b, d); (iii) scattering in co-variation diagrams, such as SiO_2 or FeO_T vs. MgO (Fig. 13.1b-c) (Herzberg, 2004); and (iv), dispersion of clinopyroxene Mg# for constant whole-rock Mg# (ca. 90) (Fig.12.6c); the same decoupling is valid for Al_2O_3 and TiO_2 of whole-rocks and clinopyroxene (Fig.12.6d,f), but Al_2O_3 and Ti abundance in clinopyroxene can be modified by subsolidus re-equilibration with spinel and by later metasomatism, respectively. The diagram TiO_2 in clinopyroxene vs. TiO_2 in whole-rock was used by Le Roux et al. (2007) to prove that lherzolites from the Lherz massif in the Pyrenees were formed by refertilization. According to these authors melt depletion gives a positive correlation in this diagram, while lherzolites resulting from refertilization show variable TiO_2 in whole-rock at quasi-constant TiO_2 in clinopyroxene. In other words, TiO_2 concentration in clinopyroxene stays constant at variable differentiation index in refertilized lherzolites (Embey-Iszstin, 2016), which is not our case (Fig.12.6f). The problem with this refertilization process is that it can result in similar but reverse trends as melt depletion in co-variation diagrams for basaltic components and mildly incompatible trace elements vs. differentiation indexes (Bodinier & Godard, 2004; Griffin et al., 2009; O'Reilly & Griffin, 2013) (Fig.2.5). However, O'Reilly & Griffin (2013) argue that melt depletion trends should be concave-upward as those modelled by Niu (1997) in figure 13.2a, because incompatible elements are more rapidly depleted with respect to compatible ones as melt is extracted (see also Fig.13.1). This would be also the case of mildly incompatible elements

respect to Mg# (Canil et al., 2004), whereas linear trends, as in figures 12.10c-f could result from mixing between a more refractory peridotite and a basaltic melt.

The products of melt-rock reaction at high melt fraction vary as a function of the reactants (viz., mantle wall-rock and percolating melt). In figure 12.3, it is shown that clinopyroxene mode does not show the greatest deviation with respect to melt depletion trends (Fig.12.3c), but olivine and orthopyroxene modes (Fig.12.3a-b, d); olivine could be dissolved and orthopyroxe could grow at olivine expense. Especially in most lherzolites, olivine is under melt depletion trends and PM mode, whereas orthopyroxene is ≥30% and over melting trends in most porphyroclastic and equigranular lherzolites. As regards clinopyroxene, it shows a good negative correlation with the degree of melting (F) estimated following Takazawa et al. (2000) (Fig.13.3), but lherzolites display more scattered. For instance, for F=10±1%, the clinopyroxene mode estimates range from 9 to 12%. Also, lherzolite BB.08.101 with much higher F (20%) shows almost similar clinopyroxene mode (8%). Finally, two of the most fertile lherzolites (BB.08.18, SC.11.52) have clinopyroxene mode higher than 16%. Therefore, it is likely that clinopyroxene mode could be also determined by melt-rock interaction in some lherzolites. Increasing orthopyroxene and falling olivine were related either to interaction with SiO_2-rich melts or fluids derived from partial melting of a subduction slab (transformed into amphibolite or eclogite) (Kelemen et al., 1998; Grégoire et al., 2001; Ionov, 2010) that passed upward into mantle peridotite, according to reactions like:

$$Ol + SiO_2 \leftrightarrow Opx + melt2\ (IV)$$

However, only two porphyroclastic lherzolites (CA.12.03, SC.11.49) are SiO_2 enriched with respect to melt depletion trends (Fig.13.1b), which is a typical feature of SSZ peridotites (Herzberg, 2004). In addition, neither whole-rock nor clinopyroxene multielement patterns of these lherzolites show systematic characteristics of interaction with this type of melt/fluid (e.g., spikes at Rb, Sr, Th, U, Pb in clinopyroxene; Fig.12.15; 12.25). Moreover, previous isotopic data of lherzolite xenoliths indicate typical compositions of DMM-type mantle, with only some harzburgites showing isotopic evidence of having been affected by subduction-related melts/fluids (Galán & Oliveras, 2014). Finally, even the accessory amphibole found in rare lherzolites does not show typical compositions of subduction-related amphiboles (Fig.8.16). In summary, subduction-related melt (fluid)-rock interaction is not clear for these lherzolites.

Nevertheless, Kelemen et al. (1998) suggested that reaction (IV) and reaction (V) below could also take place when cooling, decompressing, mantle-derived magmas enter the conductive boundary layer in the uppermost mantle.

$$Opx + melt1 \leftrightarrow Ol + SiO_2melt\ (V)$$

At first, the melt-rock interaction tends to dissolve pyroxenes and to produce olivine, enriching the resulting melts in SiO_2, because olivine volume expands with decreasing P. Later on, if reaction (V) goes on until the magmas become saturated in orthopyroxene, continuous cooling and reaction of such melts would produce orthopyroxene-rich solids. Finally the cooling liquid will become saturated in ol-opx-cpx+ (aluminous phase) and could create pyroxene-rich lherzolite. Our orthopyroxene-rich lherzolites could have experienced the second stage and a few lherzolites could have arrived to the third stage described by Kelemen et al. (1998). In addition, it is observed that among the lherzolites with orthopyroxene mode≥ 30%, there are three groups of clinopyroxene REE patterns: very LREE depleted (SC.11.16), slightly LREE depleted (BB.08.97, SC.11.49, SC.11.52, BB.08.38, BB.08.54) and LREE enriched (BB.08.18, CA.12.03). This means that there is no relationship between LREE enrichment and fertility measured as the CaO concentration (Fig.12.16b; 12.27c). Therefore, it is inferred that the percolating melt(s) was either variably LREE enriched or depleted and very depleted and did not modify greatly the LREE abundance in clinopyroxene, as it has been discussed in other examples (e.g., Ackerman et al., 2015). An alternative explanation is that variable LREE enrichment in lherzolite cliniopyroxene is related to different degree of interaction with the percolating melt (Ichiyama et al., 2016), but this option does not fit with the fact that all these lherzolites have similar amount of orthopyroxene (Fig.12.13b). Whatever the case, lherzolite SC.11.16 with very depleted LREE clinopyroxene (Fig.12.22b) would be the least affected by melt-rock interaction.

In summary, melt-rock interaction processes between refractory peridotites and ascending asthenospheric melts, most likely tholeiitic and trace element depleted, could have modified the studied SCLM after melt depletion, causing mainly olivine dissolution and precipitatation of pyroxenes, especially orthopyroxene. However, reactions such as (IV) and (V) must have achieved equilibrium rapidly since microstructural evidence of mutual orthopyroxene and olivine replacement can be seen in the same sample (Fernández-Roig et al. 2017).

(3) ***Ion-exchange reaction between rock and percolating melt(fluids) at low fraction melt(fluid) or metasomatism*** occurred in a few studied lherzolites, where amphibole exits only as accessory mineral (modal metasomatism), and in all harzburgites and three lherzolites (BB.08.18, BB.12.01, CA.12.03) with clinopyroxene strongly enriched in the most incompatible elements (cryptic metasomatism). On the one hand, amphibole was found only in a few lherzolites where this phase shows compositions characteristic of disseminated-type amphibole formed in a within-plate setting (see section 13.3). Trace element composition of this phase is also in agreement with this classification: amphibole REE pattern is similar to that of coexisting clinopyroxene (Fig.12.22b; 12.24). $(La/Yb)_N$ ratio (0.69) in this amphibole is similar to that of disseminated amphibole in the Lherz massif (Zanetti et al., 1996). Although multielement pattern of amphibole shows distinc spikes at Rb-Ba, Nb-Ta, Sr and Ti (Fig.12.26), this phase does not influence much the whole-rock pattern. On the other hand, the cryptic metasomatism caused decoupling between the abundances of the most incompatible elements and differentiation indexes (Fig.12.11; 12.19) and mildly incompatible element concentrations (Fig.12.21b), and good positive correlation between the most incompatible elements (Fig.12.12; 12.20), both in whole-rocks and clinopyroxene. Harzburgite clinopyroxene is variable LREE-MREE enriched: two groups of patterns were differentiated according to this enrichment (more enriched group 1 and less enriched group 2; Fig.12.14d; 12.22d). The fractionament between LREE and HREE is normally strong [$(La/Yb)_N$= 1.25-23.2 in harzburgite clinopyroxene: $(La/Yb)_N$= 7.76-27.2 in whole-rock], but not so much between LREE [$(La/Nd)_N$=0.6-2.0 in clinopyroxene; $(La/Nd)_N$= 0.9-5.8 in whole-rock]. Metasomatized lherzolites only show LREE enrichment, with strong fractionament between them [lherzolite group 1 patterns with $(La/Yb)_N$= 10.2-26.1 and $(La/Nd)_N$= 2.8-21.4]. Lherzolites less or non affected by metasomatism are slightly LREE enriched or depleted (group 2 REE patterns) or very depleted (group 3 REE patterns) (Fig.12.22a-b; 12.25a-b). Most of the clinopyroxene LREE enriched patterns have been attributed to chromatographic fractionation of REE during the percolation of volatile rich low melt fraction through LREE depleted peridotites (Navon & Stolper, 1987; Bodinier et al., 1990). However, two exceptions of clinopyroxene REE patterns in harzburgites (BB.12.03, BB.12.09) stand out because their $(La/Nd)_N$ ratio is less than 1 showing smooth convex-upward or "n" shape patterns (Fig.12.22d; 12.27a). This type of REE pattern in harzburgites was also found by Bianchini et al. (2007) and have been usually explained by clinopyroxene equilibration with mantle alkaline melts (Irving & Frey, 1984; Bodinier et al., 1987; Witt-Eickschen et al., 1993).

It is worth noting that most whole-rock REE patterns are concordant with clinopyroxene REE patterns, but for two exceptions with $(La/Nd)_N$ higher in whole-rock (BB.08.80, BB.08.57; Fig.12.23). Such discrepancy is not uncommon among cryptically metasomatized mantle peridotites, and has been usually explained by the entrapment of enriched melts in clinopyroxene or by the presence of microcomponents (Bedini & Bodinier, 1999; Garrido et al., 2000; Schmidberger & Francis, 2001, Kourim et al., 2014). Discrepancies are also notable with other highly incompatible elements such as Nb, Ta and Pb. There are Ta and Pb spikes in whole-rock (Fig.12.15), whereas both elements show negative anomalies in clinopyroxene (Fig.12.25). Moreover, $(Nb/Ta)_N$ ratio is much lower than the PM value in whole-rock, whereas it is >1 and variable in clinopyroxene. These discrepancies are most likely due to analytic artifacts in whole-rock analyses for Ta and Pb. Another difference that could be explained is the positive Rb spike respect to Ba in lherzolites from Sant Corneli (Fig.12.15), which does not appear in clinopyroxene multielement diagrams (Fig.12.25). Some of these lherzolites are those with secondary K-feldspar in coronae surrounded spinel, which are explained by host basalt impregnation (section 13.3). In addition, $(Zr/Hf)_N$ ratio is much fractionated in whole-rock (< 1; Fig.12.16c) than in clinopyroxene, where it shows values close to the PM ratio (Fig.12.27b). This difference could be explained by the presence of other phases (e.g., orthopyroxene) that capture Zr and Hf in a different proportion than clinopyroxene.

Cryptic metasomatism also caused increasing Th-U, Nb and Sr abundance, all elements showing good positive correlation with LREE (Fig.12.12; 12.20). Th and U usually show positive anomalies with respect to Nb-Ta, which in turn present negative anomalies respect to LREE. Sr spike respect to MREE is rarely observed in clinopyroxene (CA.12.03 in figure 12.25b). Zr might be also increased along with Ti in some harzburgites, but different trends between these two elements (Fig.12.21a) and between Zr and Ce (Fig.12.20f) in harzburgites respect to lherzolites could be also due to different melting episodes experimented by both peridotites. $(Zr/Hf)_N$ ratio varies from very fractionated (0.35-0.20) with respect to the PM (Table 12.4), in very depleted lherzolite clinopyroxene not affected by cryptic metasomatism (lherzolites with group 3 REE patterns; SC.11.16, BB.08.57 in Fig.12.22b-c), to non fractionated in lherzolites with group 1 and 2 REE patterns and in all harzburgites (0.67-1.15). Increasing Zr/Hf ratio towards the most refractory peridotites is more in favour of its being influenced by metasomatism than by partial melting: Zr/Hf ratio is suspected to decrease with the degree of melting if clinopyroxene is the

most important phase contributing to the melt (Takazawa et al., 2000). Other features of peridotites affected by cryptic metasomatism are negative anomalies at Zr and Ti in whole-rock (Fig.12.15) and at Zr-Hf and Ti in clinopyroxene (Fig.12.25). These anomalies are more accentuated in harzburgites: Ti/Eu ratio is lower in metasomatized lherzolites (group 1 REE pattern) and harzburgites than in non-metasomatized lherzolites (group 2 and 3 REE pattens) (Table 12.4). The only harzburgite that does not have negative anomaly at Ti is BB.12.04 with the "u" shaped REE pattern. In spite of this, BB.12.04 shows the lowest Ti, Zr and Hf (Fig.12.25d) and the highest Ti/Eu ratio (11848 in Table 12.3), which is most likely due to light cryptic metasomatism.

Fractionament between elements with similar behaviour is key to interpret the nature of metasomatic components, but there are contradictory hypotheses. For instance, high Zr/Hf and Nb/Ta ratios, along with negative anomalies of these elements respect to REE and low Th/U ratio have been related to carbonatite metasomatism (Rudnick et al., 1993; Green, 1995; Foley et al., 2001). However, other authors consider that these ratios are not related to the nature of percolating metasomatic agents, but controlled by reactive porous flow of a single agent (usually an alkaline silicate melt) given carbonatitic derivatives or silica saturated melts (Bodinier et al., 2004; Rivalenti et al., 2004). Rivalenti et al. (2004) also suggested as alternative that negative anomalies at Zr-Hf and depletion of HREE respect to LREE could be due not to carbonatitic metasomatism but to previous circulation of the percolating melt through a garnet bearing mantle, since garnet partition HFSE and HREE respect to LREE. The degree of fractionament between LREE and HREE vs. the Ti/Eu ratio in clinopyroxene has been widely used to separate carbonatitic from silicate melt metasomatism (Coltorti et al. 1999; Fig.12.28). In our case, only two harzburgite clinopyroxene (BB.08.20, BB.12.02) plot within the field of carbonatitic metasomatism as three previously studied harzburgites (Galán et al., 2008; Galán & Oliveras, 2014). In contrast, the other metasomatized peridotites would have most likely interacted with an alkaline silicate melt. This would explain the high level of LREE(-MREE) enrichment, increasing Nb, small fractionament between Zr and Hf, and small negative anomaly at Ti. The introduction of these HFSE along with LREE-MREE excludes H_2O rich fluids as metasomatic agents. Carbonatitic and silica melt cryptic metasomatism could be considered as separated events. However, since the two harzburgites with signature of carbonatitic metasomatism do not present other feautures typical of this metasomatism, such as high

fractionament between Th and U, high Zr/Hf ratio, which are usually associated with the presence of secondary clinopyroxene, apatite and/or carbonate, we are more in favour of a sole metasomatic agent: an alkaline silicate melt evolving by percolation-reaction as it was posited by Galán et al. (2008) for similar previously studied xenoliths. According to this model, the migration of alkaline silicate melts through the mantle, for example by channeled porous flow (Dijkstra et al., 2003), would cause a single-stage, but heterogeneous, metasomatism through melt infiltration in the wall-rock (i.e., migration by diffuse porous flow; Dijkstra et al., 2003), accompanied by chromatographic fractionation-reaction at decreasing melt mass (Bodinier et al., 2004). The process would lead to the evolution of the percolating melt and to the formation of carbonate rich derivatives extremely LREE enriched. The different types of metasomatism (modal and cryptic) would be determined by the proximity of the peridotites to the channels and/or by interaction with a similar agent at different melt/rock ratio. For example, lherzolites with disseminated amphibole would be closer to the melt channels, while harzburgites and lherzolites affected only by cryptic metasomatism would be at greater distance. Nevertheless, in both cases the melt/rock ratio would have been low since amphibole never became an essential mineral. The two harzburgites with convex-upward (n shaped) clinopyroxene REE patterns (BB.12.03, BB.12.09), characteristic of being equilibrated with a silicate melt, could also result from interaction with the alkaline silicate melt, but at higher melt/rock ratio than clinopyroxene with higher chromatographic REE fractionation (Ackerman et al., 2015). Similar trace element enrichment and multielement patterns for harzburgites and the most metasomatized lherzolites suggest that both peridotites were affected by the same metasomatism.

According to REE chromatographic fractionation models (Navon & Stolper, 1987; Bodinier et al., 1990), LREE enrichment cannot overrate LREE abundance in the percolating melt. LREE enrichment of metasomatized lherzolites and harzburgites fits with that of rocks from the two alkaline episodes cropping out in the area: alkaline lamprophyres of Upper Cretaceous age (Solé et al., 2003; Ubide et al., 2012, 2014a, b; Esteve et al., 2014) and host alkali basalts and basanites of Neogene-Quaternary age (Cebriá et al., 2000). However, taking into account that interaction with host lavas only caused reaction microstructures at the xenolith-lava contact, while xenolith that experimented cryptic metasomatism are fully equilibrated, we are more in favour of the Cretaceous alkaline lamprophyres and carbonatitic derivatives as metasomatic agents.

Furthermore, since LREE enrichment is negatively correlated with fertility in harzburgites and non-correlated in lherzolites (Fig.12.16b; 12.27c), we suggest that metasomatism post-dated melt-depletion and possible refertilization processes. In addition, since the degree of LREE enrichment is neither related to microstructures (e.g., porphyroclastic lherzolites are from very LREE depleted to very LREE enriched; Fig.12.14b; 12.22b) nor to fabric strength or J index (Fernández-Roig et al., 2015; see below), the cryptic metasomatism would have been pre-kinematic with respect to the late Alpine deformation which formed the porphyroclastic and equigranular lherzolites (Fernández-Roig et al., 2017). This is consistent with the Cretaceous alkaline metasomatic agent. There is neither clear relationship between LREE enrichment and equilibrium T (Fig.13.4a-b): the two most enriched lherzolites show similar T_{Bkn} to other non-metasomatized lherzolites, whereas harzburgites show a reverse trend. In contrast, fractionament between LREE shows a positive correlation with T_{Ca} for lherzolites (the most enriched lherzolites show the highest T_{Ca} with few exceptions), whereas harzburgites display similar $(La/Nd)_N$ ratio for variable high T_{Ca}. Websterite plots among the harzburgites (Fig.13.4a-b).

Finally, it is worth noting that one of the most depleted lherzolite (SC.11.16) is Cu enriched and has a notable amount of sulphides. In fact, Cu shows different trends for lherzolites and harzburgites (Fig.12.10g) and its abundance in a few porphyroclastic lherzolites with frequent sulphides overrates the PM values (Fig.12.10g). Therefore, if Cu-rich sulphides are related to melt-rock interaction, either the melt was S enriched but depleted in lithophile incompatible elements, or the abundance of Cu-rich sulphides is not related to the cryptic alkaline metasomatic. Alternatively, the high sulphide concentration could be inherited from earlier petrogenetic processes and redistributed during later recrystallization of these rocks. This hypothesis is in agreement with the fact that interstitial (type 3) sulphides in lherzolite SC.11.16, are the most abundant.

(4) ***<u>The origin of websterites</u>*** will be discussed taken into account their major element mineral compositions and trace element abundance in their clinopyroxene. Major element compositions of the essential minerals are similar to those of harzburgite minerals and show lower Mg# than in previously studied websterites, (Fig.8.1; 8.4; 8.7). The clinopyroxene of the new websterite is also more MREE-HREE depleted than in previously studied pyroxenites (Fig.12.22). It also has convex-upward REE pattern similar to those of harzburgites BB.08.20, BB.12.02 reflecting equilibrium with a silicate melt. However, the websterite clinopyroxene is Ti enriched with

respect to harzburgite clinopyroxene for similar Mg# (Fig.8.4b; 8.7e) and websterite phlogopite is rich in Ti (Fig.8.17), suggesting that the co-existing silicate melt was alkaline. This melt could be similar to those causing the modal and cryptic metasomatism (Galán et al., 2008). The websterites could be cumulates as Galán et al. (2008) suggested or alkaline melt-rock (harzburgite) interaction products (Porreca et al., 2006; Le Roux et al., 2016; Tilhac et al., 2016 and references there in). The latter hypothesis would explain better less differentiated composition and more depleted REE patterns of our websterite clinopyroxene than that of Galán et al. (2008).

13.7.3. Evolution of the SCLM in NE Iberia: relationships between petrogenetic episodes and CPO

We will approach this issue considering our geochemical results and those previously published on xenoliths from the CVZ (Bianchini et al., 2007; Galán et al., 2008, 2011; Galán & Oliveras, 2014), along with the CPO results of this study and the main tectonothermal events registered by the crust in NE Iberia. A summary of inferred mantle processes in relation to the main tectonothermal events in NE Iberia is presented in figure 13.5.

Evolving trends from fertile lherzolites to refractory harzburgites in co-variation diagrams of basaltic components, compatible and mildly incompatible trace elements vs. differentiation indexes, in both whole-rock (Fig.12.4a-b; 12.9; 12.10a,c-f; 12.13) and clinopyroxene (Fig.12.18a,c,d,f; 12.21c), could be interpreted as the result either of secular evolution or of a dichotomy in processes experimented by the SCLM (Griffin et al., 2009).

On the one hand, in the secular hypothesis, the heterogeneous composition of this mantle would be due to melt depletion of a PM in one single stage or in several stages at different ages followed by metasomatism at low melt fraction. Different melting stages, at least for lherzolites respect to harzburgites, would be consistent with discontinuous compositional trends between both peridotites mentioned in previous section 13.6 or with the fact that lherzolites and harzburgites show very different Sr-Nd isotopic compositions. In figure 13.6, harzburgite clinopyroxene (Bianchini et al., 2007; Galán & Oliveras, 2014) shows very radiogenic Sr coupled to unradiogenic Nd. These isotopic values reflect the time-integrated effects of low Sm/Nd and high Rb/Sr ratios of harzburgites, probably over a long period of time after an ancient subduction-related hydrous fluid/melt metasomatism (Galán & Oliveras, 2014). Such

metasomatism could have taken place before or subsequent to the mantle partial melting in a SSZ or collision zone, either during the Variscan orogenesis or most likely during a pre-Variscan tectonothermal episode (Galán & Oliveras, 2014) (Fig.13.5). In contrast, most lherzolite clinopyroxene in figure 13.6 shows isotopic compositions close to a DMM-type mantle and one of them (Olt-4f of Bianchini et al., 2007), with higher radiogenic Nd. Lherzolite Olt-4f is characterized by very depleted REE patterns of clinopyroxene, similar to those of our samples BB.08.57 and SC.11.16 (Fig.12.22b-c). The isotopic composition of Olt-4f clinopyroxene would be the result of its time-integrated high Sm/Nd ratio (0.81), evidence of the presence of garnet during earlier melt extraction (Bianchini et al., 2007). So far, the only available ages are Lu-Hf model ages with respect to CHUR (1.0- 0.6 Ga) for two of these highly depleted lherzolites (Bianchini et al., 2007), which do not seem affected neither by refertilization nor by cryptic metasomatism. These Middle-Upper Proterozoic ages indicate that these lherzolites were isolated from the convecting asthenosphere since those times. The ages of melt depletion or isolation from the asthenosphere for the other lherzolites and harzburgites are unknown. For similar xenoliths in the MCF, Wittig et al. (2007) provided a depleted mantle-model age of 360 Ma, which they related to Variscan subduction.

On the other hand, our results (section 13.6) supporting melt-rock interaction at high melt/rock ratio are more consistent with a dichotomy in processes during this SCLM evolution. In such a case, an older and more refractory mantle, which might be represented by the harzburgites, would have interacted with percolating melts resulting from mantle melting during episodes of subduction, collision and/or asthenospheric upwelling. These would lead to refertilization of the older harzburgites, but it is not to exclude that melt depletion of material similar to the PM may have produced refractory juvenile peridotites incorporated to the SCLM, at the same time that more refractory peridotites were being refertilized (Griffin et al., 2009). These juvenile peridotites could be the most depleted lherzolites separated from the asthenosphere during the Middle-Upper Proterozoic mentioned above. In such a case, the age of these lherzolites would indicate not only their incorporation to the SCLM, but also the age of one of the possible refertilization episodes experimented by this SCLM. There could be other refertilization episodes, pre-dating and/or post-dating the Middle-Upper Proterozoic age (Fig. 13.5), but since we do not have other geochronological data, this option is merely speculative. Whatever the case, the percolating melts would have been tholeiitic and with isotopic DMM-type

compositions according to the slight LREE depletion or enrichment of most lherzolite clinopyroxene, and with available isotopic data for most of them (Fig.12.22a-c; 13.6). It is worth noting that for similar lherzolites in the Lherz massif, Le Roux et al. (2007) suggested refertilization processes related to percolation of Late-Variscan MORB-type basalts. However this age was recently questioned because the formation ages of websterite layers related by these authors to the refertilization processes are older (1.8-1.5; Early-Middle Proterozoic; Le Roux et al., 2016). In the case study, what we know is that basic rocks of tholeiitic affinity (representing the likely percolating melts interacting with the mantle), either Hercynian or post-Hercynian, do not crop out in the area. The only rocks of this type are the Cambro-Ordovician amphibolites of Guilleries, which show characteristics of tholeiitic within plate basalts (Reche, 1994), but unluckily there are no isotopic compositions available for them.

In addition, Le Roux et al., (2008) suggested that there was a feedback between refertilization processes and deformation in the Lherz massif: deformation intensity increases with increasing volume of percolating melts. According to the hypothesis of Le Roux et al. (2008), the response of the rocks' microstructure to deformation depend on the balance between strain intensity and the volume of percolating melts. Thus, in harzburgites and lherzolites from Lherz, where strain dominated the evolution at very low melt fractions, the olivine developed a [100]-fiber fabric, whereas when the amount of melt was more abundant and the strain lower, the dominant olivine fabric was [010]-fiber. In the sudied xenoliths, the facts observed are different: all harzburgites, lherzolites and the websterite with protogranular microstructure show the same olivine deformation fabric, [010]-fiber type. The intensity of deformation or olivine fabric strength (J index of Bunge, 1982) shows a roughly negative correlation with differentiation indexes, such as MgO and Y abundances in both whole-rock and clinopyroxene for these protogranular peridotites (trend 1 in Fig.13.7a-c). This correlation is interpreted as due to increasing amount of orientated olivine crystals in the most refractory peridotites, not to higher amount of percolating melt. Annealing subsequent to earlier deformation caused by axial shortening or transpression during the Variscan orogenesis was considered to be the main cause of the olivine [010]-fiber fabric (Fernández-Roig et al., 2017), because (i) Variscan orogenesis is the most important tectonothermal event that affected the overlying crust; (ii) the mantle is assumed to be usually deformed coherently with the crust (Vauchez et al., 2012); and (iii), the Variscan orogenesis is characterized by late W-E to NW-SE orientated strike-slip faults,

compatible with transpressional deformation, in the nearby Pyrenees (Carreras & Capellà, 1998; Carreras 2001). These faults could have deformed not only the crystalline crustal basement, but also the underlying SCLM. Subsequent annealing and grain growth would have preserved the transpressional fabric and been stimulated by the percolation of low fractions of metasomatic melts responsible for the modal and cryptic metasomatism observed in all harzburgites and few lherzolites. Taken into account the alkaline silicate nature of the metasomatic melt discussed in section 13.6, one of the most likely candidates would be the Upper Cretaceous alkaline lamprophyres and the other, the melt from which the cumulative (group II) xenoliths of the Roca Negra volcano (La Garrotxa sub-zone) were formed. The Cretaceous alkaline lamprophyres show heterogeneous Sr-Nd isotopic compositions, but rooted in the Common Mantle Reservoir (CMR) of Lustrino and Wilson (2007) (Fig.13.6a-b). This is also the case of the group II xenoliths of the Roca Negra volcano (field A in Fig.13.6a) and of the previously studied websterite. The percolation of the mafic alkaline silicate melts and carbonatite derivatives through lherzolites and previously metasomatized harzburgites, would have affected their composition quite differently: the alkaline metasomatic component would have been REE enriched with respect to both peridotites, but more isotopically depleted with regard to previously metasomatized harzburgites and more enriched with regard to DMM lherzolites. This would lead to reversed metasomatic trends in figure 13.6b for lherzolites and harzburgites. Olivine J index is also over 4 in the most metasomatized peridotites (Fig.13.7d), all with higher $(La/Yb)_N$ ratio than in non metasomatized lherzolites. These other lherzolites are mostly porphyroclastic and variable LREE depleted. They have olivine orthorhombic, rare [100]-fiber fabric, or transition fabrics between them and with [010]-fiber type. The J index of these other olivine fabrics is < 4 in most samples (ie. the intensity of deformation is lower) and is not correlated neither with differentiation indexes nor with $(La/Yb)_N$ ratio (trend 2 in Fig. 13.7a-c). Furthermore, in most of these porphyroclastic and equigranular lherzolites pyroxene [001] axes are not aligned with olivine [100] axis (Fig.10.7; Table 10.1). This inconsistency was related to post-kynematic melt-rock interaction (Soustelle et al., 2009; 2010; Zaffarana et al., 2014) since the presence of reactive-melt flow would have enhanced diffusion processes that contribute to weaken the olivine CPO. In the samples discussed here, when pyroxene J index in porphyroclastic and equigranular lherzolites could be estimated, it is even higher than that of olivine and both are positively correlated (Fernández-Roig et al., 2017). These results seem to contradict the late to post-kinematic character of the melt-rock interaction. Moreover, microstructural evidence of olivine

being replaced by clinopyroxene was not observed: grain boundaries between neocrystals of both phases are straight or slightly curved; only porphyroclastic lherzolite CA.12.03 shows occasional orthopyroxene porphyroclasts with both olivine embayment and rare rounded olivine inclusions. It is worth noting that both porphyroclastic lherzolite CA.12.03 (with orthorhombic fabric) and equigranular lherzolite BB.08.57 (orthorhombic-[100]-type fabric) provide the lowest T estimates, the highest bias between T_{Bkn} and T_{Ca} estimates and the highest difference between porphyroclast and neocrystal T (Table 9.1). These thermometric results suggest chemical disequilibrium in these samples and cast doubt on the existence of more effective diffusion enhanced by the presence of significant amount of melt during the development of the olivine orthorhombic and [100]-fiber fabrics. In spite of these drawbacks, the fact that some of these lherzolites are among the most fertile, with the lowest olivine mode (e.g., SC.11.49; CA.12.03 in Table 12.1), points in favour of refertilization processes. Nevertheless, this refertilization could have been pre-kinematic with respect to the development of olivine orthorhombic and [100]-fiber fabrics. Fernández-Roig et al. (2017) interpreted these other olivine fabrics in lherzolites as due to late Alpine extensional shear zones developed at decreasing T and P (Vauchez et al., 2012) that led to the formation of Neogene basins and the ECRIS. Moreover, since there are no relationships between the olivine J index of porphyroclastic and equigranuar lherzolites and differentiation or enrichment indexes (trend 2 in Fig.13.7a-c), we infer that this transtensional episode also post-dated the modal and cryptic metasomatism. This inference is more in favour of the Cretaceous alkaline lamprophyres as metasomatic agents than of the alkaline melts related to the cumulative (group II) xenoliths, precursors of the host lavas (Neumann et al., 1999). The fact that porphyroclastic and equigranular lherzolites are variable LREE enriched, from very depleted (SC.11.16 with [100]-fiber fabric) to very enriched (CA.12.03 with orthorhombic fabric): suggests that finer grained recrystallization caused by the extensional deformation episode did not enhance cryptic metasomatism, but affected previously metasomatized peridotites. In addition, there is no clear relationship between LREE enrichment and equilibrium T (Fig.13.4a-b): the most enriched lherzolites are porphyroclastic equilibrated at lower T as the other depleted porphyroclastic lherzolites are. Therefore, equilibrium T is related to late deformation episode rather than to cryptic metasomatism in lherzolites. In summary, although there is compositional evidence of melt-rock interaction at high melt/rock ratio (stealth metasomatism or refertilization), we could not establish the feedback between this process and deformation episodes experimented by the

SCLM in NE Iberia. In contrast, cryptic metasomatism could have contributed to annealing, grain growth and preservation of earlier transpressional olivine [010]-fiber fabric in protogranular lherzolites and harzburgites with the highest J index (Fig.13.7).

Finally, coronae surrounded amphibole and spinel and spongy rims in clinopyroxene crystals would be most likely developed after the late Alpine transtensional deformation and before the xenolith transport by the host lava. The main evidence is that clinopyroxene spongy rims are developed in both neocrystals and porphyroclasts and dissolved at the contact with the spinel coronae. The relationship between the amphibole coronae (patches) and deformation could not be established. However, the fluids released by the amphibole breakdown could be essential to enhance local clinopyroxene (i.e., spongy rim development) and orthopyroxene melting. The resultant SiO_2-enriched melts would have reacted with spinel during the upwelling of the SCLM, shortly before its fragmentation by the host lavas. This melt-rock interaction episode at low melt/rock ratio would have decreased fO_2 values (Fig.9.4). A non-deformed microband of gabbronorite in one equigranular lherzolite (BB.08.38) is also a rare evidence of limited percolation of tholeiitic melts at this later stage.

13.8. The subcontinental lithospheric mantle of NE Iberia compared to other domains of the European SCLM

This comparison was approached by Galán et al. (2008) and Galán & Oliveras (2014), who concluded that compositions and evolutionary trends of the SCLM of NE Spain are similar to those of nearby mantle domains beneath the western European rift system, such as the southern domain of the MCF, the Cabezo Tallante xenoliths in SE Spain, and to the peridotitic massif of Lherz in the Pyrenees. These domains of the SCLM are characterized by the presence of mostly spinel lherzolites and harzburgites with average composition more fertile than the SCLM represented by xenoliths from the north of MCF (Downes et al., 2003) (Fig. 9), the Vogelsberg area (Witt-Eickschen, 1993), the Rhön area of Germany (Witt-Eickschen & Kramm, 1997) and the Eger rift area in Polonia (Puziewicz et al., 2015).

To previous comparisons, we have incorporated the SCLM beneath the Volcanic Camp of Calatrava (Villaseca et al., 2010; Bianchini et al., 2010), also represented by xenoliths in Neogene-Quaternary lavas. Calatrava xenoliths also suggest a fertile SCLM, but mainly formed of protogranular spinel lherzolites, although there are also subordinate harzburgites, wehrlites,

olivine websterites and dunites. One difference to highlight between the Calatrava xenoliths and those from the CVZ is the more frequent presence of amphibole and phlogopite in the former, with compositions related to subduction type metasomatism (Villaseca et al., 2010). In contrast, amphibole compositions in the CVZ xenoliths are more typical of within-plate metasomatism (Fig.8.16). Subduction related metasomatism or refertilization is also invoked for Fe-rich lherzolites from Calatrava by Bianchini et al. (2010). Dominant olivine B-type CPO in the Calatrava xenoliths, suggesting deformation under relatively low mantle temperatures, significant water-activity and elevated strain rates, is also consistent with a suprasubduction setting (Puelles et al., 2016). In contrast, dominant olivine AG-type fabric in the CVZ xenoliths is more typical of high T, dry conditions and low stress deformation (Fernández-Roig et al., 2017). The age of the subduction episode in Calatrava remains uncertain: Cenozoic suprasubduction realm related to (Alpine) Betic Cordillera (Villaseca et al., 2010), which is not registered in NE Iberia, or suprasubduction realm related to the SW Iberian Cadomian orogen, which was active between the late Ediacaran and the early Cambrian (see Fig. 13.5 for correlations). In Calatrava xenoliths, later metasomatism related to alkaline silicate melt was also registered (Villaseca et al., 2010), but it was explained as due to interaction with the alkaline host lavas shortly before their intrusion.

As regards Tallante xenoliths, our peridotites compare well with anhydrous lherzolites and harzburgites (Beccaluva et al., 2004; Fig.12.7; 12.16; 13.6a) from SE Spain, but there are more isotopically evolved harzburgites in the CVZ (Fig.13.6a) than in Tallante. However, clinopyroxene rich lherzolites often containing plagioclase, amphibole-phlogopite bearing harzburgites, orthopyroxenites and composite xenoliths, which are found among the xenoliths of Tallante (Beccaluva et al., 2004; Rampone et al., 2010; Bianchini et al., 2011), are rarely or never found among those from the CVZ. New data on Tallante Xenoliths were recently published by Hidas et al. (2016) and by Marchesi et al. (2017). Hidas et al. (2016) focused on olivine CPO of porphyroclastic and equigranular lherzolites which are dominated by the [100]-fiber-type, the least common type in the CVZ xenoliths. They interpreted this fabric as due to simple shear or transtensional deformation related to the change from subduction-compression to within-plate extension. This interpretation is not very different from our interpretation of olivine orthorhombic and [100]-fiber fabrics (Fig.13.5) in porphyroclastic and equigranular lherzolites. Marchesi et al. (2017) provided new geochemical data for the Tallante xenoliths and interpreted

them differently from Beccaluva et al. (2004). According to Beccaluva et al. (2004) spinel lherzolites and harzburgites are the result of partial melting followed by two metasomatic episodes: an earlier mainly cryptic metasomatism related to silica-undersaturated alkaline melt causing variable LREE and Sr–Nd isotopic enrichment, from Depleted Mantle (DM) to Enriched Mantle (EMI) end-members; and a second metasomandatism related to silica-oversaturated hydrous melts, producing the formation of amphibole/phlogopite-bearing orthopyroxene-rich harzburgites containing olivine–orthopyroxenite and gabbronorite lenses. The second metasomatism is characterized by evolved Sr–Nd isotopic values. These evolved Sr–Nd isotopic data closely approach those recorded in the Miocene calc-alkaline and potassic volcanism of the Betic Cordillera, suggesting that this signature could have been inherited from subduction-derived metasomatizing melts during the Tertiary orogenic events of the Betic–Alboran region. For Marchesi et al. (2017), these peridotites derive from residues of around 20% partial melting and experienced different types of mantle metasomatism, mostly stealth metasomatism, due to different melt-rock reactions: (1) reaction with melt caused the addition of both pyroxenes and the dissolution of olivine in most xenoliths; (2), subordinate consumption of orthopyroxene and enrichment in clinopyroxene and olivine in other xenoliths; and (3), rare dissolution of orthopyroxene and addition of olivine in one xenolith. These varieties of stealth metasomatism were mostly induced by reactions of the peridotites with relatively FeO_T-rich/SiO_2-poor melts (tholeiitic type) produced by melting of a pyroxenite-peridotite veined lithosphere with highly heterogeneous Sr-Nd-Pb isotopic compositions. Melting of this lithospheric mantle was caused by upwelling of the asthenosphere related to back-arc extension in the Late Oligocene-Early Miocene (i.e., during the Tertiary orogenic events of the Betic–Alboran region). However, orthopyroxene replacement by olivine and clinopyroxene was related to SiO_2-poor alkaline melt-mantle reactions. These other percolating melts are similar to the Late Miocene-Quaternary alkaline basalts enclosing the mantle xenoliths. From this synthesis on Tallante xenoliths, one conclusion stands out: the main metasomatic processes in this area seem to be related to Tertiary subduction and late Neogene-Quaternary extension. In the SCLM of NE Spain, the main metasomatic processes (stealth, modal and cryptic metasomatism) might have been older (Fig.13.5).

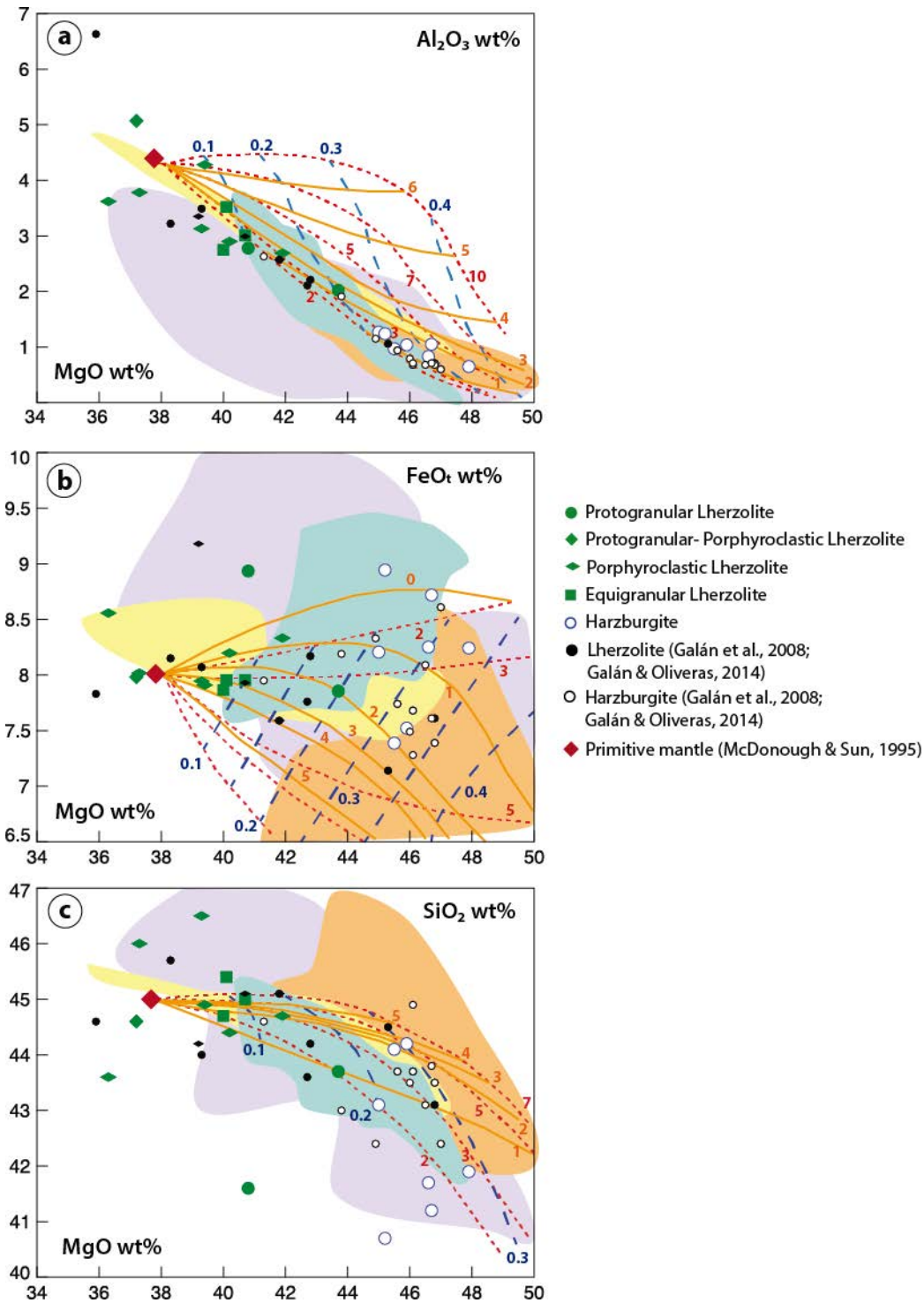

Fig.13.1. a) Al_2O_3 vs. MgO concentration in whole-rock compositions of xenoliths from the CVZ, included data by Galán et al. (2008) and Galán & Oliveras (2014), with the fractional melt-depletion trends modelled by Herzberg (2004). b) Idem for FeO_t vs. MgO. c) Idem for SiO_2 vs. MgO. The green field represents abyssal peridotites, the yellow field corresponds to the Ronda peridotites, the orange field includes cratonic mantle peridotites and the violet field the peridotites from active subduction zones. Red discontinuous lines: initial melting pressures; orange continuous lines: final melting pressures; blue dashed lines, melt fractions (Herzberg, 2004).

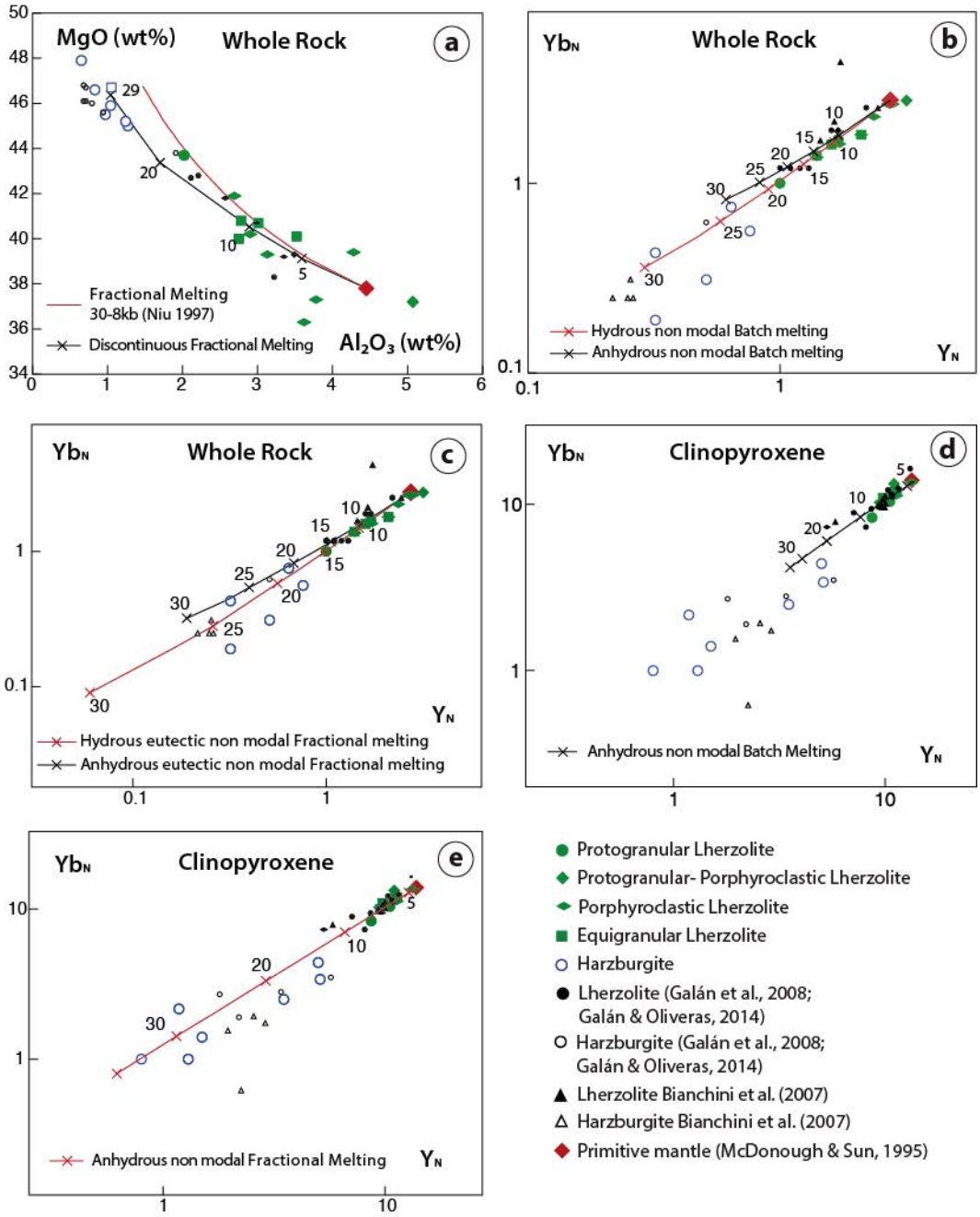

Fig.13.2. a) Al_2O_3 vs MgO diagram for whole-rock compositions showing the residual fractional melting trend (3-8Gpa) from a PM after the model by Niu, (1997, 2004) and for a discontinuous fractional melting. b) Yb_N vs. Y_N diagram for whole-rock compositions with two estimated residual non modal batch melting trends from the PM: one is anhydrous non modal batch melting and the other hydrous non modal batch melting (partition coefficients by Johnson et al. (1990) and Gaetani et al. (2003). d) Yb_N vs. Y_N diagram for residual clinopyroxene from the PM, using the batch melting model by Norman et al. (1999) with partition coefficients by Gaetani et al. (2003). e) Residual clinopyroxene trend after the fractional melting of Norman et al. (1999). CI normalising values and PM source by McDonough and Sun (1995).

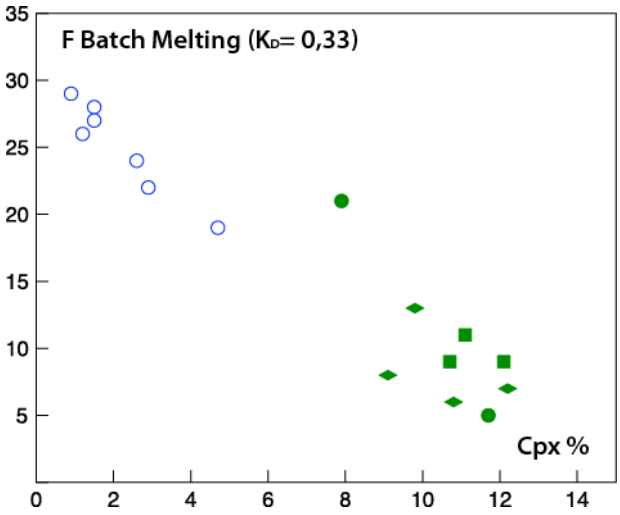

Fig.13.3. Degree of melting after Takazawa et al. (2000) vs. clinopyroxene mode. Symbols as in figures 13.1-13.2

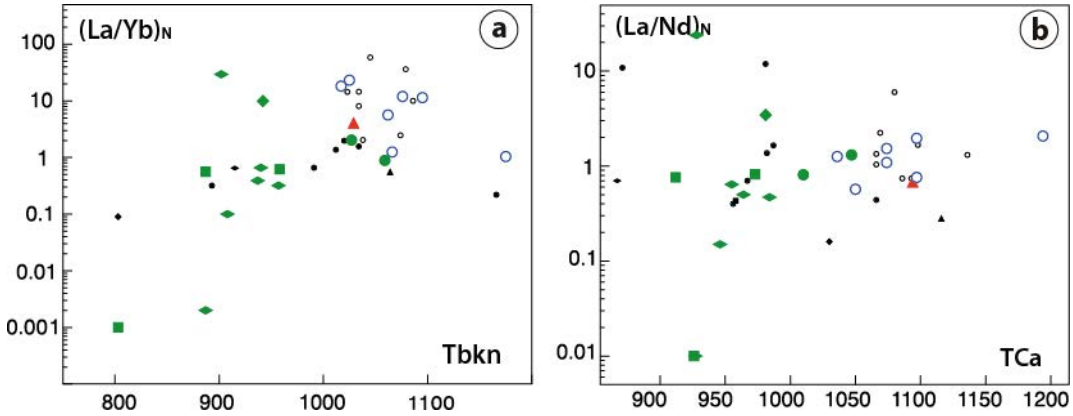

Fig.13.4. a) $(La/Yb)_N$ of clinopyroxene vs. T_{Bkn} and b) $(La/Nd)_N$ of clinopyroxene vs. T_{Ca}. Symbols as in figures 13.1-13.2

Tectonothermal event	Basic magmatic episode	Age	Mantle process	Model age (Lu-Hf)	Olivine CPO
ECRIS **Within plate volcanism**	Extrusion of mafic alkaline host lavas with mantle xenoliths	Neogene-Quaternary	Mantle melting- Melt-rock interaction at low melt/rock ratio in the SCLM overgrowth microstructures, gabbronorite microband		Orthorhombic or [100] fiber ⇧ Transtension (porphyroclastic-equigranular lherzolites)
Alpine orogenesis		Upper Mesozoic-Current Cenozoic			[010]-fiber (?) ⇧ Transpression?
Rifting episode	Alkaline lamprophyres	Upper Cretaceous	Mantle melting- Melt-rock interaction at low melt/rock ratio in the SCLM: formation of olivine websterites, modal and cryptic metasomatism in peridotites		[010]-fiber ⇧ Annealing-grain growth (protogranular peridotites-websterites)
Rifting episode	Calc-alkaline lamprophyres	Upper Permian	Mantle melting- Melt-rock interaction? in the SCLM		[010]-fiber ⇧ Annealing-grain growth (protogranular peridotites)
Variscan orogenesis	Late Variscan mafic-intermediate rocks (calc-alkaline magmatism)	Upper Devonian-Middle Permian	Mantle melting- Melt-rock interaction at high melt/rock ratio (?) in the SCLM Subduction or collision-related metasomatism (?)		[010]-fiber ⇧ Transpression (protogranular peridotites)
Rifting episode	Bimodal series (within-plate tholeiitic amphibolites)	Cambro-Ordovician	Mantle melting Melt-rock interaction at high melt/rock ratio (?) in the SCLM		(?)
Cadomian orogeny?		Upper Proterozoic-Lower Cambrian	Mantle melting Melt-rock interaction at high melt/rock ratio (?) in the SCLM	1.0-0.6Ga	Lherzolites-harzburgites
Subduction episode?		Middle-Lower Proterozoic	Subduction related metasomatism (?)- Mantle melting (?)		Harzburgites?

Fig. 13.5. Possible sequential event in the evolution of the SCLM of NE Iberia

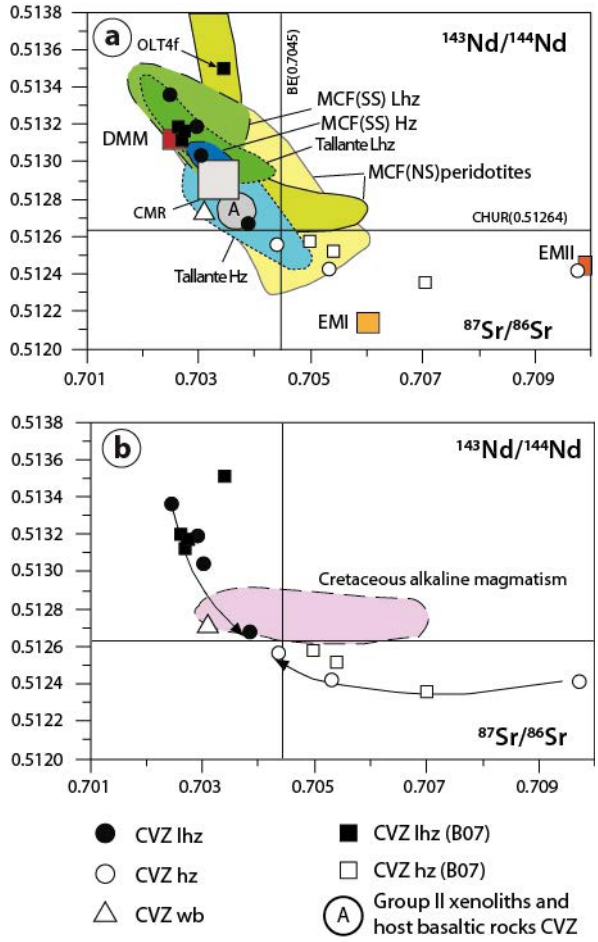

Fig.13.6. a) $^{143}Nd/^{144}Nd$ vs. $^{87}Sr/^{86}Sr$ of lherzolite (Lhz), harzburgite (Hz) and olivine websterite (Wb) clinopyroxene from CVZ after Galan & Oliveras (2014) modified. Other data sources: B07- Bianchini et al. (2007); Tallante (Ta) anhydrous lherzolite and harzburgite- Beccaluva et al. (2004); undifferentiated lherzolite and harzburgite clinopyroxene from the northern suite (NS) of Massif Central, France (MCF)- Downes et al. (2003); lherzolite and harzburgite clinopyroxene from the southern suite (SS) of MCF- Zangana et al. (1997); MCF undifferentiated lherzolite and harzburgite clinopyroxene- Downes & Dupuy (1987); A- group II xenoliths from the Roca Negra volcano (Neumann et al., 1999) matching the host basaltic rocks of the CVZ (Cebriá et al., 2000); squares with diagonal pattern- references for average normal DMM (Workman and Hart, 2007), EMI (Lustrino & Dallai, 2003) and EMII (Workman et al., 2004); CHUR-Hamilton et al. (1983); Bulk Earth (BE)- De Paolo & Wasserburg (1976); grey rectangle- Continental Mantle Reservoir (CMR) (Lustrino & Wilson, 2007). b) $^{143}Nd/^{144}Nd$ vs $^{87}Sr/^{86}Sr$ diagram for clinopyroxene of the CVZ xenoliths and compositional area for the likely Upper Cretaceos metasomatic component. Data sources for Cretaceous alkaline magmatism from the Pyrenees (Rossy et al., 1992) and for the Catalan Coastal ranges (Ubide, 2013) .The opposite arrows indicate the trends of lherzolites and harzburgites caused by a metasomatic agent, with isotopic compositions similar to that of websterites.

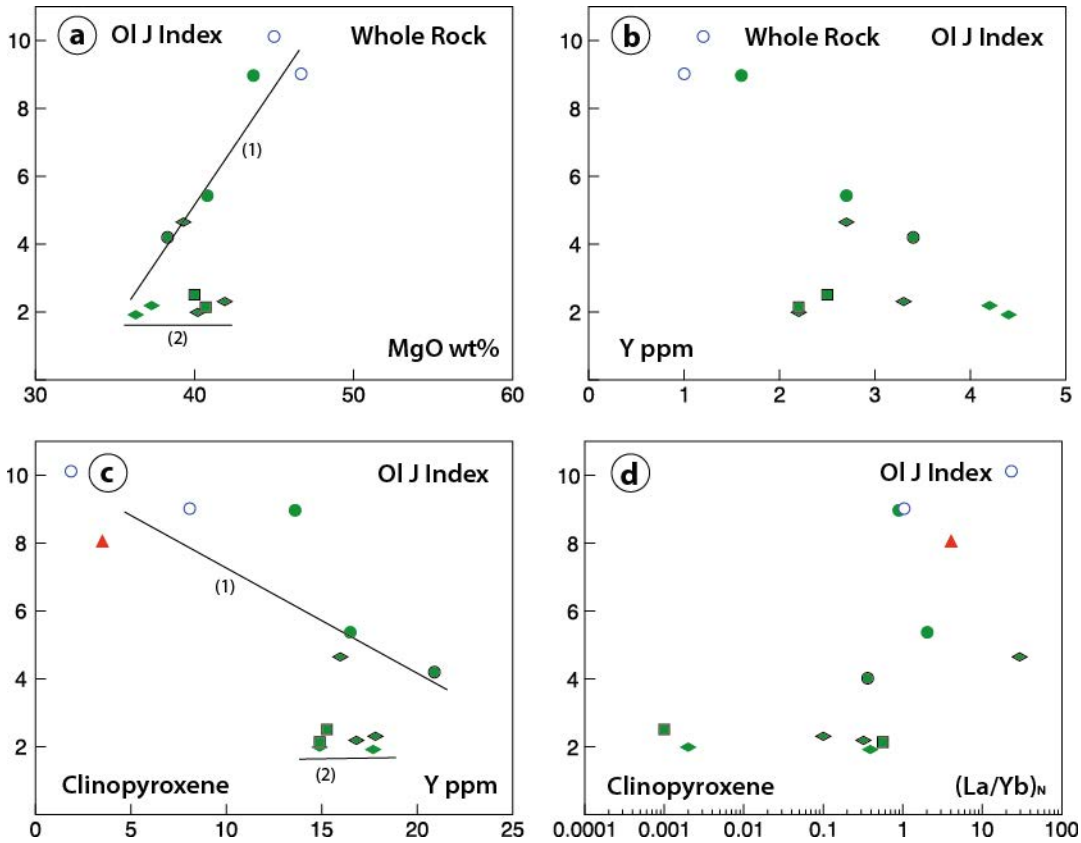

Fig. 13.7. Olivine J index vs. a) whole-rock MgO abundance, b) whole-rock Y abundance, c) clinopyroxene Y abundance and d) clinopyroxene $(La/Yb)_N$ ratio for peridotite and websterite clinopyroxene of this study. Symbols with incoherent olivine and pyroxenes fabrics are surrounded with a black line. (1) Trend defined by protogranular harzburgites and lherzolites with olivine [010]-fiber fabric. (2) Trend defined by porphyroclastic and equigranular lherzolites with olivine orthorhombic and [100]-fiber fabric.

Rock Type	Fo% Ol	Mg# Opx	Cr# Opx	Mg# Cpx	Cr# Cpx	Mg# Sp	Cr# Spl
Protogranular Websterites	90.6- 91.7	90.7- 90.9	16.8- 19.3	91.8- 92.5	21.8- 25.6	-	-
Protogranular Harzburgites	90.4- 91.7	91.1- 92.2	13.2- 19.2	90.7- 93.1	17.7- 26.4	65.3- 71.1	39.5- 54.9
Protogranular Lherzolites	89.1- 91.0	90.3- 91.2	5.2- 10.0	90.7- 91.3	6.9- 12.9	73.8- 79.2	9.6- 23.7
Transitional Lherzolites	89.5- 89.7	89.8- 89.9	4.6- 5.8	89.1- 89.7	6.7- 7.9	75.1- 81.0	9.7- 12.3
Porphyroclastic Lherzolites	89.0- 90.2	89.5- 90.6	5.0- 6.7	89.5- 91.7	7.1- 9.1	73.5- 77.3	9.7- 14.7
Equigranular Lherzolites	89.1- 90.2	89.7- 90.5	4.7- 6.9	89.4- 91.8	7.1- 10.0	74.1- 81.2	10.5- 12.4

Table 13.1 Compositional ranges of forsterite (Fo%) in olivine (Ol), Mg# and Cr# of orthopyroxene (Opx), clinopyroxene (Cpx) and spinel (Spl) in the different types of peridotites and the websterite.

Sample	Rock type and microsructure	F (K_D=0.33) Batch melting	F (K_D=0.33) Fractional melting
BB.08.20	Pg Hz	22.5	21.9
BB.08.52	Pg Hz	27.6	26.8
CA.12.02	Pg Hz	27.3	26.4
BB.12.02	Pg Hz	29.2	28.4
BB.12.03	Pg Hz	26.2	25.5
BB.12.09	Pg Hz	19.5	19.2
BB.12.04	Pg Hz	24.4	23.9
BB.08.101	Pg Lhz	20.8	20.1
BB.12.01	Pg Lhz	5.1	5.3
BB.08.18	PgPc Lhz	-2.7	-2.6
BB.08.80	Pc Lhz	12.9	12.6
BB.08.97	Pc Lhz	6.8	6.6
CA.12.03	Pc Lhz	6.2	6.0
SC.11.16	Pc Lhz	7.9	7.7
SC.11.52	Pc Lhz	-12.3	-11.4
SC.11.49	Pc Lhz	-2.6	-2.4
BB.08.54	Eg Lhz	9.1	8.8
BB.08.57	Eg Lhz	9.3	8.9
BB.08.38	Eg Lhz	11.2	10.8

Table 13.2. Degree of melting of the CVZ peridotites estimated after Takazawa et al. (2000).

	Niu (1997)	Herzberg (2004)	Johnson et al. (1990)	Norman (1998)	Takazawa et al. (2000)
FM F (%) Lhz	5 < F < 20	5 < F < 20	F < 18	F < 10	5 < F < 20
FM F (%) Hz	F ≈ 30	20 < F < 35	20 < F < 30	10 < F < 36	19 < F < 28

Table 13.3. Estimates for the degree of fractional melting from the PM using different inverse methods

CHAPTER 14

CONCLUSIONS

1) The new sampling confirmed that the subcontinental lithospheric mantle in NE Iberia is mainly formed of "anhydrous" spinel lherzolites (ca. 56%) and harzburgites (ca. 40%), with minor presence of olivine websterite (ca. 4%). Amphibole is an accessory mineral in sporadic lherzolites. Accessory phlogopite was only found in olivine websterite. Base metal sulphides are other accessory phases, especially in lherzolites.

2) Harzburgites, most lherzolites and websterites show protogranular microstructures, but there are also lherzolites with finer-grained porphyroclastic (ca. 15%) and equigranular microstructures (ca. 10%). Porphyroclastic lherzolites dominate among the xenoliths from the Sant Corneli volcano (La Selva), whereas lherzolites from La Garrotxa volcanoes show all microstructures. Overgrowth microstructures, such as clinopyroxene spongy rims and coronae surrounded spinel and amphibole, were also found in a few lherzolites. These are not preferentially developed at the contact with the host lava as the pyrometamorphic microstructures are (e.g., crosscutting microveins and coronae surrounded orthopyroxene). Overgrowth microstructures post-dated the formation of porphyroclast and neocrystals.

3) Compositions of main silicates and spinel reflect an overall gradual variation from lherzolites to harzburgites as in previous studies, but lherzolites display scattered Compositions of minerals in the olivine websterites are very similar to those in harzburgites. This is in contrast with data from previously studied pyroxenites, which are more differentiated, suggesting the existence of different types of pyroxenites. No relationships were found between differentiation indexes of minerals (e.g., Mg#, Cr#) and microstructure types in lherzolites. However, spinel shows different evolutionary trend and clinopyroxene has lower jadeite component in porphyroclastic and equigranular lherzolites respect to protogranular lherzolites. In most cases, no compositional differences were found for porphyroclasts and neocrystals of a same mineral in lherzolites. Exceptions are the compositions of phases in overgrowth microstructures (viz., clinopyroxene spongy rims, coronae surrounded spinel and amphibole) and in rare gabbronorite microbands. In these

coronae and microbands, plagioclase co-exists with spinel that show Cr-richer compositions than in the main lherzolite spinel. Clinopyroxene in these overgrowth microstructures shows heterogeneous compositions, but usually with lower jadeite component than in the main clinopyroxene. That is to say, deformation causing finer-grained porphyroclastic and equigranular lherzolites and development of overgrowth microstructures took place during mantle upwelling.

4) Four types of base metal sulphides were found according to textural relationships with silicates and spinel, but all types show similar compositions. Sulphide mineral associations are the breakdown products of high temperature (1000-900 °C) monosulphide solid solutions and Cu intermediate solid solution at falling temperature (T< 600 °C).

5) Estimates with the two-pyroxene thermometer indicate higher equilibrium T for protogranular harzburgites (T_{Bkn}: 1072 ±49°C), lherzolites (T_{Bkn}: 1063 ±28°C) and websterites (T_{Bkn}: 1048 ±28°C) than for porphyroclastic (T_{Bkn}: 918±27 °C) and equigranular lherzolites (T_{Bkn}: 913± 73 °C). Therefore, the deformation episode that affected porphyroclastic and equigranular lherzolites not only took place at falling P but also at decreasing T. Subsolidus evolution of this SCLM, according to thermobarometric estimates, took place at fO_2 between +0.6 and -1.8, expressed as Δlog units respect to the QFM buffer. No significant difference was found for fO_2 of harzburgites and lherzolites or between different microstructural types of lherzolites. However, the lowest fO_2 values were provided by lherzolites with reaction coronae surrounded spinel.

6) Harzburgites, the websterite and most lherzolites have olivine AG-type or [010]-fiber deformation fabric. The remaining lherzolites show A-type or orthorhombic fabric, except in one case, which shows D-type or [100]-fiber fabric. Transitions between all types are observed. There are overall positive correlations of olivine mode and equilibrium T with respect to the fabric strength: the J index decreases from protogranular harzburgites, clinopyroxene-poor lherzolites and websterite towards porphyroclastic and equigranular lherzolites equilibrated at lower T and P. In most xenoliths, orthopyroxene and clinopyroxene CPO are coherent with olivine AG- type deformation fabric~~s~~. Incoherence between olivine and pyroxene CPO is more frequent in porphyroclastic and equigranular lherzolites with AG-, A- and D-type deformation fabrics. Olivine AG-type fabric is related to deformation by simple shear or transpression, probably associated with late-Hercynian strike-slip shear zones, and to subsequent annealing during late Hercynian decompression, Permian and Cretaceous rifting episodes. Transformation of AG-type fabric into A- and D-

types was due to changes in the deformation regime, from simple shear or transpression to mainly transtension, during late Alpine extensional movements that led to the formation of Neogene basins.

7) Calculated seismic properties indicate that Vp distribution displays a well-defined maximum aligned with the maximum of olivine [100] axis. In most xenoliths, maximum values of AVs are also within the "foliation" plane and the direction of S1 polarization planes tends to be aligned with the olivine [100] axis. Refractory harzburgites, less fertile lherzolites and the websterite show higher anisotropy than the recrystallized porphyroclastic and equigranular lherzolites.

8) Comparison with available SKS-wave splitting suggests that most of the measured seismic anisotropy would be explained by the lithospheric contribution, if the SCLM fabrics record mainly transpression and transtensional deformation.

9) Whole-rock geochemistry indicates gradual depletion of basaltic components, and mildly incompatible trace elements from lherzolites to harzburgites and no relationship between composition and microstructural types of lherzolites. These evolutionary trends in co-variation diagrams could be interpreted as due to either melt depletion, in one or several stages, or a dichotomy in processes, that is to say both melt depletion and/or stealth metasomatism determined the composition of the SCLM. Lower olivine mode and higher orthopyroxene mode with respect to melt depletion trends modelled from a Primitive Mantle are more in favour of the dichotomy in processes. Stealth metasomatism or refertilization processes, via percolation of basaltic melts at high melt/rock ratio, could occur at more than one stage. The percolating melts were most likely tholeiitic-basalt type either slightly LREE depleted or enriched.

10) Melt depletion estimates from different models indicate that lherzolites and harzburgites could be formed by fractional melting from a Primitive Mantle. The degree of melting estimated ranges from 5 to 20% for lherzolites and from 20 to 35% for harzburgites. However, melt depletion history was most likely different for both peridotites: harzburgites could result from earlier mantle melting and metasomatism episodes, in a suprasubduction or collision zone, whereas these episodes are not registered by lherzolites.

11) Melt depletion took place in the spinel lherzolite field, but extreme LREE-MREE depleted patterns in two lherzolite clinopyroxene and an "u" shaped REE pattern in one harzburgite clinopyroxene reflect garnet signature at an earlier melting stage.

12) Other melt(fluids)-rock interaction, but at lower melt fraction, caused formation of accessory amphibole (modal metasomatism) in a few lherzolites and cryptic metasomatism in all harzburgites and some lherzolites. This cryptic metasomatism is responsible for clinopyroxene enrichment in the most incompatible elements (LREE, MREE, Th-U, Nb, Sr, Zr). Both types of metasomatism were caused by alkaline silicate melts, in a within-plate setting. The most likely metasomatic agent was Upper Cretaceous alkaline magmas that crop out nearby as camptonite dykes. During their channeled and diffuse percolation through the lithospheric mantle, these alkaline melts evolved by chromatographic fractionation-reaction at decreasing melt mass, which led to the formation of carbonatitic derivatives. Only two harzburgite clinopyroxene show evidence of carbonatitic metasomatism.

13) The olivine websterites are interpreted as products of crystal fractionation and interaction with mantle wall-rocks, at short distance from the channels through which the previous alkaline metasomatic agent percolated.

14) Post-Variscan metasomatism enhanced annealing, grain growth and the preservation and strength of earlier transpressional olivine [010]-fiber deformation fabric: this fabric strength increases towards the most refractory and metasomatized harzburgites. In contrast, lower strength of later olivine orthorhombic and [100]-fiber deformation fabrics and the absence of correlation between their olivine J index and compositional parameters, suggest that most significant petrogenetic mantle processes were pre-kinematic with respect to shear zones related to Late Alpine extension.

15) Only clinopyroxene spongy rims and coronae surrounded amphibole and spinel were post-kinematic with respect to the Late Alpine deformation episode. These microstructures are interpreted as due to melt (fluid)-rock interaction at low melt fraction during mantle decompression, shortly before the xenoliths were transported by the host lava.

16) Mantle xenoliths from NE Iberia compare well with mantle xenoliths and peridotitic massifs from neighbouring domains but some differences stand out:

i) Annealing in lherzolites and harzburgites from the Lherz massif, in the Pyrenees, are not as widespread as in the studied xenoliths; moreover, lherzolites and harzburgites from Lherz do not show the same olivine deformation fabric: [100]-fiber is characteristic of harzburgites, whereas lherzolites show both [010]-fiber and [100]-fiber types;

(ii) In the Calatrava volcanic field in Central Iberia, harzburgites are not as common as in the Catalan Volcanic Zone; in addition, amphibole is more frequent in Calatrava xenoliths with compositions characteristic of subduction-related metasomatism, whereas in NE Iberia, amphibole compositions are more characteristic of whithin-plate mantle metasomatism; olivine deformation fabrics in Calatrava are also different and characteristic of deformation conditions in suprasubduction settings;

(iii) Tallante xenoliths include clinopyroxene rich lherzolites often containing plagioclase, amphibole-phlogopite bearing harzburgites, orthopyroxenites and composite xenoliths, which are rarely or never found among those from the CVZ; the main olivine deformation fabric is [100]-fiber, which is rare in xenoliths from the CVZ. Deformation episodes and the main metasomatic processes in the SCLM from SE Iberia would be related to Tertiary subduction and late Neogene-Quaternary extension, whereas in NE Iberia these processes would be older.

REFERÈNCIES

Abramson, E.H., Brown, J.M., Slutsky, L.J., Zaug, J., 1997. The elastic constants of San Carlos olivine to 17 GPa, Geophysical Research,102, 12253– 12263.

Ackerman, L., Mahlen, N., Jelínek, E., Medaris Jr., G., Ulrych, J., Strnad, L., Mihaljevic, M., 2007. Geochemical and evolutionn of subcontinental lithospheric mantle in Central Europe: evidence from peridotite xenoliths of the Kozákov Volcano, Czech Republic. Journal of Petrology, 48, 2235–2260.

Ackerman, L., Spacek, P., Medaris Jr, G., Hegner, E., Svojtka, M., Ulrych, J., 2012. Geochemistry and petrology of pyroxenite xenoliths from Cenozoic alkaline basalts, Bohemian Massif. Journal of Geosciences, 57(4), 199-219.

Ackerman, L., Medaris Jr, G. L., Špaček, P., Ulrych, J., 2015. Geochemical and petrological constraints on mantle composition of the Ohře(Eger) rift, Bohemian Massif: peridotite xenoliths from the České Středohoří Volcanic complex and northern Bohemia. International Journal of Earth Sciences, 104(8), 1957-1979.

Ackerman, L., Bizimis, M., Haluzová, E., Sláma, J., Svojtka, M., Hirajima, T., Erban, V., 2016. Re–Os and Lu–Hf isotopic constraints on the formation and age of mantle pyroxenites from the Bohemian Massif. Lithos, 256, 197-210.

Alard, O., Griffin, W.L., Lorand, J.P., Jackson, S.E., O'Reilly, S.Y., 2000. Non- chondritic distribution of the highly siderophile elements in mantle sulphides. Nature, 407, 891–894.

Alard, O., Lorand, J.P., Reisberg, L., Bodinier, J.L., Dautria, J.M., O'Reilly, S.Y., 2011. Volatile-rich metasomatism in Montferrier xenoliths (Southern France): implications for the abundances of calcophile and highly siderophile elements in the subcontinental mantle. Journal of Petrololgy, 52, 2009–2045

Allègre, C.J., Turcotte, D.L., 1986. Implications of a two-component marble-cake mantle. Nature, 323, 123-127.

Amelinckx, S., Dekeyser, W., 1959. The structure and properties of grain boundaries. Solid State Physics, 8, 325–499.

Ancochea, E., 2004. El vulcanismo neógeno peninsular. In: Vera, J.A. (Ed.), Geología De España. SGE-IGME. Madrid. 671–672.

Aoki, K.I., Shiba, I., 1973. Pyroxenes from lherzolite inclusions of Itinomegata, Japan. Lithos, 6(1), 41-51.

Arai, S., 1994. Characterization of spinel peridotites by olivine-spinel compositional relationships: review and interpretation. Chemical Geology, 113, 191–204.

Araña, V., Aparicio, A., Martín Escorza, C., Garcia Cacho, L., Ortiz, R., Vaquer, R., Barberi, F., Ferrara, G., Albert, J., Gassiot, X., 1983. El volcanismo neógeno- cuaternario de Cataluña: caracteres estructurales, petrológicos y geodinámicos. Acta Geológica Hispánica, 18, 1–17.

Asch, K., 2005. IGME 5000: 1:5 Million International Geological Map of Europe and Adjacent Areas - final version for the internet.- BGR, Hannover.

Aulbach, S., Griffin, W.L., Pearson, N.J., O'Reilly, S.Y., Kivi, K., Doyle, B.J., 2004. Mantle formation and evolution, Slave Craton: constraints from HFE abundances and RE–Os isotope systematics of sulphide inclusions in mantle xenocrysts. Chemical Geology, 208, 61–88.

Ave Lallemant, H.G., 1967. Structural and petrofabric analysis of an "alpine- Type" peridotite. The lherzolite of the French Pyrenees. Leidsche Geologische Mededlingen, 42, 1-57.

Ayala, C., Torne, M., Pous, J., 2003. The lithosphere–asthenosphere boundary in the western Mediterranean from 3D joint gravity and geoid modelling: tectonic implications. Earth and Planetary Sciences Letters, 209, 275–290.

Azambre, B., Fabriès, J., 1989. Mesozoic evolution of the upper mantle beneath the eastern Pyrenees: evidence from xenoliths in Triassic and Cretaceous alkaline volcanics of the eastern Corbières (France). Tectonophysics, 170 (3–4), 213–230.

Ballhaus, C., Berry, R.F., Green, D.H., 1991. High pressure experimental calibration of olivine-orthopyroxene-spinel oxygen geobarometer: implications for the oxidation state of the upper mantle. Contributions to Mineralogy and Petrology, 107, 27–40

Bali, E., Szabó, Cs., Vaselli, O., Török, K., 2002. Significance of silicate melt pockets in upper mantle xenoliths from the Bakony–Balaton Highland Volcanic Field, Western Hungary. Lithos, 61, 79–102

Ballhaus, C., Berry, R. F., Green, D. H., 1990. Oxygen Fugacity Controls in the Earth's Upper Mantle. Nature; 348, 437-440.

Ban, M., Witt-Eickschen, G., Klein M., Seck H. A., 2005. The origin of glasses in hydrous mantle xenoliths from the West Eifel, Germany: incongruent break down of amphibole. Contributions to Mineralogy and Petrology, 148, 511–523.

Baptiste, V., Tommasi, A., Demouchy, S., 2012. Deformation and hydration of the lithospheric mantle beneath the Kaapvaal Craton, South Africa. Lithos, 149, 31–50.

Barnes, S.J., Roeder, P.L., 2001. The range of spinel compositions in terrestrial mafic and ultramafic rocks. Journal of Petrology, 42, 2279–2302.

Barnolas, A., Teixell, A., Duran, H. Escuer, J., 1994. Mapa Geológico de España (Mapa). Escala 1:50000. Banyoles, 295. Madrid.

Barruol, G., Mainprice, D., 1993. A quantitative evaluation of the contribution of crustal rocks to the shear wave splitting of teleseismic sks waves. Physics of the Earth and Planetary Interiors, 78, 281–300.

Barruol, G., Souriau, A., Vauchez, A., Diaz, J., Gallart, J., Tubia, J., Cuevas, J., 1998. Lithospheric anisotropy beneath the Pyrenees from shear wave splitting. Journal of Geophysical Research, 103, 30039–30054.

Barruol, G., Deschamps, A., Coutant, O., 2004. Mapping upper mantle anisotropy beneath SE France by sks splitting indicates Neogene asthenospheric flow induced by apenninic slab roll-back and deflected by the deep alpine roots. Tectonophysics 394, 125–138.

Bascou, J., Tommasi, A., Mainprice, D., 2002. Plastic deformation and development of clinopyroxene lattice preferred orientations in eclogites. Journal of Structural Geology, 24, 1357–1368.

Bascou, J., Delpech, G., Vauchez, A., Moine, B.N., Cottin, J.Y., Barruol, G., 2008. An integrated study of microstructural, geochemical, and seismic properties of the lithospheric mantle above the Kerguelen Plume (Indian Ocean). Geochemistry, Geophysics, Geosystems. 9, Q04036.

Bascou, J., Doucet, L.S., Saumet, S., Ionov, D.A., Ashchepkov, I.V., Golovin, A.V., 2011. Seismic velocities, anisotropy and deformation in Siberian Cratonic Mantle: EBSD data on xenoliths from the Udachnaya Kimberlite. Earth and Planetary Sciences Letters, 304, 71–84.

Beccaluva, L., Bonadiman, C., Coltorti, M., Salvini, L., Siena, F., 2001a. Depletion events, nature of metasomatizing agent and timing of enrichment processes in lithospheric mantle xenoliths from the Veneto volcanic province. Journal of Petrology, 42 (1), 173–187.

Beccaluva, L., Bianchini, G., Coltorti, M., Perkins, W.T., Siena, F., Vaccaro, C., Wilson, M., 2001b. Multistage evolution of the European lithospheric mantle: new evidence from sardinian peridotite xenoliths. Contributions to Mineralogy and Petrology, 142, 284–297.

Beccaluva, L., Bianchini, G., Bonadiman, C., Siena, F., Vaccaro, C., 2004. Coexisting anorogenic and subduction-related metasomatism in mantle xenoliths from the Betic Cordillera (southern Spain). Lithos, 75, 67–68.

Bedini, R.M., Bodinier, J.L., 1999. Distribution of incompatible trace elements between the constituents of spinel peridotite xenoliths: ICP-MS data from the East African Rift. Geochimica et Cosmochimica Acta, 63(22), 3883-3900.

Ben Ismaïl, W., Mainprice, D., 1998. An olivine fabric database: an overview of upper mantle fabrics and seismic anisotropy. Tectonophysics, 296, 145–157.

Beyer, E.E., Griffin, W.L., O'Reilly, S.Y., 2006. Transformation of Archean lithospheric mantle by refertilization; evidence from exposed peridotites in the Western Gneiss region, Norway. Journal of Petrology, 47, 1611-1636

Bianchini, G., Beccaluva, L., Bonadiman, C., Nowell, G., Pearson, G., Siena, F., Wilson, M., 2007. Evidence of diverse depletion and metasomatic events in harzburgite– lherzolite mantle xenoliths from the Iberian Plate (Olot, NE Spain): implications for lithosphere accretionary processes. Lithos, 94, 25–45.

Bianchini, G., Beccaluva, L., Bonadiman, C., Nowell, G.M., Pearson, D.G., Siena, F., Wilson, M., 2010. Mantle metasomatism by melts of HIMU piclogite components: new in- sights from Fe-lherzolite xenoliths (Calatrava Volcanic District, central Spain). In: Coltorti, M., Downes, H., Grégoire, M., O'Reilly, S. (Eds.), Petrological Evolution of the European Lithospheric Mantle. Geological Society, London, Special Publications 337, 107–124.

Bianchini, G., Beccaluva, L., Nowell, G.M., Pearson, G., Siena, F., 2011. Mantle xenoliths from Tallante (Betic Cordillera): insights into the multi-stage evolution of the South Iberian Lithosphere. Lithos 124, 308–318.

Bodinier, J.L., Godard, M., 2003. Orogenic, ophiolitic, and abyssal peridotites. In: Carlson, R.W., (Ed.). The mantle and core. Treatise on geochemistry, 2. Elsevier, Oxford, United Kingdom. 103-170.

Bodinier, J.L., Dupuy, C., Dostal, J., 1988. Geochemistry and petrogenesis of eastern pyrenean peridotites. Geochimica et Cosmochimica Acta, 52(12), 2893-2907.

Bodinier, J.L., 1989. Distribution des terres rares dans les massifs lherzolitiques de Lanzo et de l'Ariège. Montpellier: Centre Géologique et Géophysique de Montpellier, Université des Sciences et Techniques du Languedoc, 177 pp.

Bodinier, J.L., Merlet, C., Bedini, R.M., Simien, F., Remaidi, M., Garrido, C.J., 1996. Distribution of niobium, tantalum, and other highly incompatible trace elements in the lithospheric mantle: the spinel paradox. Geochimica et Cosmochimica Acta, 60, 545–550.

Bodinier, J.L., Garrido, C.J., Chanefo, I., Bruguier, O., Gervilla, F., 2008. Origin of pyroxenite– peridotite veined mantle by refertilization reactions: evidence from the Ronda Peridotite (Southern Spain). Journal of Petrology, 49, 999–1025.

Bolós, X., Barde-Cabusson, S., Pedrazzi, D., Martí, J., Casas, A., Lovera, R., Nadal-Sala, D., 2015. Volcano structural-analysis of La Garrotxa volcanic Field (NE Iberia): implications for the plumbing system. Tectonophysics, 642, 58–70.

Borghini, J.L., Fumagalli, G.P., Rampone, E., 2010. The stability of plagioclase in the upper mantle: Subsolidus experiments on fertile and depleted lherzolite. Journal of Petrology, 51(1–2), 229–254.

Borghini, J.L., Fumagalli, G.P., Rampone, E., 2011. The geobarometric significance of plagioclase in mantle peridotites: A link between nature and experiments, Lithos, 126(1–2), 42–53.

Bonadiman, C., Coltorti, M., Duggen, S., Paludetti, L., Siena, F., Thirwall, M.F., Upton, B.J., 2008. Palaeozoic subduction-related and kimberlite or carbonatite metasomatism in the Scottish lithospheric mantle. Geological Society, London, Special Publication, 293(1), 303-333.

Boyd, F.R., 1989. Composition and distinction between oceanic and cratonic lithosphere. Earth nd Planetary Science Letters, 96, 15–26.

Brey, G.P., Köhler, T., 1990. Geothermobarometry in four-phase lherzolites II. New thermobarometers, and practical assessment of existing thermobarometers. Journal of Petrology, 31, 1353–1378.

Brown, G.M., Pinsent, R.H., Coisy, P., 1980. The petrology of spinel-peridotite xenoliths from the Massif Central, France (in The Jackson volume). American Journal of Science, 280-A, 471-498.

Bunge, H.J., 1982. Texture Analysis in Materials Sciences. Buttleworth, London (593 pp.).

Burnham, O.M., Rogers, N.W., Pearson, D.G., Van Calsteren, P.W., Hawkesworth, C.J., 1998. The petrogenesis of eastern Pyrenean peridotites; an integrated study of their whole-rock geochemistry and Re-Os isotope composition. Geochimica et Cosmochimica Acta, 62, 2293-2310.

Butjosa, L., Enrique, P., Galán, G., 2013. Las hornblenditas, gabros y dioritas del macizo del Montnegre (Barcelona, Cordilleras Costero Catalanas). Geogaceta, 54, 35–38.

Bystricky, M., Kunze, K., Burlini, L., Burg, J.P., 2000. High shear strain of olivine aggregates: Rheological and seismic consequences. Science, 290(5496), 1564-1567.

Cabri, L.J., 1973. New data on phase relations in the Cu-Fe-S system. Economic Geology, 68, 443–444.

Canil, D., 2004. Mildly incompatible elements in peridotites and the origins of mantle lithosphere. Lithos, 77, 375–393.

Carpenter, R.L., Edgar, A.D., Thibault, Y., 2002. Origin of spongy textures in clinopyroxene and spinel from mantle xenoiths, hessian depression, Germany. Mineralogy and Petrology, 74, 149–162.

Carreras, J., Capella, I., 1994. Tectonic levels in the palaeozoic basement of the Pyrenees: a review and a new interpretation. Journal of Structural Geology, 16, 1509–1524.

Carreras, J., Druguet, E., 2014. Framing the tectonic regime of the NE Iberian Variscan segment. Geological Society, London, Special Publications, 405, 249-264.

Carreras, J., 2001. Zooming on northern Cap de Creus shear zones. Journal of Structural Geology 23, 1457–1486.

Carter, N.L., Avé Lallemant, H.G., 1970. High temperature flow of dunite and peridotite. Geological Society of America Bulletin, 81, 2181–2202.

Carter, N.L,, Baker, D.W., George, R.P., 1972. Seismic Anisotropy, Flow, and Constitution of the Upper Mantle. Flow and Fracture of Rocks, V16. Geophysical Monograph series.

Cebriá, J.M., López-Ruiz, J., Doblas, M., Oyarzun, R., Hertogen, J., Benito, R., 2000. Geochemistry of the Quaternary alkali basalts of Garrotxa (NE Volcanic Province, Spain): a case of double enrichment of the mantle lithosphere. Journal of Volcanology and Geothermal Research, 102, 217–235.

Chai, M., Brown, J.M., Slutsky, L.J., 1997. The elastic constants of an aluminous orthopyroxene to 12.5 Gpa. Journal of Geophysical Research, 102, 14779–14786.

Coe, R.S., Kirby, S.H., 1975. The Orthoenstatite to Clinoenstatite Transformation by Shearing and Reversion by Annealing: Mechanism and Potential Application. Contributions to Mineralogy and Petrology, 52, 29-55.

Collins, M.D., Brown, J.M., 1998. Elasticity of an upper mantle clinopyroxene. Physics and Chemistry of Minerals, 26, 7–13.

Coltorti, M., Grégoire, M., 2008. Metasomatism in oceanic and continental lithospheric mantle: introduction. Geological Society, London, Special Publications, 293(1), 1-9.

Coltorti, M., Bonadiman, C., Hinton, R.W., Siena, F., Upton, B.G.J., 1999. Carbonatite metasomatism of the oceanic upper mantle: evidence from clinopyroxenes and glasses in ultramafic xenoliths of Grande Comore, Indian Ocean. Journal of Petrology, 40, 133–165.

Coltorti, M., Beccaluva, L., Bonadiman, C., Salvini, L., Siena, F., 2000. Glasses in mantle xenoliths as geochemical indicators of metasomatic agents. Earth and Planetary Science Letters, 183, 303–320.

Coltorti, M., Beccaluva, L., Bonadiman, C., Faccini, B., Ntaflos, T., Siena, F., 2004. Amphibole genesis via metasomatic reaction with clinopyroxene in mantle xenoliths from Victoria Land, Antarctica. Lithos, 75, 115-139.

Coltorti M., Bonadiman, C., Faccini, B., Ntaflos, T., Siena, F., 2007. Slab melt and intraplate metasomatism in Kapfenstein mantle xenoliths (Styrian Basin, Austria). Lithos 94, 66–89.

Craig, J.R., Kullerud, G., 1969. Phase relations in the Cu–Fe–Ni–S system and their applications to magmatic ore deposits. In: Wilson, H.D.B., (Ed.) Magmatic ore deposits. Economic Geology Monographs, 4, 343–358.

Craig, J.R., 1973. Pyrite–pentlandite assemblages in the Fe-Ni-S system. American Journal of Science, 273A, 496–510.

Cruz, E., Galán, G., Fernández–Roig, M., Oliveras, V., Martínez, F.J., 2014. Types of sulphides in mantle xenoliths from the Catalan Volcanic Zone (NE Spain). Macla, 19, 77–78

Cvetković, V., Downes, H., Prelević, D., Jovanović, M., Lazarov, M., 2004. Characteristics of the lithospheric mantle beneath East Serbia inferred from ultramafic xenoliths in Palaeogene basanites. Contributions to Mineralogy and Petrology, 148(3), 335-357.

Dañobeitia, J.J., Arguedas, M., Gallart, J., Banda, E., Makris, J., 1992. Deep crustal configuration of the Valencia Trough and its balearic borders from extensive refraction and wide-angle reflection seismic profiling. Tectonophysics, 203, 37–55.

Dawson, J.B., 1984. Contrasting types of upper-mantle metasomatism. Kimberlites II: The Mantle and Crust-Mantle Relationships, 289-294

De Kloe, R., 2001. Deformation Mechanisms and Melt Nano-Structures in Experimentally Deformed Olivine–Orthopyroxene rocks With Low Melt Fractions. An Electron Microscopy Study. (Ph.D. Thesis). Utrecht University (173 pp.).

DePaolo, D.J., Wasserburg, G.J., 1976. Inferences about magma sources and mantle structure from variations of ^{143}Nd/^{144}Nd. Geophysical Research Letters, 3, 743–746.

Deer, W.A., Howie, R.A., Zussman, J., 1992. An introduction to The Rock Forming Minerals. Prentice Hall, 696 pp.

Delpech, G,. 2004. Trace Element and Isotopic Fingerprints in Ultramafic Xenoliths From the Kerguelen Arcipelago (South Indian Ocean). (PhD thesis). Etienne Universities, Macquarie–St.

Delpech, G., Lorand, J.P., Grégoire, M., Cottin, J.Y., O'Reilly, S.Y., 2012. In-situ geochemistry of sulfides in highly metasomatized mantle xenoliths from Kerguelen, southern Indian Ocean. Lithos, 154, 296–314.

Demouchy, S., Schneider, S.E., Mackwell, S.J., Zimmerman, M.E., Kohlstedt, D.L. (2009). Experimental deformation of olivine single crystals at lithospheric temperatures. *Geophysical Research Letters*, *36*(4).

Dèzes, P., Schmid, S.M., Ziegler, P.A., 2004. Evolution of the European Cenozoic Rift System: interaction of the Alpine and Pyrenean orogens with their foreland lithosphere. Tectonophysics, 389, 1–33.

Díaz, J., Gallart, J., Morais, I., Silveira, G., Pedreira, D., Pulgar, J.A., Dias, N.A., Ruiz, M., González-Cortina, J.M., 2015. From the Bay of Biscay to the High Atlas: completing the anisotropic characterization of the upper mantle beneath the westernmost Mediterranean region. Tectonophysics, 663, 192–202.

Díaz, N., Gimeno, D., Losantos, M., Segura, C., 1996. Las traquitas de Arenys d'Empordá (Alt Empordà, NE de la Península Ibérica): características generales. Geogaceta, 20, 572-575.

Díaz, J., Gil, A., Gallart, J., 2013. Uppermost mantle seismic velocity and anisotropy in the Euro-Mediterranean region from Pn and Sn tomography. Geophysical Journal International, 192, 310–325.

Djikstra, A.H., Drury, M.R., Vissers, R.L.M., Newman, J., 2002. On the role of melt–rock reaction in mantle shear zone formation in the Othris peridotite massif (Greece). Journal of Structural Geololgy 24, 1431–1450.

Dijkstra, A.H., Barth, M.G., Drury, M.R., Mason, P.R.D., Vissers, R.L.M., 2003. Diffuse porous melt flow and melt–rock reaction in the lithospheric mantle at a slow-spreading ridge: a structural petrology and LA-ICP-MS study of the Othris Peridotite Massif (Greece). Geochemistry Geophysics Geosystems. 4, 8613.

Donville, B., 1973a. Ages potassium–argon des vulcanites du Haut Ampurdan (Nord–Est de l'Espagne). Implications stratigraphiques. Comptes Rendus de l'Académie des Sciences, Paris, 276, 2497–2500.

Donville, B., 1973b. Ages potassium–argon des vulcanites du Bas Ampurdan. Comptes Rendus de l'Académie des Sciences, Paris, 276, 3253–3256.

Donville, B., 1973c. Ages potassium–argon des roches volcaniques de la depresion de La Selva (NE de l'Espagne). Comptes Rendus de l'Académie des Sciences, Paris, 277, 1–4.

Dornbush, H.J., Weber, K., Skrotzki, W., 1994. Development of microstructure and texture in high-temperature mylonites from the Ivrea Zone. In: Burg, J.P., Siegesmund, D., Skrotzki, W., Weber, K. ,(Eds). Textures of Geological Materials. DGM Informationsgesellschaft, Oberursel. 187–201.

Downes, H., Coltorti, M., 2008. Mantle xenoliths in space and time in Europe. Geophysical Research Abstracts, Vol. 10, EGU2008-A-10330, 2008. SRef-ID: 1607-7962/gra/EGU2008-A-10330

Downes, H., Dupuy, C., 1987. Textural, isotopic and REE variations in spinel peridotite xenoliths, Massif Central, France. Earth and Planetary Science Letters, 82, 121–135.

Downes, H., Seghedi, I., Szakacs, A., Dobosi, G., James, D.E., Vaselli, O., Rigby, I.J., Ingram, G.A., Rex, D., Pecskay, Z., 1995. Petrology and geochemistry of late Tertiary/Quaternary mafic alkaline volcanism in Romania. Lithos 35, 65-82.

Downes, H., Kostoula, T., Jones, A.P., Beard, A.D., Thirlwall, M.F., Bodinier, J.L., 2002. Geochemistry and Sr–Nd isotopic compositions of mantle xenoliths from the Monte Vulture carbonatite–melilitite volcano, central southern Italy. Contributions to Mineralogy and Petrology, 144, 78–92.

Downes, H., Reichow, M.K., Mason, P.R.D., Beard, A.D., Thirlwall, M.F., 2003. Mantle domains in the lithosphere beneath the French Massif Central: trace element and isotopic evidence from mantle clinopyroxenes. Chemical Geology, 200, 71–87.

Downes, H., Dupuy, C., 1987. Textural, isotopic and REE variation in spinel peridotite xenoliths, Massif Central, France. Earth and Planetary Science Letters, 82, 121–135.

Downes, H., 2001. Formation and modification of the shallow sub-continental lithospheric mantle: a review of geochemical evidence from ultramafic xenolith suites and tectonically emplaced ultramafic massifs of Western and Central Europe. Journal of Petrology, 42, 233–250.

Dromgoole, E.L., Pasteris, J.D., 1987. Interpretation of the sulfide assemblages in a suite of xenoliths from Kilbourne Hole, New Mexico. Geological Society of America, Special Papers, 215, 25–45.

Droop, G.T.R., 1987. A general equation for estimating Fe (super 3+) concentrations in ferromagnesian silicates and oxides from microprobe analyses, using stoichiometric criteria. Mineralogical Magazine, 51, 431-435.

Eggler, D.H., Lorand, J.P., 1993. Mantle sulfide geobarometry. Geochimica et Cosmochimica Acta 57, 2213–2222.

Embey-Isztin, A., Scharbert, H.G., Dietrich, H., Poultidis, H., 1989. Petrology and geochemistry of peridotite xenoliths in alkali basalts from the Transdanubian volcanic region, western Hungary. Journal of Petrology, 30, 79-105

Enrique, P., 2009. Las espesartitas, camptonitas y bostonitas del complejo intrusivo de Aiguablava (Cadenas Costeras Catalanas): cartografía y composición. Geogaceta, 47, 125–128.

Esteve, S., Enrique, P., Galán, G., 2014. The camptonites in the multiple intrusion of Platja Fonda (Girona, NE Spain): mechanisms of intrusion and geochemistry. Journal of Geosciences, 59, 23–40.

Falus, G., Tommasi, A., Ingrin, J., Szabó, Cs., 2008. Deformation and seismic anisotropy of the lithospheric mantle in the Southeastern Carpathians: a mantle xenolith study. Earth and Planetary Science Letters, 272, 50–64.

Falus, G., Tommasi, A., Soustelle, V., 2011. Effect of dynamic recrystallization on olivine crystal preferred orientations in mantle xenoliths deformed under varied stress conditions. Journal of Structural Geology, 33, 1528–1540.

Falus, G., 2004. Microstructural analysis of upper mantle peridotites: their application in understanding mantle processes during the formation of the Intra-Carpathian Basin System (Ph.D. Thesis). Department of Petrology and Geochemistry, Eftvfs University, Budapest, 164 pp.

Femenias, O., Coussaert, N., Berger, J.. Mercier, J.C.C., Demaiffe, D., 2004. Metasomatism and melting history of a Variscan lithospheric mantle domain: evidence from the Puy Beaunit xenoliths (French Massif Central). Contributions to Mineralogy and Petrology, 148, 13-28.

Fernández-Navarro, L., 1907. Formaciones volcánicas de la provincia de Gerona. En Memorias de la Real Sociedad Española de Historia Natural, T. IV, Mem 5.

Fernández-Roig, M., Galán, G., 2015. Microestructuras y química mineral de lherzolitas en xenolitos mantélicos de Cataluña (NE España). Geogaceta, 57, 3–6.

Fernández-Roig, M., Galán, G., Mariani, E., 2017. Deformation and seismic anisotropy of the subcontinental lithospheric mantle in NE Spain: EBSD data on xenoliths from the Catalan Volcanic Zone. Tectonophysics, 698, 16-37.

Fialin, M., Wagner, C., 2015. Aluminum and iron behavior in glasses from destabilized spinels: A record of fluid/melt mineral interaction in mantle xenoliths from Massif Central, France. American Mineralogist, 100(7), 1411-1423.

Fleet, M.E., 2006. Phase equilibria at high temperatures. In: Vaughan, D.J., (Ed.) Sulphide mineralogy and geochemistry. Reviews in Mineralogy and Geochemistry, 61, 365–419.

Foley, S.F., Petibon, C.M., Jenner, G.A., Kjarsgaard, B.A., 2001. High U/Th partitioning by clinopyroxene from alkali silicate and carbonatite metasomatism: An origin for Th/U disequilibrium in mantle melts? Terra Nova, 13(2), 104-109.

Frank, F.C., 1950. Report on the Conference on Plastic Deformation of Crystalline Solids. Carnegie Institut of Technology and Office of Naval Research, Washington (150 pp).

Franz, L., Wirth, R,. 1997. Thin intergranular melt films and melt pockets in spinel peridotite xenoliths from the Rhön area (Germany): early stage of melt generation by grain boundary melting. Contributions to Mineralogy and Petrology, 129, 268–283.

Frey, F.A., Green, D.H., 1974. The mineralogy, geochemistry and origin of lherzolite inclusions in Victorian basanites. Geochimica et Cosmochimica Acta, 38, 1023–1059.

Frey, F.A., Prinz, M., 1978. Ultramafic inclusions from San Carlos, Arizona: petrologic and geochemical data bearing on their petrogenesis. Earth and Planetary Science Letters, 38, 129–176.

Frost, D.J., McCammon, C.A., 2008. The redox state of Earth's mantle. Review Earth Planetary Science, 36, 389–420.

Gaetani, G.A., Kent, A.J., Grove, T.L., Hutcheon, I.D., Stolper, E.M., 2003. Mineral/melt partitioning of trace elements during hydrous peridotite partial melting. Contributions to Mineralogy and Petrology, 145(4), 391-405.

Gagnon, J.E., Fryer, B.J., Samson, I.M., Williams-Jones, A.E., 2008. Quantitative analysis of silicate certified reference materials by LA-ICPMS with and without an internal standard. Journal of Analytical Atomic Spectrometry, 23, 1529–1537.

Galán, G., Fernández-Roig, M., 2016. Geoquímica de roca total y fábricas de deformación del olivino en xenolitos mantélicos del NE de España: claves para la evaluación de la petrogénesis y la deformación del manto litosférico. Geo-Temas, 16 (1), 411-414.

Galán, G., Oliveras, V., 2014. Melting and metasomatism in the lithospheric mantle of NE Spain: geochemical and Sr\Nd isotopic characteristics. Chemical Geology, 366, 75–89.

Galán, G., Oliveras, V., Paterson, B., 2006. Types of metasomatism in ultramafic xenoliths enclosed in Neogene Quaternary alkaline mafic lavas from Catalonia (NE Spain). Geophysical Research Abstracts, 8, abstract number 05961.

Galán, G., Oliveras, V., Paterson, B.A., 2008. Types of metasomatism in mantle xenoliths in Neogene–Quaternary alkaline mafic lavas from Catalonia (NE Spain). In: Coltorti, M., Grégoire, M. (Eds.). Metasomatism in Oceanic and Continental Lithospheric Mantle. Geological Society, London, Special Publication, 293, 121–153.

Galán, G., Oliveras, V., Paterson, B.A., 2011. Thermal and redox state of the subcontinental lithospheric mantle of NE Spain from thermobarometric data on mantle xenoliths. International Journal of Earth Science, 100, 81–106.

Galán, G., Cruz, E., Fernández-Roig, M., Martínez, F.J., Oliveras, V., 2016. Mineral associations and major element compositions of base metal sulphides from the subcontinental lithospheric mantle of NE Spain. Mineralogy and Petrology, 110(1), 87-101.

Galán, G., 2004. Partial melting and metasomatism in the subcontinental lithospheric mantle of NE Spain. Geochimica et Cosmochimica Acta, 68, A 723.

Gallart, J., Pous, J., Boix, F., Hirn, A., 1991. Physical constraints on the crustal structure of the Olot volcanic area, Northeastern Iberian Peninsula. Journal of Volcanology and Geothermal Research, 47, 33–44.

Gallart, J., Olivera, C., Correig, A.M., 1984. Aproximación geofísica a la zona volcánica de Olot (Girona). Estudio local de sismicidad. Revista de Geofisica, 40, 205–226.

Gao, S., Rudnick, R.L., Carlson, R.W., McDonough, W.F., Liu, Y.-S., 2002. Re\Os evidence for replacement of ancient mantle lithosphere beneath the North China Craton. Earth and Planetary Science Letters, 198, 307–322.

Garrido, C.J., Bodinier, J.L., Alard, O., 2000. Incompatible trace element partitioning and residence in anhydrous spinel peridotites and websterites from the Ronda orogenic peridotite. Earth and Planetary Science Letters, 181, 341–358.

Gasparik, T., 1987. Orthopyroxene thermometry in simple and complex systems. Contributions to Mineralogy and Petrology, 96, 357–370.

Gee, D.G., Stephenson, R.A., 2006. The European lithosphere: an introduction. In: Gee, D.G., Stephenson, R.A., (Eds.) European lithosphere dynamics. Geological Society. 1-9.

Gil-Peña, I., Barnolas, A., Villas, E., Sanz-López, J., 2004. El Ordovícico Superior de la Zona Axial. In: Vera, J.A., (Ed.) Geología de España. SGE-IGME, Madrid. 247–249.

Glahn, A., Sachs, P. M., Achauer, U,. 1992. A teleseismic and petrological study of the crust and upper mantle beneath the geothermal anomaly Urach/SW-Germany. Physics of the Earth and Planetary Interiors, 69(3-4), 176-206.

Godard, G., Van Roermund, H.L.M., 1995. Deformation-induced clinopyroxene fabrics from eclogites. Journal of Structural Geology, 17, 1425–1443.

Gong, Z., Langereis, C.G., Mullender, T.A.T., 2008. The rotation of Iberia during the Aptian and the opening of the Bay of Biscay. Earth and Planetary Science Letters, 273, 80–93.

González-Jiménez, J.M., Villaseca, C., Griffin, W.L., O'Reilly, S,Y., Belousova, E.,Ancochea, E., Pearson, N.J., 2014, Signifcance of ancient sulphide PGE and Re–Os signatures in the mantle beneath Calatrava, Central Spain. Contributiions to Mineralogy and Petrology, 168, 1047.

Green, T.H., 1995. Significance of Nb/Ta as an indicator of geochemical processes in the crust-mantle system. Chemical Geology, 120, 347-359.

Grégoire, M., Chevet, J., Maaloe, S., 2010. Composite xenoliths from spitsbergen: Evidence of the circulation of MORB-related melts within the upper mantle. Geological Society Special Publication, 337, pp. 71-86.

Griffin, W.L., O'Reilly, S.Y., Ryan, C.G., 1999. The compositions and origin of subcontinental lithospheric mantle. In: Frei, Y., Bertka, C.M., Mysen, B.O. (Eds.), Mantle Petrology: Field Observations and High-Pressure Experimentation: A Tribute to Francis R. (Joe) Boyd. Geochemical Society Special Publication, 6. The Geochemical Society, Houston, pp. 13–45.

Griffin, W.L., Graham, S., O'Reilly, S., Pearson, N.J., 2004. Lithosphere evolution beneath the Kaapvaal Craton: Re–Os systematics of sulfides in mantle-derived peridotites. Chemical Geology, 208, 89–118.

Griffin, W.L., O'Reilly, S.Y., Afonso, J.C., Begg, G.C., 2009. The composition and evolution of lithospheric mantle: a re-evaluation and its tectonic implications. Journal of Petrology, 50, 1185–1204.

Guzmics, T., Kodolányi, J., Kovács, I., Szabó, C., Bali, E., Ntaflos, T., 2008. Primary carbonatite melt inclusions in apatite and in K-feldspar of clinopyroxene-rich mantle xenoliths hosted in lamprophyre dikes (Hungary). Mineralogy and Petrology, 94(3-4), 225-242.

Guo, J., Griffin, W.L., O'Reilly, S.Y., 1999. Geochemistry and origin of sulphide minerals in mantle xenoliths: Qilin, southeastern China. Journal of Petrology, 40, 1125–1149.

Haggerty, S.E., 1995. Upper mantle mineralogy. Journal of Geodynamics, 20, 331-364.

Hamilton, P.J., O'Nions, R.K., Bridgwater, D., Nutman, A., 1983. Sm–Nd studies of Archean metasediments and metavolcanics from West Greenland and their implications for the Earth's early history. Earth and Planetary Science Letters, 62, 263–272.

Harte, B., 1977. Rock nomenclature with particular relation to deformation and recrystallisation textures in olivine-bearing xenoliths. Journal of Petrology, 85, 279–288.

Harvey, J.A., Gannoun, A., Burton, K.W., Schiano, P., Rogers, N.W., Alard, O., 2010. Unravelling the effects of melt depletion and secondary infiltration on mantle Re-Os isotopes beneath the French Massif Central. Geochimica et Cosmochimica Acta, 74,293–320.

Hattori, K.H., Arai, S., Clarke, D.B., 2002. Selenium, tellurium, arsenic and antimony contents of primary mantle sulfide. The Canadian Mineralogist, 40, 637–650.

Hawthorne, F.C., Oberti, R., 2007. Amphiboles: Crystal Chemistry. Reviews in Mineralogy and Geochemistry, 67(1), 1-54

Hellebrand, E., Snow, J.E., Dick, H.J., Hofmann, A.W., 2001. Coupled major and trace elements as indicators of the extent of melting in mid-ocean-ridge peridotites. Nature, 410, 677–681

Helmstaedt, H., Anderson, O.L., Gavasci, A.T., 1972. Petrofabric studies of eclogite, spinel- websterite, and spinel-lherzolite xenoliths from kimberlite-bearing breccia pipes in southeastern Utah and northeastern Arizona. Journal of Geophysical Research, 77(23), 4350-4365.

Henry, P., Azambre, B., Montigny, R., Rossy, M., Stevenson, R.K., 1998. Late mantle evolution of the Pyrenean sub-continental lithospheric mantle in the light of new 40Ar–39Ar and Sm–Nd ages on pyroxenites and peridotites (Pyrenees, France). Tectonophysics, 296, 103–123.

Hermann, W., Berry, R.F., 2002. MINSQ — a least squares spread-sheet method for calculating mineral proportions from whole rock major element analysis geochemistry. Exploration Environment Analysis, 2, 361–368.

Herzberg, C., 1993. Lithosphere peridotites of the Kaapvaal craton. Earth and Planetary Science Letters, 120, 13–29.

Herzberg, C., 1999. Phase equilibrium constraints on the formation of cratonic mantle. In: Fei, Y., Bertka, C., Mysen, B.O., (Eds.), Mantle Petrology: Field Observations and High Pressure Experimentation: A Tribute to Francis R. (Joe) Boyd. Geochemical Society Special Publication, 6, 241–257.

Herzberg, C., 2004. Geodynamic information in peridotite petrology. Journal of Petrology, 45, 2507–2530

Hidas, K., Falus, G., Szabó, C., Szabó, P.J., Kovács, I., Földes, T., 2007. Geodynamic implications of flattened tabular equigranular textured peridotites from the Bakony–Balaton Highland volcanic field (Western Hungary). Journal of Geodynamics, 43, 484–503.

Hidas, K., Konc, Z., Garrido, C.J., Tommasi, A., Vauchez, A., Padrón-Navarta, J.A., Marchesi, C., Booth-Rea, G., Acosta-Vigil, A., Szabó, Cs., Varas-Reus, M.I., Gervilla, F., 2016. Flow in the western Mediterranean shallow mantle: Insights from xenoliths in Pliocene alkali basalts from SE Iberia (eastern Betics, Spain), Tectonics, 35, 2657–2676

Higgie, K., Tommasi, A., 2014. Deformation in a partially molten mantle: constraints from plagioclase-lherzolites from Lanzo, Western Alps. Tectonophysics, 615–616, 167–181.

Holtzman, B.K., Kohlstedt, D.L., Zimmerman, M.E., Heidelbach, F., Hiraga, T., Hustoft, J., 2003. Melt segregation and strain partitioning; implications for seismic anisotropy and mantle flow. Science, 301, 1227–1230.

Horn, I., Foley, S.F., Jackson, S.E., Jenner, G.A., 1994. Experimentally determined partitioning of high field strengt and selected transition elements between spinel and basaltic melt. Chemical Geology, 117, 193-218.

Ichiyama, Y., Morishita, T., Tamura, A., Arai, S., 2016. Peridotite xenoliths from the shiribeshi seamount, Japan sea: Insights into mantle processes in a back-arc basin. Contributions to Mineralogy and Petrology, 171(10), 86.

Ionov, D.A., Dupuy, C., O'Reilly, S.Y., Kopylova, M.G., Genshaft, Y.S., 1993. Carbonate peridotite xenoliths from Spitsbergen: implications for trace element signature of mantle carbonate metasomatism. Earth and Planetary Science Letters, 119, 283–297.

Ionov, D., Griffin, D.W., O'Reilly, S.Y.,1997. Volatile-bearing minerals and lithophile trace elements in the upper mantle. Chemical Geology, 141, 153–184.

Ionov, D.A., 2010. Petrology of mantle wedge lithosphere: New data on supra-subduction zone peridotite xenoliths from the andesitic Avacha volcano, Kamchatka, Journal of Petrology, 51, 327–361.

Ionov, D. A., Doucet, L.S., Ashchepkov, I.V., 2010. Composition of the lithospheric mantle in the Siberian craton: New constraints from fresh peridotites in the Udachnaya-East kimberlite, Journal of Petrology, 51, 2177–2210.

Irving, A.J., 1980. Petrology and geochemistry of composite ultramafic xenoliths in alkalic basalts and implications for magmatic processes within the mantle. American Journal of Science, 280, 389–426.

Ishimaru, S., Arai, S., Ishida, Y., Shirasaka, M., Okrugin, V.M., 2007. Melting and multi-stage metasomatism in the mantle wedge beneath a frontal arc inferred from highly depleted peridotite xenoliths from the Avacha volcano, southern Kamchatka. Journal of Petrology, 48(2), 395-433.

Ismail, M., Delpech, G., Cottin, J., Grégoire, M., Moine, B.N., Bilal, A., 2008. Petrological and geochemical constraints on the composition of the lithospheric mantle beneath the syrian rift, northern part of the Arabian plate. Geological Society Special Publication, 293, 223-251.

Jammes S., Lavier, L., Manatschal, G., 2010, Extreme crustal thinning in the Bay of Biscay and theWestern Pyrenees: from observation to modelling. Geochemistry, Geophysics, and Geosystems (G3), 11, Q10016.

Johanesen, K.E., Platt, J.P., 2015. Rheology, microstructure, and fabric in a large scale mantle shear zone, Ronda Peridotite, Southern Spain. Journal of Structural Geology, 73, 1–17.

Johnson, K., Dick, H.J., Shimizu, N., 1990. Melting in the oceanic upper mantle: an ion microprobe study of diopsides in abyssal peridotites. Journal of Geophysical Research: Solid Earth, 95(B3), 2661-2678.

Jones, A.P., Kostoula, T., Stoppa, F., Woolley, A.R., 2000. Petrography and mineral chemistry of mantle xenoliths in a carbonate-rich melilititic tuff from Mt. Vulture volcano, southern Italy. Mineralogical Magazine, 64(4), 593-613.

Juez-Larre, J., Andriessen, P.A.M., 2002. Post Late Paleozoic Tectonism In The Southern Catalan Coastal Ranges (NE Spain), Assessed By Apatite Fission Track Analysis. Tectonophysics, 349, 1-4.

Juez-Larre, J., Andriessen, P.A.M., 2006.Tectonothermal evolution of the northeastern margin of Iberia since the break-up of Pangea to present, revealed by low-temperature fission-track and (U-Th)/He thermochronology; a case history of the Catalan Coastal Ranges. Earth and Planetary Science Letters. 243, 159-180.

Jung, H., Karato, S.I., 2001. Water-induced fabric transitions in olivine. Science, 293, 1460–1464.

Jung, H., Katayama, I., Jiang, Z., Hiraga, T., Karato, S., 2006. Effect of water and stress on the lattice-preferred orientation of olivine. Tectonophysics, 421, 1–22.

Jung, H., Park, M., Jung, S., Lee, J., 2010. Lattice preferred orientation, water content, and seismic anisotropy of orthopyroxene. Journal of Earth Sciences, 21, 555–568.

Jung, S., Jung, H., Austrheim, H., 2014. Characterization of olivine fabrics and mylonite in the presence of fluid and implications for seismic anisotropy and shear localization. Earth Planets Space, 66, 46.

Kaczmarek, M.A., Müntener, O., 2008. Juxtaposition of melt impregnation and high- temperature shear zones in the upper mantle; field and petrological constraints from the perature shear zones in the upper mantle; field and petrological constraints from the Lanzo Peridotite (Northern Italy). Journal of Petrology, 49, 2187–2220.

Kaczmarek, M.A., Reddy, S.M., 2013. Mantle deformation during rifting: constraints from quantitative microstructural analysis of olivine from the East African Rift (Marsabit, Kenya). Tectonophysics, 608, 1122–1137.

Kaczmarek, M.-A., Tommasi, A., 2011. Anatomy of an extensional shear zone in the mantle (Lanzo Massif, Italy). Geochemistry Geophysics Geosystems, 12, Q0AG06.

Karato, S., 1995. Effects of water on seismic wave velocities in the upper mantle. Proceedings of the Japan Academy, 71, 61–66.

Karato, S.I., Toriumu, M., Fujii, T., 1980. Dynamic recrystallization of olivine single crystals during high-temperature creep. Geophysical Research Letters, 7, 649–652.

Karato, S.I., Jung, H., Katayama, I., Skemer, P., 2008. Geodynamic significance of seismic anisotropy of the upper mantle: new insights from laboratory studies. Annual Review of Earth and Planetary Science, 36, 59–95.

Katayama, I., Karato, S., 2006. Effects of temperature on the B- to C-type fabric transition in olivine. Physics of the Earth and Planetary Interiors, 157, 33–45.

Katayama, I., Jung, H., Karato, S.I., 2004. New type of olivine fabric from deformation experiments at modest water content and low stress. Geology, 32, 1045–1048.

Kelemen, P.B., Dick, H.J.B., Quick, J.E., 1992. Formation of harzburgite by pervasive melt/ rock reaction in the upper mantle. Nature, 358, 635–641.

Kitakaze, A., 2008. Sugakiite, $Cu(Fe,Ni)_8S_8$, a new mineral species from Hokkaido, Japan. The Canadian Mineralogist, 46, 263-267.

Klébesz, R., Gráczer, Z., Szanyi, G., Liptai, N., Kovács, I., Patkó, L., Pintér, Z., Falus, G., Wesztergom, V., Szabó, C., 2015. Constraints on the thickness and seismic properties of the lithosphere in an extensional setting (Nógrád-Gömör Volcanic Field, Northern Pannonian Basin). Acta Geodaetica et Geophysica, 50, 133–149.

Klemme, S., O'Neill, H.StC., 2000. The near-solidus transition from garnet lherzolite to spinel lherzolite. Contribtions of Mineralogy and Petrology, 138, 237-248.

Köhler, T.P., Brey, G.P., 1990. Calcium exchange between olivine and clinopyroxene calibrated as a geothermobarometer for natural peridotites from 2 to 60 Kb with applications. Geochimica et Cosmochimica Acta, 54, 2375–2388.

Kornprobst, J., Piboule, M., Roden, M., Tabit, A., 1990. Corundum-bearing Garnet Clinopyroxenites at Beni Bousera (Morocco): Original Plagioclase-rich Gabbros Recrystallized at Depth within the Mantle? Journal of Petrology, 31, 717-45.

Kourim, F., Bodinier, J L., Alard, O., Bendaoud, A., Vauchez, A., Dautria, J.M., 2014. Nature and evolution of the lithospheric mantle beneath the Hoggar Swell (Algeria): a record from mantle xenoliths. Journal of Petrology, 55(11), 2249-2280.

Kovács, I., Falus, G., Stuart, G., Hidas, K., Szabó, C., Flower, M.F.J., Hegedus, E., Posgay, K., Zilahi-Sebess, L., 2012. Seismic anisotropy and deformation patterns in upper mantle xenoliths from the central Carpathian-Pannonian Region: asthenospheric flow as a driving force for Cenozoic extension and extrusion? Tectonophysics 514–517, 168–179.

Kullerud, G., 1963. Thermal stability of pentlandite. The Canadian Mineralogist, 7, 353–366.

Kurat, G., Palme, H., Spettel, B., Baddenhausen, H., Hofmeister, H., 1980. Geochemistry of ultramafic xenoliths from Kapfenstein, Austria: evidence for a variety of upper mantle processes. Geochimica et Cosmochimica Acta, 44, 45-60 .

Kretz, R., 1983. Symbols for rock forming minerals. American Mineralogist, 68, 277–279.

Lagabrielle, Y., Bodinier, J.L., 2008. Submarine reworking of exhumed subcontinental mantle rocks: field evidence from the Lherz peridotites, French Pyrenees. Terra Nova, 20, 11–21.

Lagabrielle, Y., Labaume, P., de Saint Blanquat, M., 2010. Mantle exhumation, crustal denudation, and gravity tectonics during Cretaceous rifting in the Pyrenean realm (SW Europe): Insights from the geological setting of the lherzolite bodies. Tectonics, 29, TC4012.

Lago, M., Galé, G., Arranz, E., Gil, A., 2004a. El magmatismo pérmico. In: Vera, J.A. (Eds), Geología de España. SGE-IGME, Madrid. 271-272.

Lago, M., Arranz, E., Gil, A., Galé, G., Pocovi, A., 2004b. El magmatismo toleítico triásico de la Cordillera Pirenaica. In: Vera, J.A. (Eds), Geología de España. SGE-IGME, Madrid. 276-277.

Lago, M., Arranz, E., Gil, A., Pocovi, A., 2004c. Magmatismo asociado. In: Vera, J.A. (Eds), Geología de España. SGE-IGME, Madrid. 522-525.

Le Maitre, R.W., 2002. Igneous Rocks; A Classification and Glossary of Terms. University Press, Cambridge, Cambridge. 236 pp.

Le Roux, V., Bodinier, J.L., Tommasi, A., Alard, O., Dautria, J.M., Vauchez, A., Riches, A.J.V., 2007. The Lherz spinel lherzolite: refertilized rather than pristine mantle. Earth and Planetary Science Letters, 259, 599–612.

Le Roux, V., Tommasi, A., Vauchez, A., 2008. Feedback between deformation and melt percolation in an exhumed lithosphere–asthenosphere boundary. Earth and Planetary Science Letters, 274, 401–413.

Le Roux, V., Nielsen, S.G., Sun, C., Yao, L., 2016. Dating layered websterite formation in the lithospheric mantle. Earth and Planetary Science Letters 454, 103-112.

Leake, B.E., 1978. Nomenclature of amphiboles. American Mineralogist, 63, 1023-1052.

Lee, K., Jiang, Z., Karato, S., 2002. A scanning electron microscope study of the effects of dynamic recrystallization on lattice preferred orientation in olivine. Tectonophysics, 351, 331–341.

Lee, C.T., 2002. Platinum-group element geochemistry of peridotite xenoliths from the Sierra Nevada and the Basin and Range California. Geochimica et Cosmochimica Acta, 66, 3987–4005.

Lenoir, X., Garrido, C.J., Bodinier, J.L., Dautria, J.M., 2000. Contrasting lithospheric mantle domains beneath the Massif Central (France) revealed by geochemistry of peridotite xenoliths. Earth and Planetary Science Letters, 181, 359–375.

Lenoir, X., Garrido, C., Bodinier, J.L., Dautria, J.M., Gervilla, F., 2001. The recrystallization front of the Ronda peridotite: evidence for melting and thermal erosion of lithospheric mantle beneath the Alboran Basin. Journal of Petrology, 42, 141–158.

Lewis, C.J., Vergés, J., Marzo, M., 2000. High mountains in a zone of extended crust: insights into the Neogene-Quaternary topographic development of northeastern Iberia. Tectonics, 19, 86–102.

Lister, C.R.B., 1977. Estimators for heat flow and deep rock properties based on boundary layer theory. Tectonophysics, 1, 157-171.

Llobera Sánchez, 1983. Petrologia de los enclaves del volcán Roca Negra (Olot, NE España). Acta Geológica Hispánica, 18, 19-25.

Llovet, X., Galán, G., 2003. Correction of secondary X-ray fluorescence near grain boundaries in electron microprobe analysis: application to thermobarometry of spinel lherzolites. American Mineralogist, 88, 121–130.

López Ruiz, J., Rodríguez Badiola, E., 1985. La región volcánica Mio-Pleistocena del NE de España. Estudios Geologicos, 41, 105–126.

Lorand, J.P., Alard, O., 2001. Platinum-group element abundances in the upper mantle: new constraints from in situ and whole rock analyses of massif central xenoliths (France). Geochimica et Cosmochimica Acta, 65, 2789–2806

Lorand, J.P., Conquéré, F., 1983. Contribution à l'étude des sulfures dans les enclaves de lherzolites a spinelle des basaltes alcalins (Massif Central et du Languedoc, France). Bulletin de Mineralogie, 106, 585–606.

Lorand, J.P., Luguet, A., Alard, O., 2013. Platinum-group element systematics and petrogenetic processing of the continental upper mantle: a review. Lithos, 164-167, 2–21.

Lorand, J.P., 1989. Abundance and distribution of Cu–Fe–Ni sulfides, sulfur, copper and platinum group elements in orogenic-type spinel lherzolite massifs of Ariege (Northeastern Pyrenees, France). Earth and Planetary Science Letters, 93, 50–64.

Losantos, M., Montaner, J., Solà, J., Mató, E., Sampsó, J.M., Picart, J., Calvet, F., Enrique, P., Ferrés, M. Y Solé, J., 2000. Mapa geològic de Catalunya 1:25.000, Palafrugell 335- 1- 1 (79-25). ICC (Servei Geològic de Catalunya).

Lu, J., Zheng, J., Griffin, W.L., O'Reilly, S.Y., Pearson N.J., 2015 Microscale effects of melt infiltration into the lithospheric mantle: Peridotite xenoliths from Xilong, South China. Lithos, 232, 111–123.

Lustrino, M., Dallai, L., 2003. On the origin of EM-I end-member. Neues Jahrbuch für Mineralogie - Abhandlungen, 179, 85–100.

Lustrino, M., Wilson, M., 2007. The circum-mediterranean anorogenic cenozoic igneous province. Earth-Science Reviews, 81(1-2), 1-65.

Mainprice, D., Nicolas, A., 1989. Development of shape and lattice preferred orientations: application to the seismic anisotropy of the lower crust. Journal of Structural Geology, 11, 175-189.

Mainprice, D., Silver, P.G., 1993. Interpretation of sks-waves using samples from the sub-continental lithosphere. Physics of the Earth and Planetary Interiors, 78, 257–280.

Mainprice, D., Barruol, G., Ben Ismaïl, W., 2000. The seismic anisotropy of the Earth's mantle: from single crystal to polycrystal. In: Karato, A.M.F.S., Libermann, R.C., Masters, G., Stixrude, L. (Eds.), AGU Geophysical Monograph 117. AGU, Washington, DC, 237–264.

Mainprice, D., Tommasi, A., Couvy, H., Cordier, P., Frost, D.J., 2005. Pressure sensitivity of olivine slip systems and seismic anisotropy of Earth's upper mantle. Nature, 433, 731–733.

Mainprice, D., Bachmann, F., Hielscher, R., Schaeben, H., 2015. Descriptive tools for the analysis of texture projects with large datasets using MTEX—strength, symmetry and components. In: Faulkner, D.R., Mariani, E., Mecklenburgh, J. (Eds.), Rock Deformation From Field, Experiments and Theory. A Volume in Honour of Rutter. Geological Society, London, Special publication, 409, 251–271.

Mainprice, D., 2007. Seismic Anisotropy of the Deep Earth From a Mineral and Rock Physics Perspective. In: Schubert, G. (Ed.),Treatise on Geophysics vol. 2. Elsevier Ltd., Oxford, 437–492.

Mallarach, J.M., 1998. El vulcanisme prehistoric de Catalunya. Diputació de Girona, 322 pp.

Marchesi, C., Konc, Z., Garrido, C. J., Bosch, D., Hidas, K., Varas-Reus, M. I., Acosta-Vigil, A., 2017. Multi-stage evolution of the lithospheric mantle beneath the westernmost mediterranean: Geochemical constraints from peridotite xenoliths in the eastern betic cordillera (SE spain). Lithos, 276, 75-89.

Martí, J., Mallarach, J.M., 1987. Erupciones hidromagmáticas en el volcanismo cuaternario de Olot (Girona). Estudios Geologicos 43, 31-40.

Martí, J., Mitjavila, J., Roca, E., Aparicio, A., 1992. Cenozoic magmatism of the Valencia trough (western Mediterranean): relationship between structural evolution and volcanism. Tectonophysics, 203, 145-165

Martí, J., Pujadas, A., Ferrés, D., Planagumà, L., Mallarach, J.M., 2001. El vulcanisme. Guia de camp de la Zona Volcànica de la Garrotxa, 2nd edn. Parc Natural de la Zona Volcànica de la Garrotxa, Generalitat de Catalunya, Departament de Medi Ambient.

Martí, J., Planagumà, L., Geyer, A., Canal, E., Pedrazzi, D., 2011. Complex interaction between Strombolian and phreatomagmatic eruptions in the Quaternary monogenetic volcanism of the Catalan Volcanic Zone (NE of Spain). Journal of Volcanology and Geothermal Research, 201, 178–193.

Martí, J., 2004. La región volcánica de Gerona. In: Vera, J.A. (Ed.), Geología de España. SGE-IGME. Madrid. 672–675.

Martínez-Poza, A.I., Druguet, E., Castaño, L.M., Carreras, J., 2014. Dyke intrusion into a pre-existing joint network: the Aiguablava lamprophyre dyke swarm (Catalan Coastal Ranges). Tectonophysics, 630, 75–90.

Matusiak-Malek, M., Puziewicz, J., Ntaflos, T., Grégoire, M., Benoit, M., Klügel, A., 2014. Two Contrasting Lithologies in Off-rift Subcontinental Lithospheric Mantle beneath Central Europe- the Krzeniów (SW Poland) Case Study. Journal of Petrology, 55(9), 1799-1828.

Matusiak-Malek, M., Puziewicz, J., Ntaflos, T., Grégoire, M., Downes, H., 2010. Metasomatic effects in the lithospheric mantle beneath the NE Bohemian Massif: a case study of Lutynia (SW Poland) peridotite xenoliths. Lithos, 117, 49–60.

Mauffret, A., Durand de Grossouvre, B., Dos Reis, A.T., Gorini, C., Nercessian, A., 2001. Structural geometry in the eastern Pyrenees and western Gulf of Lion (Western Mediterranean). Journal of Structural Geology. 23, 1701-1726.

Mauler, A., Bystricky, M., Kunze, K., Mackwell, S., 2000. Microstructures and lattice preferred orientations in experimentally deformed clinopyroxene aggregates. Journal of Structural Geology, 22(11), 1633-1648.

McDonough, W.F., Sun, S.-S., 1995. Composition of the Earth. Chemical Geology, 120, 223–253.

McDonough, W.F., Rudnick, R.L., 1998. Mineralogy and composition of the upper mantle. In: Hemley, R., (Ed.), Ultrahigh-pressure mineralogy; physics and chemistry of the Earth's deep interior, Reviews in Mineralogy, Mineralogical Society of America, Washington, DC, United States, 37, 139-164.

McInnes, B.I., Gregoire, M., Binns, R.A., Herzig, P.M., Hannington, M.D., 2001. Hydrous metasomatism of oceanic sub-arc mantle, Lihir, Papua New Guinea: petrology and geochemistry of fluid-metasomatised mantle wedge xenoliths. Earth and Planetary Science Letters, 188(1), 169-183.

McKenzie, D., 1978. Some remarks on the development of sedimentary basins, Earth and Planetary Science Letters, 40, 25-32.

McLaren, A.C., Etheridge, M.A., 1976. A transmission electron microscope study of naturally deformed orthopyroxene. Contributions to Mineralogy and Petrology, 57, 163-177.

Medaris, L. G., Ackerman, L., Jelínek, E., Michels, Z.D., Erban, V., Kotková, J., 2015. Depletion, cryptic metasomatism, and modal metasomatism of central European lithospheric mantle: evidence from elemental and Li isotope compositions of spinel peridotite xenoliths, Kozákov volcano, Czech Republic. International Journal of Earth Sciences, 104, 1925–1956.

Menzies, M.A., 1987. Alkaline rocks and their inclusions: A window on the Earth's interior. Geological Society Special Publication, 30, 15-27.

Mercier, J.C.C., Nicolas, A., 1975. Textures and fabrics of upper mantle peridotites as illustrated by xenoliths from basalts. Journal of Petrology, 16, 454–487.

Middlemost, E.A., 1975. The basalt clan. Earth-Science Reviews, 11(4), 337-364.

Misra, K.C., Fleet, M.E., 1973. The chemical compositions of synthetic and natural pentlandite assemblages. Economic Geology, 68, 518–539

Moine, B.N., Grégoire, M., O'Reilly, S.Y., Sheppard, S.M.F., Cottin, J.Y., 2001. High field strength element (HFSE) fractionation in the upper mantle: evidence from amphibole-rich composite mantle xenoliths from the Kerguelen Islands (Indian Ocean), Journal of Petrology, 42, 2145–2167.

Montigny, R., Azambre, B., Rossy, M., Thuizat, R., 1982. Etude K/Ar du magmatisme basique lié au Trias supérieur des Pyrénées. Conséquences méthodologiques et paléogéographiques. Bulletin de Minéralogie, 105, 673–680.

Montigny, R., Azambre, B., Rossy, M., Thuizat, R., 1986. K-Ar study of Cretaceous magmatism and metamorphism in the Pyrenees: age and length of rotation of the Iberian Peninsula. Tectonophysics, 129, 257–273.

Morimoto, N., Fabries, J., Ferguson, A.K., Ginzburg, I.V., Ross, M., Seifert, F.A., Zussman, J., Aoki, K., Gottardi, G., 1988. Nomenclature of pyroxenes. American Mineralogist, 73, 1123–1133.

Müller, W.F., Walte, N., Miyajima, N., 2008. Experimental deformation of ordered natural omphacite: A study by transmission electron microscopy. European Journal of Mineralogy, 20(5), 835-844

Muñoz, J.A., 1992. Evolution of a continental collision belt: ECORS-Pyrenees crustal balanced cross-section. In: McClay (Ed.), Thrust Tectonics. Chapman & Hall, London, 235–246.

Murgulov, V., Griffin, W.L., O'Reilly, S.Y., 2011. Lithospheric mantle evolution beneath northeast Australia. Lithos, 125, 405–422.

Naldrett, A. J., Craig, J. R., Kullerud, G., 1967. The central portion of the Fe-Ni-S system and its bearing on pentlandite exsolution in iron-nickel sulfide ores. Economic Geology, 62(6), 826-847.

Navon, O., Stolper, E., 1987. Geochemical consequences of melt percolation - the upper mantle as a chromatographic column. Journal of Geology, 95, 285–307

Nazé, L., Doukhan, N., Doukhan, J.C., Latrous, K., 1987. A TEM study of lattice defects in naturally and experimentally deformed orthopyroxenes. Bulletin de Minéralogie, 110, 497–512.

Nédli, Z., Tóth, T.M., Downes, H., Császár, G., Beard, A., Szabó, Cs., 2010. Petrology and geodynamical interpretation of mantle xenoliths from Late Cretaceous lamprophyres, Villány Mts (S Hungary). Tectonophysics, 489, 43–54

Neumann, E.-R., Martí, J., Mitjavila, J., Wulff-Pedersen, E., 1999. Origin and implications of mafic xenoliths associated with Cenozoic extension-related volcanism in the Valencia Trough, NE Spain. Mineralogy and Petrology, 65, 113–139.

Nicolas, A., Christensen, N.I., 1987. Formation of anisotropy in upper mantle peridotites—a review. In: Fuchs, K., Froidevaux, C. (Eds.), Composition, Structure and Dynamics of the Lithosphere–Asthenosphere System. Geodyn. Ser. AGU, Washington DC, 111–123.

Nicolas, A., Boudier, F., Boullier, A.M., 1973. Mechanisms of flow in naturally and experimentally deformed peridotites. American Journal of Science, 273, 853–876.

Nicolas,A., Achauer, U., Daignieres, M., 1994. Rift initiation by lithospheric rupture. Earth and Planetary Science Letters, 123, 281-298.

Niu, Y., 1997. Mantle melting and melt extraction processes beneath ocean ridges: evidence from abyssal peridotites. Journal of Petrology, 38, 1047–1074.

Niu, Y., 2004. Bulk-rock major and trace element compositions of abyssal peridotites: implications for mantle melting, melt extraction and post-melting processes beneath mid-ocean ridges. Journal of Petrology, 45(12), 2423-2458.

Nixon, P.H., 1987. Mantle xenoliths. John Wiley & Sons, Chichester. 844pp.

Norman, M.D., 1998. Melting and metasomatism in the continental lithosphere: laser ablation ICPMS analysis of minerals in spinel lherzolites from eastern Australia. Contributions to Mineralogy and Petrology, 130(3), 240-255.

O'Brien, H.E., Peltonen, P., Vartiainen, H., 2005. Kimberlites, carbonatites and alkaline rocks. In: Lehtinen, M., Nurmi, P.A., Rämö, O.T., (Eds.) Precambrian Geology of Finland – key to the evolution of the Fennoscandian Shield. Developments in Precambrian Geology, 14, 605–644.

O'Reilly, S.Y., Griffin, W.L., 2013. Moho vs crust-mantle boundary: Evolution of an idea. Tectonophysics, 609, 535–546.

O'Reilly, S.Y., Chen, D., Griffin, W.L., Ryan, C.G., 1997. Minor elements in olivine from spinel lherzlite xenoliths: implications for thermobarometry. Mineralogical Magazine, 61, 257–269.

Oliveras, V., 2009. Xenòlits mantèl·lics lligats al vulcanisme neògeno-quaternari de Catalunya: caracterització, processos i condicions d'equilibri. (Tesis doctoral) Universitat Autonoma de Barcelona. 210pp.

Oliveras, V., Galán, G., 2006. Petrología y mineralogía de los xenolitos mantélicos del volcán la Banya del Boc (Girona). Geogaceta, 40, 107–110.

Oliveras, V., Galán, G., 2007. Condiciones P-T en xenolitos mantélicos de los volcanes la Banya del Boc y el Puig d'Adri (Girona). Geogaceta, 43, 19-22.

Palasse, L.N., Vissers, R.L.M., Paulssen, H., Basu, A.R., Drury, M.R., 2012. Microstructural and seismic properties of the upper mantle underneath a rifted continental terrane (Baja California): an

example of sub-crustal mechanical asthenosphere? Earth and Planetari Science Letters, 60–71, 345–348.

Palme, H., O'Neill, H.St.C., 2003. Cosmochemical estimates of mantle composition. In: Carlson, R.W., (ed) Treatise Geochemistry, Vol. 2—Mantle Core. Elsevier Pergamon, Oxford, pp. 1-38.

Passchier, C., Trouw, R., 2005. Microtectonics. Springer-Verlag Berlin Heidelberg. 372pp.

Parkinson, I.J., Pearce, J.A., 1998. Peridotites from the Izu–Bonin–Mariana forearc (ODP Leg 125): evidence for mantle melting and melt–mantle interaction in a supra-subduction zone setting. Journal of Petrology, 39(9), 1577-1618.

Parkinson, I.J., Arculus, R.J., Eggins, S.M., 2003. Peridotite xenoliths from Grenada, Lesser Antilles island arc. Contributions to Mineralogy and Petrology, 146(2), 241-262.

Pearson, D.G., Canil, D., Shirey, S.B., 2003. Mantle samples included in volcanic rocks: xenoliths and diamonds. In: Carlson, R.W., Holland, H.D., Turekian, K.K. (Eds.), Treatise on Geochemistry, 2. Elsevier, Amsterdan, pp. 171–275.

Peltonen, P., Brügmann, G., 2006. Origin of layered continental mantle (Karelian craton, Finland): Geochemical and Re–Os isotope constraints. Lithos, 89, 405–423.

Perinelli, C., Orlando, A., Conte, A. M., Armienti, P., Borrini, D., Faccini, B., Misiti, V., 2008. Metasomatism induced by al- kaline magma in the upper mantle of northern Victoria Land (Antarctica): an experimental approach. In: Coltorti, M., Grégoire, M. (eds) Metasomatism in Oceanic and Continental Lithospheric Mantle. Geological Society, London, Special Publications, 293, 279–302.

Philippot, P., Van Roermund, H.L.M., 1992. Deformation processes in eclogitic rocks: evidence for the rheological delamination of the oceanic crust in deeper levels of subduction zones. Journal of Structural Geology, 14, 1059–1077.

Pike, J.E.N,. Schwarzmann, E.C,. 1976. Classification on textures in ultramafic xenoliths. Journal of Geology 85, 49-61.

Porreca C., Selverstone J., Samuels K., 2006, Pyroxenite xenoliths from the Rio Puerco volcanic field, New Mexico: Melt metasomatism at the margin of the Rio Grande Rift. Geosphere, 2, 333–351.

Poujol, M., Boulvais, P., Kosler, J., 2010. Regional-scale Cretaceous albitization in the Pyrenees: evidence from in situ U–Th–Pb dating of monazite, titanite and zircon. Journal of the Geological Society London 167, 751–767.

Powell, W., O'Reilly, S., 2007. Metasomatism and sulfide mobility in lithospheric mantle beneath eastern Australia: implications for mantle Re–Os chronology. Lithos, 94(1), 132-147.

Prior, D.J., Mariani, E., Wheeler, J., 2009. EBDS in earth Sciences: Applications, common practice, and challenges. In: Schwartz, A.J., Kumar, M., Adams, B.L., Field, D.P., (Eds.), Electron Backscatter Diffraction in Materials Science. Springer, pp. 345–360.

Puelles, P., Ábalos, B., Gil Ibarguchi, J.I., Sarrionandia, F., Carracedo, M., Fernández-Armas, S., 2016. Petrofabric and seismic properties of lithospheric mantle xenoliths from the Calatrava volcanic field (Central Spain). Tectonophysics, 683, 200–215.

Puziewicz, J., Koepke, J., Gregoire, M., Ntaflos, T., Matusiak-Malek, M., 2011. Lithospheric mantle modification during Cenozoic rifting in Central Europe: evidence from the Ksieginki nephelinite (SW Poland) xenolith suite. Journal of Petrology, 52, 2107–2145.

Puziewicz, J., Matusiak-Małek, M., Ntaflos, T., Grégoire, M., Kukula, A., 2015. Subcontinental lithospheric mantle beneath Central Europe. International Journal of Earth Science (Geol Rundsch), 104, 1913.

Python, M., Ceuleneer, G., 2003. Nature and distribution of dykes and related melt migration structures in the mantle section of the Oman ophiolite. Geochemistry Geophysics Geosystems, 4(7), 8612.

Rampone, E., Piccardo, G.B., Vannucci, R., Bottazzi, P., Ottolini, L., 1993. Subsolidus reactions monitored by trace element partitioning: the spinel- to plagioclase-facies transition in mantle peridotites. Contributions to Mineralogy and Petrology, 115, 1–17.

Rampone, E., Piccardo, G.B., Hofmann, A.W., 2008. Multi-stage melt–rock interaction in the Mt. Maggiore (Corsica, France) ophiolitic peridotites: microstructural and geochemical evidence. Contributions to Mineralogy and Petrology, 156(4), 453-475.

Rampone, E., Vissers, R.L.M., Poggio, M., Scambelluri, M., Zanetti, A., 2010. Melt migration and intrusion during exhumation of the Alboran lithosphere: the Tallante mantle xenolith record (Betic Cordillera, SE Spain). Journal of Petrology, 51, 295–325.

Reche, J., 1994. El metamorfismo de Medio-Alto grado de las anfibolitas Cor. Aporte de nuevos datos naturales. Recopilación de datos empiricos y construccions de un nuevo modelo petrogenetico. (Tesis doctoral). Universitat Autònoma de Barcelona.

Rehfeldt, T., Obst, K., Johansson, L., 2007. Petrogenesis of ultramafic and mafic xenoliths from Mesozoic basanites in southern Sweden: constraints from mineral chemistry. International Journal of Earth Sciences, 96, 433-450.

Riches, A.J.V., Rogers, N.W., 2011. Mineralogical and geochemical constraints on the shallow origin, ancient veining, and multi-stage modification of the Lherz peridotite. Geochimica et Cosmochimica Acta, 75, 6160–6182.

Rivalenti, G., Zanetti, A., Mazzucchelli, M., Vannucci, R., Cingolina, C.A., 2004. Equivocal carbonatite markers in the mantle xenoliths of the patagonia backarc: The Gobernador Gregores case (Santa Cruz Province, Argentina). Contributions to Mineralogy and Petrology, 147(6), 647-670.

Robinson, P., 1980. The composition space of terrestrial piroxenes - internal and external limits. In: Prewitt, C.T. (Ed.), Reviews in mineralogy, vol. 7: Pyroxenes. Mineralogical Society of America, Washington, D.C., 419-490.

Roca, E., 1994 La evolución geodinámica de la Cuenca Catalano-Balear y áreas adyacentes desde el Mesozoico hasta la actualidad. Acta Geologica Hispánica, 29, 3-25.

Rocco, I., Lustrino, M., Morra, V., Melluso, L., 2012. Petrological, geochemical and isotopic characteristics of the lithospheric mantle beneath Sardinia (Italy) as indicated by ultramafic xenoliths enclosed in alkaline lavas. International Journal of Earth Sciences, 101, 1111e1125.

Roeder, P.L., Emslie, R.F., 1970. Olivine-liquid equilibrium. Contributions to Mineralogy and Petrology, 29(4), 275-289.

Roubault, M., 1982. Détermination des minéraux des roches au microscope polarisant. Éditions Lamarre-Poinat, Paris.

Rossi, P., Cocherie, A., Fanning, C.M., Ternet, Y., 2003. Datation U–Pb sur zircons des dolérites tholéiitiques pyrénéennes (ophites) à la limite Trias–Jurassique et relations avec les tufs volcaniques dits "infra-liasiques" nord-pyrénéens. Comptes Rendus Geoscience, 335, 1071–1080.

Rossy, M., Azambre, B., Albarede, F., 1992. REE and Sr\Nd isotope geochemistry of the alkaline magmatism from the Cretaceous North Pyrenean Rift Zone (France–Spain). Chemical Geology, 97, 33–46.

Rubio-Godoy, A., 19987. Vulcanisme a la serralada litoral: els afloraments de Sant Corneli. Atzavara, 5, 59-62.

Rudnick, R.L., McDonough, W..F, Chappell, B.W., 1993. Carbonatite metasomatism in the northern Tanzanian mantle: petrographic and geochemical characteristics. Earth and Planetary Science Letters, 114, 463-475.

San Miguel de la Cámara, M., 1932. Notas petrográficas. Treballs Museu Ciències Naturals de Barcelona, 6, 7.

Saula, E., Picart, J., Mató, E., Llenas, M., Losantos, M., Berasategui, X., Agustí, J., 1996. Evolución geodinámica de la fosa del Empordà y de las Sierras Transversales. Acta Geológica Hispánica, 29, 55–75.

Savage, M.K., 1999. Seismic anisotropy and mantle deformation: what have we learned from shear wave splitting? Reviews of Geophysics, 37, 65–106.

Schmidberger, S.S., Francis, D., 2001. Constraints on the trace element composition of the Archean mantle root beneath Somerset Island, Arctic Canada. Journal of Petrology, 42(6), 1095-1117.

Shaw, C.S.J., Dingwell, D.B., 2008. Experimental peridotite–melt reaction at one atmosphere: a textural and chemical study. Contributions to Mineralogy and Petrology, 155, 199–214.

Shaw, C.S.J., 2009. Textural development of amphibole during breakdown reactions in a synthetic peridotite. Lithos, 110, 215–228.

Shaw, C.S.J., Heidelbach, F., Dingwell, D.B., 2006. The origin of reaction textures in mantle peridotite xenoliths from Sal Island, Cape Verde: the case for ''metasomatism'' by the host lava. Contributions to Mineralogy and Petrology, 151, 681–697.

Shaw, C.S.J., 1997. Origin of sulfide blebs in variably metasomatized mantle xenoliths, Quaternary west Eifel volcanic field, Germany. The Canadian Mineralogist, 35, 1453–1463.

Silver, P.G., Chan, W.W., 1988. Implications for continental structure and evolution from seismic anisotropy. Nature, 335, 34–39.

Simon, N.S.C., Irvine, G.J., Davies, G.R., Pearson, D.G., Carlson, R.W., 2003. The origin of garnet and clinopyroxene in "depleted" Kaapvaal peridotites, Lithos, 71, 289-322.

Skemer, P., Warren, J.M., Kelemen, P.B., Hirth, G., 2010. Microstructural and rheological evolution of a mantle shear zone. Journal of Petrology, 51, 43–53.

Sobolev, V.N., McCammon, C.A., Taylor, L.A., Snyder, G.A., 1999. Precise mossbauer milliprobe determination of ferric iron in rock-forming minerals and limitations of electron microprobe analysis. American Mineralogist, 84(1-2), 78-85.

Solé Sabaris, L., 1962. Observaciones sobre la edad del volcanismo gerundense. Memorias de la Real Academia de Ciencias y Artes de Barcelona, 34, 359–372.

Solé, J., Pi, T., Enrique, P., 2003. New geochronological data on the late cretaceous alkaline magmatism of the northeast iberian peninsula. Cretaceous Research, 24(2), 135-140.

Soustelle, V., Tommasi, A., Bodinier, J.-L., Garrido, C.J., Vauchez, A., 2009. Deformation and reactive melt transport in the mantle lithosphere above a large-scale partial melting domain: the Ronda Peridotite Massif, Southern Spain. Journal of Petrology, 50, 1235–1266.

Soustelle, V., Tommasi, A., Demouchy, S., Ionov, D.A., 2010. Deformation and fluid, a rock interaction in the supra-subduction mantle: microstructures and water contents in peridotite xenoliths from the Avacha Volcano, Kamchatka. Journal of Petrology, 51, 363–394.

Špacek, P., Ackerman, L., Habler, G., Abart, R., Ulrych, J., 2013. Garnet breakdown, symplectite formation and melting in basanite-hosted peridotite xenoliths from Zinst (Bavaria, Bohemian Massif). Journal of Petrology, 54, 1691–1723

Stosch, H.G., 1981. Sc, Cr, Co and Ni partitioning between minerals from spinel peridotite xenoliths. Contributions to Mineralogy and Petrology, 78, 166-174.

Su, B.X., Zhang, H.F., Sakyi, P.A., Yang, Y.H., Ying, J.F., Tang, Y.J., Qin, K.Z., Xiao, Y., Zhao, X.M., Mao, Q., Ma, Y.G., 2011. The origin of spongy texture in minerals of mantle xenoliths from the Western Qinling, central China. Contributions to Mineralogy and Petrology, 161, 465–482.

Sugaki, A., Shima, H., Kitakaze, A., Harada, H., 1975. Isothermal phase relations in the system Cu-Fe-S under hydrothermal conditions at 350 °C and 300 °C. Economic Geology, 70, 806–823.

Suhr, G., 1993. Evaluation of upper mantle microstructures in the Table Mountain massif (Bay of Islands Ophiolite). Journal of Structural Geology, 15, 1273–1292.

Swanson, S.E., Kay, S.M., Brearley, M., Scarfe, C.M., 1987. Arc and back-arc xenoliths in Kurile-Kamchatka and western Alaska. In: Nixon, P.N. (ed) Mantle xenoliths. Wiley, Chichester, pp 303–318.

Szabó, C.S., Bodnar, R.J., 1995. Chemistry and origin of mantle sulfides in spinel peridotite xenoliths from alkaline basaltic lavas, Nógrád- Gömör Volcanic Field, northern Hungary and southern Slovakia. Geochimica et Cosmochimica Acta, 59, 3917–3927.

Szabó, C., Falus, G., Zajac, Z., Kovács, I., Bali, E., 2004. Composition and evolution of lithosphere beneath the Carpathian–Pannonian Region: a review. Tectonophysics, 393, 119–137.

Tabor, F.A., Tabor, B.E., Downes, H., 2010. Quantitative characterization of textures in mantle spinel peridotite xenoliths. In: Coltorti, M., Downes, H., Gregoire, M., O'Reilly, S., (eds) Petroleum evaluation Europe lithospheric mantle. Geological Society of London, London, pp 195–211

Takazawa, E., Frey, F.A., Shimizu, N., Obata, M., 2000. Whole rock compositional variations in an upper mantle peridotite (Horoman, Hokkaido, Japan): are they consistent with a partial melting process?. Geochimica et Cosmochimica Acta, 64(4), 695-716.

Tang, Y., Zhang, H., Nakamura, E., Ying, J., 2011. Multistage melt/fluid-peridotite interactions in the refertilized lithospheric mantle beneath the north china craton: Constraints from the Li-Sr-Nd isotopic disequilibrium between minerals of peridotite xenoliths. Contributions to Mineralogy and Petrology, 161(6), 845-861.

Taylor, 1998. An experimental test of some geothermometer and geobarometer formulations with application to the thermobarometry of fertile lherzolite and garnet websterite. Neues Jahrbuch für Mineralogie - Abhandlungen, 172, 281-408.

Teixell, A., 2004. Estructura cortical de la Cordillera Pirenaica. In: Vera, J.A. (Eds), Geología de España. SGE-IGME, Madrid. 320-321.

Tikoff, B., Fossen, H., 1999. Three-dimensional reference deformations and strain facies. Journal of Structural Geology, 21(11), 1497-1512.

Tilhac, R., Ceuleneer, G., Griffin, W.L., O'Reilly, S.Y., Pearson, N.J., Benoit, M., Henry, H., Girardeau, J., Grégoire, M., 2016. Primitive Arc Magmatism and Delamination: Petrology and Geochemistry of Pyroxenites from the Cabo Ortegal Complex, Spain. Journal of Petrology, egw064.

Tommasi, A., Tikoff, B., Vauchez, A., 1999. Upper mantle tectonics: three-dimensional deformation, olivine crystallographic fabrics and seismic properties. Earth and Planetary Science Letters, 168, 173–186.

Tommasi, A., Vauchez, A., Ionov, D., 2008. Deformation, static recrystallization, and reactive melt transport in shallow subcontinental mantle xenoliths (Tok Cenozoic Volcanic Field, SE Siberia). Earth and Planetary Science Letters, 272, 65–77.

Tommasi, A., Mainprice, D., Canova, G., Chastel, Y., 2000. Viscoplastic self-consistent and equilibrium-based modeling of olivine lattice preferred orientations: implications for the upper mantle seismic anisotropy. Journal of Geophysical Research: Solid Earth, 105, 7893–7908.

Tonarini, S., D'Orazio, M., Armienti, P., Innocenti, F., Scribano, V., 1996. Geochemical features of eastern Sicily lithosphere as probed by Hyblean xenoliths and lavas. European Journal of Mineralogy-Ohne Beihefte, 8(5), 1153-1174.

Tournon, J., 1968. Le volcanisme de la province de Gérone (Espagne). Études de basaltes quaternaires et de leurs enclaves. (Thèse 3e Cycle). Université de Paris. 120 pp.

Ubide, T., 2013. The cretaceous alkaline magmatism in northeast Iberia. Igneous processes and geodynamic implications. (Tesis doctoral). Universidad de Zaragoza. 223pp.

Ubide, T., Lago, M., Arranz, E., Galé, C., Larrea, P., 2010. The lamprophyric sub-vertical dyke swarm from Aiguablava (Catalonian Coastal Ranges): petrology and composition. Geogaceta, 49, 75–78.

Ubide, T., Arranz, E., Lago, M., Galé, C., Larrea, P., 2012. The influence of crystal settling on the compositional zoning of a thin lamprophyre sill: a multi-method approach. Lithos 132–133, 37–49.

Ubide, T., Wijbrans, J. R., Gale, C., Arranz, E., Lago, M., Larrea, P., 2014a. Age of the Cretaceous alkaline magmatism in northeast Iberia: implications for the Alpine cycle in the Pyrenees. Tectonics, 33(7), 1444-1460.

Ubide, T., Galé, C., Arranz, E., Lago, M., Larrea, P., 2014b. Clinopyroxene and amphibole crystal populations in a lamprophyre sill from the Catalonian Coastal Ranges (NE Spain): a record of magma history and a window to mineral-melt partitioning. Lithos, 184, 225-242.

Ulrich, S., Mainprice, D., 2005. Does cation ordering in omphacite influence development of lattice-preferred orientation? Journal of Structural Geology, 27, 419–431.

Upton, B.G.J., Downes, H., Kirstein, L.A., Bonadiman, C., 2011. The lithospheric mantle and lower crust-mantle relationships under Scotland: a xenolithic perspective. Journal of the Geological Society, 186, 873-886.

Van Calsteren, P.W., 1978. Geochemistry of the polymetamorphic mafic-ultramafic complex at Cabo Ortegal (NW Spain). Lithos, 11(1), 61-72.

Van Der Wal, D., Chopra, P., Drury, M., Fitzgerald, J., 1993. Relationships between dynamically recrystallized grain size and deformation conditions in experimentally deformed olivine rocks. Geophysical Research Letters, 20, 1479–1482.

Vauchez, A., Garrido, C., 2001. Seismic properties of an asthenospherized lithospheric mantle: constraints from lattice preferred orientations in peridotite from the Ronda Massif. Earth and Planetary Science Letters, 192, 235–249.

Vauchez, A., Tommasi, A., Barruol, G., Maumus, J., 2000. Upper mantle deformation and seismic anisotropy in continental rifts. Physics and Chemistry of the Earth, 25, 111–117.

Vauchez, A., Barruol, G., Tommasi, A., 1997. Why do continents break-up parallel to ancient orogenic belts?. Terra Nova, 9(2), 62-66.

Vauchez, A., Tommasi, A., Barruol, G., 1998. Rheological heterogeneity, mechanical anisotropy and deformation of the continental lithosphere. Tectonophysics, 296, 61–86.

Vauchez, A., Dineur, F., Rudnick, R.L., 2005. Microstructure, texture and seismic anisotropy of the lithospheric mantle above a mantle plume. Insights from the Labait Volcano xenoliths (Tanzania). Earth and Planetary Science Letters, 232, 295–314.

Vauchez, A., Tommasi, A., Mainprice, D., 2012. Faults (shear zones) in the Earth's Mantle. Tectonophysics 558–559, 1–27.

Vegas, R. (1994). A tectonic model for the volcanic province of Olot (NE Spain). Geogaceta, 15, 121-123.

Villaseca, C., Ancochea, E., Orejana, D., Jeffries, T.E., 2010. Composition and evolution of the lithospheric mantle in central Spain: inferences from peridotite xenoliths from the Cenozoic Calatrava volcanic field. In: Coltorti, M., (Eds.), Petrological Evolution of the European Lithospheric Mantle. Geological Society, London, Special Publications 337, pp. 125–151.

Vissers, R.L.M., 1992. Variscan extension in the Pyrenees. Tectonics, 11, 1369–1384.

Voigt, M., Von der Handt, A., 2011. Influence of subsolidus processes on the chromium number in spinel in ultramafic rocks. Contributions to Mineralogy and Petrology, 162(4), 675-689.

Vollmer, F.W., 1990. An application of eigenvalue methods to structural domain analysis. Geological Society of America Bulletin, 102, 786–791.

Vonlanthen, P., Kunze, K., Burlini, L., Grobety, B., 2006. Seismic properties of the upper mantle beneath Lanzarote (Canary Islands): model predictions based on texture measurements by EBSD. Tectonophysics, 428, 65–85.

Wagner, C., Deloule, E., 2007. Behaviour of Li and its isotopes during metasomatism of French Massif Central lherzolites. Geochimica et Cosmochimica Acta, 71(17), 4279-4296.

Walter, M.J., Sisson, T.W., Presnall, D.C., 1995. A mass proportion method for calculating melting reactions and application to melting of model upper mantle lherzolite. Earth and Planetary Science Letters, 135(1-4), 77-90.

Walter, M.J., 2003. Melt extraction and compositional variability in mantle lithosphere. In: Carlson, R.W., (ed) Treatise Geochemistry, Vol. 2—Mantle Core. Elsevier Pergamon, Oxford, pp 363–394

Wang, K.L., O'Reilly, S.Y., Honda, M., Matsumoto, T., Griffin, W.L., Pearson, N.J., Zhang, M., 2010. Co-rich sulfides in mantle peridotites from Penghu Islands, Taiwan: Footprints of Proterozoic mantle plumes under the Cathaysia Block. Journal of Asian Earth Sciences, 37, 229–245.

Wang, Y., Han, B., Griffin., W.L., Zhang, l., Shu, G., 2012. Post-Entrainment Mineral-Magma Interaction in Mantle Xenoliths from Inner Mongolia, Western North China Craton. Journal of Earth Science, 23, 54–76

Wenk, H. R., Bennett, K., Canova, G. R., Molinari, A., 1991. Modelling plastic deformation of peridotite with the self-consistent theory. Journal of Geophysical Research: Solid Earth, 96(B5), 8337-8349.

Wernicke, B., 1981. Low angle normal faults in Bassin and Range province. Nappe tectonics in an extending orogen, Nature, 291, 645- 648.

Wernicke, B., 1985. Uniform-sense normal simple shear of the continental lithosphere. Canadian Journal of Earth Sciences, 22(1), 108-125.

Wilson, M., Downes, H., 2006. Tertiary-Quaternary intra- plate magmatism in Europe and its relationship to mantle dynamics. In: Gee, D.G., Stephenson, R., (eds.) European lithosphere dynamics. Geological Society of London Memoir 32. London: Geological Society of London, pp. 147-166.

Witt-Eickschen, G., Kramm, U., 1997. Mantle Upwelling and Metasomatism beneath Central Europe: Geochemical and Isotopic Constraints from Mantle Xenoliths from the Rhön (Germany). Journal of Petrology, 38, 479–493.

Witt-Eickschen, G., Seck, H.A., Mezger, K., Eggins, S.M., Altherr, R., 2003. Lithospheric mantle evolution beneath the eifel (Germany): constraints from Sr–Nd–Pb isotopes and trace element abundances in spinel peridotite and pyroxenite xenoliths. Journal of Petrology, 44,1077–1095.

Wittig, N., Baker, J.A., Downes, H., 2007. U–Th–Pb and Lu–Hf isotopic constraints on the evolution of sub-continental lithospheric mantle, French Massif Central. Geochimica et Cosmochimica Acta, 71, 1290–1311.

Wood, B.J., 1991. Oxygen barometry of spinel peridotites. In: Lindsley, D.H., (ed) Oxide minerals: petrologic and magnetic significance. Reviews in Mineralogy and Geochemistry, 25, 417–431.

Wood, B.J., Blundy, J.D., 1997. A predictive model for rare earth element between clinopyroxene and anhydrous silicate melt. Contributions to Mineralogy and Petrology, 129, 166–181.

Workman, R.K., Hart, S.R., Jackson, M., Regelous, M., Farley, K.A., Blusztajn, J., Kurz, M., Staudigel, H., 2004. Recycled metasomatized lithosphere as the origin of the Enriched Mantle II (EM2) end-member: evidence from the Samoa volcanic chain. Geochemistry Geophysics Geosystems, 5, Q04008.

Wörner, G., Zindler, A., Staudigel, H., Schmincke, H.U., 1986. Sr, Nd, and Pb isotope geochemistry of Tertiary and Quaternary alkaline volcanics from West Germant. Earth and Planetary Science Letters, 79, 107-119.

Xu, Y., Menzies, M.A., Vroon, P., Mercier, J.C., Lin, C., 1998. Texture–Temperature–Geochemistry Relationships in the Upper Mantle as Revealed from Spinel Peridotite Xenoliths from Wangqing, NE China. Journal of Petrology, 39 (3) 469–493.

Zaffarana, C., Tommasi, A., Vauchez, A., Grégoire, M., 2014. Microstructures and seismic properties of south Patagonian mantle xenoliths (Gobernador Gregores And Pali Aike). Tectonophysics, 621, 175–197.

Zanetti, A., Mazzucchelli, M., Rivalenti, G., Vannucci, R., 1999. The Finero phlogopite- peridotite massif: an example of subduction-related metasomatism. Contributions to Mineralogy and Petrology, 134, 107–122.

Zhang, J., Green, H.W., Bozhilov, K., 2006. Rheology of omphacite at high temperature and pressure and significance of its lattice preferred orientations. Earth and Planetary Science Letters, 246, 432–443.

Zhang, H.F., Ying, J.F., Shimoda, G., Kita, N.T., Morishita, Y., Shao, J.A., Tang, Y.J., 2007. Importance of melt circulation and crust-mantle interaction in the lithospheric evolution beneath the North China Craton: evidence from Mesozoic basalt-borne clinopyroxene xenocrysts and pyroxenite xenoliths. Lithos, 96(1), 67-89.

Microestructuras y química mineral de lherzolitas en xenolitos mantélicos de Cataluña (NE España)

Microstructures and mineral chemistry of lherzolites in mantle xenoliths from Catalonia (NE Spain)

Mercè Fernández-Roig y Gumer Galán

Departament de Geologia. Universitat Autònoma de Barcelona. Edifici C (Sur), 08193 Bellaterra, Barcelona, España.
merce.fernandez@uab.cat, gumer.galan@uab.cat

ABSTRACT

Spinel lherzolite xenoliths from the Catalan Volcanic Zone show three main types of microstructures: protogranular, porphyroclastic and equigranular. Major element chemistry of minerals suggests that there is no compositional relationship between the three types. However, the evolution of the jadeitic component of clinopyroxene on the one hand, and the spinel composition on the other hand would be related to deformation. These compositional trends along with thermobarometric data indicate that more deformed lherzolites were reequilibrated at lower temperature and pressure than the least deformed ones. Porphyroclastic and equigranular microstructures were most likely originated by shearing during the early stages of the Neogene rifting.

Key-words: *Xenoliths, spinel lherzolites, microstructures, deformation, thermobarometry.*

RESUMEN

Los xenolitos de lherzolitas con espinela en la Zona Volcánica de Cataluña muestran tres tipos principales de microestructuras: protogranulares, porfidoclásticas y equigranulares. La química de elementos mayores de los minerales indica que no hay relación composicional entre los tres tipos. Sin embargo, las tendencias del componente jadeítico en el clinopiroxeno y de la composición de la espinela sí estarían influenciadas por la deformación. Estas tendencias, junto con los datos termobarométricos, indican que las lherzolitas más deformadas se reequilibraron a menor temperatura y presión que las menos deformadas. Las microestructuras porfidoclásticas y equigranulares se originaron probablemente en relación con zonas de cizalla durante el desarrollo inicial del rift *neógeno.*

Palabras clave: *Xenolitos, lherzolitas con espinela, microestructuras, deformación, termobarometría.*

Geogaceta, 57 (2015), 3-6.
ISSN (versión impresa): 0213-683X
ISSN (Internet): 2173-6545

Fecha de recepción: 27 de junio de 2014
Fecha de revisión: 22 de octubre de 2014
Fecha de aceptación: 28 de noviembre de 2014

Introducción, objetivos y metodología

En relación con rocas basálticas alcalinas, de edad neógeno-cuaternaria en la Zona Volcánica de Cataluña (ZVC), se han encontrado xenolitos mantélicos de lherzolitas y harzburgitas con espinela, además de algunas piroxenitas, que fueron estudiados recientemente para abordar cuestiones relacionadas con la fusión parcial del manto subcontinental litosférico (MSCL), refertilización, metasomatismos, así como sobre sus condiciones de equilibrio (Bianchini *et al.*, 2007; Galán *et al.*, 2008, 2011; Galán y Oliveras, 2014). En estos trabajos previos se indica que la microestructura dominante en estas rocas es la protogranular, con variedades muy subordinadas de microestructuras porfidoclásticas y equigranulares en las lherzolitas (Mercier y Nicolas, 1975). Sin embargo, un muestreo nuevo, más exhaustivo, confirma que estos dos últimos tipos son frecuentes entre las lherzolitas, y que además no existe relación entre la geoquímica de roca total y de minerales y los tipos microestructurales (Fernández-Roig *et al.*, 2013).

El objetivo de este trabajo es integrar datos microestructurales y de química mineral de muestras nuevas con las estudiadas previamente, para evaluar el significado de la deformación en las lherzolitas y las condiciones de temperatura (T) y presión (P) a las que esta tuvo lugar. La relación entre las microestructuras de los xenolitos, el significado de la deformación, así como sus condiciones de equilibrio, se han abordado previamente en otras zonas de la placa europea (Brown *et al.*, 1980; Downes, 1990; Embey-Isztin *et al.*, 2001; Rampone *et al.*, 2010). En la mayoría de estos trabajos, se considera que las microestructuras porfidoclásticas y equigranulares derivan de las protogranulares por deformación y recristalización más intensa, durante el ascenso del manto ligado al desarrollo del *rift* centro-occidental europeo, desde el Neógeno. Se han considerado dos modelos (Downes, 1990 y referencias incluidas): (1) la deformación se produciría en bandas a gran escala, dispuestas lateralmente, bordeando diapiros mantélicos, o bien (2) la deformación ocurriría en zonas de cizalla a menor escala, situadas por encima del manto ascendente, que alternarían con zonas menos deformadas.

Un total de 48 lherzolitas nuevas se estudiaron con el microscopio petrográfico para clasificarlas desde el punto de vista textural y mineralógico. De estas, se seleccionaron 19 para analizar sus minerales por microsonda electrónica de barrido, CA-

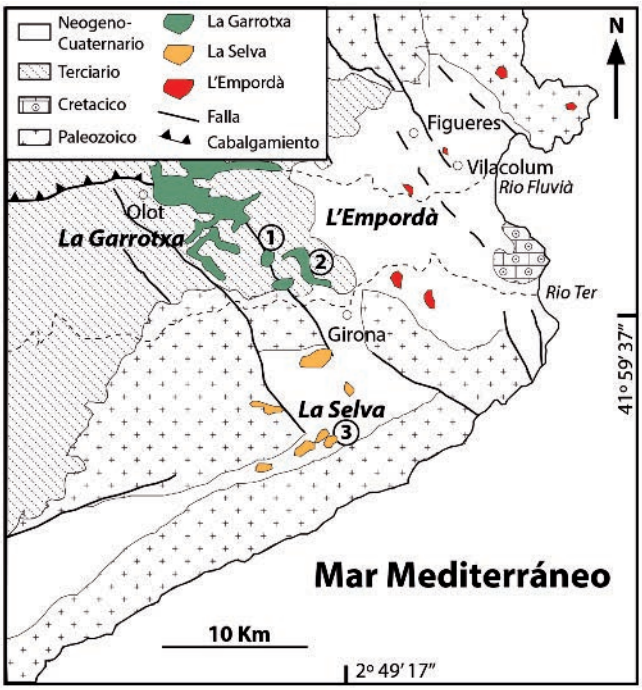

Fig. 1.- Mapa geológico simplificado de la ZVC con las tres sub-zonas que la integran, y la situación de los volcanes muestreados: La Banya del Boc (1), Canet d'Adri (2) y Sant Corneli (3) (Solé Sabaris, 1962, y Tournon, 1968 modificados).

Fig. 1.- Geological map of the CVZ, modified after Solé Sabaris (1962) and Tournon (1968). The three sub-zones of the CVZ and the location of the volcanoes are included: Banya del Boc (1), Canet d'Adri (2) and Sant Corneli (3).

MECA SX-50, en los Centros Científicos y Tecnológicos de la Universidad de Barcelona. Entre estas muestras predominan las microestructuras porfidoclásticas y equigranulares, menos estudiadas anteriormente. Las condiciones de trabajo utilizadas fueron las estándar, excepto en el análisis de piroxenos con exsoluciones, para los que se estimó una composición global media a partir de análisis puntuales realizados con un haz de electrones agrandado (50 µm).

Contexto geológico

Durante el Neógeno- Cuaternario, el NE de la Península Ibérica experimentó una distensión causada por fallas tardi-alpinas que originaron una serie de cuencas tectónicas. Estas fallas facilitaron la emisión de lavas de tipo basalto alcalino, basanita y basanita leucítica (López Ruiz y Rodríguez Badiola, 1985; Cebriá *et al.*, 2000) que aparecen en la ZVC. Esta zona representaría parte de la prolongación del *rift* centro-occidental europeo por el Mediterráneo occidental. El vulcanismo asociado es de tipo intraplaca continental, cuya actividad se distribuye en tres sub-zonas: L'Empordà, La Selva y La Garrotxa (Fig. 1).

Los xenolitos estudiados aparecen incluidos en coladas de lava, piroclastos y "necks" de los volcanes La Banya del Boc, Canet d'Adri (sub-zona de La Garrotxa) y Sant Corneli (sub-zona de La Selva (Fig.1).

En estudios anteriores se indica que las lherzolitas se habrían equilibrado a temperaturas más bajas y presiones más altas que las harzburgitas y piroxenitas (Galán *et al.* 2011).

Petrografía

Las lherzolitas con espinela estudiadas son principalmente anhidras, con anfíbol y plagioclasa como minerales accesorios muy ocasionales. La plagioclasa se encuentra en coronas alrededor de la espinela, del anfíbol y del ortopiroxeno, y sólo en una muestra aparece formando una microbanda junto con olivino, clinopiroxeno y espinela. La moda del clinopiroxeno varía entre el 5,2 y el 21% en volumen, y la de la espinela entre el 0,3 y el 8,0%. Para su descripción se han dividido en tres tipos microestructurales, aunque hay gradaciones entre todas ellas.

Lherzolitas protogranulares (Fig. 2A). Son las más frecuentes (57% del total). Se han encontrado principalmente en La Banya del Boc, pero no en Sant Corneli. Los cristales de olivino y ortopiroxeno son xenomorfos y tienen un tamaño mayor de 2 mm, bordes curvos o rectos, rara vez con contactos a 120º, y síntomas de deformación débiles, como extinción ondulante, bandas de deformación y subgranos. Los cristales de clinopiroxeno y de espinela (con un tamaño < 1 mm) son también xenomorfos (Fig. 2B) y normalmente aparecen asociados entre si y con los de ortopiroxeno. Los cristales de espinela suelen presentar formas ameboides (Fig. 2B).

Lherzolitas porfidoclásticas (Fig. 2C). Representan aproximadamente el 27% del total, y son dominantes en Sant Corneli. Los porfidoclastos de ortopiroxeno son los más abundantes (< 1 cm), aunque también los hay de olivino y menos de clinopiroxeno y de espinela. La matriz que los envuelve es de menor tamaño (< 2 mm), formada por neoblastos de los mismos minerales. Los porfidoclastos de ortopiroxeno tienen *kink bands*, lamelas de exsolución de espinela y/o de clinopiroxeno, que pueden estar deformadas, y bordes irregulares tipo "bulging". Los porfidoclastos de espinela presentan formas ameboides, a menudo estiradas (Fig. 2D). Los neoblastos muestran menos síntomas de deformación y tienen bordes ligeramente curvos, o rectos a 120º. En algunas de estas lherzolitas, especialmente en las de Sant Corneli, se observa una orientación clara, definida por la disposición de los porfidoclastos, y ocasionalmente microbandas en la matriz, enriquecidas en olivino o clinopiroxeno.

Lherzolitas equigranulares (Fig. 2E). Son las menos abundantes (16% del total), pero se localizan en las dos sub-zonas muestreadas. Se diferencian de las anteriores porque domina la matriz (tamaño de grano < 2 mm) y el número de porfidoclastos es < 5 %. Los bordes de los neoblastos son mayoritariamente rectos, a 120º, y con pocos síntomas de deformación. Los cristales de espinela son xenomorfos, más redondeados que en los tipos anteriores, y están en posición intersticial (Fig. 2F). Muy ocasionalmente, algunas de estas lherzolitas equigranulares son tabulares, porque los cristales de olivino alargados definen una foliación.

Química mineral

El contenido en forsterita (Fo) del *olivino* varía de 89,1 a 91,0% (Tabla I). No existe relación entre la composición del olivino y el tipo de microestructura, pero los contenidos más bajos en Fo corresponden a lherzolitas porfidoclásticas y equigranulares. No se han observado diferencias significativas entre el contenido en Fo de los porfidoclastos y de los neoblastos de una misma muestra.

El *ortopiroxeno* es enstatita alumínica y alumínico-cromífera, con un número Mg [#Mg= 100*Mg/(Mg+Fe_{total}) en átomos por fórmula unidad (afu)] entre 89,5 y 90,2 (Tabla I). El #Mg de esta fase tampoco

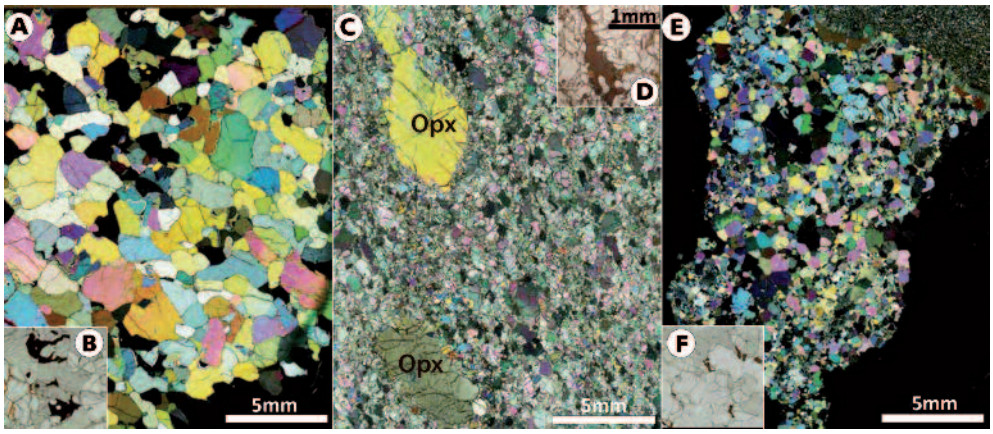

Fig. 2.- Microestructuras principales de las lherzolitas. A) Protogranular. B) Detalle de los cristales de espinela ameboide en la lherzolita 2A. C) Porfidoclástica. D) Detalle de porfidoclasto estirado y ameboide de espinela en 2C. E) Equigranular. F) Neoblasto de espinela en posición intersticial. La escala de las Figs. 2A y E es también válida para las Figs. 2B y F.

Fig. 2.- Main microstructures of lherzolites. A) Protogranular B) Detail of amoeboid spinel crystals in lherzolite 2A. C) Porphyroclastic. D) Detail of a streched and amoeboid spinel porphyroclast. E) Equigranular.. F) Interstitial spinel neoblasts. Scale for 2A and E are also valid for 2B and F.

muestra una diferencia clara entre los tres tipos de lherzolitas, pero los valores más bajos se encuentran también en las lherzolitas porfidoclásticas y equigranulares (Fig. 3A). El rango del número Cr [#Cr=100* Cr/(Cr+Al_{total}) en afu] es 4,60-10,0 (Tabla I). Tampoco se han encontrado diferencias composicionales significativas entre los porfidoclastos y los neoblastos, aunque el análisis de los primeros con un haz de electrones más ancho indica contenidos originales mayores en Al, Ca, Na y Cr. La proyección de #Mg *vs.* #Cr (no representada) muestra dispersión, así como la proyección de la concentración de Al_2O_3 *vs.* #Mg (Fig. 3A).

El *clinopiroxeno* es diópsido alumínico-cromífero, y sódico en algunas muestras. Los valores de #Mg y #Cr varían entre 89,1-91,8 y 6,70-12,8, respectivamente, registrándose también los valores más bajos en las lherzolitas deformadas (Tabla I). Tampoco hay diferencias significativas entre porfidoclastos y neoblastos, pero los análisis con un haz de electrones agrandado dan composiciones globales ligeramente más alumínicas para los primeros. No existe correlación entre #Mg y #Cr o entre el contenido en Al_2O_3 y #Mg (no representadas), ni se aprecian diferencias composicionales claras entre los tipos microestructurales. Sin embargo, si hay una correlación positiva entre Na en la posición M2 y Al en la posición M1 de los cristales (Fig. 3B). Esta figura muestra que, con algunas excepciones, la sustitución jadeítica disminuye de las lherzolitas protogranulares hacia las porfidoclásticas y equigranulares.

La *espinela* de las lherzolitas es espinela *sensu stricto,* con #Mg entre 73,5 y 79,7 y #Cr entre 9,6 y 23,7. La correlación entre estos dos parámetros (Fig. 3C) muestra dos tendencias: (1) una con buena correlación negativa entre un pequeño grupo de lherzolitas protogranulares; y (2), otra también con buena correlación negativa, pero con menor pendiente, para la mayoría de lherzolitas porfidoclásticas y equigranulares.

Condiciones de equilibrio (T, P)

El termómetro clinopiroxeno-ortopiroxeno (Brey y Köhler, 1990) proporciona los rangos de T siguientes: lherzolitas protogranulares (950-1082 ºC), porfidoclásticas (867-959 ºC), transicionales entre los dos tipos anteriores (853-953 ºC), y finalmente, para las equigranulares entre 829-995 ºC. Sin embargo, las estimaciones para las lherzolitas porfidoclásticas, en las que se ha medido la composición global de los porfidoclastos de ortopiroxeno y/o clinopiroxeno, la T son más altas (955-1125 ºC). Para establecer estos rangos se han tenido en cuenta, además de las muestras aquí estudiadas, los datos de Galán *et al.* (2011).

El barómetro clinopiroxeno-olivino (Köhler y Brey, 1990) da valores de presión dispersos e incluso incoherentes para la mayoría de las muestras. Los rangos de presión siguientes corresponden solamente a estimaciones coherentes y con buena precisión (< 20%): lherzolitas protogranulares (1,88-1,13 GPa) y todas las demás entre 0,60 y 0, 98 GPa.

Microestructura	Olivino	Ortopiroxeno		Clinopiroxeno		Espinela	
	%Fo	#Mg	#Cr	#Mg	#Cr	#Mg	#Cr
Protogranular	90,5	90,8	7,66	91,0	10,5	76,3	17,7
Transicional	89,6	89,9	5,13	89,4	7,19	78,8	10,8
Porfidoclástica	89,6	90,1	5,65	90,3	8,12	75,4	12,3
Equigranular	89,8	90,2	5,29	90,4	8,02	78,3	10,8
Desenfocado	-	89,8	6,27	89,5	7,94	-	-

Tabla I.- Media de los contenidos en forsterita del olivino, y de los valores de #Mg y #Cr en los piroxenos y espinela de las lherzolitas

Table I.- Average fosterite content in olivine, and Mg# and Cr# in pyroxenes and spinel of lherzolites.

Discusión

Los resultados obtenidos indican que las lherzolitas más fértiles se encuentran entre las que están deformadas. Ahora bien, no existe una separación clara entre el grado de fertilidad y los tipos microestructurales (Fig. 3A y C). Además, el contenido en Al_2O_3 de los piroxenos se proyecta muy disperso respecto al índice de diferenciación #Mg (Fig. 3A). En el caso de la espinela, sí existe una correlación negativa entre #Cr y #Mg que podría corresponder a un proceso de fusión parcial, pero se observan dos tendencias diferentes entre algunas lherzolitas protogranulares respecto a los otros tipos. Todo esto sugiere que o bien no existe relación entre las lherzolitas por fusión parcial, o si existió, esta relación fue borrada por procesos de deformación subsolidus.

Donde se ve mejor la influencia de la deformación en el quimismo mineral es en la evolución de algunas substituciones, como la de tipo jadeita ($^{M2}Na^{M1}Al^{M2}Ca_{-1}{}^{M1}Mg_{-1}$) en el clinopiroxeno. Esta sustitución en las muestras nuevas decrece hacia las lherzolitas porfidoclásticas y equigranulares, lo que implicaría que la deformación se desarrollaría a P decreciente (Aoki y Shiba, 1973). La figura 3C ilustra que en el

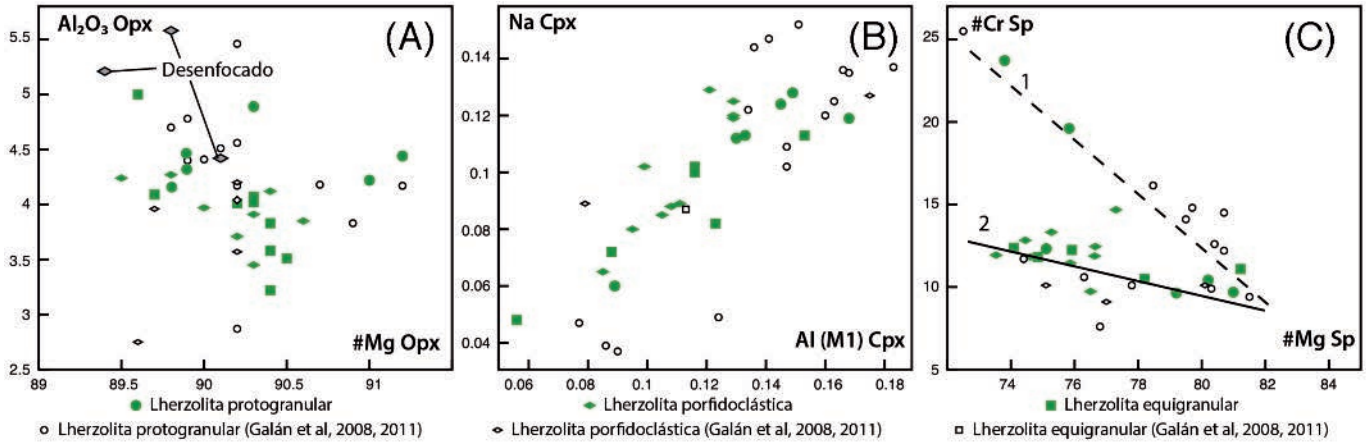

Fig. 3.- A) Dispersión del Al2O3 (% masa) vs. #Mg del ortopiroxeno. B) Tendencia decreciente del Na vs. Al, en la posición M1 (afu) del clinopiroxeno, hacia las lherzolitas más deformadas. C) #Cr vs. #Mg de la espinela mostrando dos tendencias: (1) para la mayoría de lherzolitas protogranulares y (2) para la mayoría de lherzolitas porfidoclásticas y equigranulares.

Fig. 3.- A) Scatter of Al2O3 (wt%) vs. #Mg for the orthopyroxene. B) Decreasing trend of Na vs. Al, in the M1 site of clinopyroxene (afu), towards the most deformed lherzolites. C) #Cr vs. #Mg for spinel showing two trends: (1) for most protogranular lherzolites and (2) for most porphyroclastic and equigranular lherzolites.

caso de la espinela, la tendencia (2) que se observa en las lherzolitas deformadas presenta #Cr inferior a igual #Mg que en las protogranulares, es decir, la espinela se hace más alumínica. Esto podría explicarse por una re-equilibración subsolidus, con intercambio de Al y Cr entre piroxenos y espinela, al disminuir la T y P (Barnes y Roeder, 2001; Voigt y Handt, 2011).

Los escasos datos geobarométricos y los datos geotermométricos también confirman que la deformación tuvo lugar a P y T decrecientes. Así, los valores más altos de T corresponden a lherzolitas protogranulares y a los análisis que integran exsoluciones de los porfidoclastos de clinopiroxeno y ortopiroxeno

Esta deformación a T y P decrecientes se ha observado en xenolitos mantélicos de otras áreas de la placa europea. La mayoría de autores (Downes, 1990; Embey-Isztin *et al.*, 2001; Rampone *et al.*, 2010) está de acuerdo en que se asocia a deformación en zonas de cizalla, posiblemente relacionadas con los episodios iniciales del *rift* neógeno, hipótesis que podría ser también válida en este caso.

Conclusiones

La variedad microestructural que presentan las lherzolitas con espinela en los xenolítos mantélicos de la ZVC se relacionaría con la existencia de una deformación progresiva, desde las lherzolitas protogranulares a las equigranulares, pasando por las porfidoclásticas. No se ha encontrado relación entre el grado de fertilidad y las microestructuras.

La disminución del componente jadeítico en el clinopiroxeno y la evolución de la composición de la espinela, junto con los datos termobarométricos, indicarían que la deformación tuvo lugar a T y P decrecientes.

Esta deformación estaría ligada a zonas de cizalla relacionadas con el inicio del rift neógeno.

Agradecimientos

Este trabajo se ha beneficiado de una beca FPI BES-2012-051860 y del proyecto CGL-2011-26700. Los autores agradecen los comentarios de G. Alias, S. Llana-Fúnez y I. Arenillas para mejorar el manuscrito.

Referencias

Aoki, K.I. y Shiba, I. (1973). *Lithos* 6, 41-51.

Barnes, S.J. y Roeder, P.L. (2001) *Journal of Petrology* 42(12), 2279-2302.

Bianchini, G., Beccaluva, L., Bonadiman, C., Nowell, G., Pearson G., Siena, F. y Wilson, M. (2007). *Lithos* 94, 25-45.

Brey, G.P. y Köhler, T.P. (1990). *Journal of Petrology* 31, 1353-1378.

Brown, G.M., Pinsent, R.H. y Coisy, P. (1980). *American Journal of Science* 280A, 471-498.

Cebriá, J.M., López-Ruiz, J., Doblas, M., Oyarzun, R., Hertogen, J. y Benito, R. (2000). *Journal of Volcanology and Geothermal Research* 102, 217–235.

Downes, H. (1990). *Geology* 18, 374–377.

Embey-Isztin, A., Dobosi, G., Altherr, R. y Meyer, H.P. (2001). *Tectonophysics* 331, 285-306.

Fernández-Roig, M., Galán, G., Oliveras, V., Pin C., Grégoire, M. y Devidal, J.L. (2013). En: *Mineralogical Magazine*, Goldschmidt, Conference Abstracts, p 1078.

Galán, G. y Oliveras, V. (2014). *Chemical Geology* 366, 75-89.

Galán, G., Oliveras, V. y Paterson, B.A. (2008). En: *Metasomatism in oceanic and continental lithospheric mantle* (M. Coltorti and M. Grégoire , Eds.), Geological Society, London, Special Publication, 293, 121–153.

Galán, G., Oliveras, V. y Paterson, B.A. (2011). *International Journal of Earth Sciences* 100, 81–106.

Köhler, T.P. y Brey, G.P. (1990). *Geochimica et Cosmochimica Acta* 54, 2375-2388.

López Ruiz, J. y Rodríguez Badiola, E. (1985). *Estudios Geológicos* 41, 105–126.

Mercier, J.-C. y Nicolas, A. (1975) Journal of Petrology 16, 454–487.

Rampone, E., Vissers, R., Poggio, M., Scambelluri, M. y Zanetti, A. (2010). *Journal of Petrology* 51, 295-325.

Solé Sabaris, L. (1962). *Memorias de Real Academia de las Ciencias y las Artes de Barcelona* 34, 359–372.

Tournon, J. (1968). *Le volcanisme de la province de Gérone (Espagne). Études de basaltes quaternaires et de leurs enclaves.* Thèse 3e cycle Laboratoire de Pétrographie de la Faculté de Sciences de Paris,120p.

Voigt, M. y Handt, A. (2011). *Contributions to Mineralogy and Petrology* 162(4), 675-689.

Geoquímica de roca total y fábricas de deformación del olivino en xenolitos mantélicos del NE de España: claves para la evaluación de la petrogénesis y la deformación en el manto litosférico.

Insight into lithospheric mantle petrogenesis and deformation from whole-rock geochemistry and olivine deformation fabrics in mantle xenoliths from NE Spain.

G. Galán[1]y M. Fernández-Roig[1]

1 Dept. de Geologia. Universitat Autònoma de Barcelona, Av. dels Til·lers s/n, 08193 Bellaterra, Barcelona. gumer.galan@uab.cat

Resumen: El manto subcontinental litosférico en el NE de España está formado principalmente por lherzolitas y harzburgitas con espinela y anhidras. La composición química en elementos mayores y trazas moderadamente incompatibles de estas rocas define una trayectoria comparable a la de una fusión fraccionada del manto (<30%) por descompresión. La existencia de lherzolitas muy fértiles y una dispersión mayor de estas en los diagramas de covariación sugiere también refertilización ígnea del manto litosférico. Todas las harzburgitas y algunas lherzolitas fueron posteriormente metasomatizadas por fundidos silicatados alcalinos y carbonatíticos. Ambas peridotitas experimentaron una deformación transpresiva o de cizalla simple, seguida de recristalización estática, que desarrollaron fábricas de deformación axial [010] en el olivino. Posteriormente, algunas lherzolitas se deformaron en condiciones más superficiales, en un régimen de deformación transtensivo que transformó la fábrica anterior en ortorrómbica y axial [100] con menos fuerza. La no correlación entre la fuerza de estas últimas fábricas y parámetros composicionales sugiere que la deformación transtensiva es posterior a los procesos petrogenéticos principales.

Palabras clave: Lherzolitas, Harzburgitas, Geoquímica, Olivino, Fabricas de deformación.

Abstract: *The subcontinental listhospheric mantle in NE Spain is mainly formed of anhydrous spinel lherzolites and harzburgites. Whole-rock major and milddly incompatible trace element geochemistry define a trend consistent with fractional melting (<30%) during mantle decompression. Very fertile compositions of lherzolites and their scattering in covariation diagrams also suggest igneous refetilization of the lithospheric mantle. Later on, all harzburgites and some lherzolites were metasomatized by alkaline silicate and carbonatitic melts. Both peridotites were deformed by simple share or transpression, followed by annealing, which develops olivine [010]-fiber deformation fabric. A later transtensive deformation regime, at shallower conditions, affected some lherzolites transforming the earlier deformation fabric into weaker orthorhombic and [100]-fiber types. Since there are no relationships between the strength of these later fabrics and compositional indices, the transtensive deformation may have post-dated the main petrogenetical processes.*

Key words: *Lherzolites, Harzburgites, Geochemistry, Olivine, Deformation fabrics*

INTRODUCCIÓN, ANTECEDENTES Y MARCO GEOLÓGICO

Los xenolitos mantélicos en lavas basálticas alcalinas cenozoicas representan una oportunidad única para evaluar los procesos petrogenéticos y la deformación en el manto litosférico así como la posible relación entre ambos procesos. En las lavas basálticas alcalinas pertenecientes al volcanismo neógeno-cuaternario de la Zona Volcánica de Cataluña (ZVC) se encuentran esporádicamente este tipo de xenolitos, la geoquímica de los cuales (elementos mayores y traza) se utilizará en este estudio, junto con la fuerza de la fábrica de deformación del olivino, para evaluar la posible relación entre la deformación mantélica y los procesos petrogenéticos.

Estudios previos sobre estos xenolitos son de Bianchini et al. (2007), Galán et al. (2008) y Galán y Oliveras (2014), que indican que el manto litosférico bajo la ZVC está formado principalmente por lherzolitas y harzburgitas con espinela y anhidras. Las harzburgitas tienen una microestructura protogranular, de grano algo más grueso que las lherzolitas. Estas últimas tienen microestructura protogranular (tamaño de grano> 2mm), pero también porfidoclástica y equigranular (tamaño de grano< 2mm). La geoquímica de elementos mayores y traza en minerales y rocas, y los isótopos de Sr, Nd y Hf en cristales de clinopiroxeno sugieren que estas peridotitas son el resultado de uno o varios episodios de fusión parcial y de metasomatismos posteriores, sin que se pueda descartar que la historia de harzburgitas y lherzolitas haya sido diferente y que procesos de refertilización ígnea estén detrás de la formación de algunas lherzolitas. Las estimaciones termométricas indican que la temperatura de equilibrio disminuye (1082-829 °C) de las harzburgitas y lherzolitas protogranulares hacia las lherzolitas porfidoclásticas y equigranulares, lo mismo que el contenido en jadeita del clinopiroxeno (Fernández-Roig y Galán, 2015).

Los afloramientos principales de la ZVC se localizan en Girona (Fig. 1) y se dividen en tres sub-zonas: el Empordà, la Selva y la Garrotxa. Esta actividad volcánica se relaciona con fallas tardi-alpinas de dirección NW-SE y SW-NE, que prolongan el rift cenozoico occidental europeo a lo largo de la costa mediterránea de la Península Ibérica. Los xenolitos aquí estudiados son nuevos y se recogieron en los volcanes la Banya del Boc, Canet d'Adri (ambos en La Garrotxa) y Sant Corneli, en La Selva (Fig. 1).

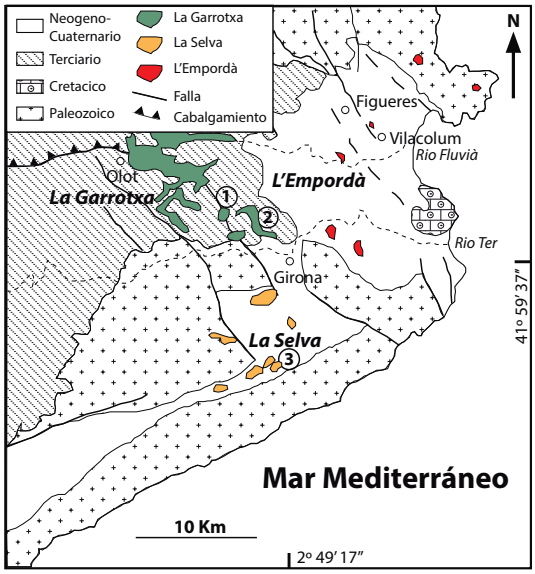

FIGURA 1. *Mapa geológico simplificado de la ZVC con las tres sub-zonas que la integran, y la situación de los volcanes muestreados: La Banya del Boc (1), Canet d'Adri (2) y Sant Corneli (3).*

RESULTADOS

Geoquímica de roca total

Se analizaron doce lherzolitas y siete harzburgitas con espinela. Entre las lherzolitas analizadas dominan las que tienen microestructura porfidoclástica y equigranular, para completar el muestreo anterior (Galán et al., 2008; Galán y Oliveras, 2014).

Estas peridotitas muestran una variación gradual en MgO desde las lherzolitas (36-44%) a las harzburgitas (44-48%), y una correlación negativa buena de este óxido con los de Al_2O_3 (Fig. 2A) y CaO, con mayor dispersión en el caso de la lherzolitas. Mayor dispersión se observa también en la covariación de otros componentes basálticos (TiO_2, Na_2O) y de SiO_2 y FeO_T respecto al MgO (no representados). Tres de las lherzolitas tienen una composición más fértil que el Manto Primitivo (MP). No hay diferencias composicionales significativas entre las lherzolitas con diferente microestructura, aunque las más fértiles son porfidoclásticas.

Los elementos traza moderadamente incompatibles (Sc, Ga, Y, Yb) muestran también una correlación negativa buena con el MgO, y entre si (Fig. 2B), pero la covariación de otros elementos traza (Cr, Sr, Ba, Nb, Ta, La, Zr) es muy dispersa. También hay una correlación positiva, entre algunos de los elementos traza más incompatibles (Th, Nb, Sr vs. La), para valores superiores a los del MP. Solo el Ni tiene una correlación positiva buena con el MgO, con valores de Ni< 2200 ppm en las lherzolitas y mayores en las harzburgitas.

Los diagramas multielementales difieren en lherzolitas y harzburgitas (Figs. 3A-B) por el contenido en Tierras Raras Pesadas (HREE) principalmente, con valores entorno a los del MP en las lherzolitas e inferiores en las harzburgitas. En las lherzolitas, la fraccionación entre las Tierras Raras ligeras (LREE) y las HREE, es muy variable (La_N/Yb_N= 0-26). En las harzburgitas también, pero el rango La_N/Yb_N es >1 (4-27) debido a la disminución de las HREE, que además están fraccionadas respecto a las REE medias (MREE) (Sm_N/Yb_N=1.6-6.3). No se observan anomalías en Eu respecto a las MREE o son poco significativas. Otras características son la presencia de una anomalía negativa general en Zr y menor en Ti respecto a las MREE, un incremento de Th y U con las LREE y la existencia de anomalías positivas ocasionales en Pb, Nb-Ta y rara vez en Rb. No hay diferencias entre los diagramas multielementales de las lherzolitas con microestructura diferente (Fig. 3A). En las harzburgitas se distinguen dos grupos: uno más empobrecido, con concentraciones de Hf y Nb-Ta no detectables, y otro grupo ligeramente más enriquecido (Fig. 3B).

Fábricas de deformación del olivino

La determinación de las orientaciones cristalográficas preferentes de olivino, por difracción de electrones retrodispersados con un SEM, en catorce lherzolitas y en tres harzburgitas, indica que la fábrica de deformación dominante es de tipo axial [010], con un índice BA (Mainprice et al., 2015) = 0,09-0,39, seguida del tipo ortorrómbico (BA= 0,42-0,48) y

ROCA	IN. BA	IN.J	OL	CPX/OPX
HZ Pg (3)	0.23-0.39 (Axial [010])	10.2-9.02	72.8-86.4	0.13-0.30
LHZ Pg (3) Pg-Pc (2)	0.25-0.29 0.23-0.42 (A [010])> Orto.)	8.97-4.20 5.72-4.69	70.4-52.2	0.36-0.38
LHZ Pc (5)	0.24-0.78 (A [010])=Orto.> A[100])	4.65-1.91	65.0-45.5	0.26-0.50
LHZ Eq (4)	0.09-0.42 (A [010])>Orto.)	5.43-1,91	71.7-53.3	0.36-0.91

TABLA I. *Fábricas de deformación del olivino, rangos de índices (IN) BA y J de las mismas, de olivino modal (% masa) y relaciones modales clinopiroxeno/ortopiroxeno en harzburgitas y lherzolitas. A:axial; Orto.: ortorrómbica; otros símbolos como en Fig. 2. Se indica número de muestras de cada tipo.*

raramente del tipo axial [100] (BA=0,78). El tipo axial [010] es más característico de harzburgitas y lherzolitas protogranulares, mientras que los otros tipos aparecen en lherzolitas porfidoclásticas y equigranulares. La fuerza de la fábrica (índice J de Ben Ismaïl y Mainprice, 1998) decrece de las fábricas de tipo axial [010] hacia los tipos ortorrómbico y axial [100] (Tabla I), aunque no linealmente. En general, el índice J se correlaciona positivamente con el contenido en MgO de las rocas y con el olivino modal, estimado a partir de los análisis químicos de roca total y de minerales, pero las lherzolitas porfidoclásticas y equigranulares, con valores de J bajos, se dispersan (no representado). La correlación del índice J con los elementos traza moderadamente incompatibles es negativa, pero las lherzolitas también se dispersan. Finalmente, no hay relación entre el índice J y la relación La_N/Yb_N

DISCUSION

Tanto los diagramas de covariación Al_2O_3 vs. MgO o entre elementos traza moderadamente incompatibles (Figs. 2A-B) indican que estos xenolitos representan residuos de una fusión fraccionada mantélica, más intensa para las harzburgitas (15-30% de fusión) que para las lherzolitas (<20%). La fusión ocurriría a presiones entre 3-2 y 0,5 GPa para la mayoría de las muestras (Fig. 2A). Ahora bien, en otros diagramas de variación (eg, SiO_2 o FeO_T vs. MgO no representados), la proyección de las peridotitas es más dispersa e indican presiones de fusión contradictorias, o bien las muestras se proyectan fuera de las trayectorias de fusión. Esto sugiere que algunas de ellas no son simples residuos de fusión, sinó posibles productos de interacción roca-fundido percolante (Herzberg, 2004), lo que también explicaría que la estimación del olivino modal en algunas lherzolitas sea inferior al de las trayectorias de fusión de un MP. La relación clinopiroxeno/ortopiroxeno es sin embargo coherente con estas trayectorias en la mayoría de las muestras, por lo que la disolución del olivino podría deberse a refertilización ígnea del manto por percolación de fundidos basálticos que generarían la neocristalización de clinopiroxeno-ortopiroxeno±espinela. Un proceso de refertilización también explicaría que algunas lherzolitas tengan una composición igual o más fértil que el MP (Fig. 2). Sin embargo, no se observan saltos composicionales significativos entre lherzolitas y harzburgitas, ni trayectorias de evolución diferentes para las dos peridotitas, como ocurre en otros ejemplos del manto litosférico que se han interpretado por procesos de refertilización.

El contenido en elementos traza más incompatibles (Figs. 3A-B) indica que harzburgitas y lherzolitas fueron posteriormente afectadas por metasomatismo, pero sus efectos son muy desiguales en las lherzolitas, que están desde muy empobrecidas a muy enriquecidas en estos elementos. Se incrementa especialmente la concentración de LREE, MREE, Th, U, Nb, Ta, Pb y

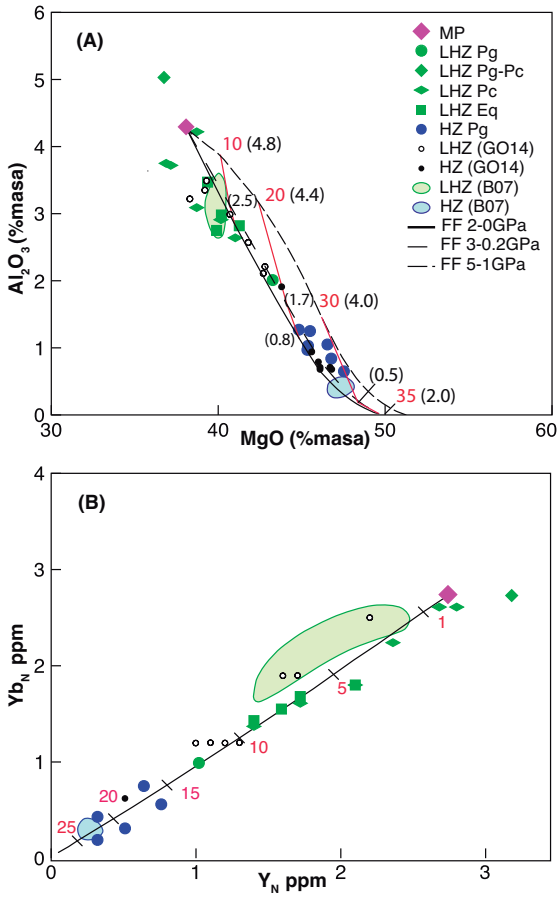

FIGURA 2. *(A) Al_2O_3 vs. MgO incluyendo datos analíticos anteriores (Bianchini et al.,2007-B07; Galán y Oliveras, 2014-GO14) y las trayectorias de fusión fraccionada por descompresión (Herzberg, 2004). Las líneas y números rojos representan porcentajes de fusión y los números entre paréntesis presiones intermedias entre la inicial y la final. (B) Yb_N vs. Y_N con la trayectoria de una fusión fraccionada no modal. Porcentajes modales del fundido y coeficientes de partición de Johnson et al. (1990). Composición del MP de McDonough y Sun (1995).*

Sr. Teniendo en cuenta que el nivel de enriquecimiento en estos elementos es comparable en las dos peridotitas, se deduce que ambas fueron afectadas por el mismo evento metasomático. Las bajas relaciones Nb/Ta (0.33-0.66) y Zr/Hf (0.56-10.5) en la mayoría de las muestras, así como la ausencia de una anomalía negativa significativa en Ti respecto a las MREE, son más características de un componente metasomático tipo fundido alcalino silicatado que carbonatítico. Sin embargo, este último podría haber afectado a las harzburgitas más empobrecidas, con concentraciones de Nb-Ta y Hf-Zr muy bajas (Fig. 3B). Finalmente, el enriquecimiento en elementos incompatibles no guarda relación con la moda estimada, por tanto, se trataría de metasomatismo(s) principalmente críptico, posterior a los efectos de posibles procesos de refertilización.

Como la fábrica de deformación axial [010] del olivino es común a lherzolitas y harzburgitas, ambas peridotitas habrían sido afectadas por el mismo régimen tectónico, de cizalla simple o transpresivo seguido de recristalización estática a alta temperatura. Posteriormente, esta fábrica se habría reactivado, a

menor temperatura y profundidad, durante un régimen de deformación transtensivo que originaría las fábricas de deformación ortorrómbicas y axial [100], más débiles, en lherzolitas recristalizadas de grano más fino (Fernández-Roig et al., *sometido*). La pérdida de correlación entre la fuerza de la fábrica y la composición química en estas lherzolitas deformadas a menor temperatura, indicaría que esta última deformación es posterior a los procesos petrogenéticos más significativos.

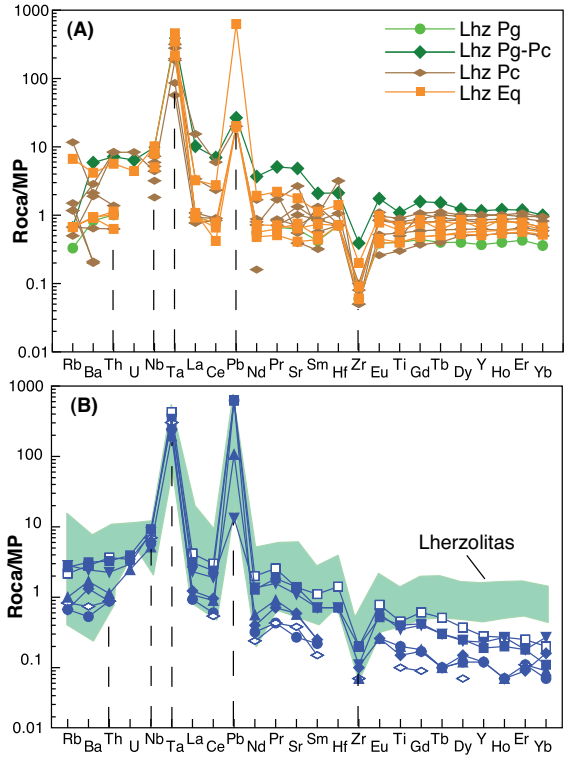

FIGURA 3. *Diagramas multielementales normalizados al MP (McDonough y Sun, 1995). A) Lherzolitas con diversas microestructuras. B) Harzburgitas con el rango composicional de lherzolitas en (A). Abreviaciones como en la Fig. 2.*

CONCLUSIONES

Las lherzolitas y harzburgitas con espinela que forman el manto litosférico en el NE de España se explicarían por procesos de fusión fraccionada (<30%), por descompresión entre 2-3 y 0,5 GPa. Procesos de refertilización ígnea podrían además explicar la mayor dispersión composicional de las lherzolitas, algunas de la cuales son muy fértiles. Todas las harzburgitas y algunas lherzolitas están además afectadas posteriormente por metasomatismo críptico. Los componentes metasomáticos serían fundidos silicatados alcalinos y carbonatíticos.

Ambos tipos de peridotitas registran un episodio de deformación transpresivo o de cizalla simple, seguido de recristalización estática, que originaron una fábrica axial [010] en el olivino. Un episodio de deformación posterior transtensivo reactivó la fábrica anterior en algunas lherzolitas y la transformó en ortorrómbica y axial [100] a menor profundidad. La ausencia de correlaciones entre la fuerza de estas fábricas posteriores y parámetros composicionales sugiere que la deformación transtensiva es posterior a los procesos petrogenéticos más importantes.

AGRADECIMIENTOS

Este trabajo ha sido financiado por el proyecto MINECO CGL2011-26700 y las becas FPI BES- 2012-051860 y EEBB-I-14-07880.

REFERENCIAS

Ben Ismaïl, W., Mainprice, D. (1998): An olivine fabric database: an overview of upper mantle fabrics and seismic anisotropy. *Tectonophysics,* 296: 145–157.

Bianchini, G., Beccaluva, L., Bonadiman, C., Nowell, G., Pearson, G., Siena, F., Wilson, M. (2007): Evidence of diverse depletion and metasomatic events in harzburgite-lherzolite mantle xenoliths from the Iberian plate (Olot, NE Spain): Implications for lithosphere accretionary processes. *Lithos,* 94: 25-45.

Fernández-Roig, M., Galán, G. (2015): Microestructuras y química mineral de lherzolitas en xenolitos mantélicos de Cataluña (NE España). *Geogaceta*, 57: 3- 6.

Fernández-Roig et al., *sometido:* Deformation and seismic anisotropy of the subcontinental lithospheric mantle in NE Spain: EBSD data on xenoliths from the Catalan Volcanic Zone. *Tectonophysics*.

Galán, G., Oliveras, V. (2014): Melting and metasomatism in the lithospheric mantle of NE Spain: geochemical and Sr-Nd isotopic characteristics. *Chemical Geolo*gy, 366:75-89.

Galán, G., Oliveras, V., Paterson, B.A. (2008): Types of metasomatism in mantle xenoliths in Neogene-Quaternary alkaline mafic lavas from Catalonia (NE Spain). En: *Metasomatism in Oceanic and Continental Lithospheric Mantle* (M. Coltorti y M. Grégoire, eds.). Geological Society, London, Special Publication 293,121-153.

Herzberg, C. (2004): Geodynamic information in peridotite petrology. *Journal of Petrology*, 45:2507-2530.

Mainprice, D., Bachmann, F., Hielscher, R., Schaeben, H. (2015): Descriptive tools for the analysis of texture projects with large dataset using MTEX: trength, symmetry and components. En: *Rock deformation from field, experiments and theory. A volume in honour of Rutter*. Geological Society, London, Special publication 409:251-271.

McDonough, W.F., Sun, S.-S. (1995): Composition of the Earth. *Chemical Geology,* 120: 223-253.

Johnson, K.T.M., Dick, H.J.B., Shimizu, N.(1990). Melting in the oceanic upper mantle: an ion microprobe study of diopsides in Abyssal peridotites. *Journal Geophysical Research*,95(B3): 2661-2678.

Tectonophysics 698 (2017) 16–37

Contents lists available at ScienceDirect

Tectonophysics

journal homepage: www.elsevier.com/locate/tecto

Deformation and seismic anisotropy of the subcontinental lithospheric mantle in NE Spain: EBSD data on xenoliths from the Catalan Volcanic Zone

Mercè Fernández-Roig [a,*], Gumer Galán [a], Elisabetta Mariani [b]

[a] Departament de Geologia, Universitat Autònoma de Barcelona, Av. dels Til·lers s/n, 08193, Bellaterra, Barcelona, Spain
[b] School of Environmental Sciences, University of Liverpool, 4 Brownlow Street, L60 3GP Liverpool, England, UK

ARTICLE INFO

Article history:
Received 24 March 2016
Received in revised form 20 December 2016
Accepted 23 December 2016
Available online 3 January 2017

Keywords:
Lithosphere
Mantle
Olivine
Pyroxene
Deformation fabric
Seismic anisotropy

ABSTRACT

Mantle xenoliths in Neogene-Quaternary basaltic rocks related to the European Cenozoic Rift System serve to assess the evolution of the subcontinental lithospheric mantle beneath the Catalan Volcanic Zone in NE Spain. Crystallographic preferred orientations, major element composition of minerals, and temperature and pressure estimates have been used to this end. The mantle consists of spinel lherzolites, harzburgites and subordinate websterites. Protogranular microstructures are found in all peridotites and websterites, but lherzolites also display finer-grained porphyroclastic and equigranular microstructures. The dominant olivine deformation fabric is [010] fiber, but subordinate orthorhombic and [100]-fiber types are also present, especially in porphyroclastic and equigranular lherzolites. The fabric strength (J index = 10.12–1.91), equilibrium temperature and pressure are higher in xenoliths with [010]-fiber fabric and decrease in those with orthorhombic and [100]-fiber type. Incoherence between olivine and pyroxene deformation fabric is mostly found in porphyroclastic and equigranular lherzolites. Seismic anisotropy, estimated from the crystal preferred orientations, also decreases (AVp = 10.2–2.60%; AVs max = 7.95–2.19%) in porphyroclastic and equigranular lherzolites. The olivine [010]-fiber fabric points to deformation by simple shear or transpression which is likely to have occured during the development of late-Hercynian strike-slip shear zones, and to subsequent annealing during late Hercynian decompression, Permian and Cretaceous rifting. Also, it cannot be excluded that the percolation of mafic magmas during these extensional events provoked the refertilization of the lithospheric mantle. However, no clear relationship has been observed between fabric strength and mineral mode and composition. Later transtensional deformation during late Alpine orogenesis, at higher stress and decreasing temperature and pressure, transformed the earlier fabric into orthorhombic and [100]-fiber type.

Comparison of seismic anisotropy estimates with the available SKS-wave splitting data suggests that most of the measured seismic anisotropy would be explained by the lithospheric contribution, if the lithospheric mantle fabrics record mainly transpression and transtensional deformation.

1. Introduction

Mantle xenoliths enclosed in volcanic rocks provide key insights into the evolution of the lithospheric mantle. These xenoliths within Neogene-Quaternary alkaline basaltic rocks from the Catalan Volcanic Zone (CVZ) in NE Spain have been previously studied in attempts to determine the composition and geochemical evolution of the subcontinental lithospheric mantle (SCLM) in this area (Bianchini et al., 2007; Galán et al., 2008, 2011; Galán and Oliveras, 2014). However, little is known about this mantle petrophysical properties and deformation history. The CVZ is part of the European Cenozoic Rift System (ECRIS) which also lies along the Iberian Mediterranean coast (Fig. 1a). The deformation affecting the SCLM could well be older though, taking into account that the overlying crust registered the Variscan and Alpine orogenesis.

Experimental studies demonstrate that plastic deformation related to mantle flow processes at different scales causes strong crystal preferred orientation (CPO) of olivine and of other mantle minerals (Karato et al., 2008 and references therein). In addition, numerical modelling shows that different deformation conditions lead to varying olivine CPO (Tommasi et al., 1999). Variables include temperature (T), pressure (P) (Couvy et al., 2004; Jung et al., 2009; Ohuchi et al., 2011), stress and H_2O concentration (Jung and Karato, 2001; Jung et al., 2006; Katayama et al., 2004; Katayama and Karato, 2006). CPO can

* Corresponding author.
E-mail addresses: merce.fernandez@uab.cat (M. Fernández-Roig), gumer.galan@uab.cat (G. Galán), mariani@liverpool.ac.uk (E. Mariani).

http://dx.doi.org/10.1016/j.tecto.2016.12.023
0040-1951/

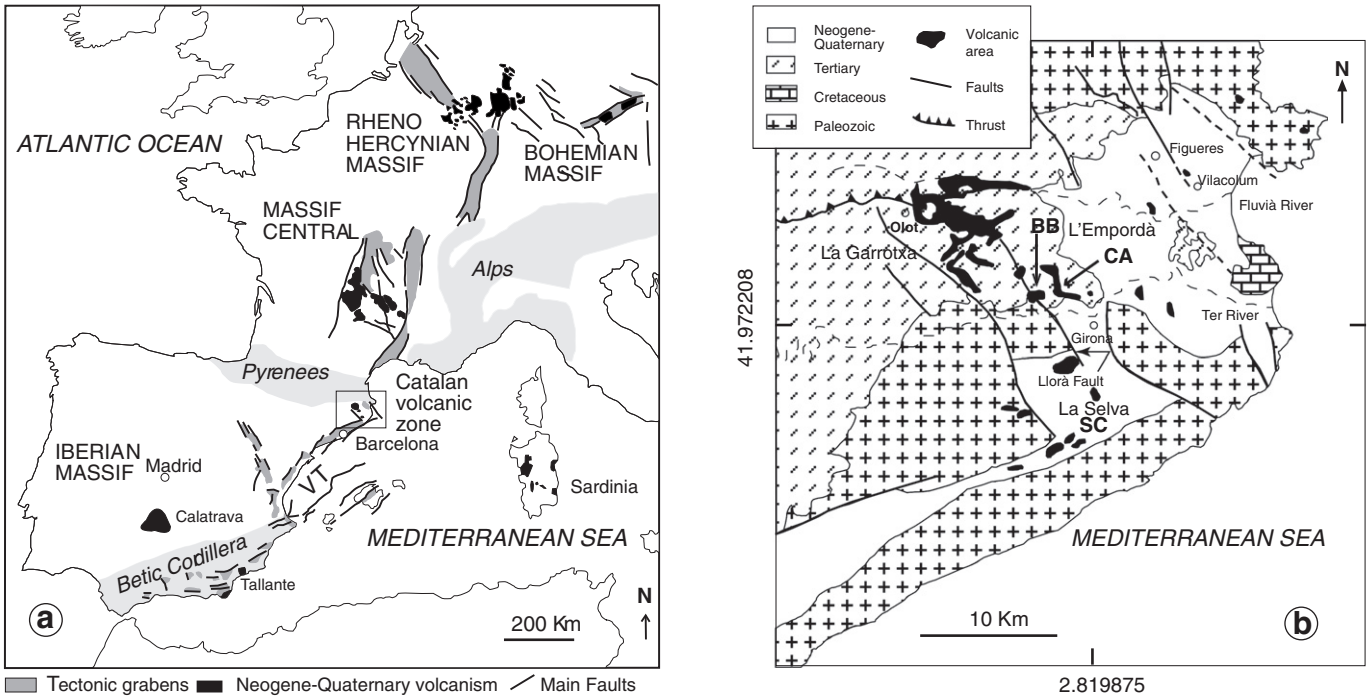

Fig. 1. Location of the Catalan volcanic zone (CVZ). (a) The CVZ within the European Cenozoic Rift System. Lighter grey represents orogenic belts. VT stands for the Valencia Trough. Modified after Martí et al. (2001). (b) Simplified geological map of the CVZ with the location of La Banya del Boc (BB), Canet d'Adri (CA) and Sant Corneli volcanoes (SC). Map modified after Solé Sabaris (1962) and Tournon (1968). Geographic ETRS89 coordinates are indicated.

also be affected by factors such as partial melting and melt percolation (Vauchez and Garrido, 2001; Holtzman et al., 2003; Rampone et al., 2010; Le Roux et al., 2008). Furthermore, CPO due to plastic deformation has been demonstrated to be the major cause of seismic anisotropy (Nicolas and Christensen, 1987; Mainprice and Silver, 1993; Mainprice et al., 2000; Mainprice, 2007). The comparison between mantle seismic anisotropy estimated from mineral CPO (Mainprice and Humbert, 1994) and regional anisotropy deduced from geophysical methods is therefore particularly useful for interpreting geodynamic and geochemical processes affecting the SCLM (Vonlanthen et al., 2006; Falus et al., 2008; Bascou et al., 2011; Palasse et al., 2012; Baptiste and Tommasi, 2014; Park et al., 2014; Park and Jung, 2015).

"Anhydrous" spinel lherzolites and harzburgites are the lithologies most frequently found in mantle xenoliths from lavas of the CVZ. Smaller numbers of websterites are also found (Bianchini et al., 2007; Galán et al., 2008). Lherzolites display variable microstructures, from protogranular (descriptive terminology by Mercier and Nicolas, 1975) or coarse granular to porphyroclastic and equigranular, whereas harzburgites and websterites display only protogranular microstructures. In this study, we evaluate the xenolith microstructures, major element compositions of minerals, T and P estimates, olivine and pyroxene CPO and resulting anisotropic seismic properties, in order to determine the deformation history, relationships with crustal tectonothermal events and thermal state of the SCLM beneath the CVZ. The results serve to explain the deformation mechanisms, geodynamic setting and evolution of this part of the European SCLM and are compared with SKS-wave splitting measurements for this area to assess the SCLM contribution to the measured seismic anisotropy.

2. Geological setting

The Catalan Volcanic Zone (CVZ) is part of the Neogene-Quaternary volcanism of the Iberian Peninsula (Ancochea, 2004), and the result of late-Alpine extensional fractures that extended the ECRIS along the Iberian Mediterranean coast (Martí, 2004 and references therein) from 35 to 0 Ma (Fig. 1a-b). This rifting produced extensional basins in the western Mediterranean off-shore (viz., the Valencia Trough, the Gulf of Lion, the Liguro-Provençal basin) and in the Catalan margin onshore (Roca and Desegaulx, 1992). However, as the extensional direction in this area is NW-SE instead of W-E, some authors (Barruol and Granet, 2002; Barruol et al., 2004) have argued that it is not related to the ECRIS event at all, but rather to back-arc spreading episodes induced by a roll-back of the Tethys slab subduction beneath the Corsica-Sardinia lithospheric block towards the NW, between 22–17 Ma.

Before the Neogene rifting, the lithosphere of this area was mainly structured by the Hercynian orogenesis and, to a lesser degree, by the Alpine orogenesis which led to the formation of the Catalan Coastal Ranges. Lithospheric extensive episodes with injections of mafic magmas in between the two orogenesis took place during the Permian (Martínez-Poza et al., 2014), when calc-alkaline to alkaline lamprophyres were intruded (Losantos et al., 2000; Enrique, 2009; Ubide et al., 2010), and during the Cretaceous, with intrusion of alkaline lamprophyres (Solé et al., 2003; Ubide et al., 2012; Esteve et al., 2014).

The CVZ is divided into three subzones (Fig. 1b): L'Empordà, La Selva and La Garrotxa, which are Neogene-Quaternary basins, mainly limited by normal NW-SE faults related to neotectonic activity (11 to 0 Ma) (Lewis et al., 2000). The xenoliths studied were collected in alkaline basaltic necks, lava flows, and pyroclasts from three volcanoes: Sant Corneli in La Selva subzone (3.5–2Ma; Donville, 1973b), and Canet d'Adri and La Banya del Boc in La Garrotxa subzone (0.1–0.01 Ma; Donville, 1973a) (Fig. 1b). The volcanic activity is linked to NW-SE Neogene normal faults, such as the Llorà fault (Fig. 1b), which has a transtensional component (Goula et al., 1999; Olivera et al., 2003). According to Bolós et al. (2014), this fault may extend down to the lower crust and lithospheric mantle controlling the eruption of alkaline mafic magmas that include lower-crust cumulates and mantle-derived xenoliths. The presence of these xenoliths is restricted to the volcanoes related to this fault.

Previous thermobarometric estimates on the mantle xenoliths from the CVZ (Galán et al., 2011), using the two-pyroxene thermometer of Brey and Köhler (1990), provide higher equilibrium T for harzburgites (1062 ± 29 °C) and websterites (up to 1257 °C) than for lherzolites

(972 ± 89 °C). Pressure estimates, using the clinopyroxene-olivine thermobarometer of Köhler and Brey (1990), range from 1.41 GPa to 0.70 GPa for lherzolites, while values of 1.02 ± 0.19 GPa are obtained for harzburgites. The lowest P in lherzolites is consistent with the existence of plagioclase in coronae around spinel in several samples. The CVZ xenoliths are classified as the off-craton type, with major and trace element compositions similar to those of other xenoliths from neighbouring European SCLM areas, for instance to those from the southern part of the Massif Central, France (Galán and Oliveras, 2014). According to these authors, lherzolites and harzburgites from NE Spain resulted from melt depletion and subsequent cryptic metasomatism. However, they do not exclude the possibility that some lherzolites, with clinopyroxene showing light Rare Earth Elements (LREE) depletion and Depleted MORB Mantle (DMM) isotopic compositions, could have been formed by refertilization of refractory, but isotopically enriched, harzburgites, via percolation and reaction with N-MORB type basalts, a theory proposed for lherzolites from the neighbouring ultramafic massif of Lherz (Eastern Pyrenees) (Le Roux et al., 2007). On the other hand, harzburgites from the CVZ underwent multi-stage metasomatism (Galán and Oliveras, 2014). An earlier episode was caused by subduction-related hydrous fluids or melts. A second metasomatic episode was mainly cryptic and related to the percolation of alkaline silicate melts and carbonatite derivatives. The latter metasomatism also affected a few lherzolites. The Sr—Nd isotopic compositions of the metasomatizing alkaline silicate melts and carbonatite derivatives were close to that of websterites (Galán and Oliveras, 2014), and within the range of the Continental Mantle Reservoir (Lustrino and Wilson, 2007). Websterites are interpreted as cumulates from the mafic alkaline silicate melts that caused the latter cryptic metasomatism (Galán et al., 2008).

3. Methods

The mineral mode (% volume) of the xenoliths was determined using the petrographic microscope with a precision stepping stage and an automatic James Swift point counter (Table 3.1E in electronic supplementary material). Microstructures were established through the optical analysis of thin sections cut in random orientation since the foliation and lineation could not be determined in most macroscopic hand specimens.

Major element mineral compositions of the samples were analyzed using an Electron Probe Microanalyser (EPM) (Cameca SX50) at the Scientific-tecnic Service of the University of Barcelona on polished thin sections. Beam current and acceleration voltage were 15 nA and 20 kV respectively, standards were both natural and synthetic, and the counting time was 10 s for all elements, except for Ca in olivine, which was 30 s. The beam width was enlarged to 50 μm in order to resolve, within uncertainty, pre-exsolved compositions of both pyroxenes in a few xenoliths. Tables 3.2E–3.3E, in supplementary electronic material, include average compositions of orthopyroxene and clinopyroxene used for thermometric estimates. Composition of both pyroxenes and other phases are summarized in Table 1.

The EPM thin sections were further prepared for quantitative crystallographic analyses, using electron backscatter diffraction (EBSD) (eg., Ben Ismaïl and Mainprice, 1998; Prior et al., 2009) by performing chemo-mechanical polishing with a 0.05 μm colloidal silica solution, and then coating with 3 nm thick carbon layer to avoid charging issues in the scanning electron microscope (SEM). EBSD was carried out in the EBSD-SEM Laboratory in the School of Environmental Sciences at the University of Liverpool, using two different SEMs: a XL30 tungsten filament SEM and a CamScan X500 CrystalProbe field emission gun (FEG) SEM, both equipped with EBSD-EDS systems from Oxford HKLTechnology. Automatic orientation mapping was carried out over the entire thin section area (~30 mm × 25 mm) of three samples (SC.11.16, BB.08.20, BB.08.101), and over an area of ~15 mm × 20 mm for the remaining thin sections, with sampling steps ranging from 30 to 50 μm depending on the sample's grain size. Accelerating voltage and working distance were 20 kV and 25 mm respectively. The Channel 5 software was used for automated indexing of all minerals present and for processing EBSD datasets. Indexation rates in the raw maps were ~65% and with generally better results for olivine than for pyroxenes, mainly due to the difficulty of polishing several coexisting mineral phases. Non-indexed areas resulted from fractures, alteration, basalt zones, grain boundaries and polishing defects. Mean angular deviation (MAD), which shows the match between lattice planes in a calculated orientation and measured lattice planes in EBSD patterns was commonly <1° (mainly ≈0.6°). Post-acquisition data processing allowed us to improve the indexation rate by using grey-scale values of band contrast images (these provide a visual report of kikuchi pattern quality) to constrain areas where non-indexed pixels could be filled with the average orientation of neighbouring pixels. During this process, isolated single pixels representing points misorientated ≥10° from the average orientation of surrounding pixels were removed first (ie., wild spikes). Then, empty pixels were replaced with the most common neighbouring orientation, if they had up eight identical neighbours. This process was repeated using sequentially seven, six, five and four identical neighbours. At each step great care was taken by using both band contrast images and micrographs to ensure that no artifacts were introduced into datasets. This method minimizes the over-counting of individual grains when extracting one orientation point per grain for the construction of pole figures (Section 7). Raw and processed EBSD maps of representative samples are included in supplementary electronic material (Fig. 3.1E).

Olivine and pyroxene CPO data are displayed in pole figures, presented as lower hemisphere stereographic projections, using the PFctf programme by Mainprice (ftp://www.gm.univ-montp2.fr/mainprice//CareWare_Unicef_Programs/). To avoid over-representation of coarse grains, pole figures were plotted by considering one point per grain. To facilitate comparison of CPO between different samples, the lineation and foliation of most of which could not be identified clearly in hand specimen, data were rotated to a standard position, using the ROTctf programme by Mainprice, with the maximum concentration of olivine [100] and [010] axes parallel to the E-W and the N-S direction, respectively (see Section 7 here below). This orientation would correspond to that expected in a sample with a horizontal E-W lineation (structural

Table 1
Fo, Mg# and Cr# range for minerals of different types of lherzolites, harzburgites and the websterite.

Rock type & microstructure	Ol (Fo%)	Opx (Mg#)	Cpx (Mg#)	Spl (Mg#)	Opx (Cr#)	Cpx (Cr#)	Spl(Cr#)
Pg Lhz	89.1–90.8	89.6–91.0	89.9–91.0	75.8–79.3	3.8–7.8	5.8–11.9	7.6–19.6
Pg Pc Lhz	89.6	89.8–89.9	89.3–89.7	75.1–75.9	4.6–5.8	6.7–9.7	9.7–12.3
Pc Lhz (unfocused)	–	89.4–89.8	90.2	–	6.4–6.6	7.4	–
Pc Lhz	89.1–90.1	89.5–90.3	89.6–91.7	73.8–77.8	4.7–5.5	7.1–8.9	9.7–13.1
Eg Lhz	89.2–90.1	89.7–90.5	90.1–91.8	75.2–78.3	3.1–6.9	7.8–10.0	11.1–15,0
Pg Hz	90.9–91.7	91.3–92.2	91.6–93.1	68.7–70.1	13.2–17.3	18.0–22.2	39.5–48.2
Pg Wb	91.5	90.9	92.5	–	19.3	25.6	–

Mineral abbreviations after Kretz (1983). Pg Pc and Eg stand for protogranular, porphyroclastic and equigranular microstructure, respectively. Wb Hz and Lhz indicate websterite, harzburgite and lherzolite.

X direction) and a vertical foliation plane (normal to the structural Z direction), if olivine had been deformed by dislocation creep with dominant activation of the high-temperature, low-stress (010)[100] slip system (Ben Ismaïl and Mainprice, 1998). Therefore, when we refer to "lineation" and "folitation" from now on, it must be understood they are inferred from CPO data. Finally, the rotation axes that accommodate all low-angle misorientations (2–15°) or subgrains are analysed within all olivine crystals of the EBSD maps and within selected olivine crystals of specific xenoliths and displayed on inverse pole figures (Section 8).

The fabric strength (Bunge, 1982) was estimated from the dimensionless number J index = $\int f(g)^2\, dg$, where f(g) is the density in the orientation distribution function at orientation g, and $dg = d\varphi 1 d\Phi d\varphi 2 \sin\Phi / 8\pi^2$, where $\varphi 1$, Φ and $\varphi 2$ are the Euler angles that define the rotations which allow for comparison between the crystallographic and external reference frames (Bunge, 1982). The J indices for all samples were calculated from the mean orientation of each grain using the SuperJctf software by Mainprice: ftp://www.gm.univmontp2.fr/mainprice//CareWare_Unicef_Programs/, using a 10° Gaussian half-width, 1° cells, and truncation of the orientation distribution function at 22°.

Further analysis of the mineral CPO was performed using the point (P), girdle (G) and random (R) fabric-type indices for olivine [100], [010] and [001] axes, and clinopyroxene (100), (010) and [001] distributions. These indices were calculated from the three eigenvalues ($\lambda 1$, $\lambda 2$, $\lambda 3$) of the normalized orientation matrix (Woodcock and Naylor, 1983; Humbert et al., 1996) for each principal crystallographic axis as: $P = \lambda 1 - \lambda 3$, $G = 2(\lambda 2 - \lambda 3)$ and $R = 3\,\lambda 3$ (Vollmer, 1990) and can be combined for a more thorough analysis of CPO symmetry. The BA index = 0.5 * (2.0 − (P010 / (G010 + P010)) − (G100 / (G100 + P100))) (Mainprice et al., 2015) and the LS index = 0.5 * (2.0 − (P010 / (G010 + P010)) − (G001 / (G001 + P001))) (Ulrich and Mainprice, 2005) were used for classifying olivine and clinopyroxene CPO, respectively. As these numerical classifications do not require knowledge of the orientation of the specimen reference frame in absolute terms, they are convenient for the analysis of mantle xenoliths.

Seismic properties were calculated for ambient T and P conditions, using single crystal elastic constants, mineral density, CPO and main mineral (olivine, orthopyroxene and clinopyroxene) mode (Table 3.1E) following Mainprice and Humbert (1994). The Anis_ctf and Poly_Adobe_VpVs software by D. Mainprice (ftp://www.gm.univmontp2.fr/mainprice//CareWare_Unicef_Programs/) was used in the computation, with the Voigt-Reuss-Hill average scheme for experimentally determined single crystal elastic constants (Abramson et al., 1997; Chai et al., 1997; Collins and Brown, 1998). In addition, the EMATRIX_average software also by D. Mainprice served to estimate the average seismic properties of the local SCLM. Calculated seismic properties are summarized in Table 3.4E (in supplementary electronic material) and displayed in lower hemisphere projections plotted following the same conventions used to represent the CPO data in pole figures (ie., one point per grain and data rotation) as described in the above paragraphs (see Section 9).

4. Petrography of xenoliths

A total of eighteen xenoliths were studied. Seventeen were new and one was previously studied (CA.44.05) by Galán et al. (2011). Selection was based on size, with those of ca., 2 × 4 cm or larger and less affected by basalt impregnation being regarded as the most suitable. These xenoliths are representative of the main lithologies found in the SCLM under the CVZ (Galán et al., 2008) and include thirteen spinel lherzolites, one plagioclase-spinel lherzolite, three spinel harzburgites, and one olivine websterite (Fig. 2). Accessory amphibole and phlogopite are present only in lherzolite BB.08.59 and in the sole websterite, respectively. Amphibole forms scarce disseminated anhedral crystals (≈100 μm in size) which can grow around spinel. Phlogopite crystals

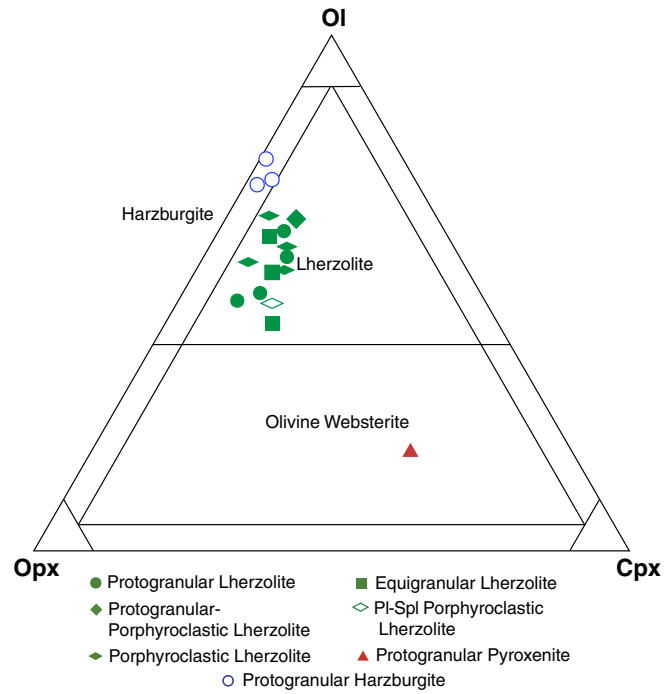

Fig. 2. Olivine-orthopyroxene-clinopyroxene diagram for ultramafic rocks (Le Maitre, 2002) with the projection of the studied mantle xenoliths classified by lithological and microstructural features.

are very sparse and subhedral (500–1000 μm at their long axis). Both lherzolites and harzburgites were taken from the Canet d'Adri and Banya del Boc volcanoes, whereas only lherzolites were found in the Sant Corneli neck. The websterite is from the Banya del Boc volcano (Fig. 1b).

The three harzburgites, four lherzolites and the websterite show protogranular or coarse granular microstructure (Fig. 3a–c) with average grain size ≥2 mm (Harte, 1977). Among these samples, one of the harzburgites (BB.12.04) and two of the lherzolites (BB.08.101, BB.08.98) show a preferred orientation of elongated olivine crystals, which gives rise to a coarse tabular microstructure. Although protogranular is the dominant microstructure, lherzolites also display finer-grained porphyroclastic and equigranular microstructures, with protogranular-porphyroclastic transitions in a few of them (Fig. 3d–f).

Lherzolites represent 60% of the SCLM rocks in this area, of which 15% are porphyroclastic and 9% are equigranular (Fernández-Roig and Galán, 2015). The mineral mode of the protogranular lherzolites is 7 to 14% clinopyroxene, 26–37% orthopyroxene, 50–65% olivine and <5% spinel. Olivine and orthopyroxene crystals are the largest (2–5 mm at the long axis), whereas clinopyroxene and spinel crystals are <2 mm. All minerals form anhedral crystals with straight or slightly curved olivine-olivine grain boundaries, occasionally at 120°. However, more interlobate grain boundaries are seen when olivine is next to other minerals, eg., bordering orthopyroxene crystals, which can include occasionally small rounded olivine crystals in random orientation (BB.08.98, BB.12.01; Fig. 4a). Spinel forms interstitial brownish-green or green crystals with frequent embayed grain boundaries (up to 1700 μm in size). These crystals can also have round shaped olivine and orthopyroxene inclusions and be orientated. Other forms of spinel are lamellae within both pyroxenes. Clinopyroxene crystals (0.5 < grain size < 2 mm) show either straight or gently curved grain boundaries. Olivine (and more rarely orthopyroxene) show sporadic evidence of intracrystalline deformation and recovery, such as undulose extinction, deformed exsolved lamellae, deformation bands and widely spaced subgrain boundaries (Figs. 4a and 3.1Eb in supplementary electronic material).

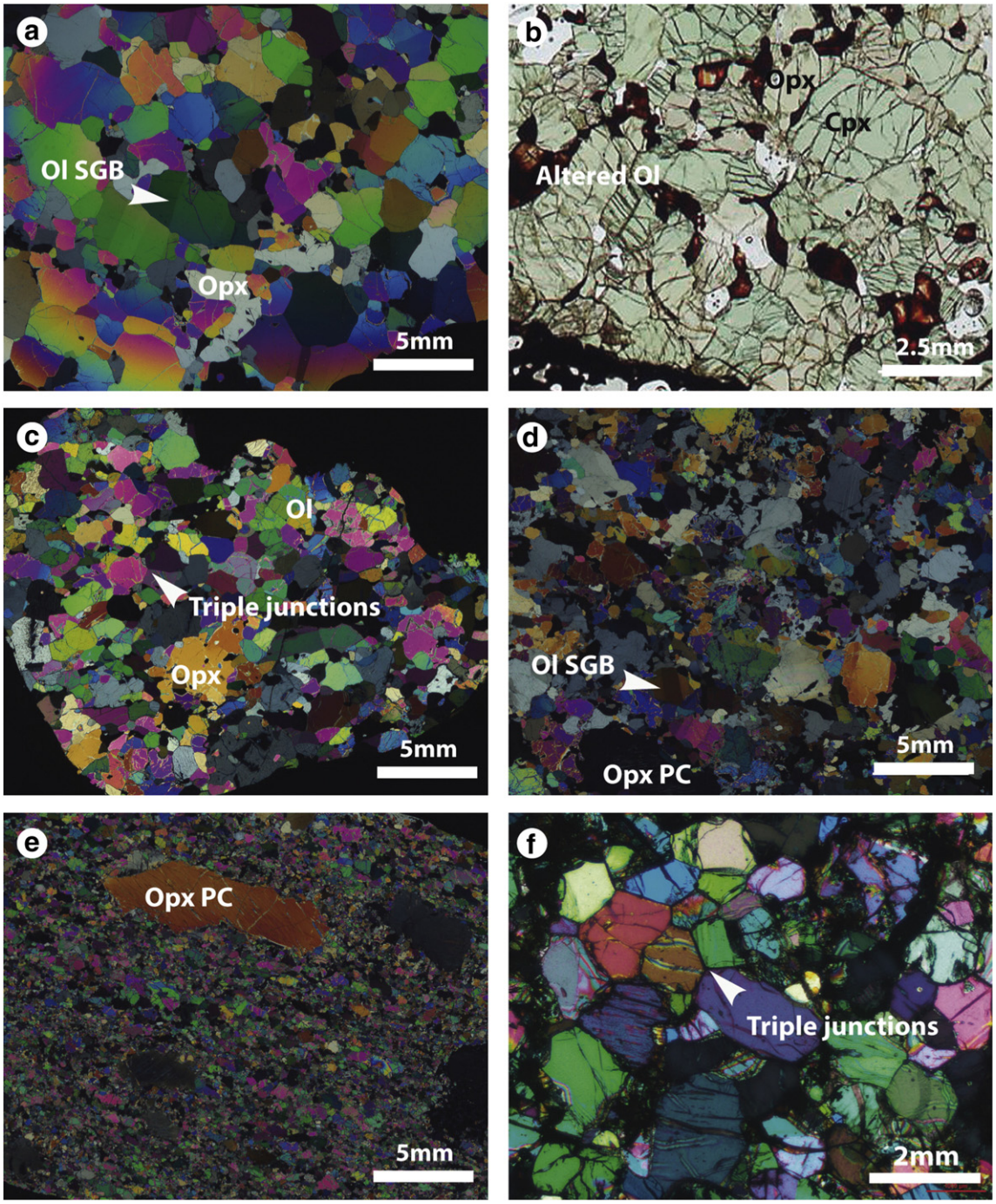

Fig. 3. Microstructures of the mantle xenoliths. (a) Protogranular harzburgite (CA.12.02) with sporadic subgrain boundaries (SGB) in olivine crystals. (b) Protogranular websterite (BB.12.17) with olivine crystals partially altered to iddingsite. (c) Protogranular lherzolite (BB.08.98) with triple junction boundaries between olivine crystals. (d) Lherzolite (BB.08.59) with transitional protogranular-porphyroclastic microstructure. (e) Elongated orthopyroxene porphyroclasts, one of them with clinopyroxene lamellae, in a finer-grained tabular matrix (lherzolite SC.11.16). (f) Equigranular lherzolite (SC.11.54) with grain boundaries at 120°. Mineral abbreviations after Kretz (1983).

Two lherzolites with transitional protogranular-porphyroclastic microstructure (BB.08.59, BB.12.13) have similar mineral mode range as the protogranular lherzolites (Table 3.1E in supplementary electronic material). These transitional samples include protogranular and finer grained (0.3 < grain size < 2 mm) areas without any specific arrangement (Fig. 3d). In the former, there is more evidence of intracrystalline deformation in olivine and orthopyroxene crystals and more frequent exsolved clinopyroxene lamellae in orthopyroxene than in the protogranular lherzolites. In the finer-grained areas, recrystallized strain-free neocrystals, or with rare subgrains, and frequent grain boundaries at 120° dominate. Spinel appears either as isolated interstitial crystals (≈50 μm) or more rarely as larger amoeboid crystals (up to 3 mm at their long axis), intergrown with orthopyroxene as "clusters" (Fig. 4b).

Porphyroclastic lherzolites (SC.11.16, SC.11.49, SC.11.52, BB.08.80, CA.12.03; Table 3.1E) (Fig. 3e) have a mineral mode range overlapping that of protogranular lherzolites. SC.11.49 stands out for showing plagioclase along with olivine, clinopyroxene and chromite forming coronae around spinel crystals. These lherzolites display mainly orthopyroxene porphyroclasts (3–11 mm at their long axis). Less frequently they display olivine, clinopyroxene and spinel porphyroclasts in a much finer matrix (0.2 < grain size < 1 mm) made up of strain-

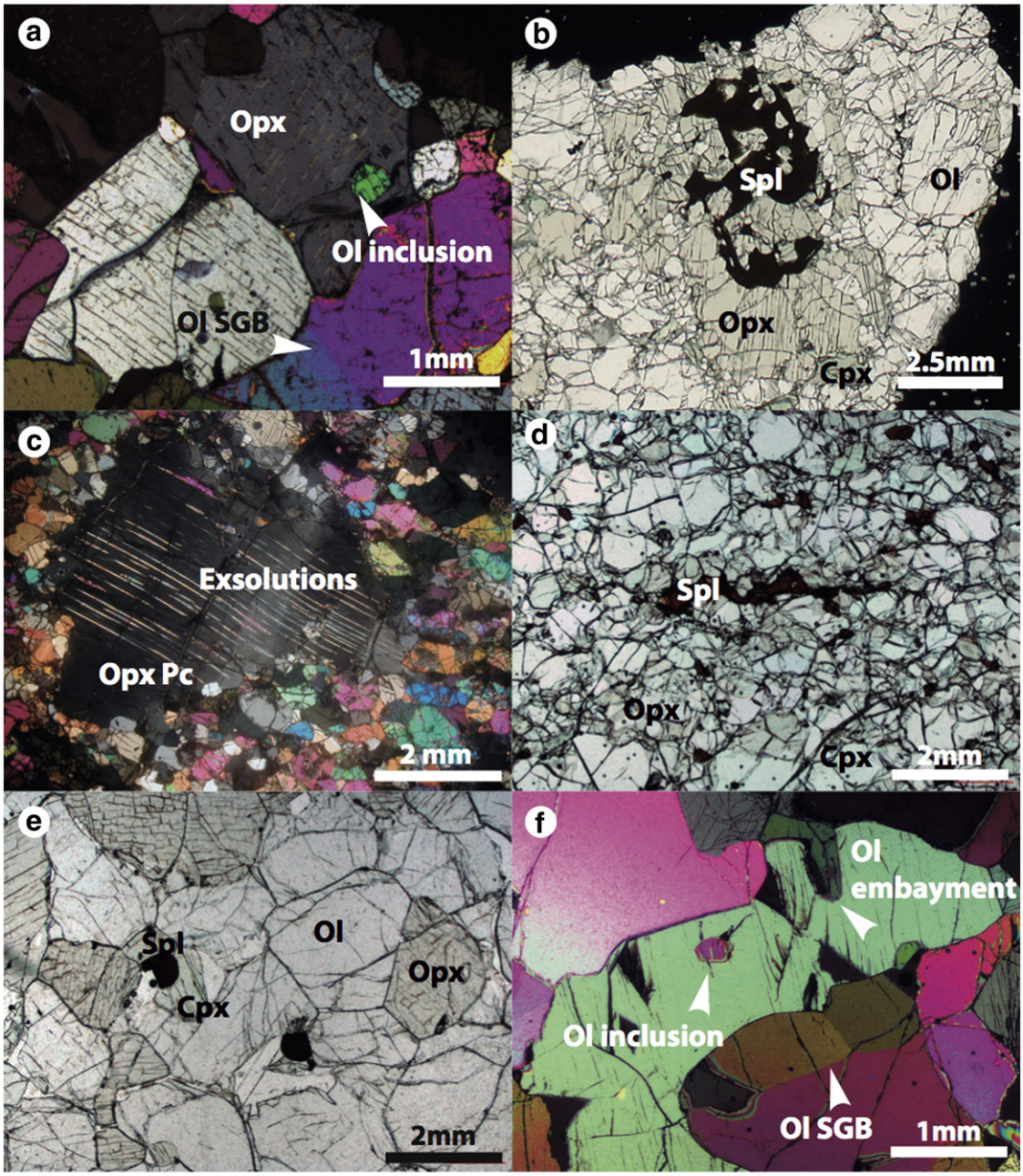

Fig. 4. Microstructural features of peridotites. (a) Subgrain boundaries in olivine crystals and olivine inclusion in orthopyroxene of lherzolite BB.08.98. (b) Amoeboid spinel crystals intergrown with orthopyroxene forming a cluster (lherzolite BB.12.13). (c) Orthopyroxene porphyroclast with bent clinopyroxene lamellae (lherzolite SC.11.52). (d) Stretched spinel crystal in porphyroclastic lherzolite SC.11.16. (e) Interstitial anhedral spinel crystals in harzburgite BB.08.20 (f) Orthopyroxene crystal embayed by olivine and with an olivine inclusion (harzburgite CA.12.02).

free neocrystals, or with sporadic subgrains, of the same minerals. Orthopyroxene porphyroclasts display evident features of intracrystaline deformation (Fig. 4c), such as frequent bent clinopyroxene and spinel lamellae at the core, undulose extinction, kinks bands and more closely spaced subgrain boundaries than in protogranular lherzolites. They also display embayment by strain-free olivine neocrystals that can be also seen as rare inclusions (eg., CA.12.03). Spinel porphyroclasts are amoeboid crystals intergrown mainly with orthopyroxene. They can be very stretched (aspect ratios from 1:3 to 1:7) and along with orthopyroxene porphyroclasts define a clear orientation (eg., in SC.11.16; Figs. 4d and 3.1Ed in electronic supplementary material). Spinel neocrystals are smaller (≈60 μm) rounded and interstitial between silicates. Clinopyroxene is mainly present as isolated and elongated clustered (aspect ratio 1:2) neocrystals (Fig. 3.1E in supplementary electronic material). Spinel lamellae are frequent in both clinopyroxene neocrystals and rare porphyroclasts. Two types of matrix were distinguished according to the shape of the grain aggregates: one is polygonal as in SC.11.49, SC.11.52, SC.11.16, whereas the other has slightly interlobate grain boundaries (BB.08.80). Finally, in two cases (SC.11.16, CA.12.03), elongated olivine neocrystals define a tabular matrix (Fig. 3e).

Most equigranular lherzolites (BB.08.38, BB.08.57, SC.11.54) are also tabular because of elongated olivine neocrystals. Those included in Table 3.1E show the highest clinopyroxene mode (12–18%), 20–37% orthopyroxene, 42–62% olivine and <5% spinel. They show less than 5% porphyroclasts (grain size up to 5 mm), mostly of orthopyroxene, in a finer grained matrix (0.3 < grain size < 1mm), where spinel is usually present as interstitial rounded crystals, or elongated crystals with

lobate grain boundaries. Grain boundaries are generally straight or slightly curved among neocrystals, with frequent triple junctions (Fig. 3f). Intracrystalline deformation or recovery features are either absent or very sporadic.

Protogranular harzburgites (BB.08.20, CA.12.02, BB.12.04) represent 36% of the total mantle xenoliths sampled so far. Those in Table 3.1E have 71–76% olivine, 21–27% orthopyroxene, 4–1% clinopyroxene and <1% spinel. Microstructure features are similar to those of protogranular lherzolites but they differ in the following aspects: (1) crystals of olivine and orthopyroxene are more coarse grained (2–6 mm at their long axis); (2) spinel crystals (100 < grain size < 700 μm) are generally darker brown anhedral and interstitial (Fig. 4e) and, more rarely, amoeboid; and (3), intracrystalline deformation or recovery features (subgrains) are sparser than in lherzolites. Interpenetrating olivine-orthopyroxene grain boundaries, with both minerals demonstrating rounded inclusions are occasionally observed in sample CA.12.02 (Fig. 4f). Moreover, it has been noted that BB.12.04 is protogranular tabular due to the orientation of elongated olivine crystals.

The websterite BB.12.17 is also protogranular, with average grain size of 2–3 mm, straight or gently curved grain boundaries and few deformation effects: only olivine crystals display undulose extinction and deformation bands.

5. Mineral chemistry

Average chemical analyses of major elements and formula unit (fu) of both pyroxenes are included in Tables 3.2E–3.3E of electronic supplementary material and a brief summary of all phases in Table 1. Compositional range of periodotite minerals are comparable to those provided by Galán and Oliveras (2014). Crystal zoning was not observed and compositions of minerals forming different types of crystals (porphyroclasts, neocrystals, lamellae) in a single sample are comparable. However, analyses of a few orthopyroxene and clinopyroxene porphyroclasts both showing mutual and spinel lamellae, performed with an enlarged electron beam (ie., unfocused analyses), indicate higher Mg number [Mg# = 100 * Mg / (Mg + Fe_t) in atoms per fu] and lower Cr number [Cr# = 100 * Cr / (Cr + Al)] in pre-exsolved compositions. The forsterite (Fo) component in olivine, Mg# and Cr# for both pyroxenes are seen to decrease from harzburgites to lherzolites (Table 1). Spinel *sensu stricto* is present in lherzolites and Mg-Al chromite in harzburgites. Cr# decreases for spinel while, by contrast, Mg# increases from harzburgites to lherzolites. These general compositional variations are consistent with both melt depletion trends and with trends resulting from the refertilization of harzburgites via the percolation of basaltic melts to give lherzolites. The websterite is of particular note because olivine and pyroxenes show similar or higher Mg# and Cr# values than do harzburgites. This is in contrast to results of a previously studied websterite which has more evolved compositions (Galán et al., 2008).

Covariation diagrams for lherzolite minerals (Fig. 5) serve to establish the relationships between their chemical compositions and the microstructure types. Harzburgites were excluded from these diagrams because they represent a more refractory system and only show protogranular microstructure.

Mg# vs. Cr# for lherzolite clinopyroxene and spinel show overlap between the three microstructural types of lherzolites (Fig. 5a-b) and a broad overall positive correlation between the two numbers only for clinopyroxene. Also Al(M1) vs. Na(M2) diagram for clinopyroxene (Fig. 5c) illustrates a positive correlation, with both elements decreasing from protogranular (-porphyroclastic) lherzolites to porphyroclastic and equigranular forms. That is to say, the jadeite substitution (^{M2}Na-$^{M1}Al^{M2}Ca-1^{M1}Mg-1$) is found in decreasing amounts as microstructure changes from coarse towards finer grained lherzolites (Fernández-Roig and Galán, 2015).

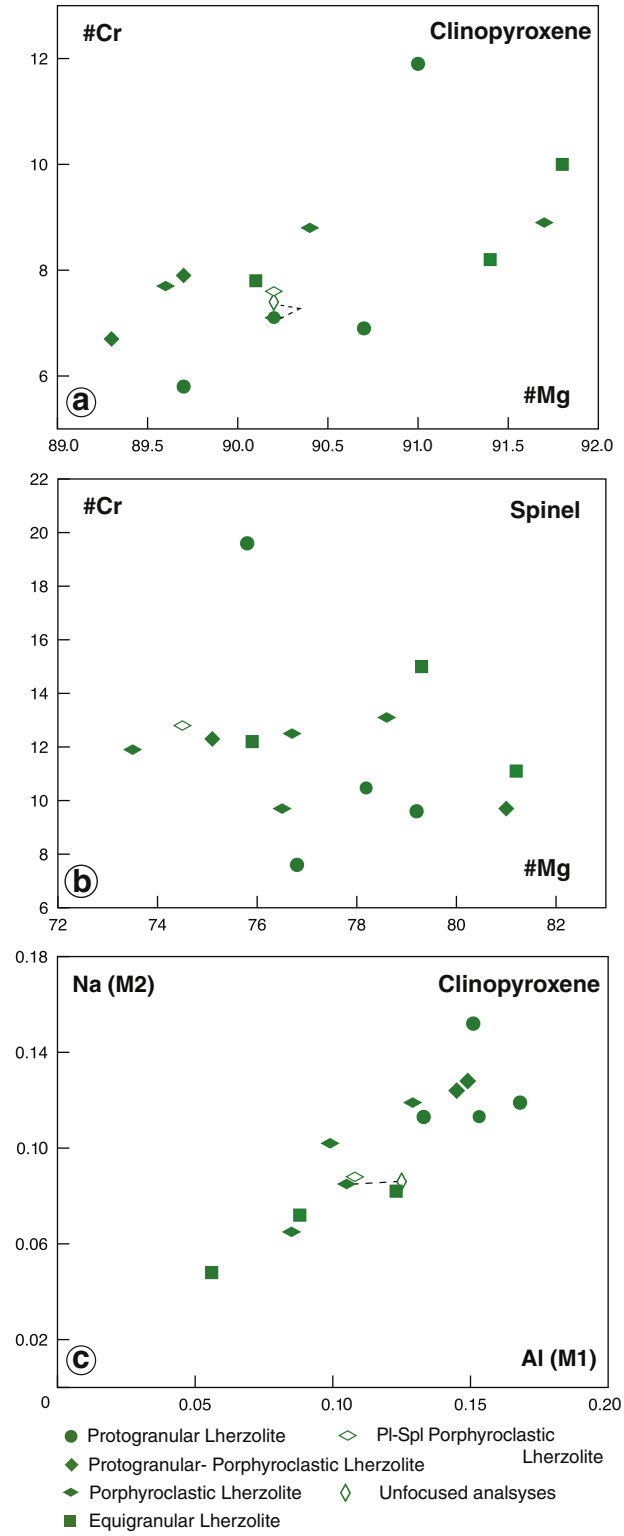

Fig. 5. Variation of mineral chemistry in lherzolites. (a) Cr# vs. Mg# in clinopyroxene. (b) Cr# vs Mg# in spinel. (c) Na in M2 site vs. Al in M1 site of clinopyroxene. Unfocused clinopyroxene analyses are related to focused analyses by dashed lines.

6. Temperature, pressure and deviatoric stress estimates

Equilibrium T were estimated with the two-pyroxene (T_{BK}) and the Ca-in-orthopyroxene ($T_{Ca\text{-}in\text{-}opx}$) thermometers (Brey and Köhler, 1990), both based on the transfer of the enstatite component between co-existing clinopyroxene and orthopyroxene. P of 15 kb was assumed

for all estimates. Several pairs of analyses from neighbouring clinopyroxene and orthopyroxene crystals were used for the average values in Table 2. Where possible, estimates from porphyroclasts and neocrystals have been presented separately. Uncertainty (1 s) is <50 °C for T_{BK} estimates and lower for the $T_{Ca\text{-}in\text{-}opx}$ values. Although estimates from both thermometers show a good positive correlation, those of $T_{Ca\text{-}in\text{-}opx}$ are somewhat higher than T_{BK} values in most samples (Fig. 6). However, most $T_{Ca\text{-}in\text{-}opx}$ are within ±50 °C of T_{BK} estimates. Bias is under 9%, except in two cases: orthopyroxene porphyroclasts in lherzolite CA.12.03 (22%) and the equigranular lherzolite BB.08.57 (18%). In the former case, bias for the neocrystals is much lower (5%) than for the porphyroclasts suggesting disequilibrium between the two different types of crystals (Fig. 6). The highest bias corresponds to $T_{BK} \leq 900$ °C, as was noted by Brey and Köhler (1990). These T are mainly registered by porphyroclastic and equigranular lherzolites.

The highest T values are registered by protogranular harzburgites and the websterite (1171 to 1006 °C; T_{BK} values). T_{BK} and $T_{Ca\text{-}in\text{-}opx}$ estimates for the protogranular lherzolites range from 1057 down to 924 °C and from 1038 to 975 °C, respectively. These ranges for lherzolites with transitional protogranular-porphyroclastic (T_{BK}: 996–931 °C, $T_{Ca\text{-}in\text{-}opx}$: 992–969 °C) and porphyroclastic microstructures (T_{BK}: 942–856 °C, $T_{Ca\text{-}in\text{-}opx}$: 1155–922 °C) are somewhat lower. Where porphyroclast and neocrystal T can be calculated separately, they do not exhibit significant differences, except for lherzolite CA.12.03 where the porphyroclast $T_{Ca\text{-}in\text{-}opx}$ value is significantly higher (1155 °C, Table 2). For two of these samples, where analyses of orthopyroxene and clinopyroxene were performed with an enlarged beam for integrating mutual and/or spinel lamellae, T_{BK} and especially $T_{Ca\text{-}in\text{-}opx}$ estimates are higher, and approximate those registered by protogranular peridotites and orthopyroxene porphyroclasts in CA.12.03 (Fig. 6; Table 2). Finally, two equigranular lherzolites register slightly lower T_{BK} (959–766 °C) estimates than do porphyroclastic lherzolites, although $T_{Ca\text{-}in\text{-}opx}$ (970–917 °C) estimates are similar.

P estimates based on the Ca-exchange reaction between co-existing clinopyroxene and olivine (Köhler and Brey, 1990) were hampered by the dependence of this barometer on both temperature and the uncertainty of Ca analysis in olivine by EPM (O'Reilly et al., 1997). Only two harzburgites (BB.12.04: 1.13 ± 0.10 GPa; BB.08.20: 0.83 ± 0.17 GPa), one protogranular lherzolite (BB.08.98: 1.51 ± 0.21 GPa), one porphyroclastic lherzolite (SC.11.49: 0.67 ± 0.10 GPa) and one equigranular lherzolite (BB.08.38: 0.60 ± 0.32 GPa) show consistent P values and low uncertainty (1 s). SC.11.49 is a plagioclase-spinel lherzolite. Decreasing P from protogranular to porphyroclastic and equigranular lherzolites is consistent with the decreasing jadeite component of their clinopyroxene (Fig. 5c).

Table 2
T estimates from the two pyroxene (T_{BK}) and Ca in orthopyroxene ($T_{Ca\text{-}in\text{-}Opx}$) thermometers of Brey and Köhler (1990). Uncertainty as ±1 standard deviation (SD).

Sample	Rock type & microstructure	TBK (°C)	SD	TCa-in-Opx (°C)	SD
BB.08.101	Pg Lhz	1053	8	1010	2
BB.12.13(p)	Pg-Pc Lhz	941	27	969	0
BB.12.13(n)	Pg-Pc Lhz	996	31	971	6
BB.08.98	Pg Lhz	1057	11	1035	4
BB.12.01	Pg Lhz	1032	19	1038	19
BB.08.59	Pg-Pc Lhz	931	11	992	6
CA.12.03(p)	Pc Lhz	902	1	1155	24
CA.12.03(n)	Pc Lhz	876	24	924	6
CA.44.05c	Pg Lhz	924	24	975	6
BB.08.57	Eq Tab Lhz	766	48	932	9
BB.08.80	Pc Lhz	866	43	946	6
SC.11.49	Pc Lhz	942	9	972	17
SC.11.49	Pc Lhz (unfocused)	955		1142	
BB.08.38	Eq Lhz	860	2	917	6
SC.11.16	Pc Lhz	856	23	922	7
SC.11.52(p)	Pc Lhz	936	14	984	13
SC.11.52(n)	Pc Lhz	918	1	968	6
SC.11.52	Pc Lhz (unfocused)	982		1067	
SC.11.54	Eq Lhz	959	20	970	12
CA.12.02	Pg Hz	1060	31	1092	12
BB.08.20	Pg Hz	1006	12	1040	6
BB.12.04	Pg Tab Hz	1171	9	1201	17
BB.12.17	Pg Wb	1054	14	1093	5

p and n stand for porphyroclasts and neocrystals, respectively. Other abbreviations as in Table 1.

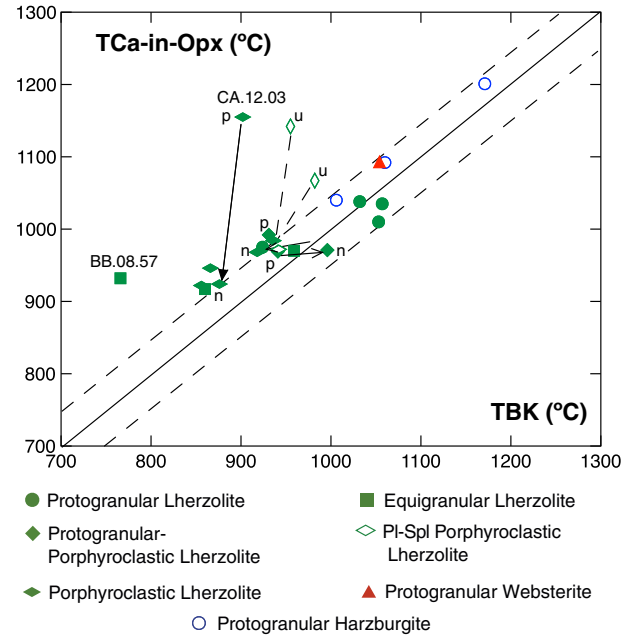

Fig. 6. $T_{Ca\text{-}in\text{-}Opx}$ vs. T_{BK} estimates for the different types of rocks. Solid lines joint porphyroclast (p) with neocrystal (n) temperatures of a single sample. Values from unfocused porphyroclasts (u) are joined to other estimates of the same sample by dashed lines. Dotted and dashed lines represent ±50°C of T_{BK}.

Finally, the average grain size of neocrystals in protogranular-porphyroclastic, porphyroclastic and equigranular lherzolites, measured using the EBSD maps, has been used to estimate the deformation stress based on the equation: $D_g = A\sigma^{-n}$ (Karato et al., 1980; Van der Wal et al., 1993), where Dg is the recrystallized grain size, σ is the differential stress, and A and n are empirical constants [Karato et al. (1980): A = 8300; n = 1.18; Van der Wal et al. (1993): A = 15000; n = 1.33]. The average grain size of neocrystals ranges from 960 μm in the protogranular-porphyroclastic lherzolite BB.12.13 to 360 μm in the porphyroclastic sample SC.11.16, which gives 6.1–14.1 MPa (Karato et al., 1980) or 8.0–16.7 MPa (Van Der Wal et al., 1993) stress values.

In summary, more porphyroclastic and equigranular lherzolites were equilibrated at lower T and P and recrystallized during higher stress deformation than was the case for protogranular harzburgites, lherzolites and the sole websterite.

7. Crystal preferred orientations

7.1. Olivine

All the harzburgites, nine of the lherzolites and the websterite show the same deformation fabric for the olivine: they are characterized by point concentration of [010] parallel to Z and girdles of [100] and [001] axes normal to each other within the structural XY ("foliation") plane (Fig. 7). The main slip system is (010)[100]. BA indices for these samples range from 0.09 to 0.39 (Table 3; Fig. 8a). The highest main density (MD) corresponds mostly to [010] axis and [100] axis shows higher MD than [001] axis, whereas the reverse holds true in lherzolite CA.44.05 and websterite BB.12.17. This fabric is classified as [010] fiber or AG-type (Ben Ismaïl and Mainprice, 1998; Mainprice, 2007). Four other lherzolites are characterized by orthogonal point concentrations of the three olivine axes. The dominant slip system is also (010)[100].

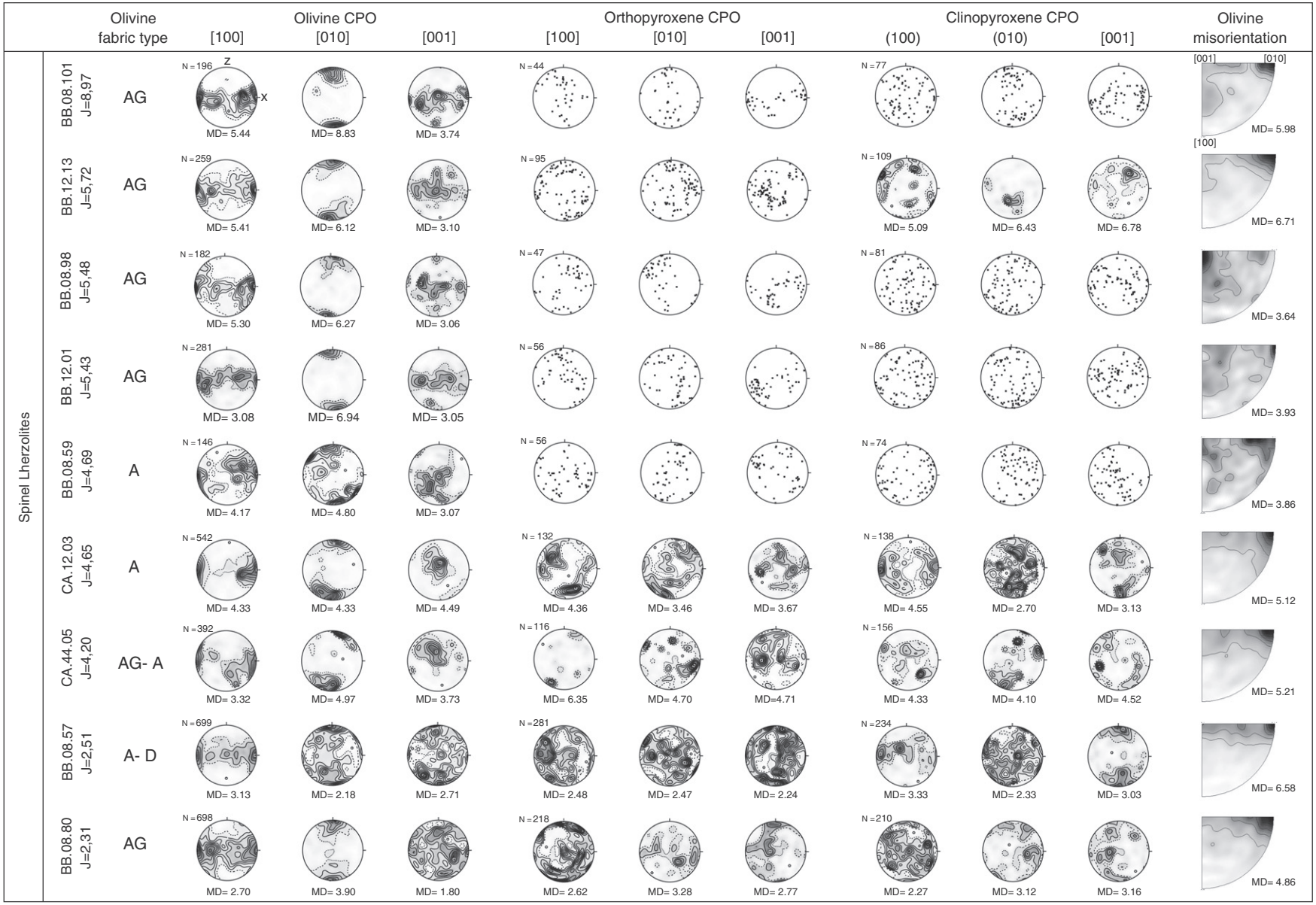

Fig. 7. Stereograms for olivine, orthopyroxene and clinopyroxene CPO rotated to match olivine [100] and [010] axes with structural X and Z directions, respectively. Stereograms were not contoured when the number of indexed grains is lower than 100. Inverse pole figures for all olivine rotation axes accommodating misorientations of less than 15° are also included (contours at 1.0 multiples of a uniform distribution intervals). Values of J index (Ben Ismaïl and Mainprice, 1998) and deformation fabric types of olivine according to values of BA index (Mainprice et al., 2015) are also included. Xenoliths are ordered according to fabric strength.

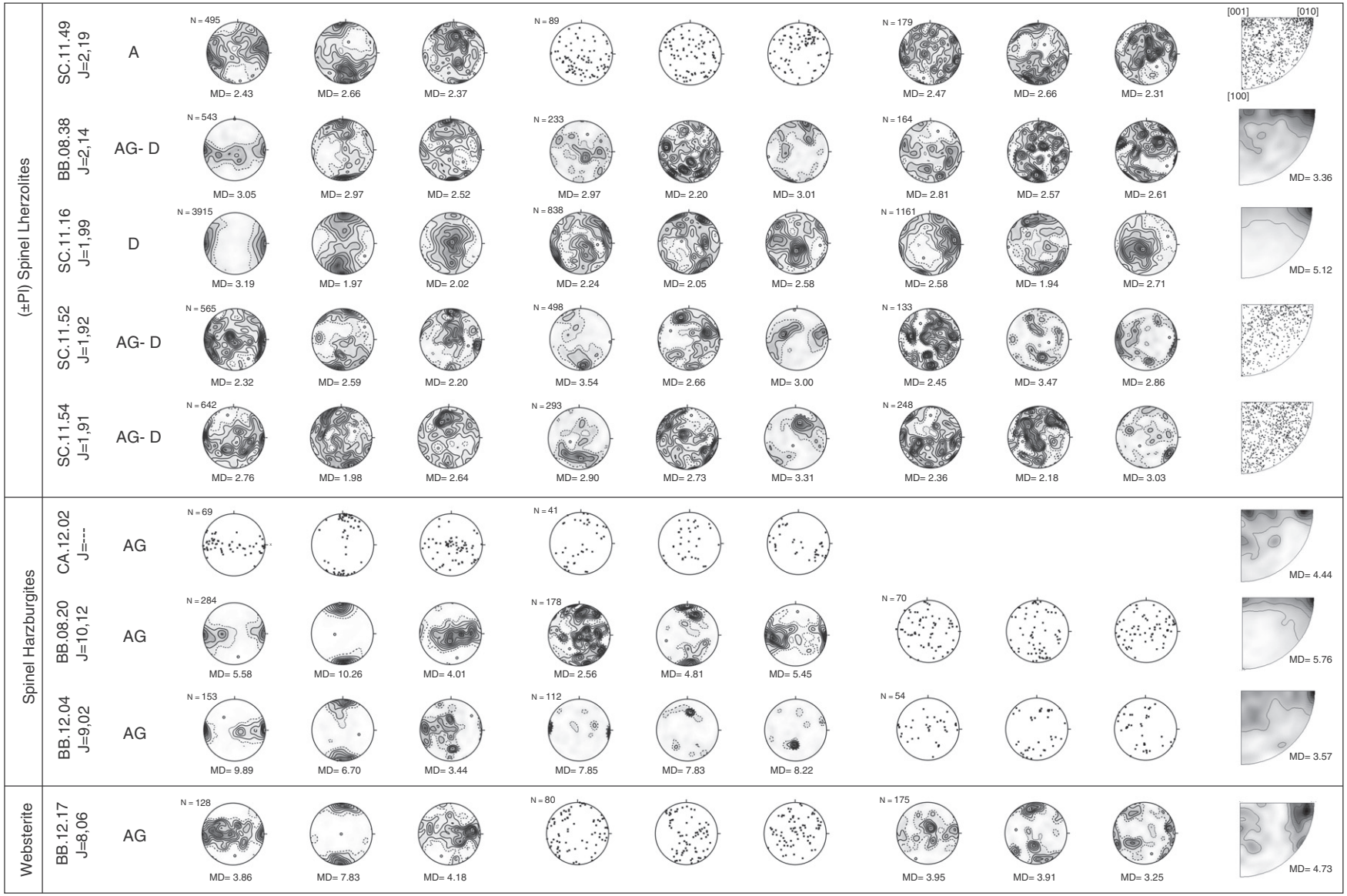

Fig. 7 *(continued)*

Table 3
BA index, types ol olivine (Mainprice et al., 2015), orthopyroxene (Jung et al., 2010) and clinopyroxene CPO along with clinopyroxene LS index (Ulrich and Mainprice, 2005), main slip systems, J index (Ben Ismaïl and Mainprice, 1998) and coherence of olivine and orthopyroxene, clinopyroxene deformation fabrics. L stands for structural X direction or inferred lineation.

Sample	Rock type & microstructure	Ol CPO		Opx CPO	Cpx CPO		Main slip systems			J Index			Ol & Opx coherence	Ol& Cpx coherence
		BA Index	Type		LS Index	Type	Ol	Opx	Cpx	Ol	Opx	Cpx		
BB.08.101	Pg Lhz	0.25	AG	ABC	0.39	SL	[100](010)	[001]{110}	[001]{110}	8.97	–	–	Yes	Yes
BB.12.13	PgPc Lhz	0.23	AG	AC?	0.51	SL	[100](010)	[001](100)	[001]{110}	5.72	–	9.49	Yes	Yes
BB.08.98	Pg Lhz	0.29	AG	BC	0.43	SL	[100](010)	[001](010)	[001]{110}	5.48	–	–	Yes	Yes
BB.12.01	Pg Lhz	0.09	AG	AC	0.27	S	[100](010)	[001](100)	[001]{110}	5.43	–	–	Yes	Yes
BB.08.59	PgPc Lhz	0.42	A	BC	0.32	SL	[100](010)	[001](010)	[100] = L	4.69	–	–	Yes	No
CA.12.03	Pc Lhz	0.48	A	–	0.86	L	[100](010)	–	[100] = L	4.65	5.34	6.37	No	No
CA.44.05	Pg Lhz	0.26	AG-A	AB	0.61	SL	[100](010)	[010](100)	–	4.20	5.82	6.56	No	No
BB.08.57	Eg Tab Lhz	0.42	A–D	–	0.73	L	[100](010)	–	[100] = L	2.51	2.44	4.54	No	No
BB.08.80	Pc Lhz	0.35	AG	–	0.49	SL	[100](010)	[001] ⊥ L	–	2.31	3.14	4.17	No	No
SC.11.49	Pc Lhz	0.47	A	BC	0.48	SL	[100](010)	[001](010)	[001]{110}	2.19	–	4.15	Yes	Yes
BB.08.38	Eg Lhz	0.28	AG-D	–	0.64	SL	[100](010)	–	–	2.14	2.62	4.85	No	No
SC.11.16	Pc Lhz	0.78	D	–	0.54	SL	[100]{0kl}	[001] ⊥ L	[100] = L	1.99	1.94	2.56	No	No
SC.11.52	Pc Lhz	0.39	AG-D	AC	0.71	L	[100](010)	[001](100)	[001]{110}	1.92	2.38	5.99	Yes	Yes
SC.11.54	Eg Lhz	0.24	AG-D	–	0.43	SL	[100](010)	–	–	1.91	3.23	4.22	No	No
CA.12.02	Pg Hz	0.23	AG	AC	–	–	[100](010)	[001](100)	–	–	–	–	Yes	–
BB.08.20	Pg Hz	0.27	AG	BC	0.19	S	[100](010)	[001](010)	[001]{110}	10.12	5.13	–	Yes	Yes
BB.12.04	Pg Tab Hz	0.39	AG	–	–	–	[100](010)	–	[100] = L	9.02	7.68	–	No	No
BB.12.17	Pg Wb	0.23	AG	BC?	0.46	SL	[100](010)	[001](010)	[001]{110}	8.06	–	6.15	Yes	Yes

BA indices range from 0.42 to 0.48. The highest MD corresponds to [010] axis in two samples (BB.08.59, SC.11.49) and to [100] and [001] in the other two cases (BB.08.57 and CA.12.03, respectively). This fabric is classified as orthorhombic (Tommasi et al., 1999) or A-type (Jung and Karato, 2001). Finally, only one lherzolite shows strong point concentration of [100] axis parallel to the structural X direction and girdles of [010] and [001] axes parallel to each other and normal to [100] (Fig. 7). This is characteristic of the [100]-fiber fabric or D-type (Karato et al., 2008). In this case, the dominant slip system is {0kl}[100], BA index is 0.78, [100] axis shows the highest MD and the MD of [001] axis is slightly higher than that of [010] axis. In spite of this numerical classification of deformation fabrics based on the BA index, there are transient types between AG-, A- and D-types in some lherzolites (Fig. 7, Table 3). For instance, CA.44.05 can be considered transitional AG-A type because both [100] and [001] axes tend to point concentrations. Other cases are transitional AG-D type (BB.08.38, SC.11.52, SC.11.54) since [001] axis tends to be normal to the structural XY ("foliation") plane instead of being within it (Fig. 7). Finally, lherzolite BB.08.57 can be considered transitional A-D type for the same reason: [001] axis tends to be normal to the "foliation" plane. It should be noted that the distribution of [100] and [001] axes is bimodal in two lherzolites with AG-D type fabric (BB.08.38, SC.11.52). In these two samples, [100] distribution is characterized by two mutually orthogonal maxima within the "foliation" plane, whereas [001] distribution is characterized by one maximum aligned with [100] axis and the other with [010] axis, that is to say normal to the "foliation" plane (Fig. 7). Finally, only in harzburgite CA.12.02 the number of grains (<100) per thin section was not sufficient for reliable statistical analysis of the fabric strength (Ben Ismaïl and Mainprice, 1998). This sample is not contoured in Fig. 7. For the remaining samples, the fabric strength or J index is variable. The highest values (10.12–5.43) correspond to the harzburgites and lherzolites which have well defined AG-type fabric. The websterite also follows this pattern. J indices for the other lherzolites range from 4.69 (A-type fabric) to 1.91 (transitional AG-D-type fabric) (Table 3).

J indices vs. BA indices display scatter, although negative correlation is observed overall (Fig. 8a). No clear relationship exists between BA indices and the microstructure types (not represented), although most BA values >0.40 correspond to porphyroclastic lherzolites. However, a better relationship is displayed between J indices and the microstructure types: J indices decrease from protogranular harzburgites and lherzolites towards porphyroclastic and equigranular lherzolites (Fig. 8b), which overlap both. The relationships between J indices and other variables are as follows: (1) there is a positive correlation with the olivine mode in peridotites (Fig. 9a) and a negative correlation with the clinopyroxene mode (not represented), although porphyroclastic and equigranular lherzolites display scatter; (2) correlation with Mg# of clinopyroxene is also positive for the protogranular (-porphyroclastic) lherzolites and harzburgites, whereas most equigranular and porphyroclastic lherzolites do not follow this trend (Fig. 9b); (3) in contrast, correlation with Na (Fig. 9c) (and Al) atoms per formula unit in clinopyroxene is broadly negative for protogranular (-porphyroclastic) lherzolites and harzburgites, but among lherzolites the concentration of both elements drops significantly from those with protogranular miscrostructure to most porphyroclastic and equigranular lherzolites; and (4), there is a roughly positive correlation with equilibrium T whether estimated with the T_{BK} or $T_{Ca\text{-}in\text{-}Opx}$ thermometers (Brey and Köhler, 1990) (Fig. 9d); porphyroclastic and equigranular lherzolites register the lowest J indices and equilibrium temperatures.

7.2. Orthopyroxene

In six lherzolites, one harzburgite and the websterite (Table 3), the analysis of orthopyroxene CPO was hindered by the paucity of grains (<100 grains per thin section). These are not contoured in Fig. 7. Nevertheless, the deformation fabric is well defined and coherent with olivine fabric in eight xenoliths (44% of the total): all are characterized by the alignment of orthopyroxene [001] and olivine [100] axes. Among these orthopyroxene CPO, three different types were identified according to Jung et al. (2010): AC-type in lherzolites SC.11.52, BB.12.01 and harzburgite CA.12.02, characterized by the alignment of [100] axis subnormal to the "foliation" plane and of [001] axis subparallel to the "lineation"; BC-type in lherzolites BB.08.98, BB.08.59, SC.11.49 and harzburgite BB.08.20, differing from the previous type by the alignment of the [010] axis subnormal to the "foliation" plane; and ABC-type in lherzolite BB.08.101, defined by girdles of both [100] and [010] axes aligned subnormal to the "foliation" plane. According to the nomenclature of Jung et al. (2010), the first and last capital letters represent the slip plane and slip direction, respectively (Table 3). In one more lherzolite (BB.12.13) and the websterite (BB.12.17) the orthopyroxene fabric is less well-defined, but these samples do show coherent fabrics with olivine. In seven other lherzolites (CA.12.03, CA.44.05, BB.08.57, BB.08.80, BB.08.38, SC.11.16, SC.11.54) and one harzburgite (BB.12.04) (44% of the total) (Table 3), the olivine and orthopyroxene fabrics are

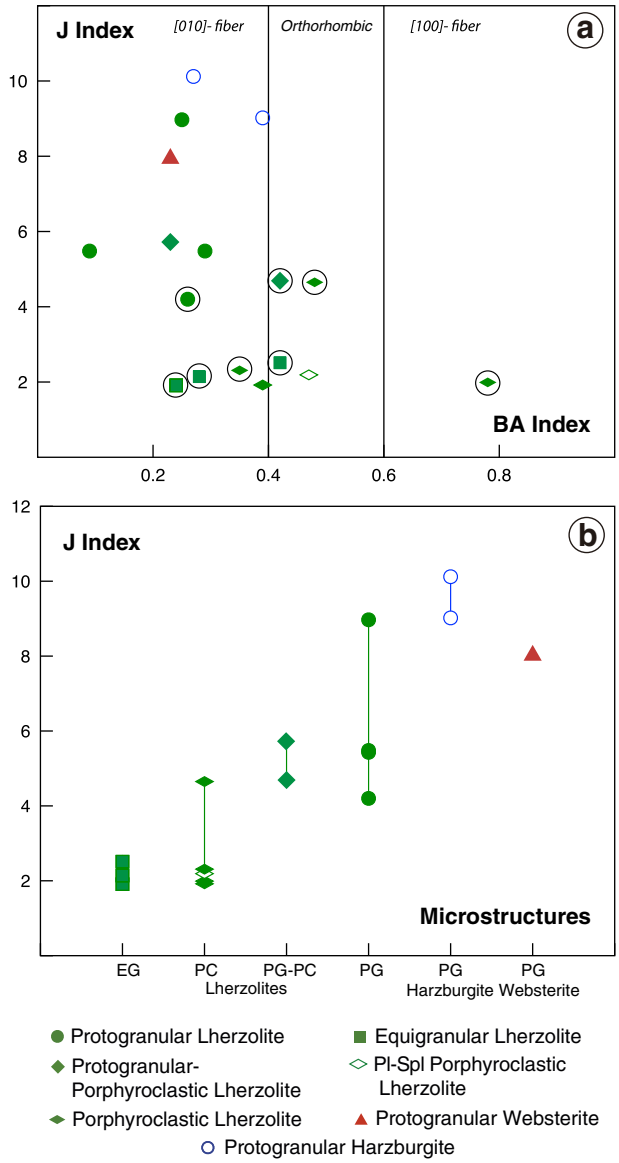

Fig. 8. (a) J index vs. BA index. Encircled symbols stand for xenoliths with incoherent olivine and clinopyroxene deformation fabrics. See text for further explanation. (b) Relationships between J index and microstructures.

incoherent. Among these samples, lherzolite CA.44.05 stands out because orthopyroxene [010] and olivine [100] axes align, therefore, the slip direction for orthopyroxene would be [010]. Lherzolite SC.11.16 and harzburgite BB.12.04 also stand out because [100] axes of both minerals are subparallels; [001] axis of both minerals are also aligned and normal to the olivine [100] axis in SC.11.16 (Fig. 7). For those samples where the analysis of orthopyroxene CPO was statistically reliable (Fig. 7; Table 3), values of J indices are similar to, or higher than, those found in lherzolite olivine, whereas the reverse holds true in harzburgites.

7.3. Clinopyroxene

The number of clinopyroxene crystals per thin section is <100 in all harzburgites and four of the lherzolites, the pole figures of which are not contoured (Fig. 7). Moreover, clinopyroxene of one harzburgite with rare crystals of this mineral was not indexed. In spite of this paucity of grains, 44% of the samples have clinopyroxe [010] and [001] axes normal and parallel, respectively, to olivine [100] axis, ie., both minerals show coherent deformation fabrics (Table 3). The dominant slip system would be {110}[001] (Bascou et al., 2002; Zhang et al., 2006). Moreover, in these samples (lherzolites BB.08.101, BB.12.13, BB.08.98, BB.12.01, SC.11.49, SC.11.52, harzburgite BB.08.20 and the websterite BB.12.17) both pyroxenes are coaxial (Table 3; Fig. 7). There are nine (50%) incoherent samples (lherzolites BB.08.59, CA.12.03, CA.44.05, BB.08.57, BB.08.80, BB.08.38, SC.11.16, SC.11.54 and harzburgite BB.12.04), which are most of them porphyroclastic and equigranular lherzolites. It is worth noting that in five of these incoherent samples, the [100] axes of both olivine and clinopyroxene align (Fig. 7). The slip direction of clinopyroxene in these samples would be [100]. However, very few dislocations have Burgers vector b = [100] (Zhang et al., 2006). For instance, the (010)[100] and (001)[100] slip systems have been rarely observed (Philippot and Van Roermund, 1992; Godard and Van Roermund, 1995; Palasse et al., 2012). Clinopyroxene fabric types (Table 3) have been classified numerically according to LS index values as follows: S-type or flattening fabric (0.19–0.27) for one harzburgite (BB.08.20) and one lherzolite (BB.12.01), where [001] axis tends to form a girdle normal to the (010) pole maximums; L-type or constriction fabric (0.71–0.86) for three lherzolites (CA.12.03, BB.08.57, SC.11.52), where [001] axis tends to concentrate and (010) poles tend to form a girdle orthogonal to [001] axis; and the intermediate SL-type (0.32–0.64) for most lherzolites and the websterite (Helmstaedt et al., 1972; Zhang et al., 2006) (Table 3). In samples where the number of both pyroxene crystals per thin section is >100, J values for clinopyroxene are higher than those of orthopyroxene in each sample (Table 3). The highest values of J index of both pyroxenes are always associated with protogranular and protogranular-porphyroclastic rocks and the lowest with porphyroclastic lherzolites. Finally, LS index is broadly negatively and positively correlated to olivine J index and BA index, respectively (Fig. 10a-b).

8. Misorientations

Deformation by dislocation creep causes not only characteristic CPO but also distinct misorientations, ie., changes in crystallographic orientation between two points. Misorientations can occur within grains or across low-angle grain boundaries (ie., subgrains). Since the orientations of subgrain boundaries and the rotation axes of subgrains depend on the dislocations which accumulate within the grain or form the boundaries (Frank, 1950; Amelinckx and Dekeyser, 1959), they can be used to infer the active slip systems during deformation (Lloyd et al., 1991). To this end, inverse pole figures (IPFs) of all rotation axes (< 15°) within all olivine crystal of the EBSD maps were considered (Fig. 7), along with the orientation of the trace of subgrain boundaries of selected olivine crystals (Fig. 11) in specific xenoliths. For instance, the isolated olivine crystal from the protogranular lherzolite BB.08.101 (Figs. 11a-c and 3.1Eb in supplementary electronic material) has subgrain boundaries with a trace subnormal to the [100] axis. This implies that the subgrain walls are mainly tilt boundaries composed of dislocations slipping in the [100] direction. Accordingly, the corresponding IPF (Fig. 11d) illustrates that the rotation axes are distributed between [001] and [010] axes, which implies that the subgrain walls were mainly formed by dislocations of the {0kl}[100] slip systems or "pencil glide". Also, stronger cluster of rotation axes around [010] than around [001] axis (Fig. 11d) suggests the predominance of the (001)[100] slip system over the (010)[100]. Therefore, if deformation was mainly accommodated by "pencil glide" dislocations, the assumption that olivine [100] maxima are parallel to the lineation would be corroborated. In the remaining xenoliths, the activation of the {0kl}[100] slip systems is consistent with the distribution of the rotation axes between [001] and [010] axes in the IPFs (Fig. 7). There are three exceptions (lherzolites SC.11.49, SC.11.52, SC.11.54) with olivine rotation axes very scattered (they are not contoured in Fig. 7). In the other samples, we observe similar densities for the distribution of [001] and [010] rotation axes in three samples (BB.08.59, BB.08.38, CA.12.02), rare [001] maxima (lherzolite BB.08.98) and [010] maxima in eleven samples (61% of the total). The last

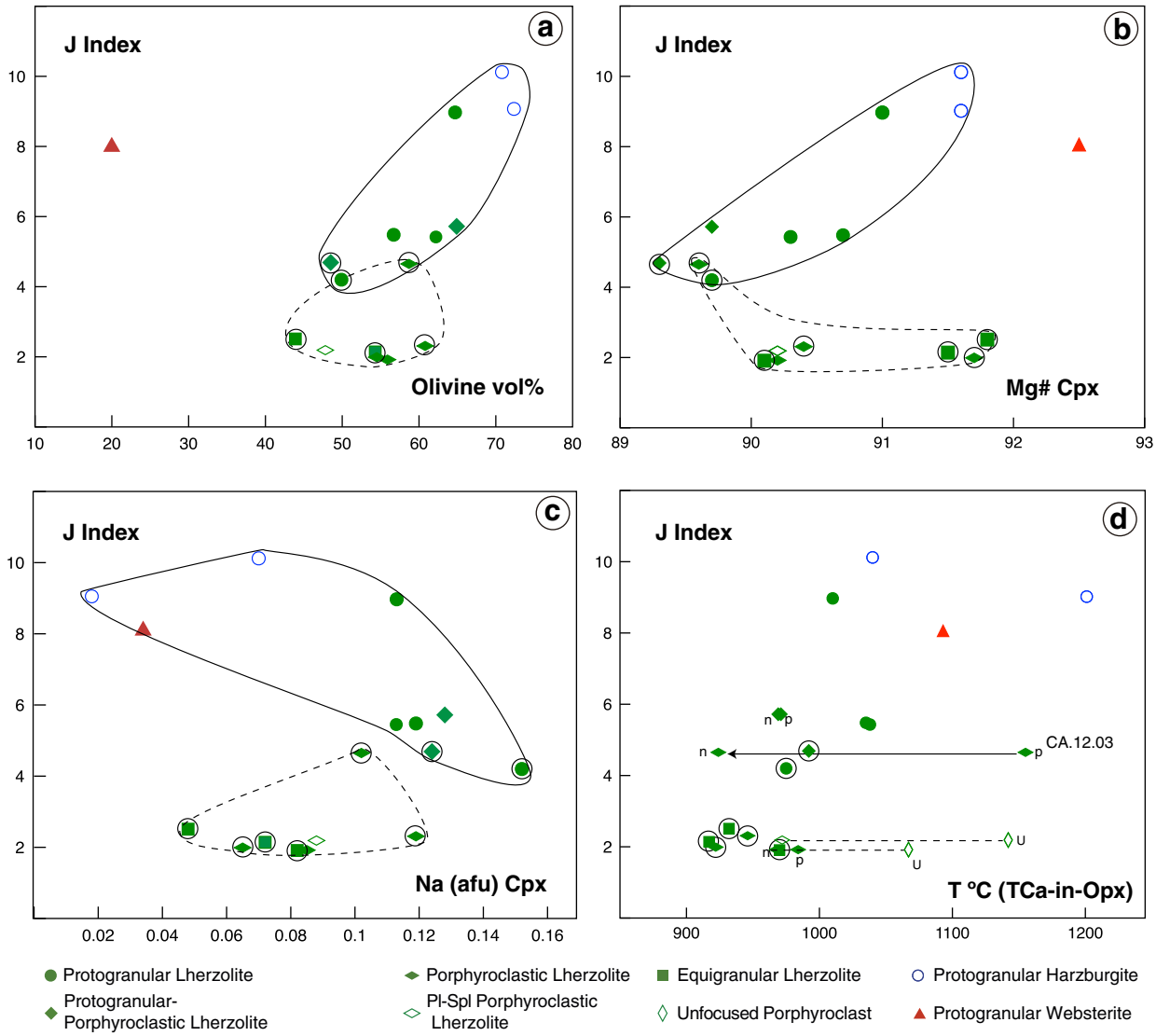

Fig. 9. (a) J index vs. olivine mode. (b) J index vs. Mg# of clinopyroxene (c) J index vs. Na (atoms per fu) in clinopyroxene. (d) T estimates with the $T_{Ca\text{-}in\text{-}opx}$ thermometer of Brey and Köhler (1990) vs. J index. Arrows with a solid line join T values corresponding to porphyroclasts (p) and neocrystals (n) of a single sample. Arrows with a dashed line join T estimates corresponding to unfocused (u) and focused analyses of a single sample. Encircled symbols represent xenoliths with incoherent olivine and clinopyroxene deformation fabrics. Solid line field in Figs a–c: protogranular and protogranular-porphyroclastic peridotites; dashed line field: porphyroclastic and equigranular lherzolites.

distribution suggests the predominance of the (001)[100] slip system over the (010)[100] in more than half of the xenoliths, contradicting the dominant slip system deduced from the AG- and A-type olivine deformation fabrics. This partial disagreement has been observed in other peridotites (Soustelle et al., 2010; Falus et al., 2011; Kaczmarek and Tommasi, 2011; Zaffarana et al., 2014) which leads to the conclusion that dislocations in subgrain boundaries may not be completely representative of the slip system activity. Alternatively, the predominance of the olivine [010] rotation axes could also imply the activation of the (100)[001] slip system (de Kloe, 2001), the presence of which is supported by the occasional presence of traces of subgrain boundaries normal to [001] maxima (Fig. 8.1E in supplementary electronic material).

9. Seismic properties

Calculated seismic properties [velocity and anisotropy of the P (Vp, A) and S-waves (Vs1, Vs2, AVs)] are summarized in Table 3.4E in supplementary electronic material and some of them illustrated in Fig. 12.

Vp patterns are similar in most samples: Vp distribution displays a well-defined maximum aligned with the maximum of olivine [100] axis and a minimum subparallel to the maximum of olivine [010] axis. Vp maximum ranges from 8.78 to 8.33 km/s, Vp minimum from 8.21 to 7.84 and AVp from 10.2 to 2.60%. AVp > 6% are found in protogranular harzburgites, protogranular lherzolites and the websterite, whereas lower values correspond to porphyroclastic and equigranular lherzolites, although there are a few exceptions (eg., CA.12.03).

S-wave birrefringence patterns are more heterogeneous. In most samples, the highest AVs values tend to form one maximum (AVs max) (eg., CA.12.03, CA.44.05, BB.08.20), two maxima (eg., BB.08.98, BB.08.57, BB.08.38, CA.12.02), or a girdle (BB.08.101, BB.12.13, BB.12.01, BB.08.80, SC.11.54, CA.12.02, BB.12.04, SC.11.49) within the structural XY plane ("foliation" defined from the CPO). In the first and the third case, the maximum is normal to the olivine [100] axis ("lineation" defined from the CPO), whereas in the second case, the two maxima are at 45° of the "lineation". Three other lherzolites (BB.08.59, SC.11.16, SC.11.52) are noteworthy because AVs maximum values tend to form a girdle normal to the "foliation" plane and with AVs max only normal to the "lineation". AVs maximum values range from 7.95 to 2.19% (Table 3.4E), with values >4% being registered by most protogranular harzburgites and lherzolites and lower values by porphyroclastic, equigranular lherzolites and the websterite. The lowest AVs value (AVs min) is generally at ca. 45° of both olivine [100] and

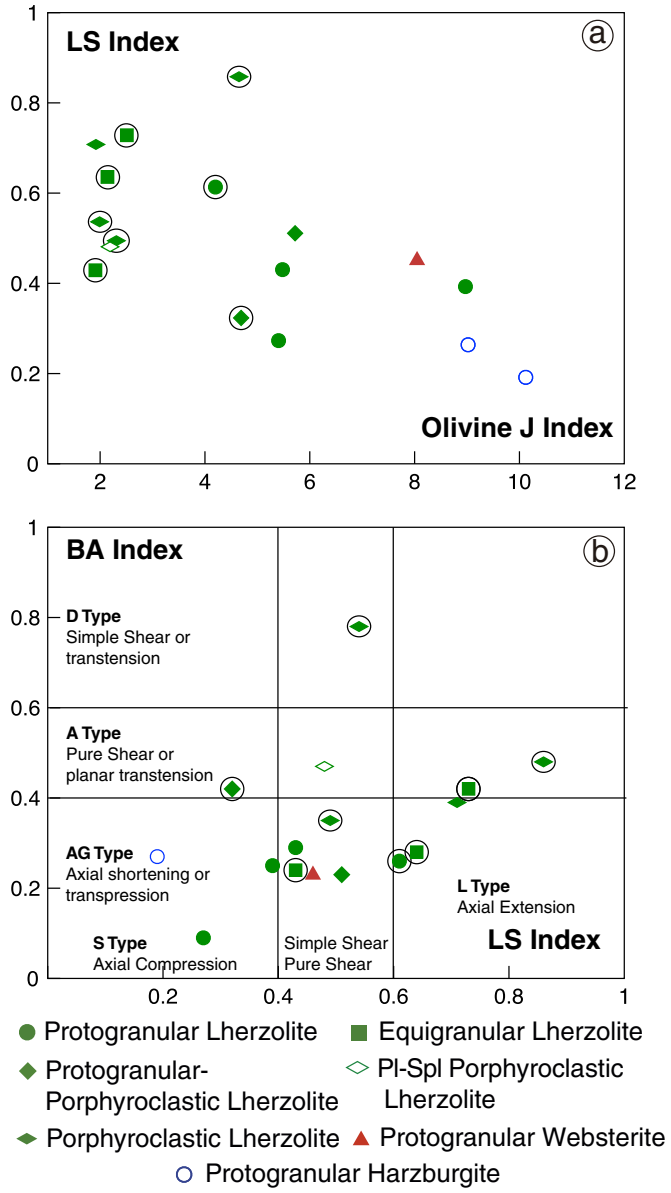

Fig. 10. (a) Clinopyroxene LS index (Ulrich and Mainprice, 2005) vs. Olivine J index. (b) Olivine BA index (Mainprice et al., 2015) vs. Clinopyroxene LS index. Deformation regimes for olivine fabrics after Tommasi et al. (1999) and for clinopyroxene fabrics after Ulrich and Mainprice (2005). Encircled symbols as in Fig. 8.

[010] maxima, and more rarely, parallel (SC.11.16) or normal (BB.08.38, BB.12.17) to the olivine [100] axis.

Finally, S1 tends to be polarized in a plane that contains the propagation direction and the olivine [100] maxima except for SC.11.16 where S1 is polarized in a direction subnormal to the olivine [100] axis (Fig. 12).

Fig. 12 and Table 3.4E also include the estimates for the average seismic properties of the local SCLM using samples weighted according to their abundance [viz., 40% harzburgites, 34% protogranular (-porphyroclastic) lherzolites, and 26% porphyroclastic and equigranular lherzolites, according to Section 3], their respective simplified mode, spinel excluded, and the CPO data in a common standard orientation (the one used for displaying the CPO in Fig. 7). This method would provide a maximum estimate for the local SCLM anisotropy since coherent deformation (similar orientation of foliation and lineation) for the whole mantle column is assumed. The Vp and S-wave birrefringence patterns are similar to those of most protogranular xenoliths.

10. Discussion

10.1. The origin of olivine CPO: relationships with pyroxene CPO, microstructures and deformation

The results of this study indicate that the dominant olivine deformation fabric in mantle xenoliths from NE Spain is [010] fiber (or AG-type) (present in 72% of the total studied samples; Fig. 7; Table 3). This CPO type also shows the highest fabric strength (Figs. 8a, 10b). This fact, along with the coherent orthopyroxene CPO in most of these xenoliths (62%; Table 3), points to deformation by dislocation creep at high T, dry conditions and low stress (Carter and Avé Lallemant, 1970; Tommasi et al., 1999). The AG-type fabric is thought to be less common than the A- and D-types in mantle rocks (Mainprice, 2007) but it has been found in different samples of both orogenic peridotitic massifs (Le Roux et al., 2008; Soustelle et al., 2009; Kaczmarek and Tommasi, 2011; Higgie and Tommasi, 2014) and mantle xenoliths: cratonic (Baptiste et al., 2012), off-craton (Tommasi et al., 2008; Hidas et al., 2007; Kovács et al., 2012) and in oceanic within-plate context (Bascou et al., 2008). In some of these examples, AG-type is the dominant deformation fabric, as in Ronda (Betic orogenic belt, S Spain) and Lanzo massifs (western Alps; Italy) (Soustelle et al., 2009; Higgie and Tommasi, 2014), in the mantle xenoliths of Tok (SE Siberia) (Tommasi et al., 2008) and in the Kerguelen islands (Indian ocean) (Bascou et al., 2008). However the AG-type fabric may be subordinate to other types, as in the nearby peridotitic massif of Lherz (Eastern Pyrenees, France), where the D-type is dominant (Le Roux et al., 2008). The other olivine fabrics in the studied SCLM are A- (22%) and D-type (6%) (Fig. 10b) which share [100] as the main glide direction with the AG-type.

Hypotheses for the origin of AG-type fabric are: (1) deformation by axial shortening or transpression (Nicolas et al., 1973; Tommasi et al., 1999; Vauchez et al., 2000); (2) melt assisted shear deformation at high T and P (Holtzman et al., 2003; Le Roux et al., 2008; Higgie and Tommasi, 2014); (3) simultaneous activation of the (010)[100] and (010)[001] slip systems under high stress and/or high water content or high P conditions (Tommasi et al., 2000; Mainprice et al., 2005; Vauchez et al., 2005; Hidas et al., 2007; Bascou et al., 2011; Jung et al., 2014); and (4), static recrystallization (annealing) (Tommasi et al., 2008; Zaffarana et al., 2014). Hypothesis (1) is characterized by girdle distribution of both olivine [100] and orthopyroxene [001] axes (Tommasi et al., 2006; Le Roux et al., 2008; Bascou et al., 2008; Higgie and Tommasi, 2014), which is only observed here in three lherzolites (BB.08.101, BB.08.98, BB.12.01) and two harzburgites (CA.12.02, BB.08.20) (Fig. 7). However, it is worth noting that deformation by axial shortening and/or simple shear is consistent with the values of the clinopyroxene LS index for most protogranular (-porphyroclastic) lherzolites, harzburgites and the sole websterite, all of them with AG-type fabric and coherent clinopyroxene fabrics (Fig. 10b). Hypothesis (2) posits that melt assisted shear deformation, either during mantle partial melting (Vauchez and Garrido, 2001; Soustelle et al., 2009) or during percolation of basaltic melts (Le Roux et al., 2008; Higgie and Tommasi, 2014), would account for AG-type deformation fabric. In the former case, the olivine mode would be increased due to incongruent melting of orthopyroxene. Local orthopyroxene replacement could also result from olivine crystallization via reaction of the peridotite with an orthopyroxene-undersaturated percolating melt (Kelemen et al., 1998; Dijkstra et al., 2003). Opposite, orthopyroxene would be increased at the expense of clinopyroxene and/or olivine if the percolating melt were SiO_2 (or orthopyroxene) saturated (Kelemen et al., 1992, 1998; Dijkstra et al., 2003), or olivine would be decreased and both pyroxenes ± spinel, garnet or plagioclase be increased, if refertilization reactions had taken place during the basaltic percolation (Lenoir et al., 2001; Dijkstra et al., 2003; Le Roux et al., 2007; Bodinier et al., 2008; Kaczmarek and Müntener, 2008; Rampone et al., 2010; Johanesen and Platt, 2015). However, the following findings do not confirm the hypothesis that pervasive refertilization would have enhanced the

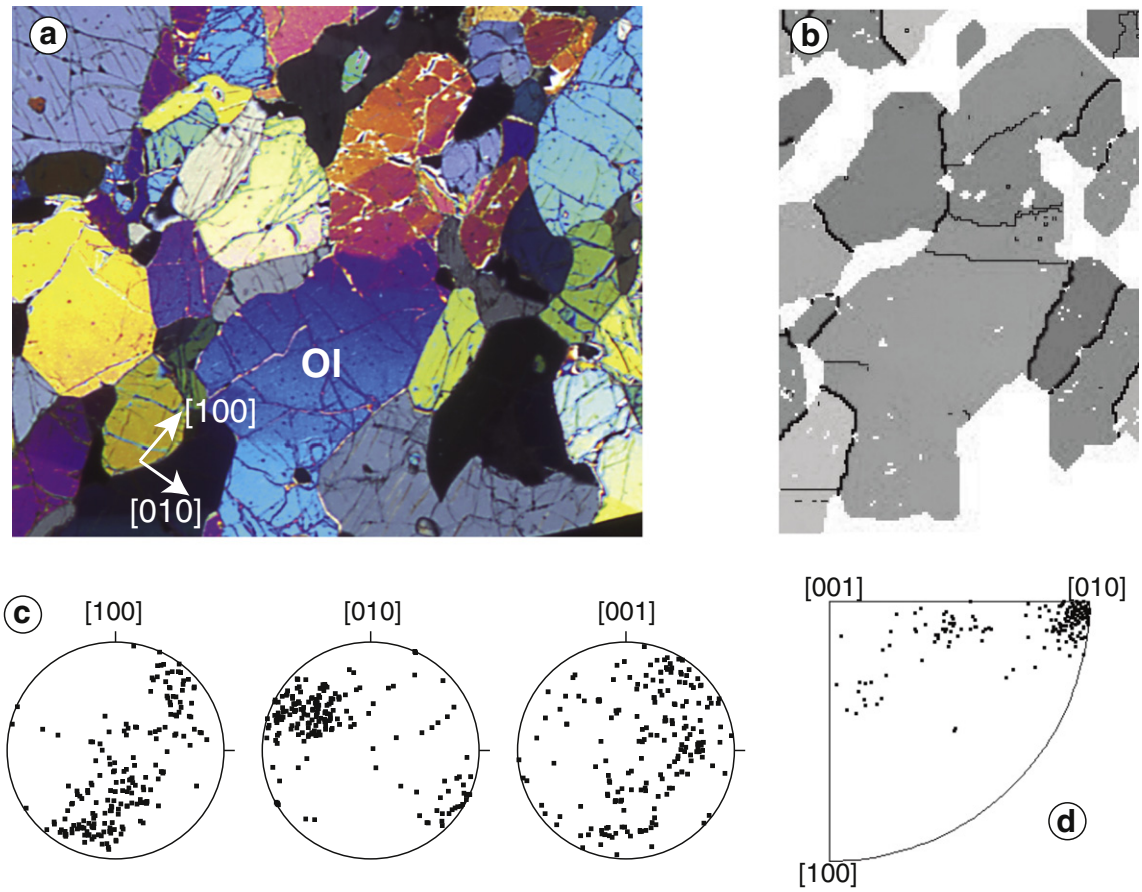

Fig. 11. (a) Large olivine crystal from protogranular lherzolite BB.08.101 with traces of subgrain boundaries subnormal to [100] indicating [100] slip direction. (b) EBSD map of the selected olivine crystal indicating the grain boundaries with thick black lines and subgrain boundaries with finer black lines. (c) Stereograms for the olivine CPO of lherzolite BB.08.101 in the original position (not rotated). (d) Inverse pole figure for the rotation axes of the selected olivine crystal accommodating misorientations of less than 15°.

development of the AG-type fabric in the protogranular (-porphyroclastic) lherzolites and harzburgites: (i) positive correlations of the J index with respect to both the olivine mode and the Mg# of clinopyroxene (Fig. 9a-b); (ii) negative correlations of the J index vs. the clinopyroxene mode (not represented) and the Al and Na (Fig. 9c) content of this mineral; and finally (iii), the scattered projection of the J index vs. orthopyroxene mode (not represented). Other microstructural features evidence of melt-rock reaction are: (i) incoherence between olivine and clinopyroxene CPO (Soustelle et al., 2010; Zaffarana et al., 2014); (ii) interpenetrating olivine-pyroxene boundaries (Dijkstra et al., 2003; Soustelle et al., 2009; Higgie and Tommasi, 2014; Zaffarana et al., 2014); and (iii), olivine inclusions in pyroxenes (Rampone et al., 2010; Soustelle et al., 2010; Zaffarana et al., 2014). Evidence (i) is present here in four lherzolites (CA.44.05, BB.08.80, BB.08.38, SC.11.54), three of which show transitional AG-A and AG-D olivine deformation fabrics (Fig. 7, Table 3). Nevertheless, these incoherent samples also show the lowest J indices (Figs. 8a–c, 10a), suggesting that if refertilization had assisted shear deformation, this process would have decreased the J index and triggered the transformation of the AG-type fabric into the other types, which contradicts hypothesis (2). Finally, sporadic evidence of (ii) and (iii) can be seen in two lherzolites (BB.08.98, BB.12.01) and one harzburgite (CA.12.02) with olivine AG-type fabric; all of them show occasional orthopyroxene crystals with olivine embayment and/or olivine inclusions (Fig. 4a, f). The fact that both microstructural features (ii and iii) are seen in the same sample (Fig. 4f) suggests that the percolating melt was at or just below orthopyroxene saturation (i.e., the reaction olivine + high-Si melt <=> orthopyroxene + low-Si melt would be close to equilibrium). Nevertheless, these occasional microstructures in a few samples do not prove that reactive percolation was widespread and responsible for the dominant olivine AG-type fabric in most xenoliths. Refertilization of earlier refractory harzburgites giving rise to spinel lherzolites via the percolation of MORB-type basaltic melts, was posited for the neighbouring Lherz massif (Le Roux et al., 2007). These refertilized lherzolites show clinopyroxene with LREE depletion and DMM mantle Sr and Nd isotopes, all of which are geochemical features of most lherzolite xenoliths from the CVZ (Galán and Oliveras, 2014). However, it is worth noting that there are significant differences between these two mantle sections: websterites are less frequent in the SCLM of NE Spain than in the Lherz massif; harzburgite xenoliths do not show porphyroclastic microstructure as often as Lherz harzburgites do; lherzolite xenoliths rarely display cm-scale websterite layering such as that seen in the Lherz massif examples; and lastly, olivine AG-type deformation fabric characterizes most protogranular harzburgite and lherzolite xenoliths from the CVZ, whereas both the weakly percolated harzburgites and highly deformed refertilized lherzolites from Lherz have olivine [100]-fiber or D-type fabric and only weakly deformed refertilized lherzolites show [010]-fiber or AG-type fabric (Le Roux et al., 2008). As regards hypothesis (3), simultaneous activation of the slip systems (010)[100] and (010)[001] is not consistent with the P-T equilibrium conditions of these rocks within the spinel lherzolite field. These are considerably lower than those considered responsible for the activation of [001] glide in experimental studies (Couvy et al., 2004; Mainprice et al., 2005; Jung et al., 2009; Ohuchi et al., 2011). However, the presence of H_2O could have also favoured the simultaneous activation of both slip systems at lower P (Jung et al., 2014), but unless H_2O were present in anhydrous minerals, this option would be unlikely since hydrous minerals are rare or absent. Predominance of the

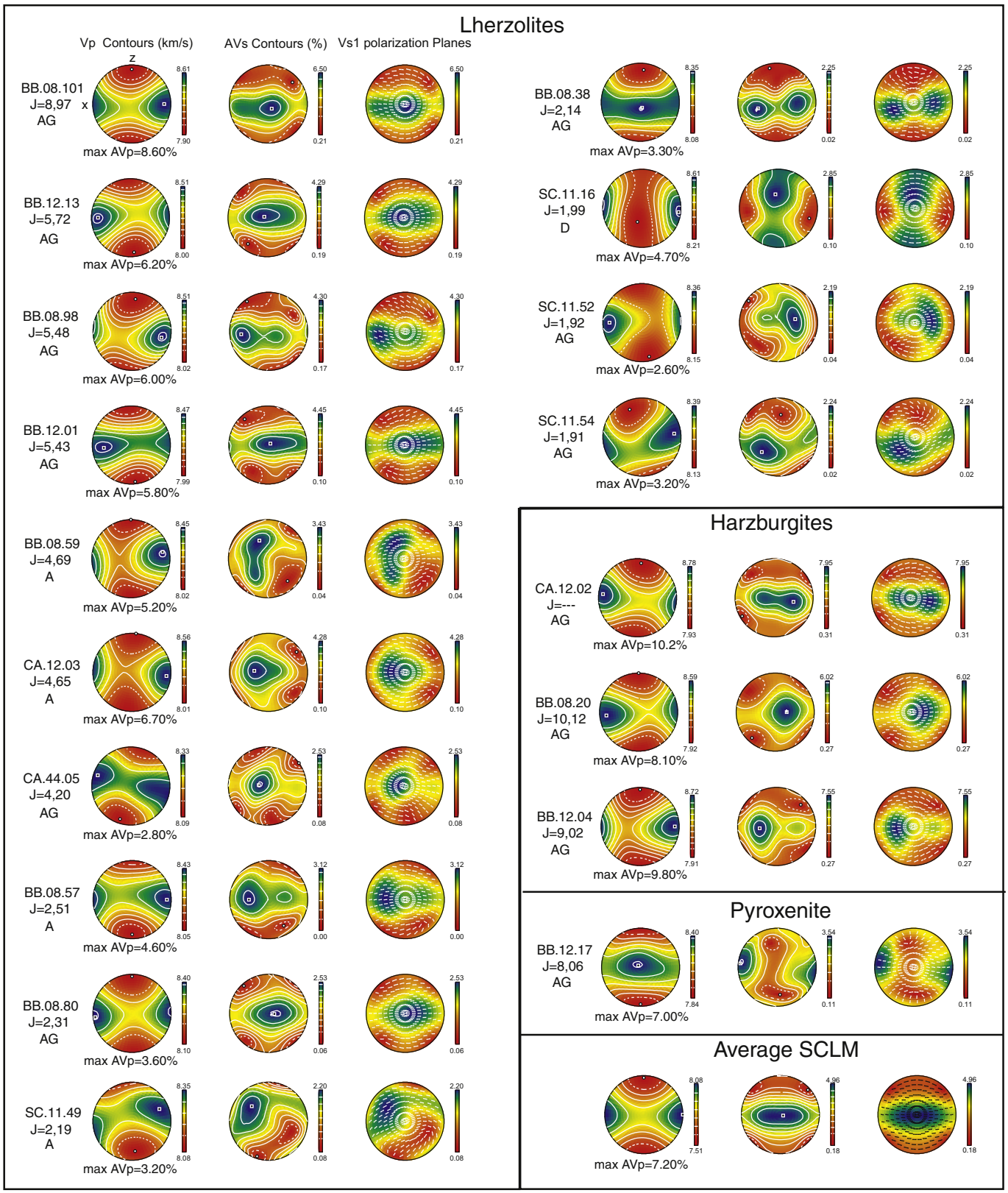

Fig. 12. Calculated seismic properties for mantle xenoliths, ordered by rock type and decreasing olivine fabric strength (J index) as in Fig. 7. 3-D distributions of P wave velocities (Vp), S-wave polarization anisotropy (AVs %) and the orientation of the fast shear-wave polarization plane (S1) are displayed from left to right for each sample. Calculated seismic properties for the average SCLM beneath the CVZ are also included.

(010)[100] slip system would be also consistent with the fact that the MD of olivine [100] axis is higher than that of [001] axis in most xenoliths with AG-type fabric. Finally, static recrystallization or annealing (hypothesis 4) seems to be compatible with: (i) the coarse-grained microstructure characteristic of protogranular peridotites and the websterite, most of them with AG-type fabric (Figs. 3a–c, 7); (ii) the

straight or slightly curved grain boundaries and interfacial angles of 120° among olivine crystals (Fig. 3a,c); and (iii), higher T estimates for these rocks (Figs. 6 and 9d). Grain growth by grain boundary area reduction (GBAR), most likely favoured by diffusion processes, would have taken place subsequent to other accommodating mechanisms of deformation based on dislocation creep, such as subgrain rotation (SR) and GBM recrystallization. In summary, the annealing hypothesis (4) is the most credible explanation for the origin of olivine AG-type deformation fabric in the case study. However the possibility of the AG-type fabric being inherited from earlier deformation stage(s) caused by axial shortening or transpression (hypothesis 1) cannot be completely ruled out, since annealing does not necessarily modify previous fabric (Vauchez and Garrido, 2001; Tommasi et al., 2008). Also, the presence of melt (Hypothesis 2) could have been a factor in deformation and/or annealing events. Taking into account that AG-type olivine fabric exists in harzburgites, lherzolites and the websterite, and since the websterites were interpreted as cumulates from percolating alkaline mafic silicate melts causing cryptic metasomatism in most harzburgites and a few lherzolites (Galán et al., 2008), it is likely that annealing was stimulated by the percolation of low fractions of these metasomatic melts and derivatives.

The other olivine deformation fabrics, A-(orthorhombic) and D-([100]-fiber) types, are mainly seen in finer-grained protogranular-porphyroclastic, porphyroclastic and equigranular lherzolites (Figs. 7, 8a, 10b), all of them with low fabric strength (Fig. 8a, Table 3) and, except for one sample, with incoherent clinopyroxene fabrics (Fig. 10b). According to experimental data (Jung and Karato, 2001), both fabrics are developed by simple shear deformation at dry conditions, low to moderate stress (A-type), high stress (D-Type), and high T, although lower for D-type than for A-type. Numerical simulations of CPO by Tommasi et al. (1999) also indicate deformation by pure shear or plane transpression for the A-type and transtension for the D-type, which agrees with deformation regimes deduced from most clinopyroxene LS index (Fig. 10b). Taking into account that both deformation fabrics are found in finer-grained peridotites, most of them equilibrated at lower T and P than those with AG-type (Figs. 5c, 6, 9d, Table 2), and that they grade to the AG- type in four samples (Table 3; Fig. 7), we deduce that the AG-type was an earlier deformation fabric later transformed into A- and D-types by changes in the deformation regime that happened at higher stress and decreasing T and P. The same conclusion was after the study of mantle xenoliths displaying similar characteristics found in the southeastern Carpathians and San Quintin (Baja California) (Falus et al., 2008; Palasse et al., 2012 and references therein) and in extensional shear zones of orogenic peridotitic massifs (Kaczmarek and Tommasi, 2011). Deformation at decreasing T and P is consistent with: (i) higher T estimates from original compositions of orthopyroxene and clinopyroxene porphyroclasts than from neocrystals (Table 2, Fig. 9c); (ii) clinopyroxene with lower jadeite component (Figs. 5c, 9c) found in porphyroclastic and equigranular lherzolites with A- and D-type fabrics; and (iii), possible activation of the olivine (100)[001] slip system along with the dominant {0kl}[100], as deduced from misorientations in lherzolites with A- and D-type fabrics and transitional of these to AG-type (eg., BB.08.59, CA.12.03, CA.44.05, BB.08.57, SC.11.16 in Figs. 7 and 8.1E in electronic supplementary material) (Carter and Avé Lallemant, 1970; Tommasi et al., 2000 and references therein; Kaczmarek and Reddy, 2013). It is worth noting that clinopyroxene and olivine fabrics in most of these samples are incoherent because olivine [100] axis and clinopyroxene [001] axis are orthogonal and both olivine and clinopyroxene [100] and/or [001] are coaxial (eg., BB.08.59, CA.12.03, BB.08.57, SC.11.16, Table 3). Therefore, the clinopyroxene slip direction may have been [100]. Although very few dislocations in this mineral have Burgers vector b = [100], they have been observed in omphacite from eclogites deformed at low T (Philippot and Van Roermund, 1992; Godard and Van Roermund, 1995) and in clinopyroxene from mantle xenoliths of San Quintin (Baja California), where these dislocations were also related to low T conditions (Palasse et al., 2012). Alternatively, it is likely that during plastic deformation at increasing stress and decreasing T, the olivine [001] slip direction had been also activated (Kaczmarek and Reddy, 2013), as it is documented from the trace of subgrain boundaries (Fig. 8.1E in supplementary electronic material) and from stronger cluster of olivine rotation axes around [010] in most of these lherzolites (Fig. 7). Accordingly the MD of olivine [001] axis is only slightly lower or even higher than the MD of [100] axis in these samples (eg., CA.12.03, CA.44.05; Fig. 7). Therefore, if the olivine [001] slip direction had been also activated, the incoherence between olivine and pyroxene CPO could be apparent. Deformation based on dislocation creep would have been accommodated mainly by SR and GBM recrystallization most likely assisted by diffusion processes. However, microstructural evidence of accommodation by grain boundary sliding has not been observed, eg., four-grain junctions (Lee et al., 2002). On the other hand, it has been suggested that decreasing J indices and incoherent olivine and pyroxene CPO are due to late to post-kinematic melt-rock reaction, causing olivine consumption and the formation of new pyroxenes ± spinel ± garnet ± plagioclase via refertilization processes (Soustelle et al., 2009, 2010; Zaffarana et al., 2014). The presence of reactive-melt flow would have enhanced diffusion processes that contribute to weaken the olivine CPO (Soustelle et al., 2009). In the samples discussed here, when pyroxene J index in porphyroclastic and equigranular lherzolites could be estimated, it is even higher than that of olivine and both are positively correlated (Table 3). These results seem to contradict the late to post-kinematic character of the melt-rock reaction process. Moreover, microstructural evidence of olivine being replaced by clinopyroxene was not observed: grain boundaries between neocrystals of both phases are straight or slightly curved; only porphyroclastic lherzolite CA.12.03 shows occasional orthopyroxene porphyroclasts with both olivine embayment and rare rounded olivine inclusions. It is worth noting that both porphyroclastic lherzolite CA.12.03 (with A-type fabric) and equigranular lherzolite BB.08.57 (A–D type fabric) provide the lowest T estimates, the highest bias between T_{BK} and $T_{Ca\text{-}in\text{-}opx}$ values (Fig. 6) and the highest difference between porphyroclast and neocrystal T in the case of CA.12.03. These thermometric results suggest chemical disequilibrium and cast doubt on the existence of more effective diffusion enhanced by the presence of significant amount of melt during the development of the olivine A- and D-type fabrics. In spite of these drawbacks, the fact that some of these lherzolites are among the most fertile (Fig. 5a-b), with the highest clinopyroxene and the lowest olivine mode (eg., BB.08.57, SC.11.49 in Table 3.1E; Fig. 9a), points in favour of likely melt-rock reaction processes leading to refertilization. Nevertheless, these processes could have been pre-kinematic with respect to the development of olivine A- and D-type fabrics and difficult to recognize from the major element composition of minerals ("stealth metasomatism" of O'Reilly et al., 1997): clinopyroxene of these samples does not show the lowest Mg# but a wide range of values overlapping that of the other lherzolites (Fig. 9b).

10.2. CPOs, seismic anisotropy and modal compositions

The seismic anisotropy of the upper mantle is mainly a function of intrinsic elastic anisotropy of the rock forming minerals, mineral mode, deformation fabric types and strength (Nicolas and Christensen, 1987; Ben Ismaïl and Mainprice, 1998; Mainprice and Silver, 1993; Mainprice et al., 2000).

Relationships between seismic anisotropy patterns and olivine deformation fabrics of the studied xenoliths are as follows: AG-and A-type fabrics share similar seismic anisotropy patterns; the slowest P-waves are normal to the structural XY ("foliation") plane, while the AVs min is at ≈45°of the maximum concentration of olivine [100] axis ("lineation"). However, maximum values of Vp and AVs within the "foliation" plane tend to be more dispersed for AG-type (eg., BB.12.01, BB.08.38) than for A-type fabric (eg., CA.12.03) (Fig. 12). SC.11.16, with olivine D-type symmetry (Fig. 12), shows highly

	Avs (%)	L (km) dt= 0.3s	L (km) dt= 0.8s	L (km) average dt= 0.6s
a) Vertical Foliation 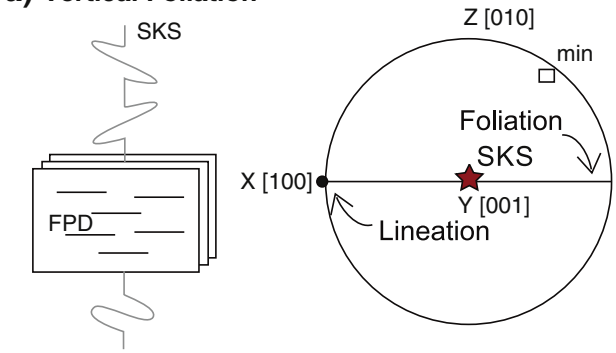	4.96	28	74	51
b) Horizontal Foliation 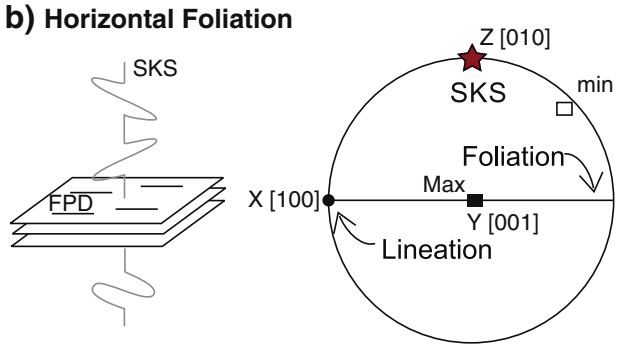	1.00	137	366	251

Fig. 13. Estimated SKS effective path length within the SCLM (L) or thickness of the mantle anisotropic layer (Mainprice and Silver, 1993; Baptiste and Tommasi, 2014) in two different end-members for the orientation of the foliation and lineation. (a) Vertical foliation and horizontal lineation. (b) Horizontal foliation and lineation. Filled and empty squares stand for maximum and minimum values of AVs. SKS splitting δt range and average for the estimates by Díaz et al. (2015) setting aside crustal contribution (Barruol and Mainprice, 1993).

distinctive seismic properties, where the highest AVs values and the S1 polarization plane are orthogonal to the "foliation" (XY) plane, whereas in the other samples they are parallel to it. This is explained by the fact that the olivine [001] axis clearly defines a girdle orthogonal to the olivine [100] axis in this xenolith (Fig. 7).

Moreover, there are positive correlations of AVp and AVs with respect to J indices (Fig. 10.1Ea–b in electronic supplementary material), which means that the dynamic recrystallization observed in porphyroclastic and equigranular lherzolites probably decreased seismic anisotropy. Finally, there are general positive and negative correlations of AVp vs. olivine mode and orthopyroxene mode (Fig. 10.1Ec–d in supplementary electronic material), respectively. No relationship has been observed with clinopyroxene mode. Variation of AVs with respect to mineral mode is similar, but there is a broadly negative correlation with the clinopyroxene mode (not shown).

In summary, our results indicate that the average seismic anisotropy of the SCLM beneath the CVZ is within the range of less fertile lherzolites and refractory harzburgites (Fig. 10.1E) which have most of them protogranular microstructure and stronger olivine deformation fabric than dynamically recrystallized porphyroclastic and equigranular lherzolites.

10.3. Seismic anisotropy from CPO versus seismic data for the SCLM in the NE Spain

Contrasting the average seismic anisotropy of the SCLM estimated from the studied mantle xenoliths (Table 3.1E) with seismic data may help to assess the thickness of the lithosphere and the deformation regime in the area. Shear-wave splitting using SKS phases is one of the most effective seismic methodologies to explore the uppermost mantle anisotropy. However, this method does not provide information about the depth distribution of the anisotropy. The fast polarization directions (FDPs) deduced from SKS-wave splitting are expected to be parallel to the mantle flow direction (Silver and Chan, 1988) and related to the CPO of olivine, which is the main cause of mantle anisotropy (Nicolas and Christensen, 1987). Barruol et al. (1998) and more recently Díaz et al. (2015) deduced the FPDs around N 120 °E and delay time (δt) range of 0.6–1.1 s for stations nearby La Garrotxa sub-zone.

Below the CVZ, AVs estimates range from 2.19 to 7.95%, therefore, the SCLM cannot be discarded in the interpretation of the SKS-wave splitting. However, assessing the SCLM contribution is hindered by the fact that mantle xenoliths provide no information on their original position and orientation. Therefore, we have assumed that Vp max, the highest AVs values and the S1 polarization plane of most samples match the FPD deduced from SKS-wave splitting in the area. That is to say, the olivine [100] axis is generally oriented ≈N120 °E as the FPD, defining a "lineation" within the "foliation" plane, the orientation of which is unknown.

In order to constrain the orientation of this "foliation" plane and to estimate the thickness of the anisotropic layer that cause the observed delay times, we have used the following equation by Mainprice and Silver (1993), following the method used by Baptiste and Tommasi (2014):

$$\delta t = L \times \frac{AVs}{\langle Vs \rangle} \quad (1)$$

where δt is the local S-wave splitting delay time, L is the SKS-wave effective path length, AVs = [Vs max − Vs min]/<Vs> in a particular

direction and <Vs> = [Vs max + Vs min]/2 for the average SCLM. Assuming that δt is mainly due to the SCLM anisotropy (Mainprice and Silver, 1993), with a smaller contribution made by the crust (0.1 s per 10 km; Barruol and Mainprice, 1993), the thickness of which is 30–26 km in this area (Gallart et al., 1984, 1991; Dañobeitia et al., 1992; Galán et al., 2011), then L is the SKS effective path length within the SCLM, ie., its thickness. For the estimates, two end-member orientations were considered: (i) vertical "foliation" and horizontal olivine [100] maxima or "lineation" and (ii) horizontal "lineation" and "foliation" (Fig. 13). SKS-wave splitting δt range (0.6–1.1 s) was taken from Díaz et al. (2015). L estimates so determined (Fig. 13) were compared to existing data on the lithosphere-asthenosphere limit (LAL) in this area. Setting aside the crustal thickness, the thickness average is 51 km for the SCLM in case (i) (Fig. 13a). This is consistent with the depth estimate for the lithosphere asthenosphere limit (LAL) (70–75 km), using gravity and geoid modelling in the shoreline of the Valencia Trough (Ayala et al., 2003) and thermobarometric data in mantle xenoliths from the CVZ (Galán et al., 2011). By contrast, the SCLM thickness average in case (ii) (Fig. 13b) is much thicker (251 km). Therefore, it is inferred that most of the measured seismic anisotropy would be explained by the lithospheric contribution, if the SCLM fabrics record mainly transpression and transtensional deformation. This inference means that the fabrics have the olivine [100] maxima ("lineation") horizontal and orientated ca. N120 °E, like that of the FPD, and the olivine [001] maxima (structural Y direction) vertical. If this were not the case, the seismological data may also be explained by other orientations of the SCLM fabric and a larger contribution of an asthenospheric deformation fabric (Díaz et al., 2015), as has been suggested for other European zones (Klébesz et al., 2015).

10.4. Deformation of the lithospheric mantle in NE Spain

Mineral CPO and resulting anisotropy in the SCLM could be the result of the last significant tectonic event, of the present asthenosphere dynamic flow, or of a combination of both factors (Savage, 1999; Vauchez et al., 2012). The interpretations of the data in the area studied are contradictory. Firstly, based on SKS-wave splitting measurements, Barruol et al. (1998) proposed that the local N120 °E FPD was mainly of lithospheric origin: subvertical E-W to NW-SE Hercynian fabrics at the base of the lithosphere would have been overprinted by similarly orientated but shallower and moderately dipping foliation related to the opening of the ECRIS, during the Miocene. For Barruol et al. (1998), the ECRIS fabrics would not have dominated the SKS signal. Secondly, Barruol et al. (2004) reconsidered the FPD in NE Spain (ie., the mantle flow) in the context of those observed in the South of the Massif Central and SE France, conflating both groups and interpreting their similar characteristics as due to a common Neogene horizontal asthenospheric flow (17–10 Ma) from the hotspot in the South of the Massif Central towards the SE France. This flow would have been induced by the previous sinking of the Apenninic slab (20–17 Ma) towards the NW beneath the Corsica-Sardinia lithospheric block, and its subsequent eastward roll-back causing the opening of the Liguro-Provençal basin (17–10 Ma). As a result, the vacuum left behind by the retreat of the slab would have been filled by the regional asthenospheric flow from the Massif Central that may be preserved since the Neogene. The origin of the anisotropy would, therefore, be related to a present-day frozen mantle flow. However, more recently, Díaz et al. (2015) proposed that the general E-W FPD in the Iberian mantle was mainly due to the current asthenospheric flow related to the absolute plate motion (APM). In spite of this general conclusion, these authors admit the existence of local FPD anomalies which is due to (i) previous "frozen-in" anisotropy caused by Hercynian and/or Alpine deformation and to (ii) the influence of the sinking and roll-back of the Apenninic slab in NE Spain, following Barruol et al. (2004).

Both hypothesis by Barruol et al. (2004) and Díaz et al. (2015) are consistent with subhorizontal foliation in the SCLM of NE Spain. However if this were to be the case, the resulting low vertical anisotropy would require a much thicker lithosphere (Fig. 13b) than that predicted by available data from gravity and geoid modelling (Ayala et al., 2003). Taking these anomalies and also the fact that a mantle is usually deformed coherently with its crust, especially by strike slip faults of lithospheric scale and in transform plate boundaries (Vauchez et al., 2012), we must conclude that the results of the current study are more consistent with the first model by Barruol et al. (1998). On the one hand, the Hercynian orogenesis, which is the most significant in the area, is characterized by late W-E to NW-SE orientated strike-slip faults, compatible with transpressional deformation, in the nearby Pyrenees (Carreras and Capella, 1994; Carreras, 2001). These faults could have deformed not only the crystalline crustal basement, but also caused subvertical foliation in the underlying SCLM which would have resulted in AG-type olivine deformation fabric. Subsequent annealing, probably aided by asthenospheric upwelling during Late Hercynian decompression and Permian and Cretaceous rifting episodes, would have preserved this fabric unchanged. The presence of mantle derived rocks, such as Late Hercynian hornblendites and hornblende gabbros (Butjosa et al., 2013), Permian calcoalcaline to alkaline lamprophyres (Losantos et al., 2000; Enrique, 2009; Ubide et al., 2010) and Cretaceous alkaline lamprophyres (Ubide et al., 2012; Esteve et al., 2014) demonstrate that mantle partial melting and melt percolation through the SCLM took place at those times. Therefore, if melt-rock reaction processes had modified the composition of the SCLM in this area, they would have likely happened at those times. Later on, the Alpine orogenesis was less intense in the Catalan Coastal Ranges than in the Pyrenees, but late Alpine extensional movements did cause the formation of Neogene basins during or post-dating the ECRIS formation. Mantle exhumation during Neogene-Quaternary periods may have taken place through extensional shear zones developed at decreasing T and P (Vauchez et al., 2012). This change in the deformation regime, from dominant transpressive to mainly transtensive, would have reactivated the earlier mantle foliation (Vauchez et al., 2000) and transformed the olivine AG-type fabric into A- and D-types, mainly through SR and GBM dynamic recrystallization most likely accompanied by diffusion processes. These mantle extensional shear zones are probably related to NW-SE Neogene normal faults, such as the Llorà fault (Fig. 1b) with a transtensional component, along which the most recent CVZ volcanoes are aligned (Bolós et al., 2014). The influence of these younger extensive shear zones in the mantle anisotropy would be minor, as suggested by Barruol et al. (1998). This is in agreement with the fact that porphyroclastic and equigranular lherzolites with olivine A- and D-type fabrics are found less frequently, implying that the Neogene deformation affected smaller volumes of the SCLM, and hence has a minor, more local contribution, to the measured SKS-wave splitting. In addition, as suggested by Barruol et al. (1998), the new foliation would be less dipping, but with the lineation orientated (W-E, NW-SE) as in the earlier foliation.

11. Conclusions

The SCLM of NE Spain is mainly formed of spinel lherzolites, harzburgites and pyroxenites (websterites), in decreasing order, as inferred from the mantle xenoliths found. All these rocks are protogranular or coarse-granular, but among lherzolites there are also subordinate porphyroclastic and equigranular microstructures, with gradual transition between them.

Both Mg# and Cr# increase from lherzolite to harzburgite silicates, whereas the reverse is true in spinel. Mineral compositions of websterite silicates are similar to those of harzburgites. No compositional differences were observed between the three microstructural types of lherzolites.

T and P estimates both decrease from protogranular peridotites and the websterite towards pophyroclastic and equigranular lherzolites recrystallized at higher stress.

Harzburgites, the websterite and most lherzolites have olivine AG-type or [010]-fiber deformation fabric. The remaining lherzolites show A-type or orthorhombic fabric, except in one case which shows D-type or [100]-fiber fabric. Transitions between all types are observed. No relationship exists between microstructure types and olivine deformation fabrics, although the highest BA indices correspond to porphyroclastic lherzolites. There are overall positive correlations of olivine mode and equilibrium T with respect to the fabric strength: the J index decreases from protogranular harzburgites, clinopyroxene-poor lherzolites and websterite towards porphyroclastic and equigranular lherzolites equilibrated at lower T and P. In most xenoliths, orthopyroxene and clinopyroxene CPO are coherent with olivine AG- type deformation fabrics. Incoherence between olivine and pyroxene CPO is more frequent in porphyroclastic and equigranular lherzolites with AG-, A- and D-type deformation fabrics. Olivine AG-type fabric is related to deformation by simple shear or transpression, probably associated with late-Hercynian strike-slip shear zones, and to subsequent annealing during late Hercynian decompression, Permian and Cretaceous rifting episodes. All these decompressional events favoured the percolation of mafic magmas through the SCLM causing metasomatism and possible refertilization. Olivine AG-type fabric was transformed later on into A- and D-types through SR and GBM dynamic recrystallization, taking place at higher stress and decreasing T and P. This would have been due to changes in the deformation regime, from simple shear or traspression to mainly transtension, during late Alpine extensional movements that led to the formation of Neogene basins.

Calculated seismic properties indicate that Vp distribution displays a well-defined maximum aligned with the maximum of olivine [100] axis. In most xenoliths, maximum values of AVs are also within the "foliation" plane and the direction of S1 polarization planes tends to be aligned with the olivine [100] axis. Refractory harzburgites, less fertile lherzolites and the websterite show higher anisotropy than the recrystallized porphyroclastic and equigranular lherzolites.

Comparison with available SKS-wave splitting data and assuming that estimates for Vp max, the highest AVs values and the direction of S1 polarization of the average mantle composition match the local FPD (N120 °E), it is inferred that most of the measured seismic anisotropy would be explained by the lithospheric contribution, if the SCLM fabrics record mainly transpression and transtensional deformation.

Supplementary data to this article can be found online at http://dx.doi.org/10.1016/j.tecto.2016.12.023.

Acknowledgments

Financial support for this study was provided by the MINECO research project CGL2011-26700 and the MINECO grants BES-2012-051860 and EEBB-I-14-07880 to MFR. We are much indebted to two anonymous reviewers who helped to improve previous versions of the manuscript. C. Reed is thanked for the English edition of the manuscript.

References

Abramson, E.H., Brown, J.M., Slutsky, L.J., Zang, J., 1997. The elastic constants of San Sarlos olivine to 17 Gpa. J. Geophys. Res. 102, 12253–12263.

Amelinckx, S., Dekeyser, W., 1959. The structure and properties of grain boundaries. Solid State Phys. 8, 325–499.

Ancochea, E., 2004. El vulcanismo neógeno peninsular. In: Vera, J.A. (Ed.), Geología De España. Sociedad Geológica de España- Instituto Geológico y Minero de España, Madrid, pp. 671–672.

Ayala, C., Torne, M., Pous, J., 2003. The lithosphere–asthenosphere boundary in the western Mediterranean from 3D joint gravity and geoid modelling: tectonic implications. Earth Planet. Sci. Lett. 209, 275–290.

Baptiste, V., Tommasi, A., 2014. Petrophysical constraints on the seismic properties of the Kaapvaal mantle root. Solid Earth 5, 1–19.

Baptiste, V., Tommasi, A., Demouchy, S., 2012. Deformation and hydration of the lithospheric mantle beneath the Kaapvaal Craton, South Africa. Lithos 149, 31–50.

Barruol, G., Granet, M., 2002. A tertiary asthenospheric flow beneath the southern French Massif Central related to the west Mediterranean extension evidenced by upper mantle seismic anisotropy. Earth Planet. Sci. Lett. 202, 31–47.

Barruol, G., Mainprice, D., 1993. A quantitative evaluation of the contribution of crustal rocks to the shear wave splitting of teleseismic sks waves. Phys. Earth Planet. Inter. 78, 281–300.

Barruol, G., Souriau, A., Vauchez, A., Diaz, J., Gallart, J., Tubia, J., Cuevas, J., 1998. Lithospheric anisotropy beneath the Pyrenees from shear wave splitting. J. Geophys. Res. 103, 30039–30054.

Barruol, G., Deschamps, A., Coutant, O., 2004. Mapping upper mantle anisotropy beneath SE France by sks splitting indicates Neogene asthenospheric flow induced by apenninic slab roll-back and deflected by the deep alpine roots. Tectonophysics 394, 125–138.

Bascou, J., Tommasi, A., Mainprice, D., 2002. Plastic deformation and development of clinopyroxene lattice preferred orientations in eclogites. J. Struct. Geol. 24, 1357–1368.

Bascou, J., Delpech, G., Vauchez, A., Moine, B.N., Cottin, J.Y., Barruol, G., 2008. An integrated study of microstructural, geochemical, and seismic properties of the lithospheric mantle above the Kerguelen Plume (Indian Ocean). Geochem. Geophys. Geosyst. 9, Q04036. http://dx.doi.org/10.1029/2007GC001879.

Bascou, J., Doucet, L.S., Saumet, S., Ionov, D.A., Ashchepkov, I.V., Golovin, A.V., 2011. Seismic velocities, anisotropy and deformation in Siberian Cratonic Mantle: EBSD data on xenoliths from the Udachnaya Kimberlite. Earth Planet. Sci. Lett. 304, 71–84.

Ben Ismaïl, W., Mainprice, D., 1998. An olivine fabric database: an overview of upper mantle fabrics and seismic anisotropy. Tectonophysics 296, 145–157.

Bianchini, G., Beccaluva, L., Bonadiman, C., Nowell, G., Pearson, G., Siena, F., Wilson, M., 2007. Evidence of diverse depletion and metasomatic events in harzburgite–lherzolite mantle xenoliths from the Iberian Plate (Olot, NE Spain): implications for lithosphere accretionary processes. Lithos 94, 25–45.

Bodinier, J.L., Garrido, C.J., Chanefo, I., Bruguier, O., Gervilla, F., 2008. Origin of pyroxenite–peridotite veined mantle by refertilization reactions: evidence from the Ronda Peridotite (Southern Spain). J. Petrol. 49, 999–1025.

Bolós, X., Barde-Cabusson, S., Pedrazzi, D., Martí, J., Casas, A., Lovera, R., Nadal-Sala, D., 2014. Volcano structural-analysis of La Garrotxa volcanic Field (NE Iberia): implications for the plumbing system. Tectonophysics 642, 58–70.

Brey, G.P., Köhler, T., 1990. Geothermobarometry in four-phase lherzolites II. New thermobarometers, and practical assessment of existing thermobarometers. J. Petrol. 31, 1353–1378.

Bunge, H.J., 1982. Texture Analysis in Materials Sciences. Buttleworth, London (593 pp.).

Butjosa, L., Enrique, P., Galán, G., 2013. Las hornblenditas, gabros y dioritas del macizo del Montnegre (Barcelona, Cordilleras Costero Catalanas). Geogaceta 54, 35–38.

Carreras, J., 2001. Zooming on northern Cap de Creus shear zones. J. Struct. Geol. 23, 1457–1486.

Carreras, J., Capella, I., 1994. Tectonic levels in the palaeozoic basement of the Pyrenees: a review and a new interpretation. J. Struct. Geol. 16, 1509–1524.

Carter, N.L., Avé Lallemant, H.G., 1970. High temperature flow of dunite and peridotite. Geol. Soc. Am. Bull. 81, 2181–2202.

Chai, M., Brown, J.M., Slutsky, L.J., 1997. The elastic constants of an aluminous orthopyroxene to 12.5 Gpa. J. Geophys. Res. 102, 14779–14786.

Collins, M.D., Brown, J.M., 1998. Elasticity of an upper mantle clinopyroxene. Phys. Chem. Miner. 26, 7–13.

Couvy, H., Frost, D.J., Heidelbach, F., Nyilas, K., Ungár, T., Mackwell, S., Cordier, P., 2004. Shear deformation experiments of forsterite at 11 Gpa–1400 °C. in the multianvil apparatus. Eur. J. Mineral. 16, 877–889.

Dañobeitia, J.J., Arguedas, M., Gallart, J., Banda, E., Makris, J., 1992. Deep crustal configuration of the Valencia Trough and its balearic borders from extensive refraction and wide-angle reflection seismic profiling. Tectonophysics 203, 37–55.

De Kloe, R., 2001. Deformation Mechanisms and Melt Nano-Structures in Experimentally Deformed Olivine–orthopyroxene rocks With Low Melt Fractions. An Electron Microscopy Study. (Ph.D. Thesis). Utrecht University (173 pp.).

Díaz, J., Gallart, J., Morais, I., Silveira, G., Pedreira, D., Pulgar, J.A., Dias, N.A., Ruiz, M., González-Cortina, J.M., 2015. From the Bay of Biscay to the High Atlas: completing the anisotropic characterization of the upper mantle beneath the westernmost Mediterranean region. Tectonophysics 663, 192–202.

Dijkstra, A.H., Barth, M.G., Drury, M.R., Mason, P.R.D., Vissers, R.L.M., 2003. Diffuse porous melt flow and melt–rock reaction in the lithospheric mantle at a slow-spreading ridge: a structural petrology and LA-ICP-MS study of the Othris Peridotite Massif (Greece). Geochem. Geophys. Geosyst. 4:8613. http://dx.doi.org/10.1029/2001GC000278.

Donville, B., 1973a. Ages potassium-argon des roches volcaniques de la depresion de La Selva (Nord-Est de L'Espagne). CR Acad. Sci. Paris 277, 1–4.

Donville, B., 1973b. Ages potassium-argon des vulcanites du Bas Ampurdan (Nord-Est de L'Espagne). CR Acad. Sci. Paris 276, 3253–3256.

Droop, G.T.R., 1987. A general equation for estimating Fe^{3+} in ferromagnesian silicates and oxides from microprobe analysis using stoichiometry criteria. Mineral. Mag. 51, 2417–2423.

Enrique, P., 2009. Las espesartitas, camptonitas y bostonitas del complejo intrusivo de Aiguablava (Cadenas Costeras Catalanas): cartografía y composición. Geogaceta 47, 125–128.

Esteve, S., Enrique, P., Galán, G., 2014. The camptonites in the multiple intrusion of Platja Fonda (Girona, NE Spain): mechanisms of intrusion and geochemistry. J. Geosci. 59, 23–40.

Falus, G., Tommasi, A., Ingrin, J., Csaba, S., 2008. Deformation and seismic anisotropy of the lithospheric mantle in the Southeastern Carpathians: a mantle xenolith study. Earth Planet. Sci. Lett. 272, 50–64.

Falus, G., Tommasi, A., Soustelle, V., 2011. Effect of dynamic recrystallization on olivine crystal preferred orientations in mantle xenoliths deformed under varied stress conditions. J. Struct. Geol. 33, 1528–1540.

Fernández-Roig, M., Galán, G., 2015. Microestructuras y química mineral de lherzolitas en xenolitos mantélicos de Cataluña (NE España). Geogaceta 57, 3–6.

Frank, F.C., 1950. Report on the Conference on Plastic Deformation of Crystalline Solids. Carnegie Institut of Technology and Office of Naval Research, Washington (150 pp.).
Galán, G., Oliveras, V., 2014. Melting and metasomatism in the lithospheric mantle of NE Spain: geochemical and Sr—Nd isotopic characteristics. Chem. Geol. 366, 75–89.
Galán, G., Oliveras, V., Paterson, B.A., 2008. Types of metasomatism in mantle xenoliths in Neogene–Quaternary alkaline mafic lavas from Catalonia (NE Spain). In: Coltorti, M., Grégoire, M. (Eds.), Metasomatism in Oceanic and Continental Lithospheric Mantle. Geological Society, London, Special Publication 293, pp. 121–153.
Galán, G., Oliveras, V., Paterson, B.A., 2011. Thermal and redox state of the subcontinental lithospheric mantle of NE Spain from thermobarometric data on mantle xenoliths. Int. J. Earth Sci. 100, 81–106.
Gallart, J., Olivera, C., Correig, A.M., 1984. Aproximación geofísica a la zona volcánica de Olot (Girona). Estudio local de sismicidad. Rev. Geofis. 40, 205–226.
Gallart, J., Pous, J., Boix, F., Hirn, A., 1991. Physical constraints on the crustal structure of the Olot volcanic area, Northeastern Iberian Peninsula. J. Volcanol. Geotherm. Res. 47, 33–44.
Godard, G., Van Roermund, H.L.M., 1995. Deformation-induced clinopyroxene fabrics from eclogites. J. Struct. Geol. 17, 1425–1443.
Goula, X., Olivera, C., Fleta, J., Grellet, B., Lindo, R., Rivera, L.A., Cisternas, A., Carbon, D., 1999. Present and recent stress regime in the Eastern part of the Pyrenees. Tectonophysics 308, 487–502.
Harte, B., 1977. Rock nomenclature with particular relation to deformation and recrystallisation textures in olivine-bearing xenoliths. J. Petrol. 85, 279–288.
Helmstaedt, H., Anderson, O.L., Gavasci, A.T., 1972. Petrofabric studies of eclogite, spinel-websterite, and spinel-lherzolite xenoliths from kimberlite-bearing breccia pipes in southeastern Utah and northeastern Arizona. J. Geophys. Res. 77, 4350–4365.
Hidas, K., Falus, G., Szabó, C., Szabó, P.J., Kovács, I., Földes, T., 2007. Geodynamic implications of flattened tabular equigranular textured peridotites from the Bakony–Balaton Highland volcanic field (Western Hungary). J. Geodyn. 43, 484–503.
Higgie, K., Tommasi, A., 2014. Deformation in a partially molten mantle: constraints from plagioclase-lherzolites from Lanzo, Western Alps. Tectonophysics 615–616, 167–181.
Holtzman, B.K., Kohlstedt, D.L., Zimmerman, M.E., Heidelbach, F., Hiraga, T., Hustoft, J., 2003. Melt segregation and strain partitioning; implications for seismic anisotropy and mantle flow. Science 301, 1227–1230.
Humbert, M., Cey, N., Mullier, J., Esling, C., 1996. Determination of mean orientation from a cloud of orientations. Application to electron backscatterring pattern measurements. J. Appl. Crystallogr. 29, 662–666.
Johanesen, K.E., Platt, J.P., 2015. Rheology, microstructure, and fabric in a large scale mantle shear zone, Ronda Peridotite, Southern Spain. J. Struct. Geol. 73, 1–17.
Jung, H., Karato, S.I., 2001. Water-induced fabric transitions in olivine. Science 293, 1460–1464.
Jung, H., Katayama, I., Jiang, Z., Hiraga, T., Karato, S., 2006. Effect of water and stress on the lattice-preferred orientation of olivine. Tectonophysics 421, 1–22.
Jung, H., Mo, W., Green, H.W., 2009. Upper mantle seismic anisotropy resulting from pressure-induced slip transition in olivine. Nat. Geosci. 2, 73–77.
Jung, H., Park, M., Jung, S., Lee, J., 2010. Lattice preferred orientation, water content, and seismic anisotropy of orthopyroxene. J. Earth Sci. 21, 555–568.
Jung, S., Jung, H., Austrheim, H., 2014. Characterization of olivine fabrics and mylonite in the presence of fluid and implications for seismic anisotropy and shear localization. Earth Planets Space 66, 46.
Kaczmarek, M.-A., Müntener, O., 2008. Juxtaposition of melt impregnation and high- temperature shear zones in the upper mantle; field and petrological constraints from the Lanzo Peridotite (Northern Italy). J. Petrol. 49, 2187–2220.
Kaczmarek, M.A., Reddy, S.M., 2013. Mantle deformation during rifting: constraints from quantitative microstructural analysis of olivine from the East African Rift (Marsabit, Kenya). Tectonophysics 608, 1122–1137.
Kaczmarek, M.-A., Tommasi, A., 2011. Anatomy of an extensional shear zone in the mantle (Lanzo Massif, Italy). Geochem. Geophys. Geosyst. 12, Q0AG06. http://dx.doi.org/10.1029/2011gc003627.
Karato, S.-I., Toriumu, M., Fujii, T., 1980. Dynamic recrystallization of olivine single crystals during high-temperature creep. Geophys. Res. Lett. 7, 649–652.
Karato, S.I., Jung, H., Katayama, I., Skemer, P., 2008. Geodynamic significance of seismic anisotropy of the upper mantle: new insights from laboratory studies. Annu. Rev. Earth Planet. Sci. 36, 59–95.
Katayama, I., Karato, S., 2006. Effects of temperature on the B- to C-type fabric transition in olivine. Phys. Earth Planet. Inter. 157, 33–45.
Katayama, I., Jung, H., Karato, S.I., 2004. New type of olivine fabric from deformation experiments at modest water content and low stress. Geology 32, 1045–1048.
Kelemen, P.B., Dick, H.J.B., Quick, J.E., 1992. Formation of harzburgite by pervasive melt/rock reaction in the upper mantle. Nature 358, 635–641.
Kelemen, P.B., Hart, S.R., Bernstein, S., 1998. Silica enrichment in the continental upper mantle lithosphere via melt/rock reaction. Earth Planet. Sci. Lett. 164, 387–406.
Klébesz, R., Gráczer, Z., Szanyi, G., Liptai, N., Kovács, I., Patkó, L., Pintér, Z., Falus, G., Wesztergom, V., Szabó, C., 2015. Constraints on the thickness and seismic properties of the lithosphere in an extensional setting (Nógrád-Gömör Volcanic Field, Northern Pannonian Basin). Acta Geod. Geophys. 50, 133–149.
Köhler, T.P., Brey, G.P., 1990. Calcium exchange between olivine and clinopyroxene calibrated as a geothermobarometer for natural peridotites from 2 to 60 Kb with applications. Geochim. Cosmochim. Acta 54, 2375–2388.
Kovács, I., Falus, G., Stuart, G., Hidas, K., Szabó, C., Flower, M.F.J., Hegedus, E., Posgay, K., Zilahi-Sebess, L., 2012. Seismic anisotropy and deformation patterns in upper mantle xenoliths from the central Carpathian-Pannonian Region: asthenospheric flow as a driving force for Cenozoic extension and extrusion? Tectonophysics 514–517, 168–179.
Kretz, R., 1983. Symbols for rock forming minerals. Am. Mineral. 68, 277–279.
Le Maitre, R.W., 2002. Igneous Rocks; A Classification and Glossary of Terms. University Press, Cambridge, Cambridge (236 pp.).
Le Roux, V., Bodinier, J.L., Tommasi, A., Alard, O., Dautria, J.M., Vauchez, A., Riches, A.J.V., 2007. The Lherz spinel lherzolite: refertilized rather than pristine mantle. Earth Planet. Sci. Lett. 259, 599–612.
Le Roux, V., Tommasi, A., Vauchez, A., 2008. Feedback between deformation and melt percolation in an exhumed lithosphere–asthenosphere boundary. Earth Planet. Sci. Lett. 274, 401–413.
Lee, K., Jiang, Z., Karato, S., 2002. A scanning electron microscope study of the effects of dynamic recrystallization on lattice preferred orientation in olivine. Tectonophysics 351, 331–341.
Lenoir, X., Garrido, C., Bodinier, J.-L., Dautria, J.-M., Gervilla, F., 2001. The recrystallization front of the Ronda peridotite: evidence for melting and thermal erosion of lithospheric mantle beneath the Alboran Basin. J. Petrol. 42, 141–158.
Lewis, C.J., Vergés, J., Marzo, M., 2000. High mountains in a zone of extended crust: insights into the Neogene-Quaternary topographic development of northeastern Iberia. Tectonics 19, 86–102.
Lloyd, G.E., Schmidt, N.-H., Mainpricc, D., Prior, D.J., 1991. Crystallographic textures. Mineral. Mag. 55, 331–345.
Losantos, M., Montaner, J., Solà, J., Mató, E., Sampsó, J.M., Picart, J., Calvet, F., Enrique, P., Ferrés, M. Y Solé, J., 2000. Mapa geològic de Catalunya 1:25.000, Palafrugell 335- 1-1 (79-25). ICC (Servei Geològic de Catalunya).
Lustrino, M., Wilson, M., 2007. The circum-Mediterranean anorogenic Cenozoic igneous province. Earth Sci. Rev. 81, 1–65.
Mainprice, D., 2007. In: Schubert, G. (Ed.), Seismic Anisotropy of the Deep Earth From a Mineral and Rock Physics PerspectiveTreatise on Geophysics vol. 2. Elsevier Ltd., Oxford, pp. 437–492.
Mainprice, D., Humbert, M., 1994. Methods of calculating petrophysical properties from lattice preferred orientation data. Surv. Geophys. 15, 575–592.
Mainprice, D., Silver, P.G., 1993. Interpretation of sks-waves using samples from the subcontinental lithosphere. Phys. Earth Planet. Inter. 78, 257–280.
Mainprice, D., Barruol, G., Ben Ismaïl, W., 2000. In: Karato, A.M.F.S., Libermann, R.C., Masters, G., Stixrude, L. (Eds.), The Seismic Anisotropy of the Earth's Mantle: From Single Crystal to PolycrystalAGU Geophysical Monograph 117. AGU, Washington, DC, pp. 237–264.
Mainprice, D., Tommasi, A., Couvy, H., Cordier, P., Frost, D.J., 2005. Pressure sensitivity of olivine slip systems and seismic anisotropy of Earth's upper mantle. Nature 433, 731–733.
Mainprice, D., Bachmann, F., Hielscher, R., Schaeben, H., 2015. Descriptive tools for the analysis of texture projects with large datasets using MTEX—strength, symmetry and components. In: Faulkner, D.R., Mariani, E., Mecklenburgh, J. (Eds.), Rock Deformation From Field, Experiments and Theory. A Volume in Honour of Rutter. Geological Society, London, Special publication 409, pp. 251–271.
Martí, J., 2004. La región volcánica de Gerona. In: Vera, J.A. (Ed.), Geología de EspañaSociedad Geológica de España. Instituto Geológico y Minero de España, Ed. pral, Madrid, pp. 672–675.
Martí, J., Pujadas, A., Ferrés, D., Planagumà, L., Mallarach, J.M., 2001. El vulcanisme. Guia de camp de la Zona Volcànica de la Garrotxa. Parc Natural de la Zona Volcànica de la Garrotxa, Generalitat de Catalunya, second ed. Departament de Medi Ambient.
Martínez-Poza, A.I., Druguet, E., Castaño, L.M., Carreras, J., 2014. Dyke intrusion into a pre-existing joint network: the Aiguablava lamprophyre dyke swarm (Catalan Coastal Ranges). Tectonophysics 630, 75–90.
Mercier, J.C.C., Nicolas, A., 1975. Textures and fabrics of upper mantle peridotites as illustrated by xenoliths from basalts. J. Petrol. 16, 454–487.
Morimoto, N., Fabries, J., Ferguson, A.K., Ginzburg, I.V., Ross, M., Seifert, F.A., Zussman, J., Aoki, K., Gottardi, G., 1988. Nomenclature of pyroxenes. Am. Mineral. 73, 1123–1133.
Nicolas, A., Christensen, N.I., 1987. Formation of anisotropy in upper mantle peridotites—a review. In: Fuchs, K., Froidevaux, C. (Eds.), Composition, Structure and Dynamics of the Lithosphere–Asthenosphere System. Geodyn. Ser. AGU, Washington, DC, pp. 111–123.
Nicolas, A., Boudier, F., Boullier, A.M., 1973. Mechanisms of flow in naturally and experimentally deformed peridotites. Am. J. Sci. 273, 853–876.
O'Reilly, S.Y., Chen, D., Griffin, W.L., Ryan, C.G., 1997. Minor elements in olivine from spinel lherzlite xenoliths: implications for thermobarometry. Mineral. Mag. 61, 257–269.
Ohuchi, T., Kawazoe, T., Nishihara, Y., Nishiyama, N., Irifune, T., 2011. High pressure and temperature fabric transitions in olivine and variations in upper mantle seismic anisotropy. Earth Planet. Sci. Lett. 304, 55–63.
Olivera, C., Fleta, J., Susagna, T., Figueras, S., Goula, X., Roca, A., 2003. Seismicity and recent deformations in the northeastern of the Iberian Peninsula. Fís. Tierra 15, 111–114.
Palasse, L.N., Vissers, R.L.M., Paulssen, H., Basu, A.R., Drury, M.R., 2012. Microstructural and seismic properties of the upper mantle underneath a rifted continental terrane (Baja California): an example of sub-crustal mechanical asthenosphere? Earth Planet. Sci. Lett. 345–348, 60–71.
Park, Y., Jung, H., 2015. Deformation microstructures of olivine and pyroxene in mantle xenoliths in Shanwang, eastern China, near the convergent plate margin, and implications for seismic anisotropy. Int. Geol. Rev. 57, 629–649.
Park, M., Jung, H., Kil, Y., 2014. Petrofabrics of olivine in a rift axis and rift shoulder and their implications for seismic anisotropy beneath the Rio Grande rift. Island Arc 23, 299–311.
Philippot, P., Van Roermund, H.L.M., 1992. Deformation processes in eclogitic rocks: evidence for the rheological delamination of the oceanic crust in deeper levels of subduction zones. J. Struct. Geol. 14, 1059–1077.
Prior, D.J., Mariani, E., Wheeler, J., 2009. EBDS in earth Sciences: Applications, common practice, and challenges. In: Schwartz, A.J., Kumar, M., Adams, B.L., Field, D.P. (Eds.), Electron Backscatter Diffraction in Materials Science. Springer, pp. 345–360.
Rampone, E., Vissers, R.L.M., Poggio, M., Scambelluri, M., Zanetti, A., 2010. Melt migration and intrusion during exhumation of the Alboran lithosphere: the Tallante mantle xenolith record (Betic Cordillera, SE Spain). J. Petrol. 51, 295–325.

Roca, E., Desegaulx, P., 1992. Analysis of the geological evolution and vertical movements in the València Trough area, western Mediterranean. Mar. Pet. Geol. 9, 167–185.
Savage, M.K., 1999. Seismic anisotropy and mantle deformation: what have we learned from shear wave splitting? Rev. Geophys. 37, 65–106.
Silver, P.G., Chan, W.W., 1988. Implications for continental structure and evolution from seismic anisotropy. Nature 335, 34–39.
Solé Sabaris, L., 1962. Observaciones sobre la edad del volcanismo gerundense. Mem. Real Acad. Cienc. Artes Barc. 34, 359–372.
Solé, J., Pi, T., Enrique, P., 2003. New geochronological data on the late Cretaceous alkaline magmatism of the northeast Iberian Peninsula. Cretac. Res. 24, 135–140.
Soustelle, V., Tommasi, A., Bodinier, J.-L., Garrido, C.J., Vauchez, A., 2009. Deformation and reactive melt transport in the mantle lithosphere above a large-scale partial melting domain: the Ronda Peridotite Massif, Southern Spain. J. Petrol. 50, 1235–1266.
Soustelle, V., Tommasi, A., Demouchy, S., Ionov, D.A., 2010. Deformation and fluid, a rock interaction in the supra-subduction mantle: microstructures and water contents in peridotite xenoliths from the Avacha Volcano, Kamchatka. J. Petrol. 51, 363–394.
Tommasi, A., Tikoff, B., Vauchez, A., 1999. Upper mantle tectonics: three-dimensional deformation, olivine crystallographic fabrics and seismic properties. Earth Planet. Sci. Lett. 168, 173–186.
Tommasi, A., Mainprice, D., Canova, G., Chastel, Y., 2000. Viscoplastic self-consistent and equilibrium-based modeling of olivine lattice preferred orientations: implications for the upper mantle seismic anisotropy. J. Geophys. Res. Solid Earth 105, 7893–7908.
Tommasi, A., Vauchez, A., Godard, M., Belley, F., 2006. Deformation and melt transport in a highly depleted peridotite massif from the Canadian Cordillera: implications to seismic anisotropy above subduction zones. Earth Planet. Sci. Lett. 252, 245–259.
Tommasi, A., Vauchez, A., Ionov, D., 2008. Deformation, static recrystallization, and reactive melt transport in shallow subcontinental mantle xenoliths (Tok Cenozoic Volcanic Field, SE Siberia). Earth Planet. Sci. Lett. 272, 65–77.
Tournon, J., 1968. Le volcanisme de la province de Gérone (Espagne). Études de basaltes quaternaires et de leurs enclaves. (Thèse 3e Cycle). Université de Paris (120 pp.).
Ubide, T., Lago, M., Arranz, E., Galé, C., Larrea, P., 2010. The lamprophyric sub-vertical dyke swarm from Aiguablava (Catalonian Coastal Ranges): petrology and composition. Geogaceta 49, 75–78.
Ubide, T., Arranz, E., Lago, M., Galé, C., Larrea, P., 2012. The influence of crystal settling on the compositional zoning of a thin lamprophyre sill: a multi-method approach. Lithos 132–133, 37–49.
Ulrich, S., Mainprice, D., 2005. Does cation ordering in omphacite influence development of lattice-preferred orientation? J. Struct. Geol. 27, 419–431.
Van Der Wal, D., Chopra, P., Drury, M., Fitzgerald, J., 1993. Relationships between dynamically recrystallized grain size and deformation conditions in experimentally deformed olivine rocks. Geophys. Res. Lett. 20, 1479–1482.
Vauchez, A., Garrido, C., 2001. Seismic properties of an asthenospherized lithospheric mantle: constraints from lattice preferred orientations in peridotite from the Ronda Massif. Earth Planet. Sci. Lett. 192, 235–249.
Vauchez, A., Tommasi, A., Barruol, G., Maumus, J., 2000. Upper mantle deformation and seismic anisotropy in continental rifts. Phys. Chem. Earth 25, 111–117.
Vauchez, A., Dineur, F., Rudnick, R.L., 2005. Microstructure, texture and seismic anisotropy of the lithospheric mantle above a mantle plume. Insights from the Labait Volcano xenoliths (Tanzania). Earth Planet. Sci. Lett. 232, 295–314.
Vauchez, A., Tommasi, A., Mainprice, D., 2012. Faults (shear zones) in the Earth's Mantle. Tectonophysics 558–559, 1–27.
Vollmer, F.W., 1990. An application of eigenvalue methods to structural domain analysis. Geol. Soc. Am. Bull. 102, 786–791.
Vonlanthen, P., Kunze, K., Burlini, L., Grobety, B., 2006. Seismic properties of the upper mantle beneath Lanzarote (Canary Islands): model predictions based on texture measurements by EBSD. Tectonophysics 428, 65–85.
Woodcock, N.H., Naylor, M.A., 1983. Randomness testing in three-dimensional orientation data. J. Struct. Geol. 5, 539–548.
Zaffarana, C., Tommasi, A., Vauchez, A., Grégoire, M., 2014. Microstructures and seismic properties of south Patagonian mantle xenoliths (Gobernador Gregores And Pali Aike). Tectonophysics 621, 175–197.
Zhang, J., Green, H.W., Bozhilov, K., 2006. Rheology of omphacite at high temperature and pressure and significance of its lattice preferred orientations. Earth Planet. Sci. Lett. 246, 432–443.

"Tot el que som és el resultat del que hem pensat" - Buda